

A FEASIBILITY STUDY OF ROAD CULVERT/BRIDGE DECK DEICING USING GEOTHERMAL ENERGY

FHWA/MT-25-002/9890-784

Final Report



August 2025

prepared for

THE STATE OF MONTANA DEPARTMENT OF TRANSPORTATION

in cooperation with

THE U.S. DEPARTMENT OF TRANSPORTATION
FEDERAL HIGHWAY ADMINISTRATION

August 2025

prepared by

Mohammad Khosravi, Associate Professor

Ethan Turner, Syed Haider Ali Sherazi, Pooria Toomani, Mehran Pourakbar

Kathryn Plymesser, Associate Professor

Kirsten Matteson, Associate Professor

Ladean McKittrick, Assistant Teaching Professor

Neda Nazemi, Assistant Professor

Faraz Dadgostari, Assistant Professor

Montana State University
Bozeman, Montana

You are free to copy, distribute, display, and perform the work; make derivative works; make commercial use of the work under the condition that you give the original author and sponsor credit. For any reuse or distribution, you must make clear to others the license terms of this work. Any of these conditions can be waived if you get permission from the sponsor. Your fair use and other rights are in no way affected by the above.

This public document was published
in electronic format at no cost for printing and distribution.

TECHNICAL REPORT DOCUMENTATION PAGE

General instructions: To add text, click inside the form field below (will appear as a blue highlighted or outlined box) and begin typing. The instructions will be replaced by the new text. If no text needs to be added, remove the form field and its instructions by clicking inside the field, then pressing the Delete key twice. Please remove this field before completing form.

1. Report No. FHWA/MT-25-002/9890-784	2. Government Accession No.	3. Recipient's Catalog No.
4. Title and Subtitle A Feasibility Study of Road Culvert/Bridge Deck Deicing Using Geothermal Energy		5. Report Date August 2025
7. Author(s) Mohammad Khosravi, Ph.D. https://orcid.org/0000-0002-2158-2973 Ethan Turner, M.Sc. http://orcid.org/0009-0000-8505-4515 Syed Haider Ali Sherazi, M.S.c. http://orcid.org/0009-0009-0477-367X Kathryn Plymesser, Ph.D., P.E. http://orcid.org/0000-0003-1915-0474 Kirsten Matteson, Ph.D. http://orcid.org/0000-0001-9367-6867 Neda Nazemi, Ph.D. http://orcid.org/0000-0003-0903-3223 Faraz Dadgostari, Ph.D. http://orcid.org/0000-0002-2965-2470 Pooria Toomani, M.Sc. http://orcid.org/0009-0007-3237-4874 Mehran Pourakbar, Ph.D. https://orcid.org/0009-0001-5738-2770 Ladean McKittrick, Ph.D. http://orcid.org/0000-0002-9168-7404		6. Performing Organization Code
		8. Performing Organization Report No.
		9. Performing Organization Name and Address Montana State University PO Box 172470 Bozeman, MT 59717-2470
12. Sponsoring Agency Name and Address Research Programs Montana Department of Transportation (SPR) 2701 Prospect Avenue PO Box 201001		11. Contract or Grant No. MDT Project # 9890-784
		13. Type of Report and Period Covered Final Report (July 2020-August 2025)
15. Supplementary Notes Conducted in cooperation with the U.S. Department of Transportation, Federal Highway Administration. This report can be found at https://doi.org/10.21949/1529566 Recommend Citation: Khosravi, M., Turner, E., Sherazi, S. H. A., Pourakbar, M., Plymesser, K., Matteson, K., Nazemi, N., & Dadgostari, F. (2025). A feasibility study of road culvert / bridge deck deicing using geothermal energy (FHWA-MT-25-002/9890-784). Montana Department of Transportation. https://doi.org/10.21949/1529566E		14. Sponsoring Agency Code 5401
		16. Abstract: Montana's severe winters challenge bridge infrastructure with snow, ice, and concrete deterioration. Traditional deicing methods are often insufficient, harmful, and costly. This research explored using shallow geothermal energy for sustainable bridge deck deicing. Through lab tests, simulations, and machine learning, the system showed it could keep bridge surfaces above freezing at -10°C with 10°C inlet fluid. Higher inlet temperatures improved performance in colder conditions. The system also reduced thermal strain, potentially extending bridge life. A machine learning framework aids future site selection and cost-benefit analyses. This research supports the Montana Department of Transportation in implementing geothermal deicing systems, improving safety, reducing maintenance, and promoting sustainable infrastructure.

17. Key Words Culverts; bridge decks; deicing; geothermal resources; highway maintenance		18. Distribution Statement No restrictions.	
19. Security Classif. (of this report) Unclassified	20. Security Classif. (of this page) Unclassified	21. No. of Pages 203	22. Price

Form DOT F 1700.7 (8-72)

Reproduction of completed page authorized

Disclaimer Statement

This document is disseminated under the sponsorship of the Montana Department of Transportation (MDT) and the United States Department of Transportation (USDOT) in the interest of information exchange. The State of Montana and the United States assume no liability for the use or misuse of its contents.

The contents of this document reflect the views of the authors, who are solely responsible for the facts and accuracy of the data presented herein. The contents do not necessarily reflect the views or official policies of MDT or the USDOT.

The State of Montana and the United States do not endorse products of manufacturers.

This document does not constitute a standard, specification, policy or regulation.

Alternative Format Statement

Alternative accessible formats of this document will be provided on request. Persons who need an alternative format should contact the Office of Civil Rights, Department of Transportation, 2701 Prospect Avenue, PO Box 201001, Helena, MT 59620. Telephone 406-444-5416 or Montana Relay Service at 711.

CHAPTER 1: INTRODUCTION	1
Problem Statement	1
Overview	2
Overview and Outline	3
CHAPTER 2: SURVEY RESULTS	5
Current Practice in Montana	6
Road Maintenance	6
Cost of Material	7
Culvert Maintenance	8
Request for Weather and Crash Dataset	9
Car Crashes in Montana	9
Weather in Montana	10
CHAPTER 3: LITERATURE REVIEW	16
Shallow Geothermal Energy: Overview	16
Primary Unit	18
Construction Technique	19
Heat exchanger pipes	20
Circulating Fluid	22
Heat Pump System	23
Power Source	24
Secondary Unit	26
Use of Geothermal Energy for Bridge Deicing: Case/Field Studies	29
Case Study 1: Jiangyin, China	29
Case Study 2: Jiangyin, China	31
Case Study 3: Central Switzerland	34
Case Study 4: City of Klamath Falls, Oregon	35
Case Study 5: Mountain Road in Japan	35
Case Study 6: Fukui City, Japan	37
Case Study 7: North Fork of Silver Creek, Oregon	37
Case Study 8: Amarillo, Texas	38
Laboratory Studies of Bridge Deck Deicing Systems	39
Pipe Spacing in the Secondary Unit	39
Borehole Depth in Primary Unit	42
Preheating the deck	42

External Heating Systems	45
Inlet Flow Rate and Temperature	46
Soil Thermal Properties	46
Effect of Bio-Cementation on Thermal Properties of Soil.....	48
Numerical Modeling Studies on the Efficiency of Shallow Geothermal Energy System	50
Inlet Fluid Temperature and Flow Rate	50
Pipe Spacing and Embedded Depth.....	55
Weather Condition (Snowfall Rate, Wind Speed, and Ambient Temperature).....	58
Optimization of Heat Extraction/Injection in Primary Unit.....	62
CHAPTER 4: BRIDGE DECK MODEL DESIGN AND CONSTRUCTION	67
Concrete Mix Design.....	67
An Overview of the Collected Mix Designs.....	67
Admixtures.....	68
Base Mix Design.....	69
Concrete Aggregate Combined Gradation.....	69
Slump Test	72
Thermal Conductivity and Resistivity	73
Numerical Model Development and Validation.....	73
Overview of the Experiments (Bowers, 2016).....	73
Weather Scenarios	74
Severe Winter Weather (February 20-22, 2015).....	74
Moderate Winter Event (February 25-26, 2015)	75
<i>Numerical Simulation of Bridge Deck Snow Melting/De-icing System</i>	76
Bridge Deck Heating and Snow Melting Process.....	77
Boundary Conditions	81
Model Development.....	84
Model Validation	85
<i>Parametric Study</i>	92
<i>Experimental Models</i>	95
<i>Concrete Mixing, Pouring, and Curing</i>	98
<i>Bridge Deck Test Preparation</i>	99
<i>Instrumentation</i>	100
Thermocouple	101
Vibrating Wire Strain Gauge Installation	102
Weather Scenarios and Testing Sequence	103

CHAPTER 5: EXPERIMENTAL RESULTS	106
Application for Bridge Deck Deicing	106
Application for Bridge Deck Snow Melting	108
Application for Mitigating Frost Action	109
Application for Mitigating Thermal Stresses	111
Application for Mitigating Early-Age Cracking	114
CHAPTER 6: NUMERICAL SIMULATION RESULTS	116
Model Development and Validation	116
Results and Discussions	117
<i>Application with 10 °C Inlet Fluid Temperature</i>	119
<i>Application with 50 °C Inlet Fluid Temperature</i>	121
Sensitivity Analysis	123
CHAPTER 7: MACHINE LEARNING BASED FEASIBILITY ANALYSIS OF GEOTHERMAL BRIDGE DECK DEICING SYSTEMS IN MONTANA	126
<i>Bridge Locations and Highways</i>	127
<i>Meteorological Data</i>	128
<i>Data Generation Using COMSOL for ML based feasibility Analysis</i>	135
<i>G.POT Method</i>	138
<i>Energy Balance</i>	139
<i>Energy Results</i>	140
<i>Data Splitting and Experimental Design</i>	143
<i>Model Selection and Training</i>	143
<i>Model Evaluation</i>	144
<i>Performance Results</i>	145
Model 1-Without Tubing:	145
Model 1-With Tubing:	146
Model 2-Without Tubing:	148
Model 2-With Tubing:	150
Feature Importance Analysis	151
<i>Temperature Prediction Interactive Tool</i>	152
CHAPTER 8: NUMERICAL MODELING – CULVERT	154
Model Development and Validation	154
Results and Discussion	155
Parametric Studies	155
Effect of Boundary Conditions	160

Sensitivity Analysis	162
CHAPTER 9: SUMMARY AND CONCLUSION	164
REFERENCES	167
APPENDIX A: SURVEY OF ROAD MAINTENANCE ACTIVITIES WITHIN MONTANA STATE	177
APPENDIX B: SURVEY OF CULVERT MAINTENANCE ACTIVITIES WITHIN MONTANA STATE	180
APPENDIX C: REQUIRED INFORMATION	182

Figure 1. Schematic of Ground Source Heat Pump (GSHP) for bridge deck deicing (redrawn after (Bowers & Olgun, 2014)).....	1
Figure 2. Research Overview.....	2
Figure 3. Road surface conditions of (a) Thompson Fall Section (b) Plains Section (Goodwin, 2003).....	8
Figure 4. Locations of MDT RWIS Sites (Map Source: https://roadreport.mdt.mt.gov/)	10
Figure 5. Monthly average weather data for 2015-2020: (a) ambient temperature, (b) relative humidity (c) wind speed, and (d) precipitation.....	11
Figure 6. Average daily temperature during coldest month, February 2019, in (a) Northern (b) Western (c) Southern (d) Eastern, and (e) Central Montana.....	12
Figure 7. Average daily temperature during warmest month, July 2018, in (a) North (b) West (c) South (d) East (e) Center of Montana.....	13
Figure 8. Percentage of global capacity used by various forms of direct geothermal energy in 2015 (Lund & Boyd, 2016)	16
Figure 9. GSHP system (Han & Yu, 2017).....	17
Figure 10. Closed loop GSHP using for (a) cooling (b) heating of secondary unit (Kavanaugh, 2006)	17
Figure 11. (a) Open-loop system (b) closed-loop system	18
Figure 12. Various attachment arrangements of heat exchanger pipes on the reinforcement cage (Sani et al., 2019).....	20
Figure 13. (a) U-shaped pipes inside an energy pile reinforcing cage (b) instrumented energy pile (Faizal et al., 2019)	21
Figure 14. Different configurations of energy loops within a GEP (Sani et al., 2019).....	21
Figure 15. The reinforcement cage of tested energy piles (a) spiral shaped (b) double U-shaped (Zarrella et al., 2013)	22
Figure 16. Process of the overall heating only in heat pump system.....	24
Figure 17. Simplified schematic of a solar assisted ground-source heat pump system (a. parallel, b. series) (Shahed & Harrison, 2009).....	24
Figure 18. Schematic view of ground-coupled heat pump combined with thermal solar collectors (Trillat-Berdal et al., 2006).....	25
Figure 19. Front and back of a PVT panel (Bakker et al., 2005)	25
Figure 20. Schematic view of tested hybrid system (Bakker et al., 2005).....	26
Figure 21. Schematic of the modified system proposed by Bernier and Shirazi (2007).....	27
Figure 22. Conceptual schematic of ground-source bridge deck deicing (Bowers & Olgun, 2014)	27
Figure 23. (a) A schematic of a possible culvert deicing system based on previous studies on the use of geothermal energy in tunnels and underground structures, (b) Various pipe configuration (c) An energy geotextile installed in an energy tunnel (Loveridge et al., 2020).....	28
Figure 24. (a) Photo of the bridge (b) schematic layout of heating system (Chen et al., 2020)	29

Figure 25. (a) Variation of heat flux, q , with the difference between the inlet fluid and the ambient temperatures, $T_{in}-T_0$, (b) the required inlet fluid temperature and heat flux to keep the deck surface temperature above freezing point (Chen et al., 2020).....	31
Figure 26. (a) Location of the studied section of the bridge (b) photo of bridge deck before pouring concrete (c) layout of bridge deck deicing (Kong et al., 2019)	32
Figure 27. Surface condition of deck surface at different hours (Kong et al., 2019).....	33
Figure 28. (a) Change in the ambient and bridge deck temperatures, (b) variation of the inlet and outlet circulating fluid temperature and the heating power of the deicing system (Kong et al., 2019)	33
Figure 29. (a) Photo of the bridge (b) schematic of a SERSO system in Switzerland (Eugster, 2007).....	34
Figure 30. Comparison of the measured ambient and surface temperature during operation (Eugster, 2007)	34
Figure 31. (a) Longitudinal closed loop on the bridge deck and (b) approach road loops in Klamath Falls, Oregon (Boyd, 2003)	35
Figure 32. Hydronic heating system using underground water storage on a mountain road in Japan (Yoshitake et al., 2011).....	36
Figure 33. Road surface condition on snowy day (a) snow covered road (b) after 9h operating of the system (Yoshitake et al., 2011).....	36
Figure 34. Temperature histories of the water storage, the bridge deck, and the approach road over one year (Yoshitake et al., 2011).....	36
Figure 35. Outline of “pipe in pile” snow melting system (a) heat storage mode during Summer (b) snow melting mode during winter (Nagai et al., 2009).....	37
Figure 36. Surface condition of heated and unheated segments of the bridge deck in Fukui City, Japan in January, 2008 (Nagai et al., 2009)	37
Figure 37. Plan view of the heated deck on Silver Creek bridge, Oregon (Minsk, 1999)	38
Figure 38. (a) Heating circuits before pouring concrete (b) close-up of supply and return manifolds (pipes in center) and thermocouple conduits terminating in enclosure at right on a bridge deck in Amarillo, Texas. (Minsk, 1999).....	39
Figure 39. (a) Location and spacing of energy piles and observation wells (b) experimental deck model. Pipes spacing are 20 cm and 30 cm in the left-side and right-side model deck, respectively. (Bowers Jr, 2016)	40
Figure 40. Photo of the deck model surface during the storm. Heat exchanger pipes have spacing of 30 cm and 20 cm in left-side and right-side model deck, respectively (Bowers Jr, 2016).	40
Figure 41. (a) The layout of experimental set-up (b) initial stage of snow melting process (c) after 30 min operation of snow melt system (Balbay & Esen, 2010).....	43
Figure 42. Variation of top surface temperatures of bridge deck and pavement slab, and air temperatures (a) borehole depth 30 m (100 ft) (b) borehole depth 90 m (295 ft)(Balbay & Esen, 2010).....	43
Figure 43. Photo of bridge surface condition during the test (SFAR: Snow Free Area Ratio) (Liu, 2005).....	44
Figure 44. Recorded average surface temperature of the bridge (Liu, 2005)	44
Figure 45. (a) The schematic of experimental set-up (b) laboratory setup (Yu et al., 2020).....	45

Figure 46. (a) Experimental set up (b) temperature contours after 0.5 day (Ghasemi-Fare et al., 2015) ...	46
Figure 47. Primary heat transfer mechanisms in a thermo-active foundation with heat exchanger pipe embedded in a concrete pile and surrounded by soil (not to scale) (Atalay, 2019)	47
Figure 48. Heat transfer paths in soil (Alrtimi et al., 2016)	47
Figure 49. Thermal conductivity and dry density of MICP-treated sand versus MICP treatment cycles (Wang et al, 2019).....	49
Figure 50. Effect of degree of saturation on (a) thermal conductivity of the MICP-treated and untreated sand (b) improvement in thermal conductivity of the MICP-treated soil (Venuleo et al., 2016)	50
Figure 51. (a) The mesh of deck model (b) distribution of temperature within the bridge deck using boreholes depths of 90 m (295 ft) (Balbay & Esen, 2013)	51
Figure 52. Meshed 3D model (Chowdhury, 2019)	51
Figure 53. Weather data and numerical model results in the coldest day of 2016, December 19, 2016, for inlet fluid temperatures of (a) 22°C (b) 38°C (Chowdhury, 2019)	52
Figure 54. Numerical baseline model configuration of the bridge deck (Yu et al., 2017).....	53
Figure 55. Effect of inlet fluid temperature on (a) average deck surface temperature (b) time required to reach above-freezing point (Yu et al., 2017).....	53
Figure 56. Effect of flow rate on (a) average deck surface temperature (b) time required to reach above-freezing point (Yu et al., 2017)	53
Figure 57. 3D Finite Element model meshing for: (a) whole model, (b) serpentine pipes, and (c) pipes and surrounding concrete (Feng & Yin, 2019).....	54
Figure 58. Surface temperature with variation of inlet flow rate (Feng & Yin, 2019)	54
Figure 59. Contours of (a) surface temperature of heated deck (b) circulating fluid temperature variation, inlet fluid temperature 30°C (86°F), ambient temperature of -25°C (-13°F), and flow rate of 0.21 l/s (0.05 gal/s) (Ho et al., 2019)	55
Figure 60. Temperature of heated pavement versus volumetric flow rate for ambient temperature of (a) -25°C (-13°F) (b) -15°C (5°F)(Ho et al., 2019).....	55
Figure 61. Comparison of surface temperature difference with (a) different pipe embedded depth in terms of pipe spacing of 15 cm (b) different pipe spacing in terms of pipe embedded depth of 15 cm (5.9 inch) (Feng & Yin, 2019).....	56
Figure 62. (a) Numerical baseline model configuration, (b) Numerical modeling mesh (Bowers Jr, 2016)	57
Figure 63. Contours of deck surface temperature for different pipe spacing when the average surface temperature reached above freezing point (Bowers Jr, 2016).....	57
Figure 64. (a) Average deck surface temperature, and (b) time required to reach above-freezing point at top surface of bridge deck (Yu et al., 2017).....	58
Figure 65. (a) Average deck surface temperature and area of deck surface above 0°C (32°F) for different ambient temperatures (b) Distribution of injected energy to the deck and lost energy for different air temperatures (Bowers Jr, 2016)	58

Figure 66. (a) Average deck surface temperature and area of deck surface above 0°C (32°F) for different wind speeds (b) Distribution of injected energy to the deck and lost energy for different wind speeds (Bowers Jr, 2016).....	59
Figure 67. (a) Average deck surface temperature (b) time required to reach above-freezing point at bridge deck surface (Yu et al., 2017)	59
Figure 68. (a) Average deck surface temperature with different snowfall rate (b) deck heating flux per surface area for different snowfall rates (Bowers Jr, 2016).....	60
Figure 69. (a) Mesh of bridge deck model and snow melting system (b) accumulated energy consumption with various snowfall rate (Liu et al., 2019)	61
Figure 70. Effects of key parameters on the efficiency of a geothermal piles after 12 hrs and 60 days of operation (Ghasemi-Fare & Basu, 2016).....	61
Figure 71. (a) Grid arrangement of boreholes (b) the Meshing of the pile and heat exchanger pipes (Bowers Jr & Olgun, 2020).....	62
Figure 72. Different extraction strategies (Bowers Jr & Olgun, 2020).....	63
Figure 73. Comparison of the net energy remaining within the energy pile grids at the end of extraction and end of operational year for three scenarios (Bowers Jr & Olgun, 2020)	64
Figure 74. Temperature distribution and BHE workloads for the optimized case. Each circle represents a BHE with its corresponding load in grayscale. Darker color shades illustrate higher BHE loads. The subsurface temperature distribution at a depth of 50 m (164 ft) is shown by colors, where high absolute temperatures appear in red and lower temperatures in blue (de Paly et al., 2012).	65
Figure 75. The subsurface temperature distribution at depth of 50 m for the optimized case and the equal heat extraction case (Beck et al., 2013)	66
Figure 76. Individual Grain Size Distribution Curves	70
Figure 77. Coarseness Factor Chart of Concrete Mix Designs	71
Figure 78. a) 0.45 Power Chart, and b) Percent Retained Chart of the Collected Mix Designs	71
Figure 79. Two proposed Concrete Mixtures after 28-day Strength Test.....	72
Figure 80. Thermal Test Setup.....	73
Figure 81. (a) Layers of reinforcement and the configuration of heat exchanger pipes, (b) Location of studied temperature sensors (plan view), and (c) Location of studied temperature sensors deck (cross section) (Bowers, 2016).....	74
Figure 82. Photograph showing the poured concrete into the deck frame works (Bowers, 2016)	74
Figure 83. Recorded surface temperature of the heated and non-heated decks, ambient temperature, cumulative snowfall, and photo of the deck model surface during the storm after: (a) 2.5 hours (b) 19.5 hours, (c) 24.5 hours, (d) 41 hours, (e) 48.5 hours of heating system operation (Bowers, 2016).....	76
Figure 84. Recorded surface temperature of the heated and non-heated decks, ambient temperature, cumulative snowfall, and photo of the deck surface condition during the test: (a) 2.5 hours, and b) 7.5 hours after the storm began (Bowers, 2016).	77
Figure 85. Heat transfer mechanisms involved in bridge heating and snow melting process	77
Figure 86. Interpretation of snow melting model proposed by Bowers (2016)	81

Figure 87. (a) The bridge deck model configuration, (b) Meshed 3D model	85
Figure 88. Experimentally recorded and predicted time histories of inlet and outlet fluid temperature.....	86
Figure 89. Comparison between experimental results and numerically predicted values of temperature at the top, middle, and bottom location within the bridge deck at (a) cross-section with heat exchanger pipes, (b) cross-section without heat exchanger pipes	87
Figure 90. The progression of the cross-sectional temperature and the top surface temperature over time obtained in this study	88
Figure 91. Variation of ambient and sky temperature during the experimental test and input heat fluxes to the numerical model (Bowers, 2016).....	88
Figure 92. Experimentally recorded and predicted time histories of inlet and outlet fluid temperature.....	89
Figure 93. Comparison between experimental results and numerically predicted values of temperature at the top, pipes, middle, and bottom locations within the deck at cross-section with heat exchanger pipes.	90
Figure 94. Comparison between experimental results and numerically predicted values of temperature at the top and middle locations within the deck at cross-section without heat exchanger pipes	91
Figure 95. Progression of the cross-sectional temperature and top surface temperature over time obtained in this study	91
Figure 96. Parametric study results for ambient temperature	92
Figure 97. a) Parametric study results for Base Model and Smaller Model and b) schematic of Base Model and Smaller Model.....	93
Figure 98. Parametric study results for a) top reinforcement cover and b) inlet fluid flow rate.....	94
Figure 99. Parametric study of a) heat exchanger pipe spacing and b) inlet fluid temperature	95
Figure 100. Model 1 design: a) 3D view, b) plan view with surface locations of sensors, and c) section views with depth location of sensors.	96
Figure 101. Model 2 Design: a) 3D view, b) plan view with surface locations of sensors, and c) section views with depth location of sensors.	97
Figure 102. a) Bridge deck model form and b) finished reinforcement grids.....	98
Figure 103. Completed form.....	98
Figure 104. a) Initial 24-hour set and b) 28-day damp towel cure.....	99
Figure 105. Cured bridge deck model.....	99
Figure 106. Bridge deck model prepared for testing.....	100
Figure 107. a) Instrumentation schematic and b) proposed locations of thermocouples and strain gauges	101
Figure 108. a) Thermocouples before welding, b) thermocouple welder, c) and welded thermocouple..	101
Figure 109. a) Completed form with thermocouples and b) closeup of placed thermocouple	102
Figure 110. Temperature sensor for monitoring thermal behavior of snow	102
Figure 111. a) Strain gauges with mounting blocks ready for epoxy and b) installed strain gauges	103

Figure 112. Montana Monthly Average Ambient Temperature for 2015-2020.	103
Figure 113. Ambient temperature and solar intensity of Model 1 weather scenarios: a) Synthetic and b) Daily Fluctuation.	104
Figure 114. Experimental testing plan for snow tests showing ambient temperature and solar intensity for a) Without geothermal system in operation and b) With geothermal system in operation - Stage 1: no snow; Stage 2: with snow/no solar; Stage 3: with snow/with solar.....	105
Figure 115. Collection and application of fresh snow on bridge deck surface to simulate realistic winter precipitation	105
Figure 116. Top surface thermocouple results for a) Synthetic and b) Daily Fluctuation Weather Scenarios without deicing system active.	107
Figure 117. Top surface thermocouple results for a) Synthetic and b) Daily Fluctuation Weather Scenarios with deicing system active.	107
Figure 118. Temperature results for with (dashed lines) and without (solid lines) geothermal system for a) Snow sensors and b) Top surface thermocouples – dashed lines: with the geothermal systems (Stage 1: no snow; Stage 2: with 1 in snow/no solar; Stage 3: with 1 in snow/with solar); solid lines: without geothermal system (Stage 1: no snow; Stage 2: with 3 in snow/no solar; Stage 3: with 3 in snow/with solar)	109
Figure 119. TA7 thermocouple results for a) Synthetic and b) Daily Fluctuation Weather Scenarios without deicing system active	110
Figure 120. TA7 thermocouple results for a) Synthetic and b) Daily Fluctuation Weather Scenarios with deicing system active.	110
Figure 121. Thermal stress mechanisms due to temperature profiles and support conditions. (regenerated based on Radolli & Green 1975).....	112
Figure 122. Top surface strains calculated from TA8 and measured from strain gauges for Model 1: a) Synthetic and b) Daily Fluctuation Scenarios	113
Figure 123. Average strains through depth of Model 1 calculated from TA7 thermocouples for the a) Synthetic and b) Daily Fluctuation Weather Scenarios	113
Figure 124. Temperature gradients from TA5 thermocouples for a) Synthetic and b) Daily Fluctuation Weather Scenarios.	114
Figure 125. Model 2 (with system) and Model 2c (without system) thermocouple results at each depth.	115
Figure 126. Predicted and experimental temperature results for the (a) Synthetic and (b) Daily Fluctuation Scenarios and strain results for the (c) Synthetic and (d) Daily Fluctuation Scenarios	118
Figure 127. (a) Positive vertical temperature gradient in concrete and steel superstructures (AASHTO 2021) and (b) positive vertical temperature gradient for bridge deck in Montana.....	119
Figure 128. (a) Average surface and minimum temperature and (b) average strain from thermal movement for 10 °C inlet temperature	120
Figure 129. Temperature profile through the bridge deck for 10 °C inlet temperature	121
Figure 130. (a) Average surface and minimum temperature and (b) average strain from thermal movement for 50 °C inlet temperature	122

Figure 131. Temperature profile through the bridge deck for 50 °C inlet temperature	123
Figure 132. Effect of various parameters on top surface temperature (a) without and (b) with solar radiation	124
Figure 133. Effect of various parameters on the minimum concrete temperature (a) without and (b) with solar radiation.....	124
Figure 134. Effect of various parameters on strain due to thermal movement (a) without and (b) with solar radiation	125
Figure 135. Effect of various parameters on the temperature gradient between the top and bottom surfaces (a) without and (b) with solar radiation	125
Figure 136. (a) Map of bridges and major roads, and (b) electric transmission lines locations in Montana	127
Figure 137. Locations of MDT RWIS stations across Montana.....	128
Figure 138. (a) Locations of MDT RWIS sites (map source: https://roadreport.mdt.gov/), (b) average ambient temperature distribution histogram for Montana, and (c) time series of ambient temperatures for 2016–2019 (site ID 150000)	129
Figure 139. Monthly average ambient temperature across Montana	130
Figure 140. a) Histogram of wind speed distribution, and b) Coefficient of variation for wind speed in Montana	131
Figure 141. Monthly average precipitation across Montana.....	132
Figure 143. Lithologies in Montana.....	133
Figure 144. Soil thermal properties across Montana: (a) spatial distribution of thermal conductivity based on USGS soil classification, and (b) spatial distribution of thermal capacity based on USGS soil classification	134
Figure 145. Ground temperature characteristics across Montana: (a) normalized frequency distribution of ground temperatures, (b) ground temperature versus depth, and (c) spatial distribution of ground temperatures and well locations.....	135
Figure 146. Distribution histograms of important features, a) Ambient temperature, b) Wind speed, c) Solar radiation, and d) Inlet temperature.....	136
Figure 147. Montana split into three energy modes based on the total energy demand over the year	141
Figure 148. Available Energy Analysis Results	141
Figure 149. Energy Demand Analysis Results	142
Figure 150. Machine learning model development process.....	Error! Bookmark not defined.
Figure 151. Schematic for stabilized temperature, time to reach stabilized temperature, and time to reach above 0oC	144
Figure 152. Outputs from Model 1 and Model 2	144
Figure 153. MAE, RMSE, and R2 score comparison for Model 1 without tubing for Stabilized temperature, time to reach stabilized temperature, and time to reach above 0oC.....	146

Figure 154. MAE, RMSE, and R2 score comparison for Model 1 with tubing for Stabilized temperature, time to reach stabilized temperature, and time to reach above 0oC.....	147
Figure 155. MAE, RMSE, and R2 score comparison for Model 2 output without tubing	149
Figure 156. MAE, RMSE, and R2 score comparison for Model 2 output with tubing	150
Figure 157. Permutation-based feature importance for FCNN model predictions visualized as radar plot: a) without tubing, and b) with tubing.....	151
Figure 158. Interactive map of Montana showing bridge deck locations	152
Figure 159. Input parameters interface for: (a) fixed parameters, and (b) variable parameters.....	153
Figure 160. Predicted surface temperature over time for a two-segment “with tubing” scenario	153
Figure 161. Effect of different ambient temperatures along the studied cut line.....	156
Figure 162. (a) Effect of different operational times on temperature along the studied cut line, (b) temperature contours after 5 hours, and (c) temperature contours after 45 hours.....	157
Figure 163. (a) Effect of different tube spacings on temperature along the studied cut line, and (b) plan view of culvert showing tube spacing.....	158
Figure 164. Effect of different fluid flow rates on temperature along the studied cut line.....	159
Figure 165. Effect of thermal conductivity of soil on temperature along the studied cut line.....	160
Figure 166. (a) Effect of ambient temperature with ice inside culvert along the studied cut line, (b) temperature contours after 5 hours, and (c) temperature contours after 50 hours.....	161
Figure 167. (a) Effect of ambient temperature with water inside culvert along the studied cut line, (b) temperature contours after 5 hours, and (c) temperature contours after 50 hours.....	162

Table 1. Fundamental strategies of MDT for road maintenance operation in winter	6
Table 2. The lowest practical melting temperature of winter maintenance materials.....	7
Table 3. MDT Winter Maintenance Annual Averages (Goodwin & Pisano, 2003).....	8
Table 4. Montana statewide car crashes due to slippery road surface conditions.....	9
Table 5. Average daily weather data obtained for five major cities in Montana	14
Table 6. Case/Field studies of bridge deck deicing/anti-icing using GSHP systems.....	30
Table 7. Experimental studies of bridge deck deicing – Secondary Unit	41
Table 8. Experimental studies of bridge deck deicing – Primary Unit	41
Table 9. Gradation and Gradation Properties of Concrete Mix Designs’ Aggregates	68
Table 10. Ingredients of the Collected Concrete Mix Designs	68
Table 11. Aim of Air Contents, and Admixtures’ Dosages of the Collected Mix Designs	69
Table 12. Mix Proportions for 2.5 cu. ft. Mix.....	69
Table 13. Average Compressive Strengths of the Collected and Proposed Concrete Mix Designs	72
Table 14. Properties of Proposed Concrete Mixture Designs	72
Table 15. Thermal Conductivity of Proposed Concrete Mix Designs	73
Table 16. Selected weather parameters and experimental test results of snow melting	75
Table 17. List of the material properties of the experimental and numerical models (Bowers, 2016)	85
Table 18 .Material properties of the experimental and numerical models.....	117
Table 19. Different levels of percentiles for empirical values and fitted distributions for ambient temperature, wind speed, and solar radiation.....	136
Table 20. Mean and standard deviation of fitted distributions for inlet temperature.....	137
Table 21. Parameter ranges, combinations and total number of models for generating the dataset without tubing from the numerical model.....	137
Table 22. Parameter ranges, combinations and total number of models for generating the dataset with tubing from the numerical model.....	138
Table 23. QBHE Variables	139
Table 24. Machine learning models used with the features and target variables for Model 1 and Model 2	143
Table 25. MAE, RMSE, and R2 score values for Model 1 without tubing for Stabilized temperature, time to reach stabilized temperature, and time to reach above 0oC.....	147
Table 26. MAE, RMSE, and R2 score values for Model 1 with tubing for Stabilized temperature, time to reach stabilized temperature, and time to reach above 0oC.....	148
Table 27. MAE, RMSE, and R2 score values for Model 2 output without tubing	149
Table 28. MAE, RMSE, and R2 score values for Model 2 output with tubing	151

STANDARD CONVERSION TABLE – ENGLISH TO METRIC				
<u>Symbol</u>	<u>To convert from</u>	<u>Multiply by</u>	<u>To determine</u>	<u>Symbol</u>
<u>LENGTH</u>				
IN	inch	25.4	millimeters	mm
FT	feet	0.3048	meters	m
YD	yards	0.9144	meters	m
MI	miles	1.609344	kilometers	km
<u>AREA</u>				
SI	square inches	645.16	square millimeters	mm ²
SF	square feet	0.09290304	square meters	m ²
SY	square yards	0.83612736	square meters	m ²
A	acres	0.4046856	hectares	ha
MI ²	square miles	2.59	square kilometers	km ²
<u>VOLUME</u>				
CI	cubic inches	16.387064	cubic centimeters	cm ³
CF	cubic feet	0.0283168	cubic meters	m ³
CY	cubic yards	0.764555	cubic meters	m ³
GAL	gallons	3.78541	liters	L
OZ	fluid ounces	0.0295735	liters	L
MBM	thousand feet board	2.35974	cubic meters	m ³
<u>MASS</u>				
LB	pounds	0.4535924	kilograms	kg
TON	short tons (2000 lbs)	0.9071848	metric tons	t
<u>PRESSURE AND STRESS</u>				
PSF	pounds per square foot	47.8803	pascals	Pa
PSI	pounds per square inch	6.89476	kilopascals	kPa
PSI	pounds per square inch	0.00689476	megapascals	Mpa
<u>DISCHARGE</u>				
CFS	cubic feet per second	0.02831	cubic meters per second	m ³ /s
<u>VELOCITY</u>				
FT/SEC	feet per second	0.3048	meters per second	m/s
<u>INTENSITY</u>				
IN/HR	inch per hour	25.4	millimeters per hour	mm/hr
<u>FORCE</u>				
LB	pound (force)	4.448222	newtons	N
<u>POWER</u>				
HP	horsepower	746.0	watts	W
<u>TEMPERATURE</u>				
°F	degrees Fahrenheit	5 X (°F – 32)/9	degrees Celsius	°C
<u>DENSITY</u>				
lb/ft ³	pounds per cubic foot	16.01846	kilograms per cubic meter	kg/m ³
<u>ACCELERATION</u>				
g	freefall, standard	9.807	meters per second squared	m/s ²

TO CONVERT FROM METRIC TO ENGLISH, DIVIDE BY THE ABOVE CONVERSION FACTORS.

CHAPTER 1: INTRODUCTION

Problem Statement

Snow and ice accumulation on bridge decks significantly reduces roadway safety, increases traffic delays, and accelerates deterioration of bridge infrastructure. The most widely used deicing method involves salts and chemical agents. However, these are largely ineffective below -9.4°C (15.1°F) and contribute to long-term damage to reinforced concrete (RC) bridges. Salt accelerates steel corrosion, reduces reinforcement cross-section, and leads to premature maintenance and rehabilitation needs (Granata & Hartt 2009; Yunovich et al. 2003). Bridge decks also face damage from thermal stresses, frost action, and early-age cracking, particularly in cold climates. Thermal stresses, resulting from restrained movements and thermal gradients, can exceed live load stresses and induce cracking (Johnson 2005; Reynolds & Emanuel 1974; Roeder & Moorty 1991; Rojas et al. 2014). These cracks permit moisture and deicing chemicals to penetrate, compounding steel corrosion and frost-related damage (Wardeh et al. 2011; Babaei & Fouladgar 1997; Johnson 2005). Though measures such as air entraining admixtures (Jackson 1944; Tunstall et al. 2021) and controlled curing practices (Wan et al. 2010; Deng et al. 2016) are helpful, they often depend on environmental conditions and construction quality.

Recently, new materials and innovative techniques such as hydronic heating systems have been used to remove ice and snow from transportation infrastructure. Several heated pavement systems have been proposed including electrically heated pavements and hydronically heated pavements. Electrically heated pavements can be utilized wherever electricity is available, however, the high voltage required and the high operation cost of using electricity discourage the widespread use of this system (Fliegel et al., 2010). Using a hydronic heating system for removing snow and ice from bridge decks has received more attention in recent years. Heat can be extracted from shallow or deep layers of earth through thermo-active foundations or boreholes based on mechanisms of heat transfer including convection, conduction and radiation (Lund & Boyd, 2016; Ghasemi-Fare & Basu, 2016). Seasonal variation of ground temperature is minimal at a depth approximately 6-9 m (20-30 ft) below the ground surface (Kusuda & Achenbach, 1965). Shallow geothermal loops below that depth are, thus, good alternatives to piles and wells for harvesting geothermal energy through heat exchange with the ground.

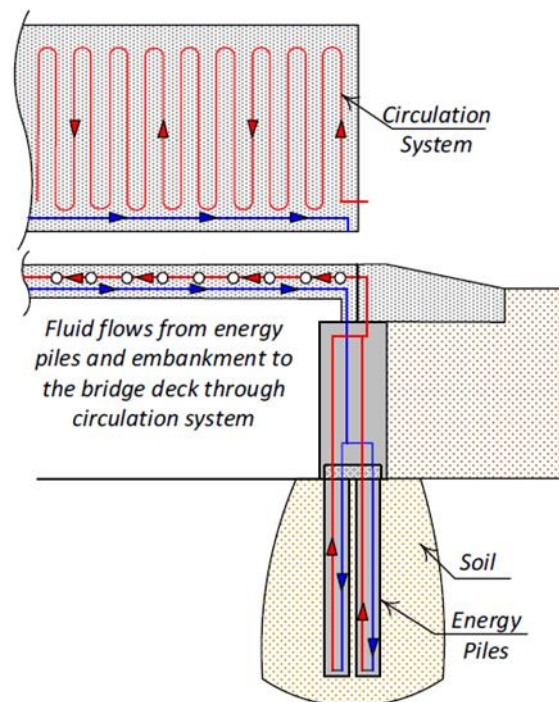


Figure 1. Schematic of Ground Source Heat Pump (GSHP) for bridge deck deicing (redrawn after Bowers and Olgun, 2014)

Geothermal deicing systems, using embedded heat exchanger pipes to circulate ground-sourced warm fluid (Figure 1), have been studied and implemented across multiple regions, including

Switzerland (Eugster, 2007), Oregon (Boyd, 2003; Minsk, 1999), Texas (Boyd, 2003), Japan (Yoshitake et al., 2011; Nagai et al., 2009), and China (Chen et al., 2020; Kong et al., 2019). These systems offer an effective and sustainable alternative to salt-based deicing, particularly in regions with extreme winter conditions. Beyond deicing, geothermal systems may also mitigate concrete deterioration. By reducing temperature fluctuations within the bridge deck, they may help prevent thermal cracking. Mohammadzadeh et al. (2023) reported up to 20°C lower surface temperatures in a geothermal-treated deck compared to a conventional deck, potentially reducing thermal stress accumulation. Habibzadeh et al. (2019) conducted a life cycle cost-benefit analysis showing that geothermal systems offer long-term economic benefits by preventing corrosion, improving traffic safety, and extending bridge service life, despite their higher initial cost. Continued research and parametric modeling are needed to optimize these systems across diverse climates and maximize both structural and economic benefits.

Overview

This study adopts a multidisciplinary approach, encompassing laboratory testing, numerical modeling, and machine learning analysis, to evaluate the feasibility of using geothermal energy for deicing/cooling transportation infrastructure in Montana (Figure 2).

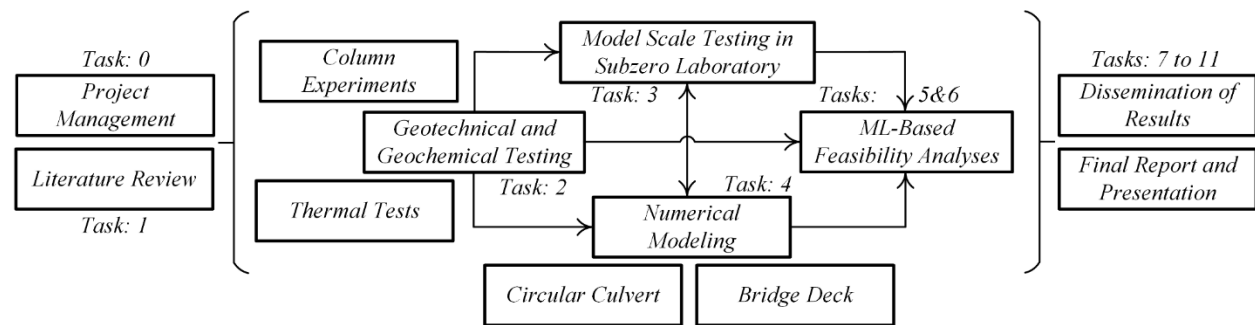


Figure 2. Research Overview

Literature Review: A comprehensive literature review was conducted to understand the current state of bridge deck deicing practices and the viability of geothermal systems as an alternative solution. This included an in-depth examination of previous studies on the use of shallow geothermal systems, such as ground source heat pumps (GSHPs), for snow and ice melting in cold climates. The review covered both domestic and international case studies, from Switzerland, Japan, China, and several U.S. states, that implemented geothermal systems in bridge decks or roadways. Technical elements such as piping layouts, thermal performance, construction methods, and energy efficiency were evaluated. In addition, deterioration mechanisms in concrete bridge decks, particularly those accelerated by freeze-thaw cycles and chemical deicing agents, were reviewed to assess the potential durability benefits of geothermal systems.

Surveys: To contextualize the research within Montana's infrastructure needs, the study included a series of surveys with Montana Department of Transportation (MDT) personnel. These surveys aimed to document existing deicing and anti-icing strategies used on bridge decks, including their effectiveness, associated costs, and operational challenges. Respondents provided insights into chemical use, mechanical removal practices, and maintenance schedules, as well as feedback on past failures or issues such as joint deterioration and corrosion. This information helped establish baseline practices and highlighted opportunities for innovation through alternative methods like geothermal heating.

Laboratory Testing: A laboratory-scale geothermal bridge deck system was developed to simulate real-world thermal behavior under controlled environmental conditions. The test setup involved a concrete slab embedded with geothermal heat exchanger tubing and connected to a heat pump. Concrete specimens were tested for thermal conductivity and strength, using standard ASTM procedures. Experiments were conducted in the Subzero Research Lab using under varying ambient temperatures and boundary conditions, with and without geothermal heating. Time-lapse images and thermal sensors were used to monitor snowmelt progression, surface temperatures, and heat transfer efficiency. These experiments helped validate modeling assumptions and demonstrated the practical feasibility of the system.

Numerical Modeling: A detailed finite element model of the geothermal bridge deck system was developed using COMSOL Multiphysics to simulate heat transfer in the slab and surrounding environment. The model incorporated boundary conditions for extreme winter scenarios and accounted for various parameters, including fluid flow rate, pipe spacing, insulation, and concrete properties. Calibration was performed using laboratory test data, enabling the model to reproduce observed temperature trends and snowmelt behavior. Subsequently, the model was used to run over 2,300 parametric simulations that systematically explored the effects of different design and environmental variables on surface temperature, heating duration, and energy efficiency. These simulations informed design recommendations and laid the groundwork for system optimization.

Machine Learning Analysis: To complement the numerical simulations, a machine learning (ML) framework was developed to predict bridge deck surface temperatures based on key input variables. Two ML models were trained using the synthetic dataset generated from the COMSOL simulations. Model 1 focused on predicting time to reach surface temperatures above 0°C, while Model 2 was designed for more general temperature prediction under diverse input conditions. The models utilized techniques such as regression trees and random forest algorithms, and were validated using cross-validation techniques. This data-driven approach enables rapid scenario testing and decision-making support for system design and operation in various climates.

Overview and Outline

This report is organized into several chapters that collectively address the study's objectives, methodology, findings, and conclusions. Chapter 1 introduces the problem statement, provides background on the limitations of conventional bridge deck deicing methods, and outlines the motivation for exploring geothermal systems. Chapter 2 presents the results of surveys conducted with MDT personnel, documenting current deicing and anti-icing strategies, associated costs, and operational challenges across Montana. Chapter 3 delivers a comprehensive literature review covering the fundamentals of geothermal energy systems, key design components, construction methods, and relevant case studies that have implemented ground source heating for bridge and roadway applications.

Chapter 4 details the laboratory testing program, including the design and construction of the bridge deck model, concrete mix characterization, and experimental setup used to simulate winter conditions and assess geothermal performance. Chapter 5 summarizes the experimental findings, focusing on thermal behavior, snowmelt performance, and surface temperature trends under varying test scenarios. Chapter 6 describes the development and calibration of a COMSOL numerical model, followed by extensive parametric studies that evaluate the influence of key system and environmental variables. Finally, Chapter 7 presents a machine learning-based tool developed to predict bridge surface temperatures using the results of over 2,300 numerical

simulations. The report concludes with a summary of findings, practical recommendations, and guidance for future research and potential pilot-scale implementation of geothermal deicing systems.

CHAPTER 2: SURVEY RESULTS

To gain insight into the Montana Department of Transportation's (MDT) current practices, challenges, and preferences related to winter road maintenance, a targeted survey was developed and distributed to MDT staff. The primary objective of the survey was to assess the effectiveness, cost, and operational feasibility of existing deicing and anti-icing strategies, as well as to identify unmet needs or pain points that might be addressed by alternative solutions such as geothermal heating systems. In doing so, the survey aimed to gather first-hand information on material usage, infrastructure performance under winter conditions, and maintenance priorities to inform the feasibility analysis of geothermal applications. The survey consisted of three main sections:

- 1) *Survey of Culvert Maintenance Activities within the State of Montana:* The first part was designed to assess current MDT practices for mitigating ice jams in culverts, as well as strategies identified in the literature. This section included the following questions:
 - What are the fundamental strategies of MDT for culvert maintenance operations in winter?
 - Please provide the average annual cost of each technology used.
 - What are the factors used in decisions about which chemicals to use?
 - What are the factors considered in the maintenance of culverts?
 - Please provide an estimate of the average annual maintenance and repair cost due to corrosion.
- 2) *Survey of Road Maintenance Activities within the State of Montana:* The second part focused on current MDT deicing and anti-icing measures for bridge decks, along with practices reported in the literature. This section included the following questions:
 - What are the fundamental strategies of MDT for bridge maintenance operations in winter?
 - Please provide an estimate of the average annual cost of each product (e.g. sand, chemicals) used.
 - Please provide an estimate of the average annual maintenance and repair cost due to corrosion.
 - What are the factors used in decisions about which chemicals to use?
 - Which abrasive materials are being used by MDT?
 - Does MDT have an abrasive clean-up plan in place?
 - How important is entry of abrasives into waterways as a negative aspect of using abrasives?
- 3) *Request for Weather and Crash Dataset:* In the third part of the survey, MDT was asked to provide the following information:
 - The time histories of the average snowfall accumulation, average temperature, wind speed, pavement surface temperature over the period of 2015 to 2020 from 73 stations of Road Weather Information System (RWIS).
 - Montana statewide car crashes with snow or ice as a contributing factor.

The collected information will be used to conduct an economic feasibility analysis, comparing geothermal-based deicing and anti-icing systems with the methods currently employed by MDT.

Current Practice in Montana

As a first step in comparing the costs of various deicing and anti-icing methods, it is essential to understand MDT's current practices. The first two sections of the survey questionnaire focused on the methods currently used by MDT to remove snow and ice from transportation infrastructure.

Road Maintenance

As summarized in Table 1, the survey identified the following three activities as the most commonly used winter maintenance strategies by MDT:

- Anti-icing to prevent snow or ice accumulation on the surface before a winter storm
- Deicing to remove snow and ice during and after a storm
- Mechanical removal

The survey results indicated that key factors influencing MDT's choice of deicing or anti-icing materials include material cost, environmental impact, ease of application, effectiveness, availability, public feedback, and potential for reducing corrosion. The effectiveness of each material depends on variables such as pavement temperature, the depth of snow and ice accumulation, and prevailing weather conditions. Prior to a cold-weather event or in its early stages, MDT may implement an anti-icing strategy. During a storm, a combination of methods, such as snow plowing, sanding, and deicing, is typically employed to clear roads and improve traction. When pavement surfaces are heavily covered with snow and fall under a "Low" condition classification (as defined in Table 1), MDT generally relies on deicing. Abrasives are most commonly used during events involving extremely low temperatures.

Table 1. Fundamental strategies of MDT for road maintenance operation in winter

Strategies and Tactics	Pavement Condition** Within-winter weather event			Pavement Condition** After/end-of-winter weather event		
	Low ¹	Medium ²	High ³	Low ¹	Medium ²	High ³
Anti-icing/Pre-wetting	X	X	X			X
Deicing	X			X		
Mechanical removal alone	X	X	X			
Mechanical removal and abrasive	X	X	X			
Mechanical removal and anti-icing	X	X	X			
Mechanical removal and deicing	X					

** Pavement Condition Categories

Pavement Condition	Pavement Snow and Ice Conditions
¹ Low	Conditions 5 and 6
² Medium	Conditions 3 and 4
³ High	Conditions 1 and 2

Condition 1: Dry/wet pavement conditions.

Condition 2: Snow accumulation occurs occasionally. There are patches of ice or packed snow.

Condition 3: Snow accumulation occurs regularly. Loose snow or slush ranging up to 5 cm (2 inches) are accumulated on the pavement surface.

Condition 4: Snow accumulation occurs regularly. Ice or packed snow with only bare wheel tracks.

Condition 5: Pavement surface is covered with ice and compacted snow.

Condition 6: Pavement surface is covered with significant amounts of snow.

The most commonly used deicing and anti-icing solutions for bridge decks in Montana are salts and other debonding chemicals, including Sodium Chloride (NaCl), Magnesium Chloride

(MgCl_2), and Potassium Acetate (KAc). According to MDT's official website, NaCl is primarily obtained through seawater evaporation, while MgCl_2 is sourced from the Great Salt Lake. These chemicals are applied in both solid and liquid forms. Solid materials are generally more effective when sufficient moisture is present on the pavement surface. Two key methods enhance the effectiveness of solid chemical treatments: (1) applying them after adequate precipitation and (2) pre-wetting the materials. NaCl is the most commonly used dry solid by MDT. Pre-wetting is typically performed at the stockpile, in the spreader, or directly at the point of discharge. Liquid chemicals, such as NaCl, MgCl_2 , and KAc, are also widely used for deicing and anti-icing, but their effectiveness diminishes at lower temperatures. Specifically, MgCl_2 and NaCl are effective down to approximately -12°C (10°F) and -9.4°C (15°F), respectively. The lowest practical melting temperatures of these winter maintenance materials are summarized in Table 2.

Table 2. The lowest practical melting temperature of winter maintenance materials (Frederickson et al., 2005)

<i>NaCl</i>		<i>MgCl₂</i>	<i>KAc</i>
<i>Solid</i>	<i>Liquid</i>	<i>Liquid</i>	<i>Liquid</i>
-9.4°C (15.1°F)	-9.4°C (15.1°F)	-12°C (10°F)	-9.4°C (15.1°F)

Previous studies have demonstrated that deicing chemicals negatively impact both the environment and infrastructure (e.g. Kelting & Laxon, 2010; Shi et al., 2018). Prolonged use of these chemicals significantly increases the maintenance costs of reinforced concrete (RC) bridges. Chemical exposure accelerates corrosion of steel reinforcement, reduces the effective cross-sectional area of the steel over time, and may ultimately lead to structural failure of RC bridge decks (e.g. Baboian, 1992; Granata & Hartt, 2009; Virmani et al., 1983; Virmani et al., 1984; White et al., 2005; Yunovich et al., 2003). Bridge deterioration remains a critical national infrastructure concern (AASHTO, 2008). The annual direct cost of corrosion in U.S. bridges is estimated to range from \$6 to \$10 billion (Koch et al., 2002). When indirect costs are considered, the total economic impact may be up to ten times higher (Yunovich et al., 2003).

Abrasive materials are commonly used for winter road maintenance in extremely cold conditions. These materials, such as sand, cinders, ash, tailings, and crushed stone, have been favored for many years due to their low cost. Unlike chemical deicers, abrasives do not melt ice; instead, they are applied to rapidly increase surface friction. MDT primarily uses crushed stone sourced from local gravel pits. However, abrasive use can have several negative environmental and operational impacts, including degradation of water and air quality, clogging of drainage facilities, harm to wildlife habitats and vegetation, soil contamination, and increased post-winter maintenance costs related to roadway and shoulder cleanup (Fischel, 2001).

Cost of Material

Information on the costs associated with products used by MDT for winter road maintenance was collected in terms of their average annual expenditures:

- NaCl is \$70/ton
- Salt Brine is \$0.32/gallon
- MgCl_2 is \$150/ton
- KAc is \$4.66/gallon

The survey results indicated that from 2015 to 2020, the average annual cost of winter road maintenance materials in Montana was approximately \$10.7 million. Estimates for labor and equipment costs will be updated in future project reports. In a 2003 case study conducted by MDT, the effectiveness of two winter maintenance strategies, anti-icing and deicing, was evaluated during a storm event affecting two segments of State Highway 200: the Plains section and the Thompson Falls section (Goodwin & Pisano, 2003). On the Plains section, an anti-icing strategy was implemented using 11,355 liters (3,000 gallons) of magnesium chloride ($MgCl_2$) applied during and after the storm. In contrast, the Thompson Falls section utilized a deicing approach, which involved pre-wetting abrasives with 3,028 liters (800 gallons) of chemicals and applying an additional 2,839 liters (750 gallons) of $MgCl_2$ for deicing. As shown in Figure 3, the pavement on the Plains section was bare following treatment, while the Thompson Falls section remained covered with ice and compacted snow, indicating the superior performance of the anti-icing strategy in this case.



Figure 3. Road surface conditions of (a) Thompson Fall Section (b) Plains Section (Goodwin, 2003)

As summarized in Table 3, the anti-icing strategy implemented on the Plains section required 44% less sand and reduced labor costs by 52%. Although it involved higher chemical usage, the total cost per lane mile was 37% lower compared to the reactive deicing strategy used in Thompson Falls (Goodwin & Pisano, 2003). These results underscore the cost-effectiveness and operational advantages of preventive over reactive winter maintenance approaches.

Table 3. MDT Winter Maintenance Annual Averages (Goodwin & Pisano, 2003)

	Thompson Falls Section	Plains Section
Sand Costs per lane mile	\$724	\$407
$MgCl_2$ Costs per lane mile	\$136	\$233
Equipment Costs per lane mile	\$327	\$182
Labor Costs per lane mile	\$564	\$273
Total Costs per lane mile	\$1,750	\$1,095

Culvert Maintenance

Culverts enable water to flow beneath roadways, preventing water accumulation along embankments. However, snow and ice buildup within culverts can reduce their flow capacity, leading to flooding and associated economic losses, particularly when blockages persist into the spring runoff season. Additionally, ice accumulation can promote the advancement of the freezing

front into frost-susceptible subsoil around the culvert, increasing the risk of frost heave in adjacent roadway sections.

"Problematic culvert ice, once formed, is typically removed using heat or other mechanical methods. According to the survey, mechanical removal was identified as MDT's most commonly used winter maintenance strategy. While a specific budget for culvert snow and ice removal was not available, survey results indicated that the total cost for cleaning drainage structures reached \$301,659 in State Fiscal Year (SFY) 2020.

Request for Weather and Crash Dataset

This section presents a summary of the data collected in the third part of the survey. The data includes: (1) the number of car crashes attributed to slippery road conditions between 2010 and 2019, and (2) weather data recorded at 73 RWIS stations across Montana from 2015 to 2020.

Car Crashes in Montana

According to the Federal Highway Administration (FHWA), approximately 5,878,000 car accidents occurred annually on U.S. roadways between 2002 and 2012, with 23% attributed to weather-related events (FHWA, 2013). Each year, crashes on snowy, slushy, or icy pavements resulted in around 1,300 fatalities, over 116,800 injuries, and an estimated economic loss of nearly \$42 billion in the U.S. (Beran & Wilfong, 1998; FHWA, 2013). In Montana, Table 4 presents the number of car crashes between 2010 and 2019 where snow or ice was a contributing factor. The data shows that, on average, 5,430 weather-related crashes occurred annually due to slippery road conditions such as ice, frost, slush, or snow. While this dataset accounts for all crash locations, a more specific estimate, the average annual number of crashes occurring on bridges, is needed to support a life-cycle cost-benefit analysis of various deicing and anti-icing strategies.

Table 4. Montana statewide car crashes due to slippery road surface conditions

	<i>Ice/Frost</i>	<i>Slush</i>	<i>Snow</i>	<i>Total</i>
2010	2951	232	2174	5357
2011	2922	251	2081	5254
2012	2060	272	1572	3904
2013	2737	233	1905	4875
2014	3491	296	2725	6512
2015	2466	206	2063	4735
2016	1929	253	1904	4086
2017	3509	360	2967	6836
2018	3668	331	2138	6137
2019	3342	220	3041	6603
Total	29075	2654	22570	54299
Average	2907	265	2257	5430

Accident records from a two-year period (1972–1973) analyzed by Agent and Dean (1976) indicated that nearly 8% of all traffic accidents involved bridges. Their study examined 350 overpasses and 360 underpasses on the interstate and parkway system, counting dual bridges as a single structure. The data also showed that the severity of bridge-related accidents on primary and secondary highways was comparable to those occurring on the interstate and parkway system. Similarly, Habibzadeh-Bigdarvish et al. (2019) analyzed crash data in Texas and found that at least 8% of all vehicular accidents occurred on bridges due to slippery road surface conditions. Applying

this percentage to Montana suggests that approximately 434 vehicle crashes occur annually on the state's bridges.

Weather in Montana

Many state transportation agencies have adopted the Road Weather Information System (RWIS) to monitor, report, and forecast road-related weather conditions. RWIS provides detailed environmental data that support winter maintenance operations for roads and bridges (Al-Kaisy & Ewan, 2017). In Montana, there are 73 RWIS stations distributed across the state, as shown in Figure 4. Each station is equipped with sensors that measure air temperature and humidity, wind speed and direction, pavement temperature, subsurface temperature, and precipitation. In addition, each site includes a camera for real-time visual monitoring. A subset of six or fewer stations is also equipped with advanced features such as enhanced precipitation sensors, visibility sensors, or infrared illuminators to improve nighttime camera imaging (Al-Kaisy & Ewan, 2017).

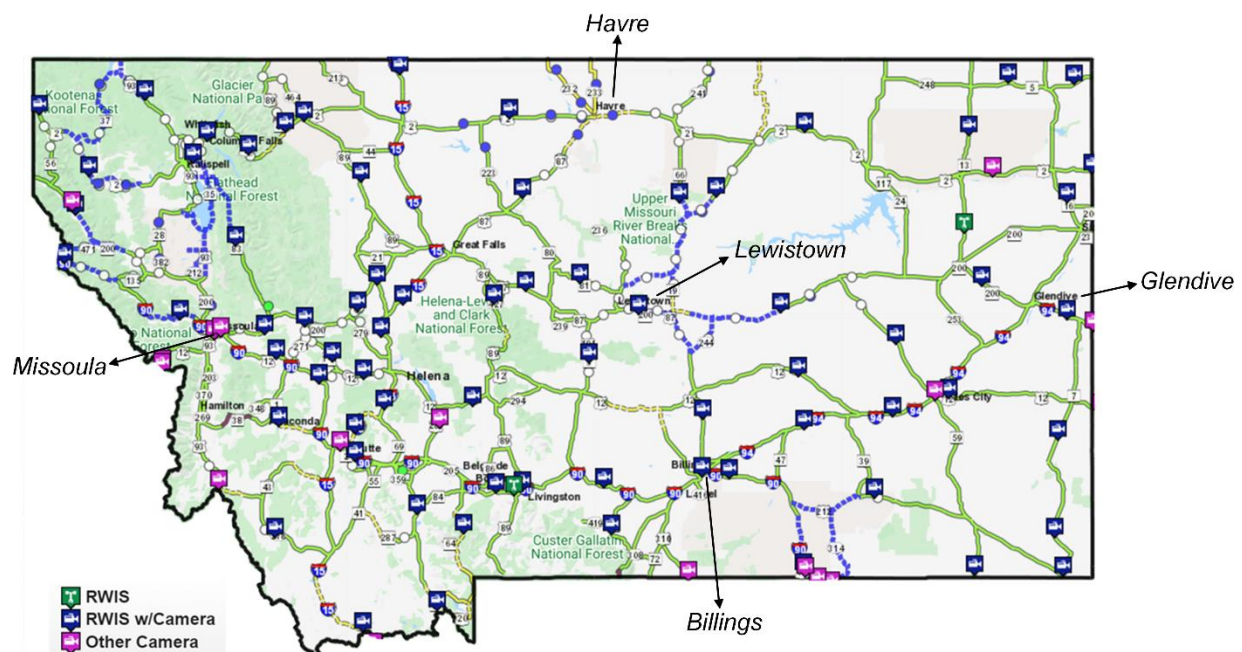


Figure 4. Locations of MDT RWIS Sites (Map Source: <https://roadreport.mdt.mt.gov/>)

The third part of the survey involved the analysis of historical weather data to support the evaluation of deicing needs across the state. Time histories of key weather parameters, including ambient air temperature, pavement surface temperature, sub-surface temperature, relative humidity, wind speed, and average snowfall accumulation, were collected from 73 Road Weather Information System (RWIS) stations across Montana for the period of 2015 to 2020. The data were averaged monthly over the five-year span to identify seasonal trends and regional climate characteristics. Representative examples from the Lookout Pass station near Missoula are shown in Figure 5. Figure 5(a) presents the monthly average ambient air temperatures, where the black line indicates the mean, and the red and blue lines represent the monthly average maximum and minimum temperatures, respectively. The RWIS data indicate that the coldest months during this period were typically November through February. In western Montana, the highest temperatures were recorded in July 2018, while the lowest occurred in February 2019. The most pronounced temperature range was observed in July 2018, with monthly average temperatures varying from 10.7°C (51.3°F) to 26.7°C (80.1°F).

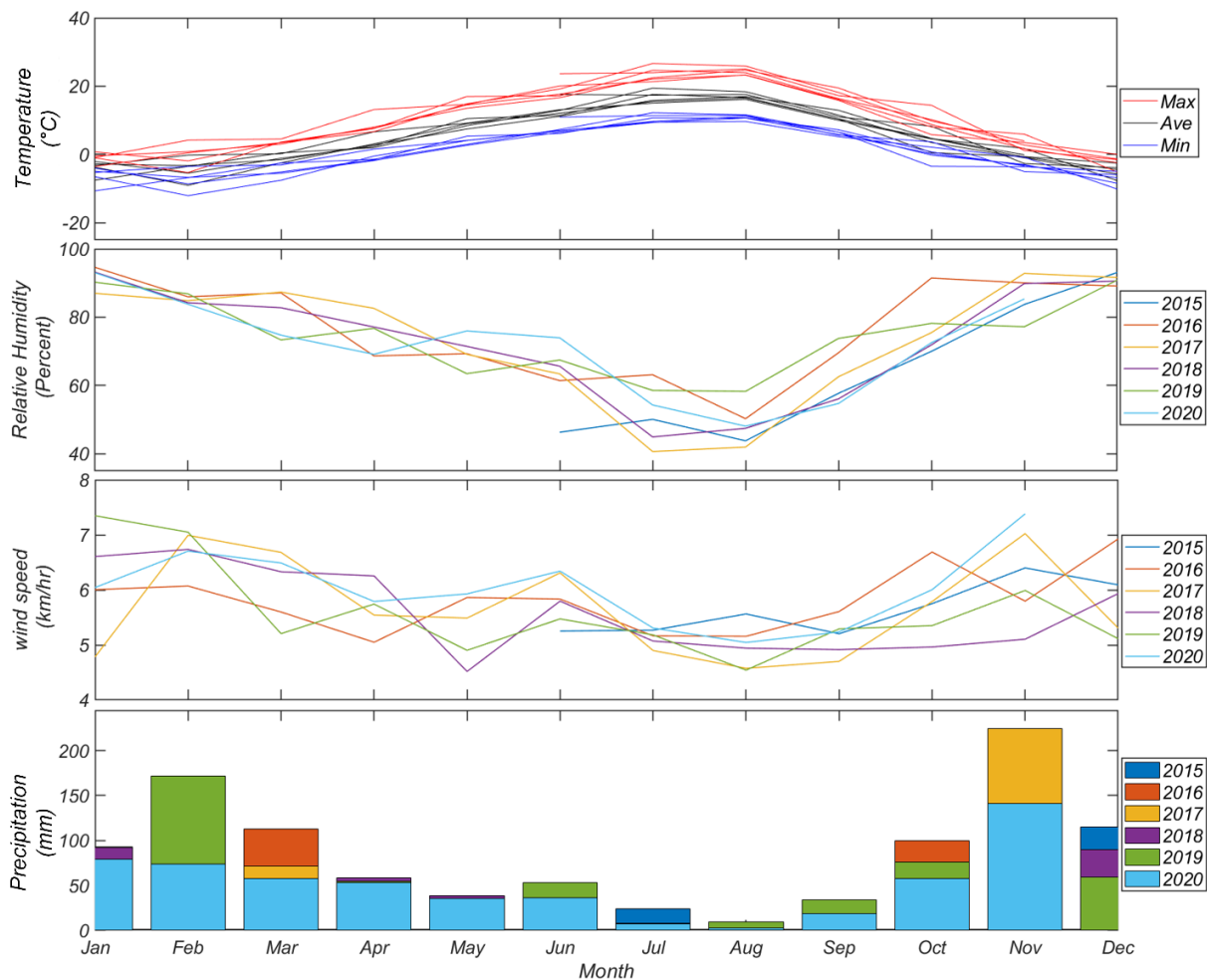


Figure 5. Monthly average weather data for 2015-2020: (a) ambient temperature, (b) relative humidity (c) wind speed, and (d) precipitation

Figure 5(b) presents the monthly average relative humidity in western Montana from 2015 to 2020. The data show that relative humidity is highest during the winter months, reaching up to 95% in January, while the summer months exhibit significantly lower values, with a minimum of 40% in July. Figure 5(c) illustrates the monthly average wind speed over the same five-year period, ranging from 4.0 to 7.4 km/hr (2.5 to 4.3 mph). Among the key parameters for designing an effective snow melting system is the snowfall rate. Figure 5(d) displays the monthly average precipitation, expressed in terms of water equivalent snowfall, at the Lookout Pass station near Missoula for the years 2015 to 2020. The data indicate that western Montana experiences higher precipitation during the winter months (November to February), with an average exceeding 112 mm (4.4 inches) in November. In contrast, precipitation levels drop significantly during the summer months (June to September), with July averaging less than 7.2 mm (0.3 inches).

Figure 6 presents the average daily temperatures recorded in five major cities across Montana during February 2019: northern (Figure 6(a)), western (Figure 6(b)), southern (Figure 6(c)), eastern (Figure 6(d)), and central (Figure 6(e)) regions. The geographic locations of these cities are shown in Figure 4. Overall, temperatures were relatively consistent across the state, with slightly lower values observed in the northern region, particularly in Havre. As shown in Figure 6(a), the lowest ambient temperature in northern Montana during February 2019 was -35°C (-

31°F), recorded at the Sunburst station. The lowest temperatures observed in the other regions were -22.5°C (-8.5°F) in the west, -26°C (-15°F) in the south (Figure 6(c)), -31.5°C (-24.7°F) in the east (Figure 6(d)), and -30.2°C (-22.4°F) in the central region (Figure 6(e)).

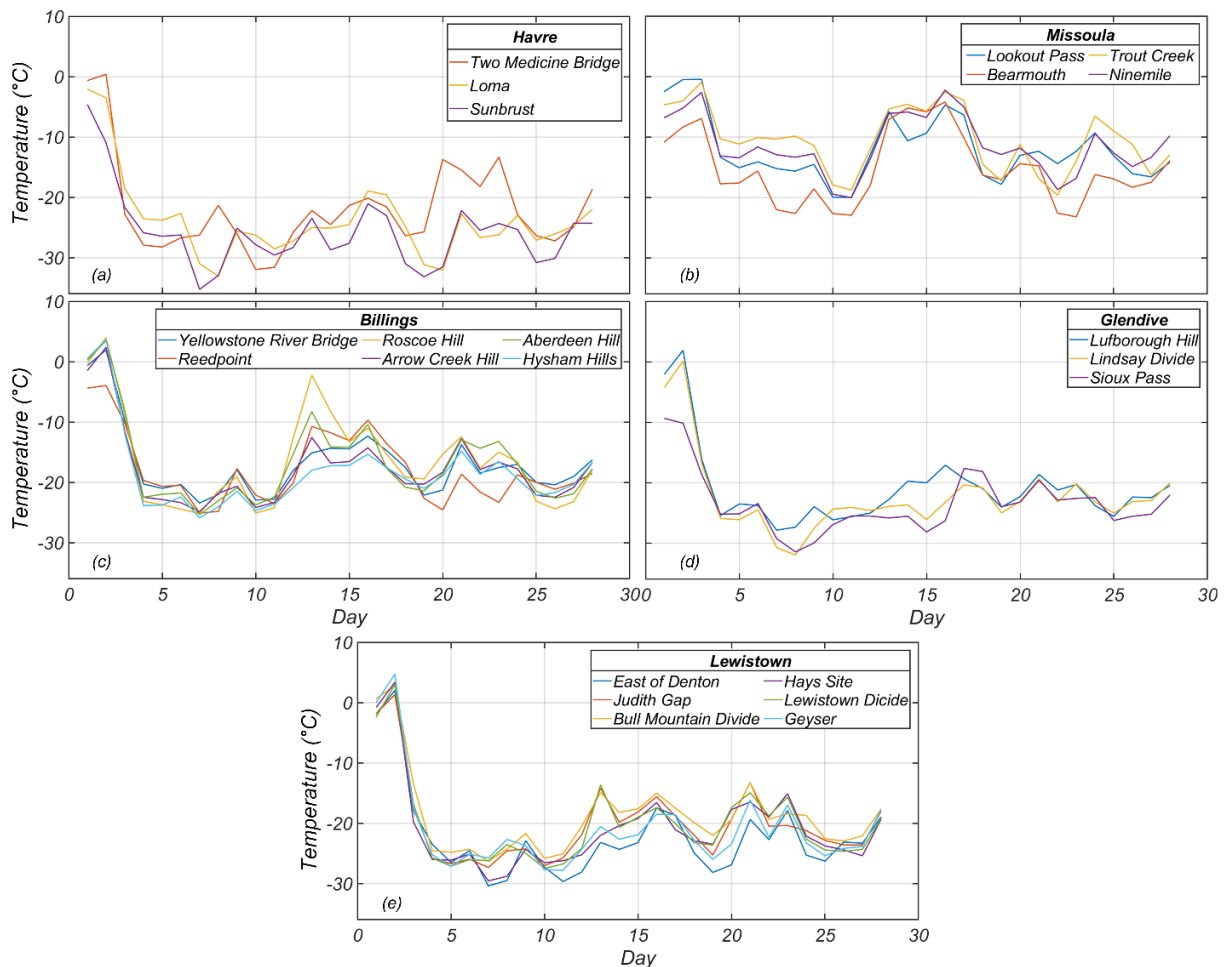


Figure 6. Average daily temperature during coldest month, February 2019, in (a) Northern (b) Western (c) Southern (d) Eastern, and (e) Central Montana

Monthly average ambient air temperatures indicate that July 2018 was the warmest month during the 2015–2020 period. Figure 7 presents the average daily temperatures for five major cities representing northern (Figure 7(a)), western (Figure 7(b)), southern (Figure 7(c)), eastern (Figure 7(d)), and central (Figure 7(e)) Montana during that month. Overall, temperatures were relatively consistent across the state, with slightly higher values observed in the northern region, particularly in Havre. As shown in Figure 7(a), the highest average daily temperature in northern Montana reached 37°C (99°F), with the Sunburst Inverness station recording the highest value among all selected locations. The peak ambient temperatures recorded in the western, southern, eastern, and central regions were 37°C (99°F), 38°C (100°F), 35.5°C (95.9°F), and 35°C (95°F), respectively.

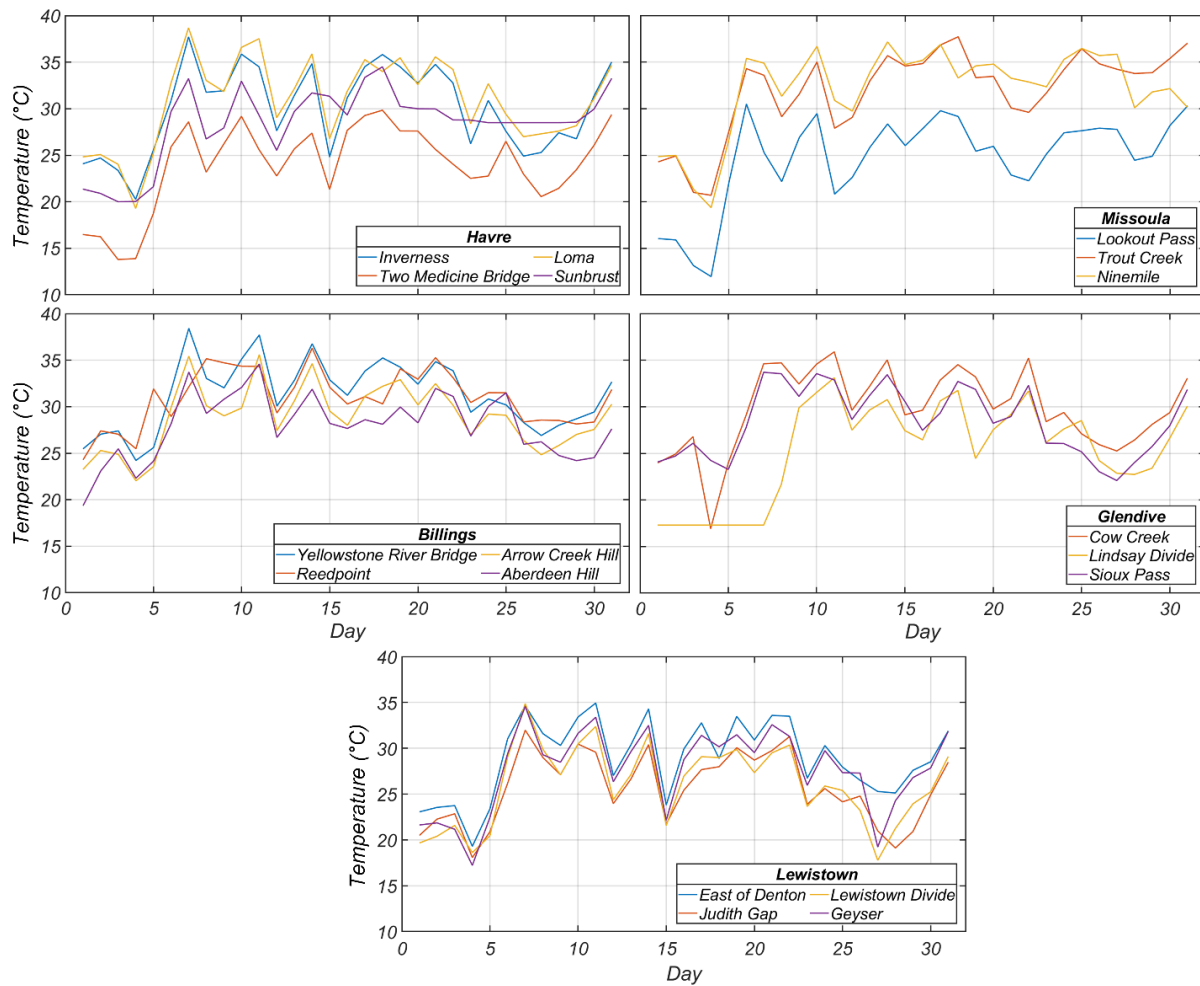


Figure 7. Average daily temperature during warmest month, July 2018, in (a) North (b) West (c) South (d) East (e) Center of Montana

Table 5 summarizes the maximum and minimum average daily values for ambient air temperature, surface temperature, subsurface temperature, and relative humidity in selected Montana cities (Missoula, Billings, Lewistown, Havre, and Glendive) over the 2015–2020 period. It also presents data on maximum snowfall rate, total snowfall accumulation, and wind speeds. Surface temperature refers to the temperature at the pavement surface, while subsurface temperature represents the temperature approximately 43 cm (17 inches) below the surface. The data show relatively consistent temperature trends across the state, with slightly warmer ambient, surface, and subsurface temperatures observed in western Montana near Missoula. In contrast, the lowest temperatures were recorded in northern and eastern regions, particularly near Havre (east of Denton) and Cow Creek near Glendive. The highest wind speed, 54.3 km/h (33.7 mph), was recorded at the Geyser station near Havre (Northern Montana).

Table 5. Average daily weather data obtained for five major cities in Montana

Area	Description	Site ID	Ambient Temperature (° C)		Surface Temperature (° C)		Sub-Temperature (° C)		Relative Humidity (%)		Wind Speed (km/hr)
			Max	Min	Max	Min	Max	Min	Max	Min	Max
Missoula	Lookout Pass	A150000	36.57	-23.57	33.65	-16.93	31.05	-7.96	100	22.00	20.75
	Bearmouth	A150002	41.64	-31.89	37.28	-20.98	32.65	-11.26	94.96	9.00	15.17
	Trout Creek	A150003	42.78	-28.27	39.04	-17.39	34.48	-8.58	93.00	24.34	9.77
	Ninemile	A150005	42.19	-27.52	38.64	-20.66	34.08	-8.86	95.00	27.76	9.3
Billings	Yellowstone River Bridge	A263000	40.96	-27.74	38.45	-19.00	31.86	-8.02	90.95	15.94	31.87
	Reedpoint	A263001	38.14	-34.11	36.00	-20.69	N/A	N/A	98.42	17.07	40.93
	Roscoe Hill	A263002	37.22	-26.35	35.35	-18.61	29.76	-9.90	87.70	9.93	33.99
	Arrow Creek Hill	A263003	38.82	-26.49	37.41	-16.58	32.92	-6.72	89.00	15.07	34.05
	Aberdeen Hill	A263004	38.06	-26.16	36.49	-17.25	30.87	-8.43	100	15.02	42.05
	Hysham Hills	A263005	39.724	-29.41	37.97	-17.92	32.26	-6.43	93.69	16.68	28.16
Lewistown	East of Denton	A268000	40.64	-34.55	38.02	-20.24	31.79	-8.88	95.00	17.00	35.23
	Judith Gap	A268001	36.19	-30.12	34.65	-19.09	30.76	-12.75	99.03	17.29	44.05
	Bull Mountain Divide	A268003	37.69	-28.01	36.13	-15.74	33.09	-8.79	100	12.39	44.2
	Hays Site	A268004	39.09	-29.56	N/A	N/A	28.78	-8.12	92.00	15.85	48.92
	Lewistown Divide	A268005	37.05	-31.45	N/A	N/A	29.97	-12.89	99.00	4.18	25.59
	Geyser	A268006	39.09	-30.42	N/A	N/A	30.01	-10.87	97.59	15.42	46.86

Table 5. Average daily weather data obtained for five major cities in Montana (Continued)

Area	Description	Site ID	Ambient Temperature (° C)		Surface Temperature (° C)		Sub-Temperature (° C)		Relative Humidity (%)		Wind Speed (km/hr)
			Max	Min	Max	Min	Max	Min	Max	Min	Max
Havre	East of Denton	A629000	41.11	-38.44	38.34	-23.39	N/A	N/A	92.00	14.42	48.10
	Judith Gap	A629001	N/A	N/A	39.49	-22.51	31.58	-13.09	N/A	N/A	-
	Bull Mountain Divide	A629002	35.74	-33.71	34.05	-26.00	28.75	-13.35	100	19.92	51.99
	Hays Site	A629003	39.78	-33.67	38.19	-21.06	N/A	N/A	100	17.36	41.84
	Lewistown Divide	A629004	39.15	-35.27	N/A	N/A	N/A	N/A	100	17.96	47.95
	Geyser	A629005	38.53	-30.71	35.71	-22.28	29.47	-11.11	100	16.55	54.32
Glendive	Lufborough Hill	A302000	39.48	-31.20	39.02	-20.29	31.55	-8.77	100	11.71	36.45
	Cow Creek	A302001	40.31	-41.60	38.72	-25.19	32.48	-12.49	100	26.69	38.71
	Lindsay Divide	A302002	38.45	-33.44	37.77	-22.02	31.16	-10.37	100	18.40	42.21
	Sioux Pass	A302004	39.68	-32.68	39.36	-24.12	31.63	-11.74	100	23.44	40.50

CHAPTER 3: LITERATURE REVIEW

Shallow Geothermal Energy: Overview

The application of geothermal energy as a renewable heat source is well established worldwide due to its environmental advantages and long-term economic benefits (Sinyak, 1994). Heat from the Earth can be extracted from shallow or deep layers using thermo-active foundations or boreholes through mechanisms of heat transfer including conduction, convection, and radiation. Common subsurface thermal storage zones include: (1) aquifers, typically used in open-loop systems; (2) boreholes; and (3) rock caverns or pits (McCartney et al., 2016). Geothermal energy has been utilized across a broad range of applications, from power generation to snow and ice melting on bridges and sidewalks. It is generally classified into low-, medium-, and high-temperature categories (Abbasy, 2009). Low- and medium-temperature sources are typically used for snow melting and for heating and cooling in residential and industrial settings via geothermal cycles, whereas high-temperature sources are primarily used for electricity generation. A global review by Lund and Boyd (2016) of geothermal energy applications in 82 countries categorized direct-use systems and highlighted that the largest share (70.9%) of global geothermal capacity is associated with geothermal heat pumps (GHPs), also known as ground source heat pumps (GSHPs) (Figure 8). GHP systems are among the most energy-efficient technologies for heating and are currently one of the fastest-growing renewable energy applications worldwide (Lund & Toth, 2020).

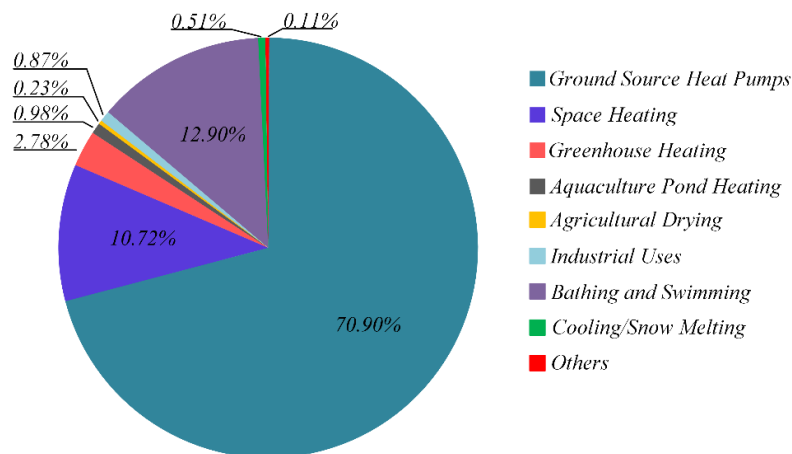


Figure 8. Percentage of global capacity used by various forms of direct geothermal energy in 2015 (Lund & Boyd, 2016)

This study focuses on the use of ground source heat pump (GSHP) systems for melting snow and ice on bridge decks and within culverts. GSHP technology leverages the relatively stable ground temperatures found below the surface. At depths of approximately 6 to 9 meters (20 to 30 feet), seasonal variations in ground temperature are minimal. Within thermo-active systems, heat exchangers can utilize this constant ground temperature as a thermal energy source to heat or cool surface structures (Brandl, 2006; Faizal et al., 2016; Kusuda & Achenbach, 1965).

A GSHP system consists of three main units, as shown in Figure 9, namely (Brandl, 2006):

- Primary unit (ground heat exchanger)
- Heat pump system, and
- Secondary unit (pipe network that delivers the heat energy to the receiving infrastructure).

"The primary unit consists of a ground heat exchanger, typically a system of pipes known as a loop, that transfers heat to or from the surrounding soil. The secondary unit is connected to the above-ground structure to be heated or cooled, such as a building, bridge deck, or pavement. These two units are linked by a circulating pump or a heat pump. The heat pump serves to raise the temperature of the heat extracted from the ground for effective use in the secondary system.

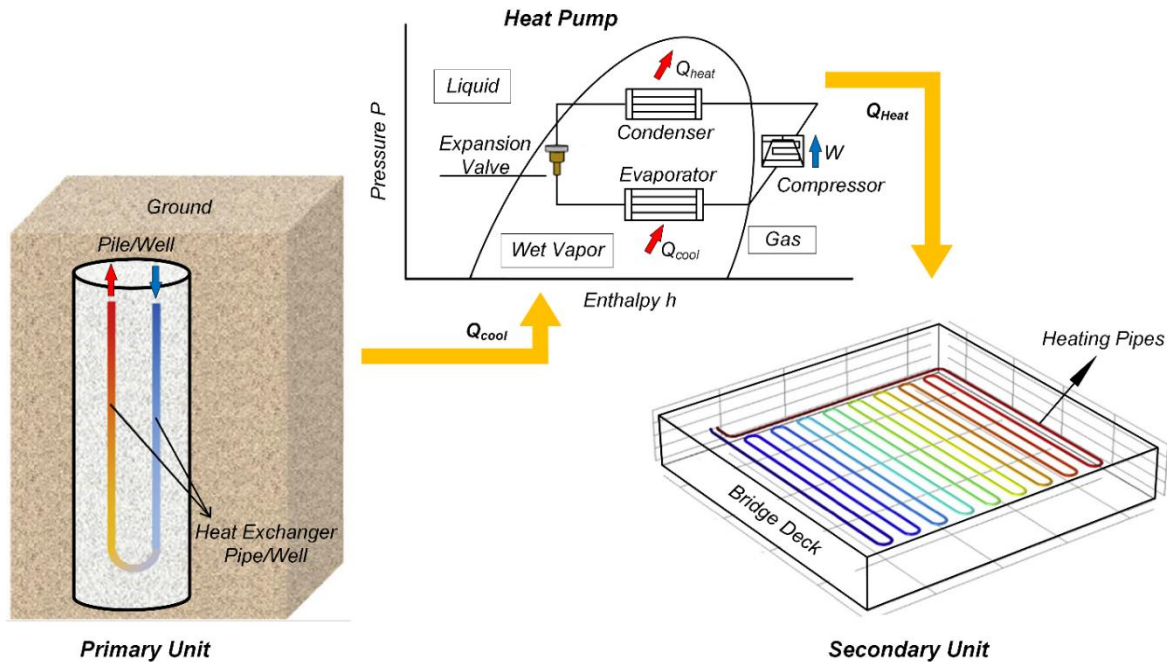


Figure 9. GSHP system (Han & Yu, 2017)

A Ground Source Heat Pump (GSHP) system can operate in either heating or cooling mode. Figure 10 illustrates a closed-loop GSHP system designed to regulate the temperature of a secondary unit. In warmer seasons, the ground, having a lower temperature than the ambient air, acts as a heat sink, absorbing excess heat from the system. Conversely, during colder months, the ground heat exchanger extracts thermal energy from the earth, utilizing the temperature gradient between the circulating fluid and the surrounding soil. The amount of heat exchanged with the ground depends on the heating or cooling demands of the structure being served (Faizal et al., 2019).

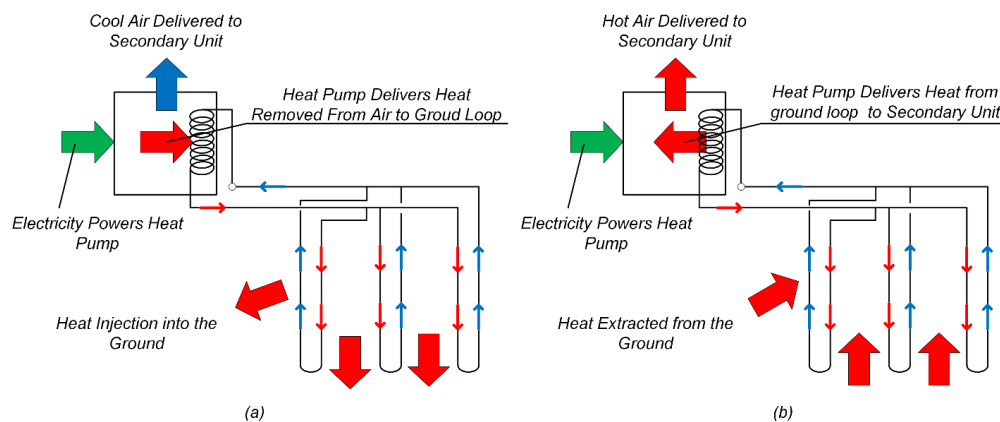


Figure 10. Closed loop GSHP using for (a) cooling (b) heating of secondary unit (Kavanaugh, 2006)

Primary Unit

There are two common primary types of geothermal unit systems: borehole heat exchangers (BHE), also known as geothermal wells, and geothermal energy pile (GEP) foundations. BHE systems have been widely used for both energy extraction and storage over the past several decades (Brandl, 2006) and are typically classified as either open-loop or closed-loop systems (Preene & Powrie, 2009). An open-loop system, also referred to as a groundwater system, uses an underground aquifer as a heat source in colder months and as a heat sink during warmer periods. As illustrated in Figure 11(a), an open-loop configuration includes both extraction and discharge wells. Groundwater is pumped from the extraction well and circulated through a heat pump, where heat is either absorbed or rejected depending on the season. The water is then returned to the aquifer through the discharge well. Because open-loop systems cycle natural groundwater, it is essential that the water's chemical composition remains unaltered before reinjection. Additionally, the aquifer must be shallow, permeable, and capable of supporting sufficient flow rates. It should contain minimal concentrations of harmful substances, such as chlorinated solvents, that could degrade pump components. The water's pH must also be suitable to prevent corrosion and fouling of coils and control valves. Despite their effectiveness, open-loop systems may incur high maintenance costs due to the complexity and sensitivity of the wells (Rafferty, 2009).

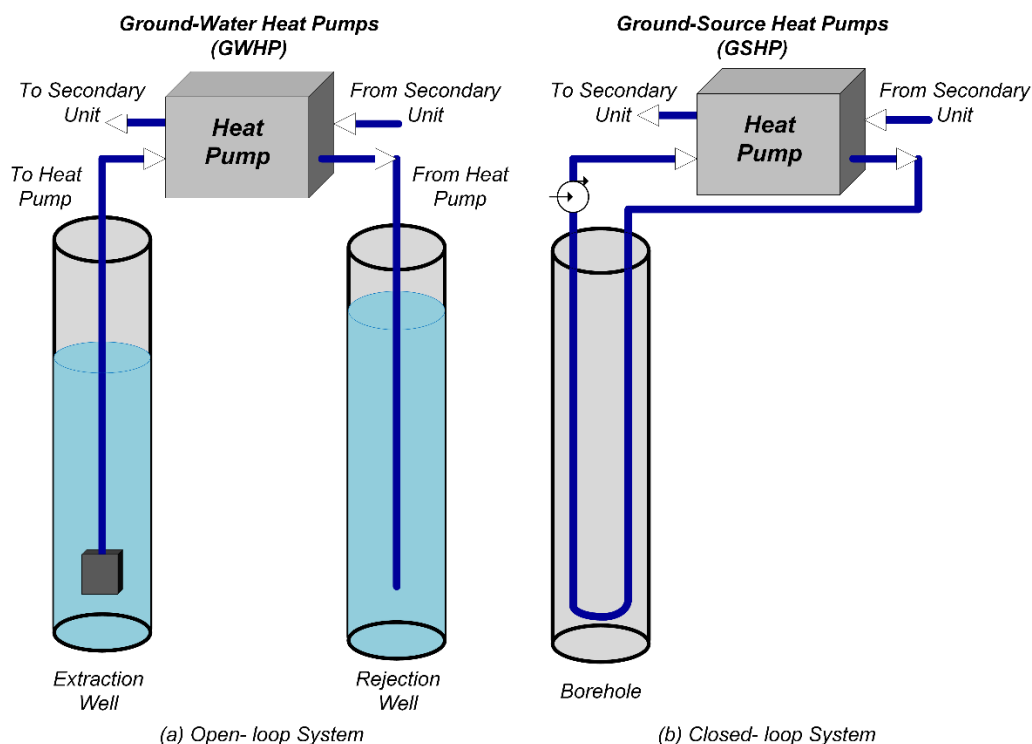


Figure 11. (a) Open-loop system (b) closed-loop system

Closed-loop (or ground-coupled) systems utilize embedded heat exchangers to extract thermal energy from the ground and transfer it to a heat pump. These systems can be installed either vertically or horizontally (Bloomquist, 2000). A simplified schematic of a vertical closed-loop system is shown in Figure 11(b). In such systems, a circulating fluid flows through heat exchanger pipes, absorbing heat from the surrounding soil. In horizontal configurations, the pipes are typically placed in excavated trenches below the frost line or embedded within the bridge's backfill abutment. In vertical systems, the pipes, often arranged in U-shaped loops, are installed in

boreholes or integrated into subsurface structural elements such as piles. To improve heat transfer, vertical boreholes are usually filled with thermally enhanced grout, which occupies the space between the borehole wall and the heat exchanger pipes. The selection of grout depends on key factors including thermal conductivity, hydraulic conductivity, bonding quality, and workability (Hiller, 2000). Hydraulic conductivity is especially important as it helps prevent leakage through faulty joints in the primary loop (Allan & Philippacopoulos, 1999). To enhance thermal performance, various additives have been incorporated into grout mixtures. Lee et al. (2010) compared graphite and silica sand as additives to bentonite-based grout and found graphite significantly improved thermal conductivity. Similarly, Kim et al. (2015) showed that increasing quartz content also enhances the thermal properties of grouting materials.

Another common primary unit type is the Geothermal Energy Pile (GEP) foundation, which serves a dual purpose: transferring structural loads to the ground and functioning as a ground heat exchanger. Due to this multifunctionality, GEPs can offer significant cost-effectiveness. These systems typically consist of reinforced concrete, chosen for its favorable thermal conductivity and high thermal storage capacity, and U-shaped pipes made from high-density polyethylene, polypropylene, polyvinyl chloride, or polybutylene (Adam & Markiewicz, 2009; Akrouch et al., 2014; Gao et al., 2008; Hamada et al., 2007; Loveridge, 2012; Park et al., 2012). Geothermal energy is harnessed in these piles by circulating a heat-absorbing fluid through the embedded pipe loops. Heat is transferred into or out of the ground via conduction and convection, driven by the thermal gradient within the surrounding soil. Both cast-in-place and precast (driven) piles can be used, although cast-in-place piles are generally preferred for geothermal applications, as they minimize damage to the heat exchanger system attached to the reinforcement cage (Mimouni, 2014). Recent studies have also focused on improving the thermal performance of GEPs by enhancing the thermal conductivity of the concrete mix. Specifically, increasing the aggregate content and reducing the cement ratio has been shown to improve heat transfer efficiency, since aggregates typically have higher thermal conductivity than cement (Loveridge, 2012).

Construction Technique

Direct pressing, ramming, and drilling are three common construction techniques used for installing geothermal boreholes. Among these, direct pressing and ramming are most frequently employed in soft soils, as they offer enhanced borehole stability and improved thermal contact with the surrounding ground. However, these methods are generally limited to shallow depths of up to 10 meters (32 feet) (Sanner & Knoblich, 1991). Drilling methods, such as hollow stem auger, solid stem auger, sonic, and rotary techniques, are used for deeper installations and vary in terms of depth capacity, cost, and penetration efficiency. The choice of drilling technique is determined by site-specific conditions and project requirements. Once the borehole is drilled, it may be stabilized using casing or grout. According to the 2010 Design and Installation Standards by the International Ground Source Heat Pump Association (IGSHPA; www.igshpa.okstate.edu), the borehole annulus must be uniformly grouted from the bottom to the surface using a tremie pipe. Heat exchanger pipes are then inserted into the fresh grout as the final step in the construction process.

Ground Energy Piles (GEPs) can be installed using either soil displacement methods or soil excavation techniques. Common construction approaches include bored piles, spun piles, and continuous flight auger (CFA) piles. In the bored pile method, a temporary casing is first driven into the ground. The soil within the casing is excavated using an auger, after which a reinforcement

cage, fitted with heat exchanger pipes, is placed. Concrete is then poured into the borehole, and the casing is subsequently removed (Mimouni, 2014; Pahud, 2013). This technique is typically used for constructing large-diameter piles, which can accommodate multiple U-loop heat exchangers. For example, at Dock Midfield in Zürich Airport, five U-shaped pipes were embedded within each 26.8-meter-deep (88 ft) GEP (Mimouni, 2014). In the spun pile method, precast concrete piles with a central void are driven into the ground. Heat exchanger pipes are then inserted into the void, which is subsequently filled with wet sand, fine gravel (Mimouni, 2014), or cement (Park et al., 2013) to ensure thermal contact. For CFA piles, a hollow auger is drilled into the ground while continuously removing soil. Concrete is pumped through the auger's hollow shaft as it is gradually withdrawn. Once the pile is formed, the reinforcement cage and heat exchanger pipes are inserted into the freshly placed concrete (Mimouni, 2014)

Heat exchanger pipes

Figure 12 illustrates various attachment configurations for heat exchanger pipes on reinforcing cages. The pipes can be affixed to either the interior (Figure 12(a)) or exterior (Figure 12(b)) of the reinforcing cage prior to its installing (Sani et al., 2019). Alternatively, the loops may be installed outside the cage by clipping them to high-strength steel rebar and embedding them into the center of the wet concrete. This approach leverages the superior thermal conductivity and thermal storage capacity of concrete compared to surrounding soil (Figure 12(c)). For precast concrete piles, a coring technique can be used to insert the pipes into the hardened concrete, though this method is generally not cost-effective due to high installation costs (Sani et al., 2019). Figure 13(a) and (b) show examples of cast-in-place bored geothermal energy piles (GEPs) with U-shaped pipe configurations installed for a residential building at Monash University in Melbourne, Australia.

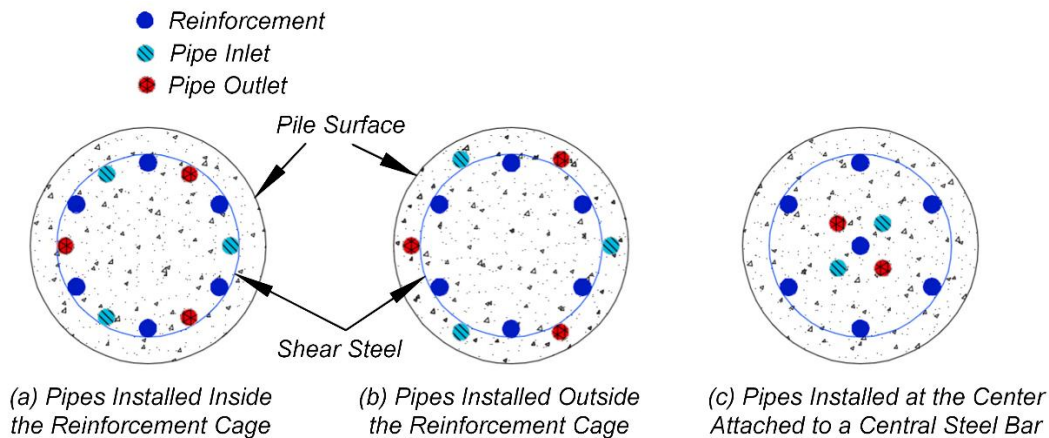


Figure 12. Various attachment arrangements of heat exchanger pipes on the reinforcement cage (Sani et al., 2019)

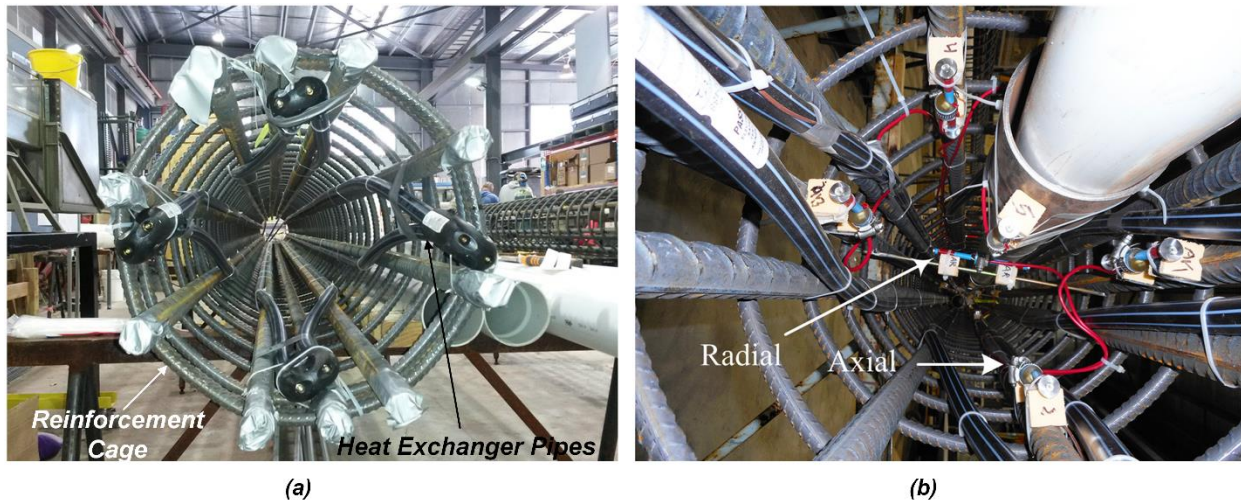


Figure 13. (a) U-shaped pipes inside an energy pile reinforcing cage (b) instrumented energy pile (Faizal et al., 2019)

Vertical loop pipes can be installed in various configurations within pile heat exchangers. Figure 14 illustrates four common pipe arrangements: U-shaped, double U-shaped, W-shaped, and spiral-shaped configurations (Gao et al., 2008; Hamada et al., 2007; Park et al., 2012; You et al., 2016). Figure 13(a) presents an example of a U-shaped pipe configuration embedded within the reinforcement cage of an energy pile, which provides heating for a six-story student dormitory at Monash University in Melbourne, Australia (Faizal et al., 2019). Figure 15(a) and (b) depict energy piles featuring double U-shaped and spiral-shaped pipe configurations, respectively, tested at a high-speed railway station project in Xinyang, Henan Province, China.

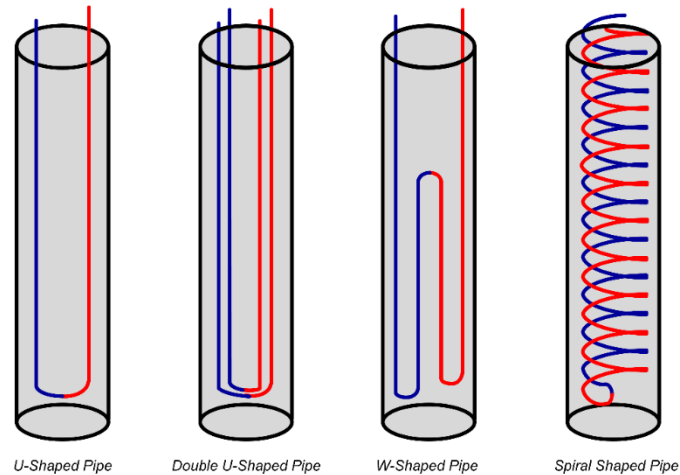


Figure 14. Different configurations of energy loops within a GEP (Sani et al., 2019)

Previous studies have highlighted the significant influence of heat pipe configuration on the efficiency of GSHP systems (i.e. Bozis et al., 2011; Lee & Lam, 2013; Park et al., 2013; Wood et al., 2012). Gao et al. (2008) conducted field experiments to evaluate the heat transfer efficiency of four different loop configurations: single U-shaped, double U-shaped, triple U-shaped, and W-shaped. Among these, the W-shaped configuration demonstrated the highest thermal performance. Similarly, Zarrella et al. (2013) assessed the thermal performance of helical (spiral-shaped), double U-shaped, and triple U-shaped pipe configurations through field testing. Their results indicated

that the helical configuration outperformed the others, delivering 23% and 40% higher thermal performance compared to the triple and double U-shaped configurations, respectively. In a related study, Kuishan et al. (2007) found that a parallel triple U-shaped configuration offered superior heat transfer performance and efficiency compared to single U-shaped, double U-shaped, W-shaped, and spiral configurations. Under comparable initial conditions, the heat release per meter of the parallel triple U-shaped configuration was approximately 87% higher than that of the single U-shaped type.

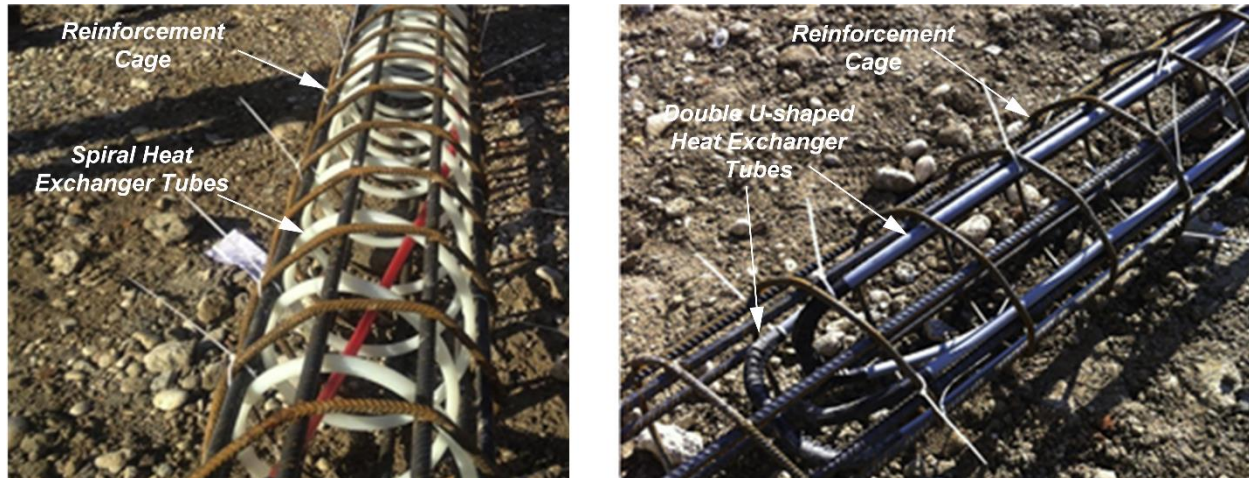


Figure 15. The reinforcement cage of tested energy piles (a) spiral shaped (b) double U-shaped (Zarrella et al., 2013)

Thompson III (2013) investigated the impact of loop quantity on the performance of ground source heat pump (GSHP) systems. The study evaluated three loop configurations, four, five, and six loops, installed in 120 cm (3.9 ft) diameter energy piles, while keeping all other parameters constant. Results showed that the outlet fluid temperature decreased as the number of loops increased, indicating enhanced heat transfer. This improvement was attributed to the greater surface area available for heat exchange within the pile. However, the study also noted that increasing the number of loops led to higher pumping power requirements due to added system resistance.

Circulating Fluid

Circulating fluid refers to the liquid that flows through heat exchanger pipes and, in heating mode, facilitates heat exchange between the ground and the heat pump. In GSHPs, several types of circulating fluids can be used. An ideal circulating fluid should have low viscosity, be environmentally friendly, and be cost-effective (Rawlings & Sykulski, 1999). Common options include water, water-antifreeze mixtures, and saline solutions. Among these, water-antifreeze solutions are widely used to prevent freezing. The most commonly used antifreezes are ethylene glycol and propylene glycol (Brandl, 2006). However, the addition of antifreeze increases fluid viscosity at low temperatures, which in turn raises the electricity consumption of the heat pump system (Loveridge et al., 2020; Rawlings & Sykulski, 1999). If the antifreeze solution contains corrosion inhibitors, it may become toxic, requiring additional precautions to prevent system leaks. According to the Agency for Toxic Substances and Disease Registry (ATSDR, 1997), under the U.S. Department of Health and Human Services, propylene glycol is considered safer than ethylene glycol, which is toxic. In the event of a leak, propylene glycol degrades quickly and is

fully soluble in water. Based on ATSDR (1997) data, the half-life of propylene glycol in water ranges from 1 to 4 days under aerobic conditions and from 3 to 5 days under anaerobic conditions. Its half-life in soil is expected to be equal to or slightly shorter than in water (ATSDR, 1997).

Heat Pump System

A heat pump system serves as the energy carrier that transfers harvested geothermal energy to the secondary unit. Geothermal heat pump systems are typically categorized based on their heat source (ASHRAE & Design, 2011). When the system uses groundwater as a heat source or sink, it is referred to as a Ground Water Heat Pump (GWHP). Conversely, if the system uses the ground itself as the heat source or sink, it is known as a Ground Source Heat Pump (GSHP). GWHP systems offer the advantages of lower initial costs and smaller space requirements (American Society of Heating & Engineers, 2003). However, they are limited by the availability of groundwater and often require higher maintenance. GSHP systems, also known as closed-loop heat pumps, are generally more environmentally friendly. One key advantage is that their collector loops are embedded in soil, which experiences less temperature fluctuation than groundwater (Sarbu & Sebarchievici, 2014). Despite these benefits, GSHP systems typically involve higher upfront costs due to the need for specialized equipment and installation procedures.

A heat pump system consists of four main components: the evaporator, condenser, compressor, and expansion valve, as illustrated in Figure 16 (Bach et al., 2016). In heating mode, the circulating fluid is first pumped through pipes embedded in geothermal piles, where it absorbs thermal energy from the ground via conduction and convection. This absorbed heat is then transferred to the evaporator, which contains a refrigerant cooler than the circulating fluid. As the refrigerant absorbs heat from the fluid, it evaporates into a gas. The vaporized refrigerant then enters the compressor, where its pressure and temperature are significantly increased. The high-temperature refrigerant flows into the condenser, where it transfers heat to the secondary unit, causing the refrigerant to condense. After releasing its heat, the refrigerant passes through an expansion valve, which reduces its pressure and temperature, restoring it to its original state. The refrigerant then returns to the evaporator, and the cycle repeats (Brandl, 2006; De Moel et al., 2010; Johnston et al., 2011).

The terms *coefficient of performance (COP)* and *energy efficiency ratio (EER)* are commonly used to describe the heating and cooling efficiency of geothermal systems that incorporate a heat pump. COP is defined as the ratio of useful thermal energy produced to the electrical power consumed. A higher COP indicates a more efficient system. The COP of a heat pump is directly related to its EER, as expressed by Equation 1 (Sarbu & Sebarchievici, 2014):

$$\text{COP} = \text{EER} / 3.413 \quad (1)$$

The COP of a GSHP system designed for a closed-loop heating configuration typically ranges from 2.5 to 4.0, while the EER for a closed-loop cooling system ranges from 10.5 to 20.0 (Heinonen et al., 1996).

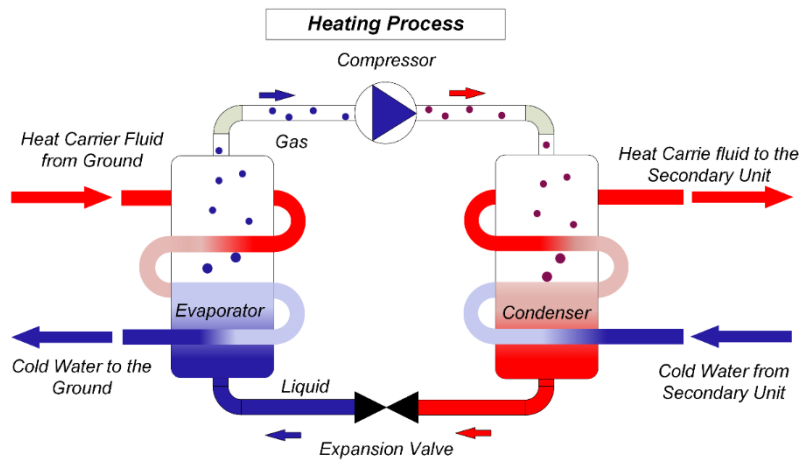


Figure 16. Process of the overall heating only in heat pump system

Power Source

As a promising strategy for enhancing energy efficiency, heat pumps can be integrated with other renewable energy sources. Among these, solar energy has been identified as the most compatible option for hybridization with GSHP systems (Leenders et al., 2000; Tagliabue et al., 2012). When combined, solar and geothermal energy can work synergistically, solar energy can be used either to reduce the thermal load on boreholes or to generate supplemental electrical power for system operation (Bakker et al., 2005; Shahed & Harrison, 2009).

Solar thermal collectors can be integrated with GSHPs in either a parallel or series configuration. In a parallel arrangement, both the solar thermal system and the GSHP operate independently and can directly supply heat to meet the system's demand. Each system functions as a primary heat source, and a control unit determines which source to use based on real-time efficiency and availability (Duffie et al., 2020). A schematic of this configuration is shown in Figure 17(a). In the series configuration, also referred to as a *solar-augmented heat pump system* (Figure 17(b)), solar thermal collectors preheat the circulating fluid before it enters the heat pump evaporator via a heat exchanger loop. This configuration enhances system performance by increasing the inlet temperature to the heat pump. Additionally, it offers the potential for seasonal thermal energy storage, where excess solar heat collected during warmer months can be stored and utilized during the winter season (Shahed & Harrison, 2009).

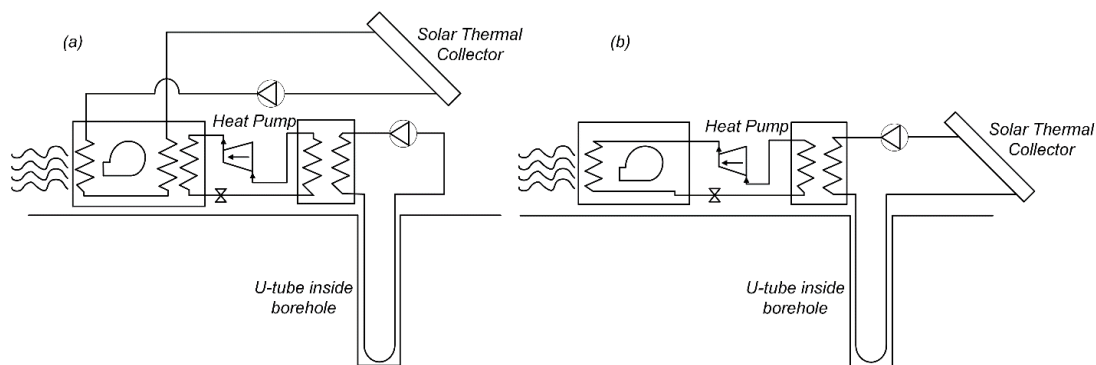


Figure 17. Simplified schematic of a solar assisted ground-source heat pump system (a. parallel, b. series) (Shahed & Harrison, 2009)

Trillat-Berdal et al. (2006) investigated the performance of a Ground Source Heat Pump (GSHP) system hybridized with solar thermal collectors in a 180 m² private residence. The system was configured in a series arrangement and included two 90-meter (295 ft) boreholes serving as the ground loop. Solar energy was used primarily to heat a water storage tank to a target temperature, with any excess solar energy injected into the ground through embedded heat exchanger loops. A schematic of the system is presented in Figure 18. The circulating fluid consisted of a 35% propylene glycol-water solution. Through analysis of system behavior and energy balances, the study found that continuous operation of the heat pump did not yield optimal performance. An average COP of 3.75 was achieved in heating mode. Over the monitoring period, 6,253 kWh of thermal energy was extracted from the ground, while 2,121 kWh of solar heat was injected into it. The study concluded that integrating solar thermal collectors can potentially reduce the number of boreholes required, thereby lowering installation costs.

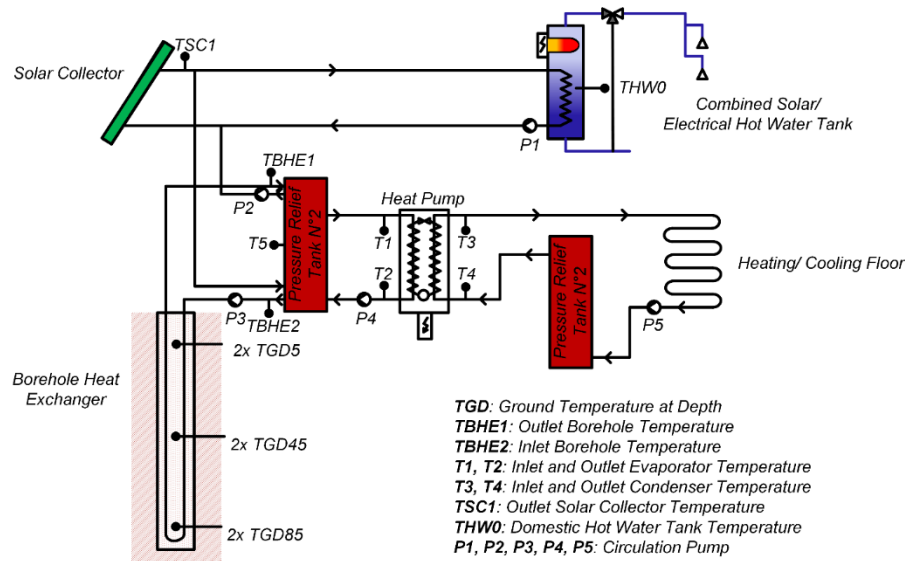


Figure 18. Schematic view of ground-coupled heat pump combined with thermal solar collectors (Trillat-Berdal et al., 2006)

Bakker et al. (2005) evaluated the performance of a solar-assisted Ground Source Heat Pump (GSHP) system at the Energy Research Centre of the Netherlands. The system employed photovoltaic/thermal (PVT) panels, which integrate photovoltaic cells with solar thermal collectors to simultaneously produce electricity and heat. Figure 19 displays the front and back views of a PVT panel used in the study. Heat generated by the PVT array was transferred to a storage vessel via a heat exchanger. During summer months, excess thermal energy was injected into the ground through embedded heat exchanger loops. In winter,



Figure 19. Front and back of a PVT panel (Bakker et al., 2005)

this stored heat was extracted using the same ground loop system, with a heat pump delivering the required heating. A schematic of the full system configuration is shown in Figure 20. Based on a ten-year average energy balance, the PVT system supplied approximately 96% of the total electricity demand of the system, including that of the pumps, electric heater, and heat pump. Additionally, the injection of solar heat into the ground proved effective in maintaining stable ground temperatures over long-term operation. This thermal stability contributed to a slight increase in the heat pump's coefficient of performance (COP), from 2.6 to 2.66.

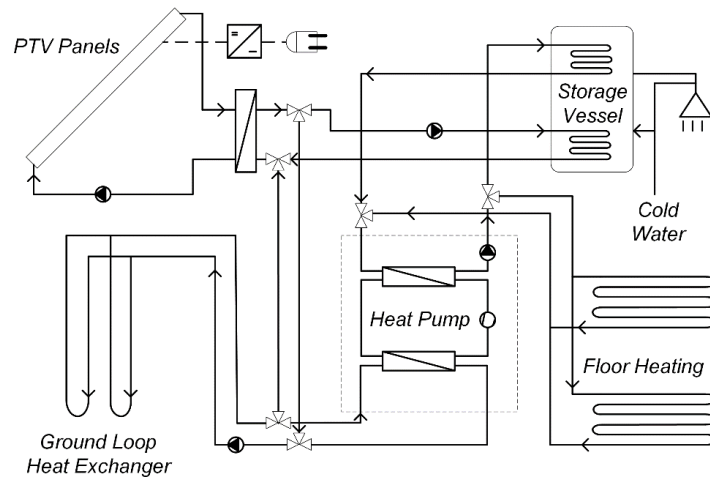


Figure 20. Schematic view of tested hybrid system (Bakker et al., 2005)

Bernier and Shirazi (2007) investigated the performance of a modified solar-assisted heat pump system featuring a dual-loop configuration. In their proposed design, two independent U-pipe loops were embedded within a single borehole, as illustrated in Figure 21. One U-loop was connected to the heat pump, while the other was linked to the solar thermal collectors. During summer, solar energy was used to heat a water tank, and any excess heat was injected into the ground via the solar loop. In winter, solar energy was either transferred directly to the heat pump loop, if the heat pump was active, or injected into the ground when the pump was not in operation. The study concluded that this configuration led to elevated ground temperatures, which enhanced the overall performance of the heat pump. Additionally, the increase in ground temperature allowed for a reduction in the required borehole depth, offering potential cost savings in system installation.

Secondary Unit

The secondary unit of a GSHP system consists of pipes embedded in bridge decks, pavements, or other infrastructure elements. This system utilizes extracted thermal energy during cold periods to heat surfaces and absorbs excess heat during warmer periods to transfer it back into the ground. In recent years, hydronic heating systems for snow melting and deicing on bridge decks have gained increased attention due to their potential for improved safety and infrastructure durability. While the harvested geothermal energy could also be applied to deicing culverts, the feasibility of using GSHP systems for this specific application has not yet been thoroughly investigated.

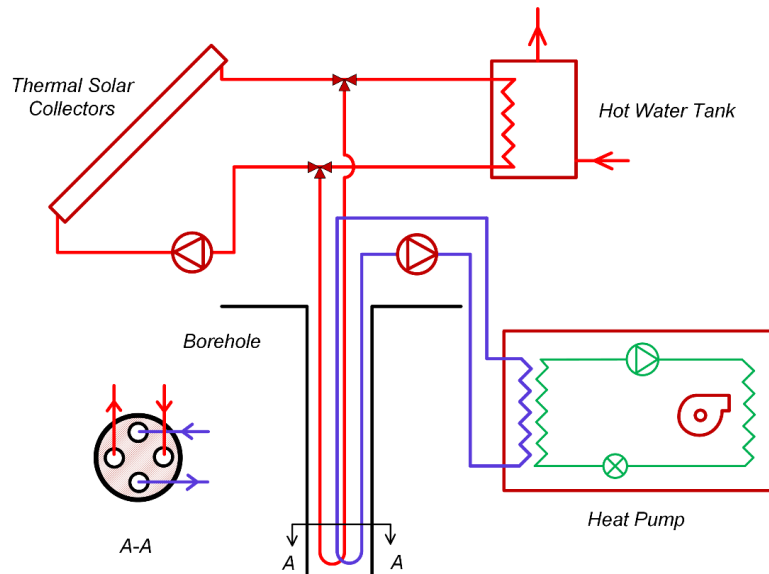


Figure 21. Schematic of the modified system proposed by Bernier and Shirazi (2007)

A schematic of a GSHP system for heating bridge decks is illustrated in Figure 22. In this configuration, circulation pipes are embedded within the substructural elements of the bridge, effectively transforming foundation components into energy foundations. To enhance ground heat exchange and overall system efficiency, additional heat exchanger loops can be installed within the bridge embankment. As the circulating fluid travels through the energy piles, absorbs geothermal heat, and passes through the embankment, it eventually flows into the bridge deck, delivering heat to the surface and preventing snow and ice accumulation.

The circulating fluid in a GSHP system can be delivered to the bridge deck either directly from the foundation (passive system) or through a heat pump (active system). In an active system, the heat pump extracts thermal energy from the fluid and uses it to efficiently raise the temperature of the circulating fluid for bridge deck deicing (Liu et al., 2007). In contrast, a passive system operates without a heat pump, relying solely on the ground temperature to control the fluid's temperature. The primary advantage of a passive system is its low energy demand, as it only requires electricity to power the circulation pumps. However, active systems, while more energy-intensive due to the additional power required for the heat pump, offer more effective and controlled heating performance.

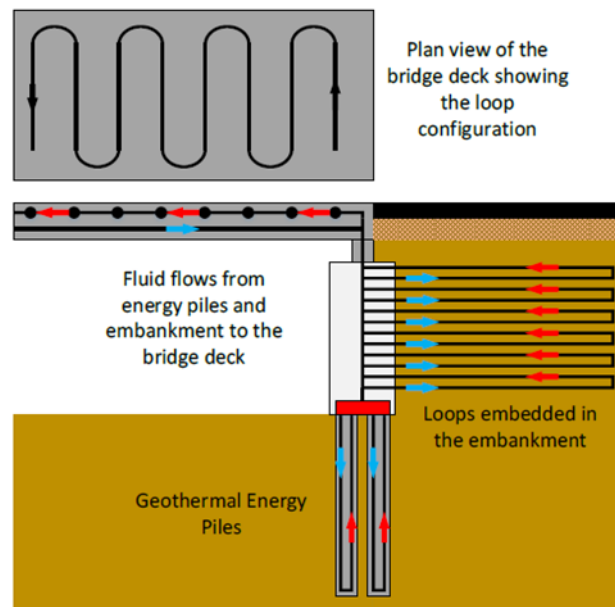


Figure 22. Conceptual schematic of ground-source bridge deck deicing (Bowers & Olgun, 2014)

A GSHP may also be adapted for ice jam mitigation and prevention in culverts. However, the application of geothermal energy for culvert deicing and anti-icing has not yet been documented in published research. As a result, no standardized design guidelines or best practices exist for such systems based on real-world experience. A schematic of a potential culvert deicing system is shown in Figure 23(a). drawing on design concepts from geothermal applications in tunnels and other underground structures. As illustrated in Figure 23(a), heat exchanger pipes can be installed within the culvert lining and deck to deliver geothermal heat. Pipe configuration is a critical factor in system efficiency, as discussed in the primary unit section. Three common configurations suitable for culvert applications include: (1) longitudinal pipes running along the culvert axis, (2) transverse pipes installed perpendicular to the flow direction, and (3) slinky coils, as shown in Figure 23(b). These pipes may be embedded either at the bottom of the culvert or within the primary lining (e.g., concrete), or they can be placed between the primary lining and a secondary layer with high thermal conductivity, such as an energy geotextile layer (Figure 23(c)) (Loveridge et al., 2020).

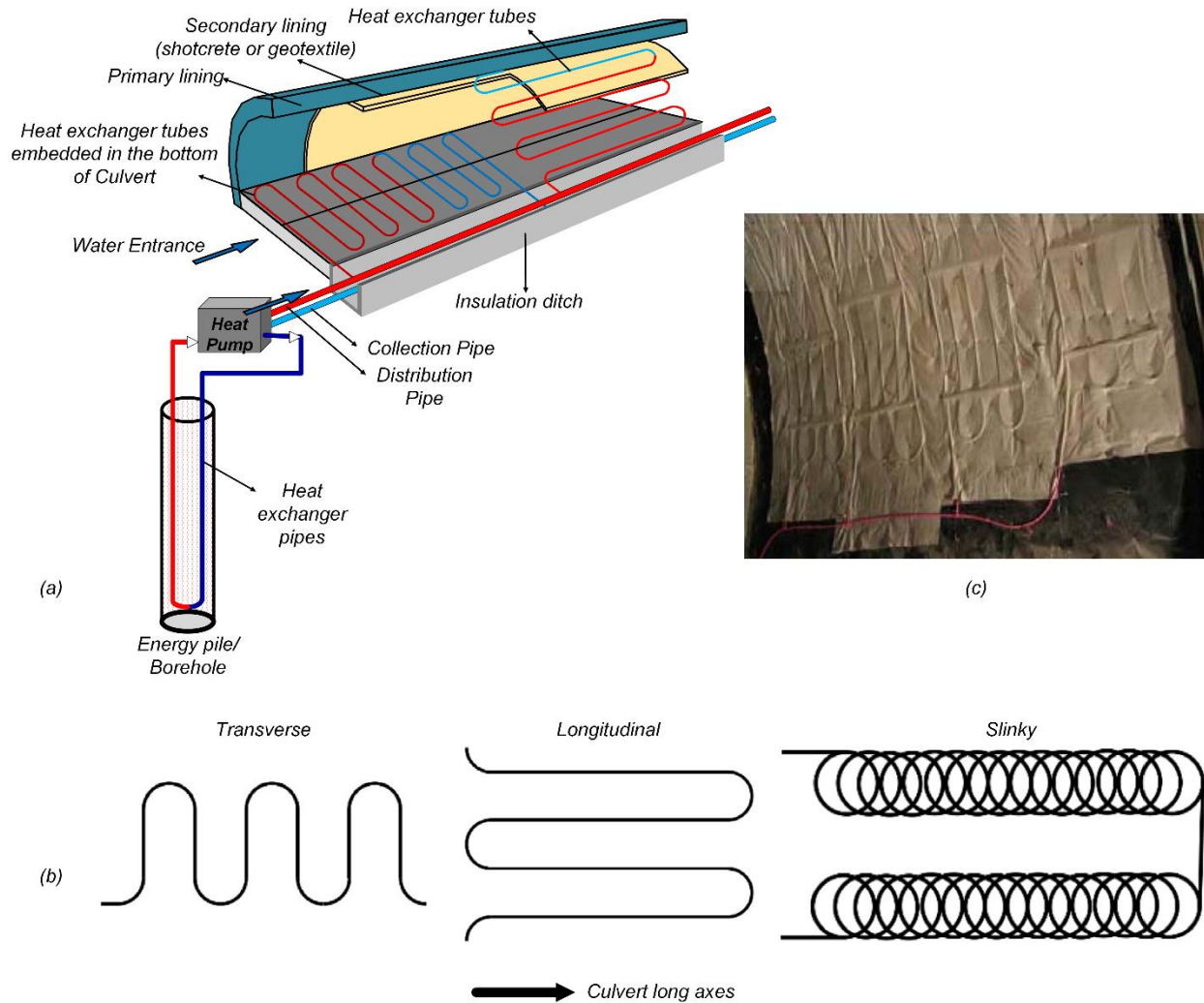


Figure 23. (a) A schematic of a possible culvert deicing system based on previous studies on the use of geothermal energy in tunnels and underground structures, (b) Various pipe configuration (c) An energy geotextile installed in an energy tunnel (Loveridge et al., 2020)

Use of Geothermal Energy for Bridge Deicing: Case/Field Studies

This section provides a brief overview of several case studies in which geothermal energy was utilized for bridge deck deicing or snow melting. The case studies examined in this report are summarized in Table 6.

Case Study 1: Jiangyin, China

Chen et al. (2020) presented the results of field tests on a heated bridge deck located in China. The bridge deck measured 30 m (98.4 ft) in length, 26 m (85.3 ft) in width, and 80 cm (2.6 ft) in thickness. Figure 24 shows a photo of the constructed bridge deck, the schematic layout of the heating system, and the sensor locations. The annual average and minimum ambient temperatures in the city were 17 °C (63 °F) and -5 °C (23 °F), respectively. During the test period, nighttime minimum temperatures ranged between 10–20 °C (50–68 °F), while daytime maximum temperatures ranged between 20–30 °C (68–86 °F). The secondary system employed Polyethylene Raised Temperature (PERT) pipes with an inner diameter of 16 mm (0.6 in), a wall thickness of 2 mm (0.08 in), and a spacing of 25 cm (10 in). A water tank served as the heat source for the deicing system. To assess the effect of fluid temperature on system performance, three inlet temperatures were tested: 30.5 °C (86.9 °F), 35.5 °C (95.9 °F), and 41 °C (106 °F). The volumetric flow rate of the heat carrier fluid was maintained at 0.79 m³/h (27.9 ft³/h). Two thermostats and a flowmeter were installed to monitor inlet and outlet fluid temperatures as well as the flow rate. The results of the study demonstrated that the transient heat flux of the system varied linearly with the temperature difference between the inlet fluid and the ambient air. As illustrated in Figure 25(a), for a constant fluid inlet temperature, the transient heat flux increased as the ambient temperature decreased.

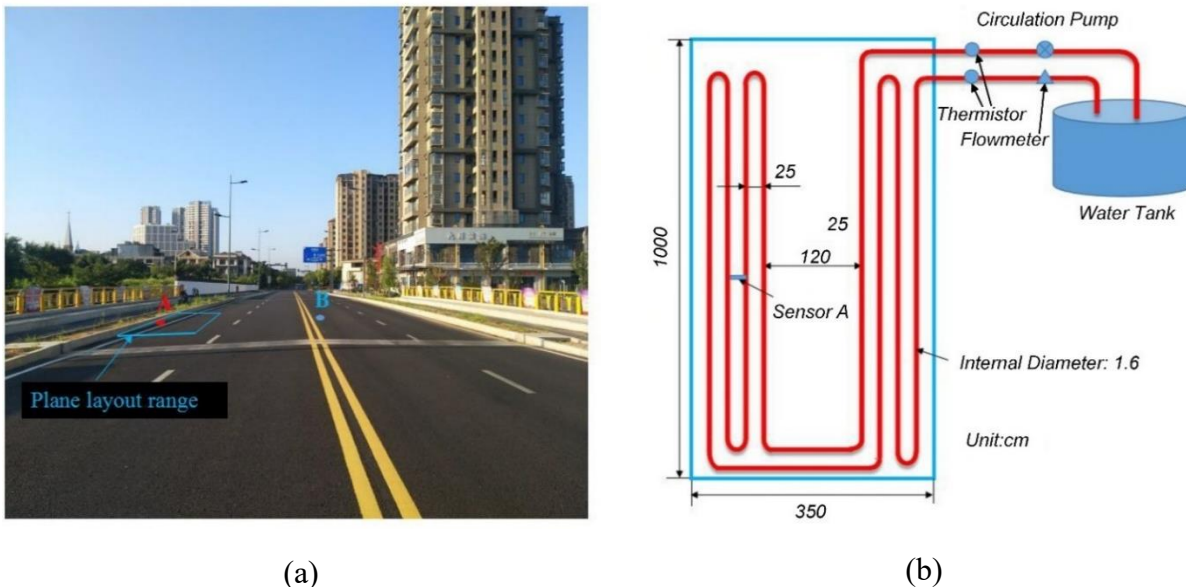


Figure 24. (a) Photo of the bridge (b) schematic layout of heating system (Chen et al., 2020)

Table 6. Case/Field studies of bridge deck deicing/anti-icing using GSHP systems

Source	Location	Snow Melting system	Heat Extraction System	Temperature Range
Xin Chen et al. (2020)	Jiangyin, China Bridge length: 30 m Bridge Width: 26 m Deck Thickness: 80 cm	Heated area: 20 m ² Fluid: Water Pipe material: Polyethylene raised temperature pipes (PERTs) Pipe diameter: 20 mm Horizontal spacing of the pipes: 25 mm	Water Tank Temperature Control Temperature: 30.5°, 35.5°, 41°	Average = 17°C Minimum = -5°C
Kong et al. (2019)	Jiangyin, China Bridge length: 36 m Bridge Width: 26 m Deck Thickness: 80 cm	Heated area: 20 m ² Fluid: Water Pipe material: Polyethylene raised temperature pipes (PERTs) Pipe diameter: 20 mm Horizontal spacing of the pipes: 25mm	Energy Pile Heat Exchange rate: 1200 W Pile length: 20 m Pile diameter: 1 m Pipe Arrangement: U shape	Ambient T = -1.5°C
Eugster (2007)	Central Switzerland	Heated area: 1300 m ² Heat Output: 100 W/m ²	Number of boreholes: 91 Depth of boreholes: 65 m	Outflow T = 10°C
Boyd (2003)	Klamath Falls, Oregon, Bridge length: 48 m Bridge width: 12.8 m	Heated area: 345.6 m ² Heat Output: 189 W/m ² Fluid: Propylene glycol solution Pipe material: Polyethylene Pipe diameter: 16 mm	Geothermal heat exchanger Well water flowing: 2.5 L/s	Inlet Fluid T to deck = 66°C Output Fluid T to deck = 43°C
Minsk (1999)	Silver Creek, in the Cascade Mountain, Oregon Bridge length: 32 m Bridge Width: 12.2 m	Heated area: 576 m ² Heat Output: 394 W/m ² Fluid: Propylene glycol solution Pipe material: Cross-linked polyethylene (PEX) Pipe diameter: 12.7 mm Horizontal spacing of the pipes: 114 mm	Ground surface heat pump Heat input: 37 W/ft ² Well water flowing: 568 L/min	Ambient T = -23°C Inlet Fluid T to deck = 49°C Output Fluid T to deck = 32°C
Minsk (1999)	Two-lane bridges on US 287 in Amarillo, Texas, Deck Length: 44.5 m Deck Width: 17.7 m	Heated area: 799 m ² Fluid: Propylene glycol-deionized water Pipe diameter: 19 mm Horizontal spacing of the pipes: 152 mm	Well Depth: 53.6 m Well Diameter: 102 mm Pipe Arrangement: Two pipe loops Filling Material: Non-shrinking bentonite	Ambient T = 1.7°C
Yoshitake et al. (2011)	Mountain road in western Japan, Bridge deck area: 430 m ² , Road area: 265 m ²	Deck Material: Concrete mixture with Polypropylene Fiber, Pipe material: Steel Pipe Horizontal spacing of the pipes: 150 mm	Underground water tank Diameter*Height: 5.5 m * 9.5 m	Ambient T = 2°C Ground temperature at a depth of 15 m = 12°C

The thermal efficiency of the deicing system was found to be influenced by three primary factors: (1) the thickness of the concrete above the heating pipes, (2) the thermal conductivity of the concrete, and (3) the heat transfer coefficient from the heated layer to the ambient air. Thermal efficiency was defined as the proportion of heat transferred from the heated layer to the top surface of the bridge deck. In this study, the average heat transfer efficiency to the deck surface was reported as 0.52. Based on this efficiency value, an equation was developed to estimate the deck surface temperature (T'_s) presented as Equation 2:

$$T'_s = 0.3T_{in} + 0.7T_0 \quad (2)$$

where T_{in} is the inlet fluid temperature ($^{\circ}\text{C}$) and T_0 is the air temperature ($^{\circ}\text{C}$). Figure 25(b) illustrates the relationship between inlet fluid temperature and the required heat flux needed to maintain the bridge deck surface temperature above 0°C (32°F) under varying ambient conditions. According to the results, when the air temperature drops below 0°C , the minimum inlet fluid temperature necessary to keep the deck surface above freezing should be approximately 2.3 times the ambient temperature. For example, given that the minimum recorded winter temperature at the project site was -5°C (23°F), the inlet fluid temperature must exceed 11.5°C (52.7°F) to ensure effective deicing.

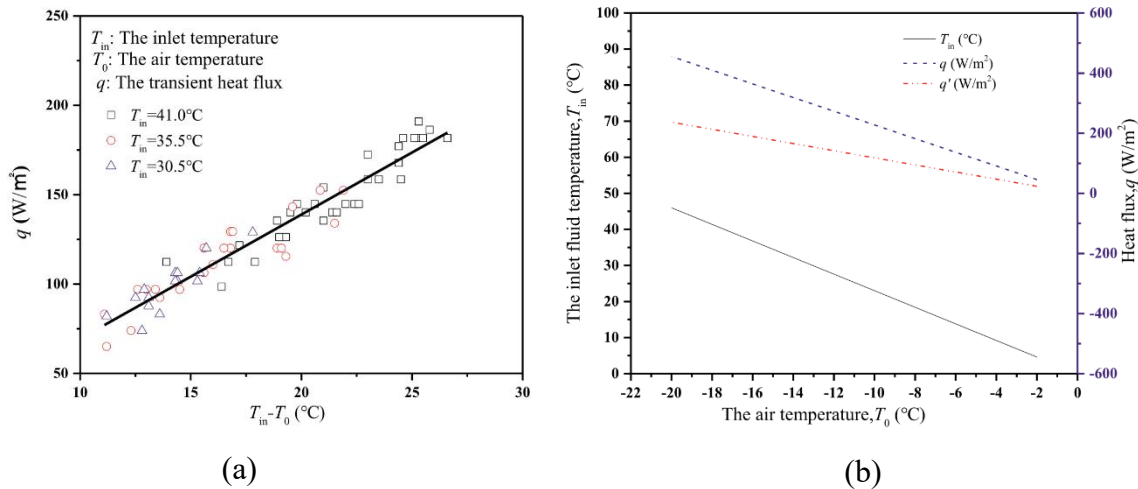


Figure 25. (a) Variation of heat flux, q , with the difference between the inlet fluid and the ambient temperatures, $T_{in}-T_0$, (b) the required inlet fluid temperature and heat flux to keep the deck surface temperature above freezing point (Chen et al., 2020)

Case Study 2: Jiangyin, China

Kong et al. (2019) Kong et al. (2019) evaluated the performance of a geothermal bridge deck deicing system that utilized pile heat exchangers under active snowfall conditions. The study was conducted in Jiangyin, China, with the primary goal of accelerating the snow-melting process on bridge surfaces. The test section measured 10 m (32.8 ft) in length, 3.5 m (11.5 ft) in width, and 0.8 m (2.6 ft) in thickness. Figure 26 illustrates the configuration of the system, including the placement of heat pipes in the bridge deck (Figure 26(a)), a photo of the setup prior to concrete placement (Figure 26(b)), and a schematic of the overall deicing system (Figure 26(c)). Polyethylene Raised Temperature (PERT) pipes, with an inner diameter of 16 mm (0.6 in) and a wall thickness of 2 mm (0.08 in), were embedded within the upper 10 cm (3.9 in) of the reinforced concrete deck at a spacing of 25 cm. The primary system consisted of 1-meter diameter energy piles, each 20 m (65.6 ft) deep, with a total heat exchange capacity of 1200 W per pile. U-shaped

polyethylene pipes, 25 mm (1 in) in outer diameter, were installed within each energy pile. A water tank served as the reservoir for the circulating fluid. At the start of the test, the fluid temperature in the tank was approximately 2 °C (35.6 °F), while the ambient air temperature was -1.5 °C (29.3 °F). The fluid entered the system at a flow velocity of 1.27 m/s (3.3 ft/s). Bridge deck temperatures were continuously monitored using embedded sensors to assess the deicing performance.

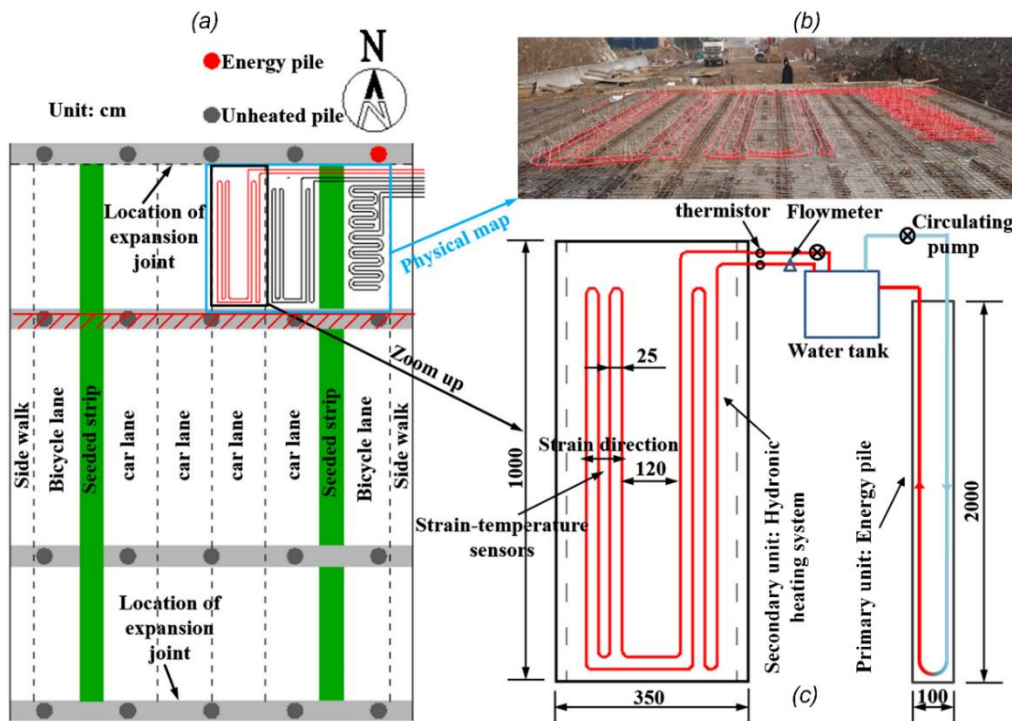


Figure 26. (a) Location of the studied section of the bridge (b) photo of bridge deck before pouring concrete (c) layout of bridge deck deicing (Kong et al., 2019)

Figure 27 shows the surface condition of the bridge deck during the operation of the geothermal deicing system at selected time intervals (0, 3, 7, 17, 25, and 27 hours). As illustrated, the system was not highly effective at melting snow during active snowfall, particularly during the first 7 hours of the experiment. However, Figure 28(a) demonstrates that continuous operation of the system maintained the bridge deck temperature at a steady 1 °C (34 °F), despite ongoing snowfall. This thermal stability is attributed to snow's natural insulating properties, which reduced the impact of ambient air temperature on both the bridge deck and the circulating fluid. Snow melting on the bridge deck began once the snowfall ceased, between hours 16 and 25 of the test. As shown in Figure 28(a) the deck temperature rose by approximately 2.8 °C (5.0 °F) a few hours after the snowfall ended, reaching a peak temperature of 3.8 °C (38.9 °F) (identified as point F in Figure 28). The deck surface temperature remained above freezing even as the ambient temperature dropped below 0 °C (32 °F). These results indicate that while geothermal systems may have limited effectiveness during active snowfall, they can significantly accelerate snow melting once snowfall stops, enhancing post-storm road safety and maintenance efficiency.

The variation in inlet and outlet circulating fluid temperatures is presented in Figure 28(b). The results indicated that the changes in fluid temperatures closely followed the trends observed in bridge deck temperatures. However, the outlet fluid temperature was consistently about 3 °C

(37 °F) higher than the deck temperature. This difference is likely due to the high inlet flow velocity of 1.27 m/s (4.2 ft/s), which enhances heat transfer efficiency. The heating power of the system was calculated to range between 55 and 70 W/m², which falls below the upper limit of 80 W/m² for heat flux. This upper limit is based on the maximum heat exchange capacity of 60 W/m for an energy pile with a diameter greater than 0.6 m (23.6 in). The lower observed heating power was attributed to heat losses occurring between the hydronic heating system and the energy pile.

Han and Yu (2017) calculated the snow-melting heat flux requirements for bridge decks under ten different design conditions. Their findings showed that achieving 95% reliability in maintaining snow-free surfaces required heat fluxes ranging from 280 to 792 W/m². However, Kong et al., (2019) reported that the heat flux provided by typical deicing systems is generally lower than this threshold. As a result, it was concluded that a shallow geothermal bridge deck deicing system without a heat pump may not be sufficient to keep the deck surface completely snow-free during active snowfall. Nonetheless, such a system can significantly accelerate the snow-melting process following snow events, as illustrated in Figure 27.

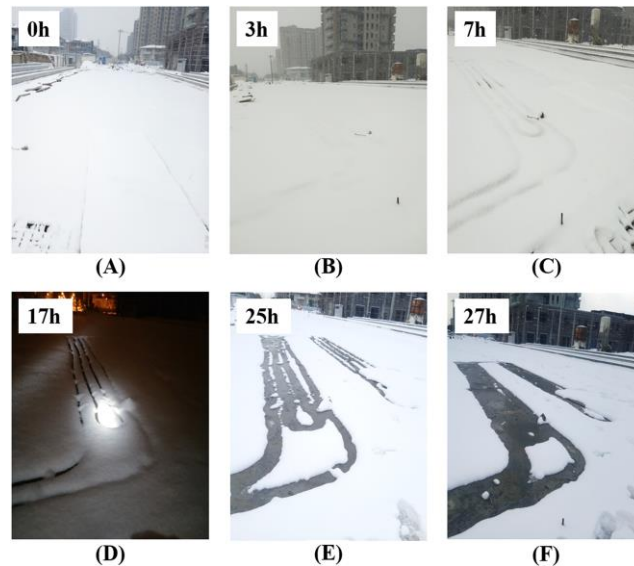


Figure 27. Surface condition of deck surface at different hours (Kong et al., 2019)

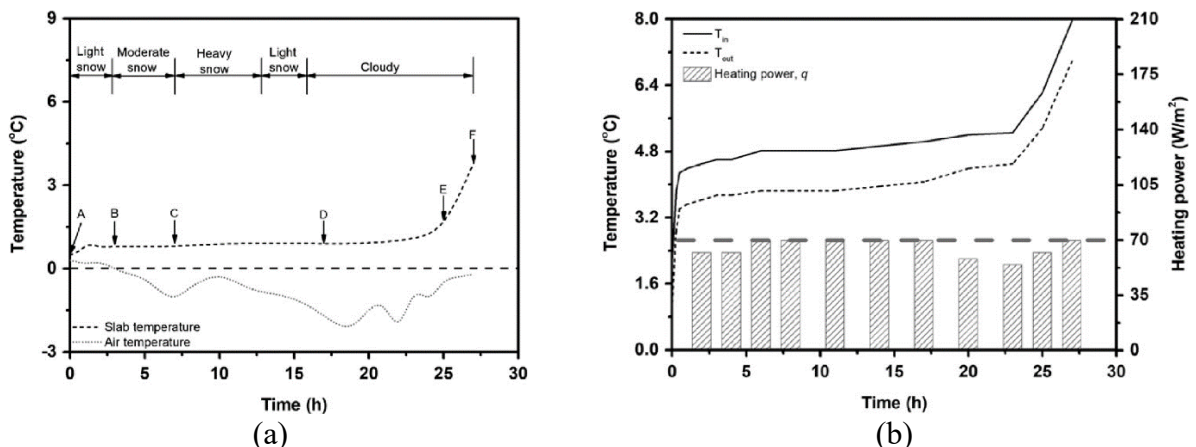


Figure 28. (a) Change in the ambient and bridge deck temperatures, (b) variation of the inlet and outlet circulating fluid temperature and the heating power of the deicing system (Kong et al., 2019)

Case Study 3: Central Switzerland

The SERSO system in Switzerland, with a total heated area of 1,300 m² (13,993 ft²), is one of the longest-running hydronic geothermal bridge deck deicing projects in the world. The system has been in continuous operation since 1994 (Eugster, 2007). Figure 29(a) and (b) show a photo of the SERSO system in operation and a schematic of the deicing system, respectively. The system was designed to prevent the accumulation and freezing of snow and other forms of precipitation on the bridge deck. It utilizes 91 borehole heat exchangers, each with a depth of 65 m (213 ft), and operates by storing thermal energy in 55,000 m³ (1,942,306 ft³) of rock during the summer. In winter, the stored thermal energy is used proactively to prevent snow accumulation on the deck. Figure 30 presents typical ambient and surface temperatures recorded during winter operation. The study concluded that continuous operation of the heating system reduces overall heat demand in winter and enables the system to function without the need for a ground source heat pump (GSHP). The thermal energy collected in summer generally exceeds the amount needed for deicing, and the surplus heat helps stabilize road surface temperatures year-round, potentially extending the lifespan of the bituminous pavement.

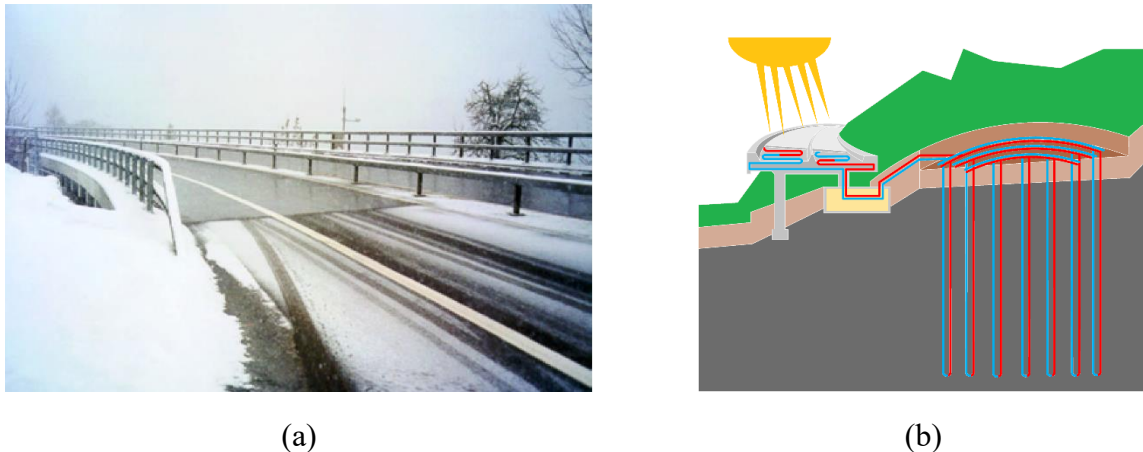


Figure 29. (a) Photo of the bridge (b) schematic of a SERSO system in Switzerland (Eugster, 2007)

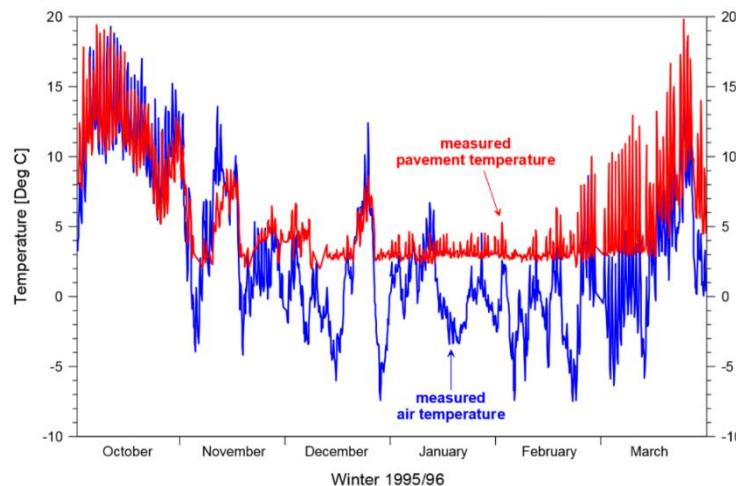


Figure 30. Comparison of the measured ambient and surface temperature during operation (Eugster, 2007)

Case Study 4: City of Klamath Falls, Oregon

A snow melting project using geothermal energy was developed through a joint effort by the Oregon Department of Transportation and the City of Klamath Falls (Boyd, 2003). The Wall Street Bridge and its approach road utilized a geothermal snow melting system, with heat supplied by the Klamath Falls District Heating System. The heated surface area included 345.6 m² (27 m × 12.8 m) on the bridge deck and sidewalks, and 614.4 m² (48 m × 12.8 m or 3720 ft²) on the approach road and sidewalks. The district heating system consisted of two production wells, a geothermal water transmission pipeline, a heat exchanger and pumping facility, and a closed-loop heating water delivery system. The circulating fluid in the bridge and approach road loops was a 35% propylene glycol mixture. Heat exchanger pipes, made of cross-linked polyethylene with an inner diameter of 16 mm (0.6 inch), were installed longitudinally on the bridge deck and sidewalks, and transversely on the approach road. Figure 31(a) and (b) show the bridge deck and approach road pipe loop layouts, respectively. The inlet and outlet temperatures of the circulating fluid were 66 °C (151 °F) and 43 °C (109 °F), respectively. The system was designed to effectively melt snow and ice during heavy snowfall events and ambient temperatures as low as -24 °C (-11.2 °F).



Figure 31. (a) Longitudinal closed loop on the bridge deck and (b) approach road loops in Klamath Falls, Oregon (Boyd, 2003)

Case Study 5: Mountain Road in Japan

An underground water storage tank measuring 9.5 m (31.1 ft) in height and 5.5 m (18 ft) in diameter was used to provide geothermal energy for a bridge system on a mountain road in Japan (Yoshitake et al., 2011). The schematic of the bridge with the hydronic heating system is illustrated in Figure 32. A schematic of the bridge and its hydronic heating system is shown in Figure 32. This system does not include a heat pump; instead, the water in the tank is passively heated by the ground to approximately the ambient ground temperature. The annual average air temperature at the site is 12 °C (54 °F), although temperatures during winter nights and early mornings often drop below 0 °C (32 °F). The system was automatically controlled and activated whenever the bridge deck temperature fell below 0.5 °C (33 °F). The heated areas included 430 m² (4628 ft²) of bridge deck and 265 m² (2852 ft²) of road surface. Water was circulated through embedded steel pipes with an inner diameter of 15 mm (0.6 inch), a wall thickness of 3.5 mm (0.14 inch), and a thermal conductivity of 43 W/m·K. The pipes were spaced horizontally at 150 mm (5.9 inch) intervals and embedded 50 mm (2 inch) below the road surface. To reduce the risk of cracking from thermal

cycling, the bridge deck was constructed using a concrete mix reinforced with polypropylene fibers.

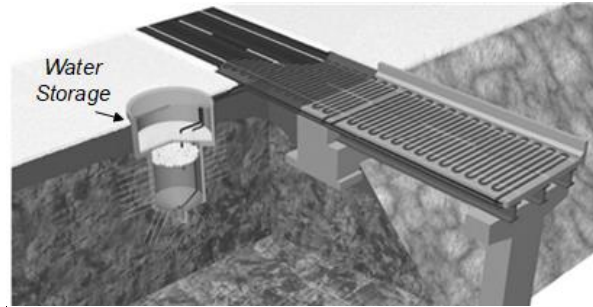


Figure 32. Hydronic heating system using underground water storage on a mountain road in Japan (Yoshitake et al., 2011)

Figure 33 illustrates the condition of the road before and after a 9-hour operation of the geothermal deicing system. As shown in the figure, the system effectively melted the accumulated snow on the bridge and approach road surfaces. Figure 34 presents the recorded temperatures of the water storage tank, bridge deck, and approach road during system operation from April 2007 to March 2008. The results demonstrate that continuous operation of the geothermal heating system successfully maintained the bridge deck and road surface temperatures above 0.5°C (33°F), thereby preventing snow accumulation throughout the winter season. During the summer, operation of the system led to an increase in the temperature of the water stored in the tank.

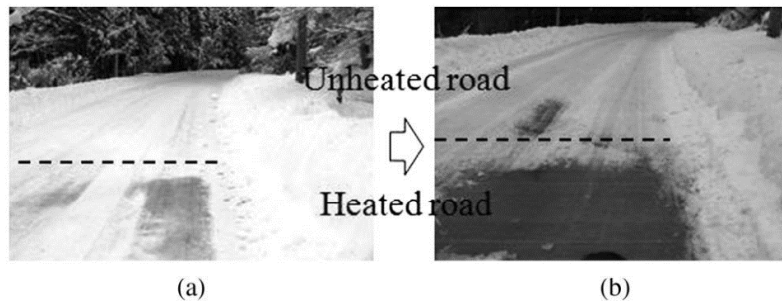


Figure 33. Road surface condition on snowy day (a) snow covered road (b) after 9h operating of the system (Yoshitake et al., 2011)

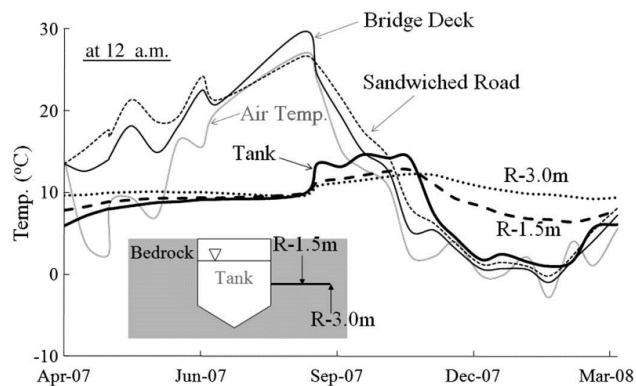


Figure 34. Temperature histories of the water storage, the bridge deck, and the approach road over one year (Yoshitake et al., 2011)

Case Study 6: Fukui City, Japan

A snow melting system known as the “pipe-in-pile snow melting system” was implemented for bridge deck deicing in Fukui City, Japan (Nagai et al., 2009). In this system, concrete piles functioned as heat exchangers between the ground and the circulating fluid (Figure 35). The total bridge surface area was 1300 m² (13,993 ft²), and 378 piles, each 128 mm (5 inches) in diameter and 23 m (75.4 ft) long, were installed beneath the bridge abutments. The system operated seasonally, storing solar energy absorbed at the pavement surface during the summer and extracting that stored heat in winter. Circulating water in the pipes transferred the heat from the ground to the bridge deck during cold weather. Figure 36 shows the bridge deck condition in January 2008, illustrating a clear distinction between heated and unheated sections. Areas equipped with heat dissipation pipes were free of snow, while untreated segments remained snow-covered.

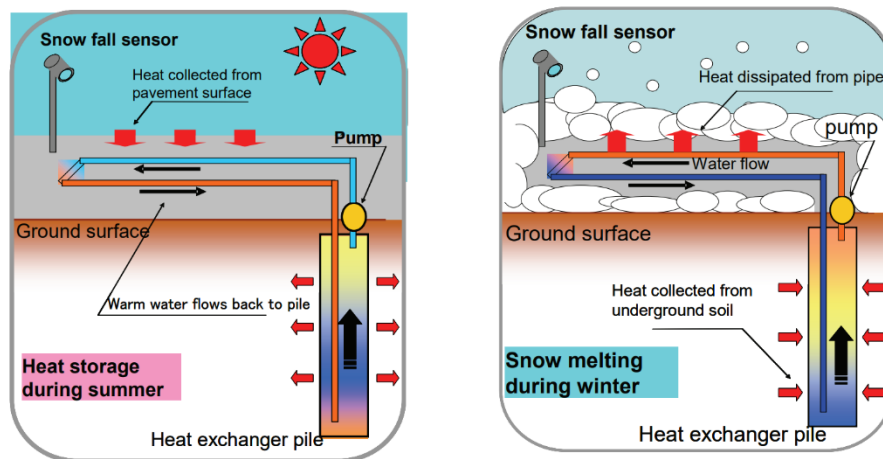


Figure 35. Outline of “pipe in pile” snow melting system (a) heat storage mode during Summer (b) snow melting mode during winter (Nagai et al., 2009)

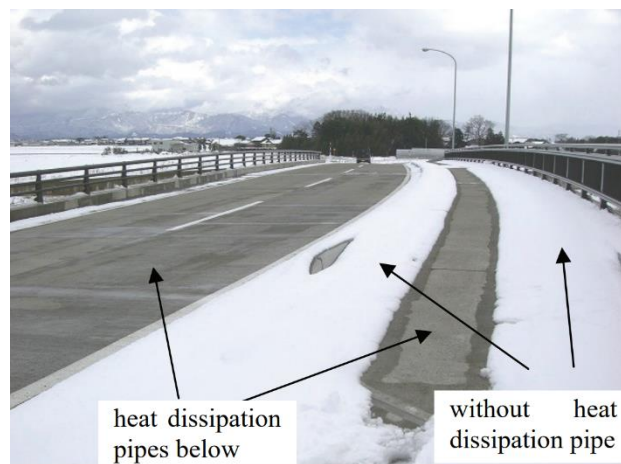


Figure 36. Surface condition of heated and unheated segments of the bridge deck in Fukui City, Japan in January, 2008 (Nagai et al., 2009)

Case Study 7: North Fork of Silver Creek, Oregon

A 32.0 m (105 ft) × 12.2 m (40 ft) two-lane bridge deck was constructed over the North Fork of Silver Creek in the Cascade Mountains, featuring an embedded hydronic heating system. The total

heated area covered 576 m² (6,200 ft²). A plan view of the heated deck is shown in Figure 37. The system was designed based on a target ambient air temperature of 23 °C (73.4 °F) and an average wind speed of 1.9 m/s (4.25 mph). The circulating fluid consisted of a 35% propylene glycol-water solution. The hydronic system was a closed-loop design with pipes placed longitudinally throughout the deck. These pipes were made of cross-linked polyethylene, with an inner diameter of 12.7 mm (0.5 inch) and a wall thickness of 1.6 mm (0.06 inch), spaced at 114 mm intervals. Heat was extracted from well water at a temperature of 11 °C (52 °F), and a 50-ton Trane liquid scroll chiller was installed in a nearby building to support the system. An electronic controller was integrated with sensors embedded in the bridge deck, including a deck surface temperature sensor and an ambient air temperature probe. This control system managed the operation of the well pump motor and heat pump by continuously monitoring key parameters: inlet and outlet fluid temperatures and pressures, well water inlet and outlet conditions, surface and ambient temperatures, and flow rates. The controller also helped prevent slush formation in the circulating fluid, which could otherwise increase viscosity and overload the pump. The average inlet and outlet fluid temperatures were recorded as 49 °C (120 °F) and 32 °C (90 °F), respectively. Operational results confirmed that the geothermal bridge deck heating system had functioned successfully since January 1995, consistently clearing snow and ice from the deck during cold weather conditions (Minsk, 1999).

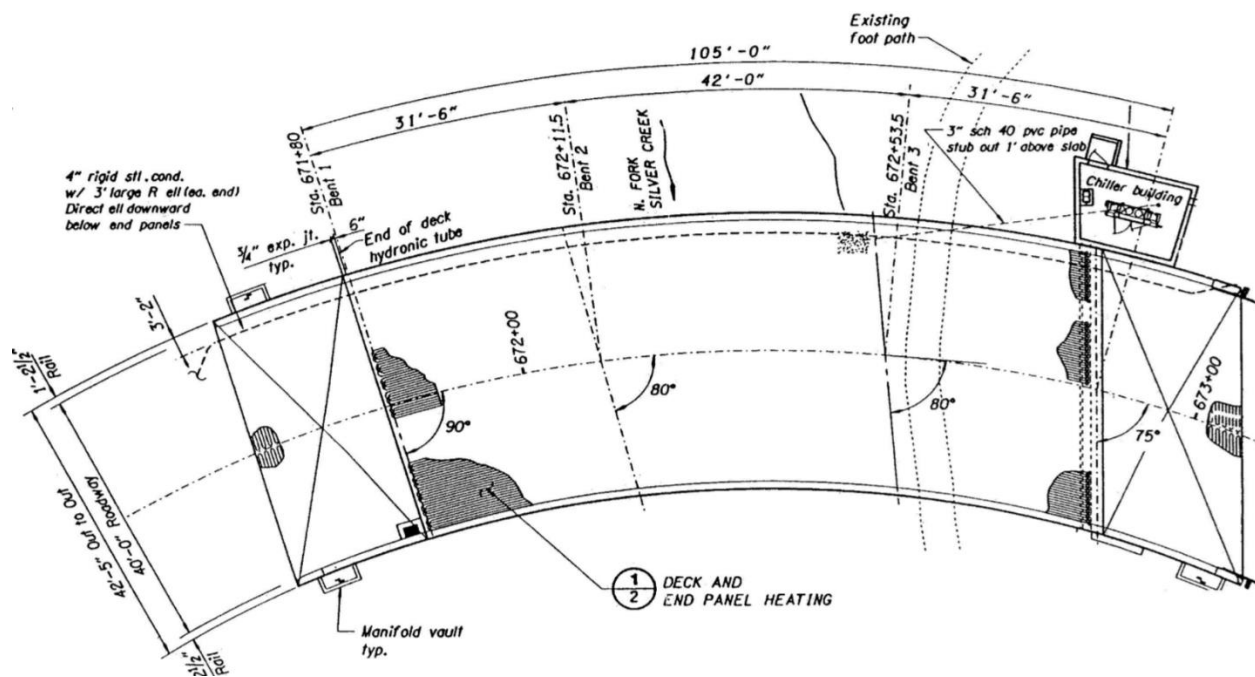


Figure 37. Plan view of the heated deck on Silver Creek bridge, Oregon (Minsk, 1999)

Case Study 8: Amarillo, Texas

Two-lane bridge decks located in Amarillo, Texas, were heated using a hydronic system powered by geothermal wells (Minsk, 1999). The primary objective of the system was to prevent ice bonding on the deck surface, rather than to melt accumulated snow. The project site experiences frequent freeze-thaw cycles during winter, with ground surface temperatures typically dropping below freezing at night. Each bridge measured 44.5 m (146 ft) in length and 17.7 m (58 ft) in width. The total heated area per bridge was 799 m², with a designed heat flux of 129 W/m². Fifty geothermal wells were installed in star-shaped patterns to extract energy. Each well was 102 mm

(4 in.) in diameter and 53.6 m (176 ft) deep, though they did not reach the groundwater table. Heat was extracted using two closed-loop pipes inside each well, grouted with non-shrinking bentonite to ensure effective thermal contact with the surrounding soil. The circulating fluid was a 50% propylene glycol–deionized water mixture, flowing through pipes with an internal diameter of 19 mm (0.75 in.). Figure 38(a) shows the heating circuits prior to concrete placement. A Vaisala Road Weather Information System (RWIS) was used to monitor road and bridge conditions and to control the hydronic heating system. Type K thermocouples were embedded near the deck surface, specifically at the outside shoulder and the right travel lane, to monitor temperature. The manifolds and thermocouple conduits are shown in Figure 38(b). The heating system was programmed to activate automatically when the bridge deck temperature dropped to 1.7 °C (35.1 °F) and precipitation was forecasted. Operational data indicated that approximately three hours were required to reach maximum operating temperature after system activation. The system functioned reliably over two winter seasons, demonstrating its effectiveness and operational stability (Minsk, 1999).



(a)



(b)

Figure 38. (a) Heating circuits before pouring concrete (b) close-up of supply and return manifolds (pipes in center) and thermocouple conduits terminating in enclosure at right on a bridge deck in Amarillo, Texas. (Minsk, 1999)

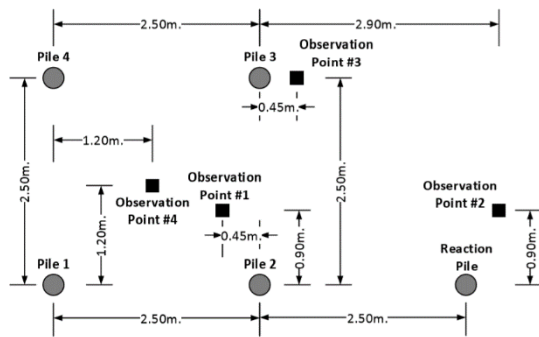
Laboratory Studies of Bridge Deck Deicing Systems

This section provides a brief overview of several laboratory studies that evaluated the performance of GSHP systems for bridge deck deicing. Key parameters investigated include pipe spacing in the secondary (bridge deck) circuit, borehole depth in the primary (ground) loop, the effects of preheating and snowfall rate, the role of external heating systems, and variations in inlet flow rate and temperature. Table 7 and 8 summarize the design features and performance characteristics of the GSHP bridge deck deicing systems examined in these laboratory experiments.

Pipe Spacing in the Secondary Unit

The thermal performance of a small-scale bridge deck deicing system was investigated by Bowers Jr. (2016) at the Virginia Tech Geotechnical Research Facility. The system utilized five energy piles (micropiles) constructed as part of the heat extraction setup. Each energy pile measured 30.5 m (100 ft) in depth and 25.4 cm (10 in.) in diameter. To monitor subsurface thermal behavior during testing, four observation boreholes were installed. The arrangement and spacing of the energy piles and observation wells are illustrated in Figure 39(a). Two types of heat exchanger piping were installed in the energy piles: 19 mm (0.75 in.) diameter HDPE pipes in a single closed-

loop configuration, and 25.4 mm (1 in.) diameter PEX pipes in both single and double closed-loop configurations. Two bridge deck models were constructed for the study, each measuring 1.3 m (4.3 ft) wide, 3.05 m (10 ft) long, and 0.254 m (10.4 in.) deep, as shown in Figure 39(b). Heat exchanger pipes were embedded within the deck models at spacings of 30 cm (12 in.) and 20 cm (8 in.) on the left and right sides, respectively. The inner and outer diameters of the pipes were 16 mm (0.62 in.) and 22 mm (0.87 in.), respectively. A 20% glycol solution was used as the circulating fluid, flowing at a rate of 15.1 L/m (1.2 gal/ft). To measure the thermal response of the deck, a total of 36 thermistors were embedded within the concrete slab.



(a)

(b)

Figure 39. (a) Location and spacing of energy piles and observation wells (b) experimental deck model. Pipes spacing are 20 cm and 30 cm in the left-side and right-side model deck, respectively. (Bowers Jr, 2016)

This study demonstrated the impact of pipe spacing on the efficiency of a bridge deck deicing system during a simulated snowstorm. As shown in Figure 40, the left side of the model deck was equipped with pipes spaced at 30 cm (12 in), while the right side used a tighter spacing of 20 cm (8 in). The results revealed that the bridge deck section with 20 cm (8 in) spacing remained completely free of snow, whereas the section with 30 cm (12 in) spacing retained snow accumulation. This indicates that the geothermal system was more effective at melting snow with closer pipe spacing. In the case of wider spacing, additional snow removal methods may be required to fully clear the deck. Nonetheless, in both configurations, the GSHP system successfully maintained deck surface temperatures above 0 °C (32 °F), preventing ice formation.



Figure 40. Photo of the deck model surface during the storm. Heat exchanger pipes have spacing of 30 cm and 20 cm in left-side and right-side model deck, respectively (Bowers Jr, 2016).

Table 7. Experimental studies of bridge deck deicing – Secondary Unit

Authors	Snow Melting System							Circulating Fluid
	Deck			Pipe				
	<i>Area (m²)</i>	<i>Thickness (cm)</i>	<i>Thermal Conductivity W/m/k</i>	<i>Inner Diameter (mm)</i>	<i>Thickness (mm)</i>	<i>Spacing (cm)</i>	<i>Material</i>	
Bowers Jr (2016)	7.2	25.4	3.0	16.0	3.0	20.3 and 30.5	PEX	40% glycol by volume, and water
Balbay and Esen (2010)	2.1	20.0		16.0	2.4	20.0	Polyethylene PX-b	25% glycol by volume, and water
Liu (2005)	112.0	20.3	1.4	25.0	2.0	15.2	High-Density Polyethylene	42% glycol by volume, and water
Yu et al. (2020)	2.2	10.2	1.9	13.0	3.0	15.2	Cross-linked polyethylene (PEX)	water and antifreeze mixture
Ghasemi-Fare et al. (2015)								Water

Table 8. Experimental studies of bridge deck deicing – Primary Unit

Authors	Heat Source			Water Tank	Ambient Tempearture
	Ground Source (Energy pile or wells)				
	Depth (m)	Diameter (cm)	Filling Material		
Bowers Jr (2016)	30.5	25.4	Grout		0° C
Balbay and Esen (2010)	30, 60, 90	15.0	Bentonite		7.3° C
Liu (2005)	66.1	13.0	Grout		17.2° C
Yu et al. (2020)	21° C to 40° C				4.3° C to 17.1° C
Ghasemi-Fare et al. (2015)	1.4	10.0	Concrete		19° C

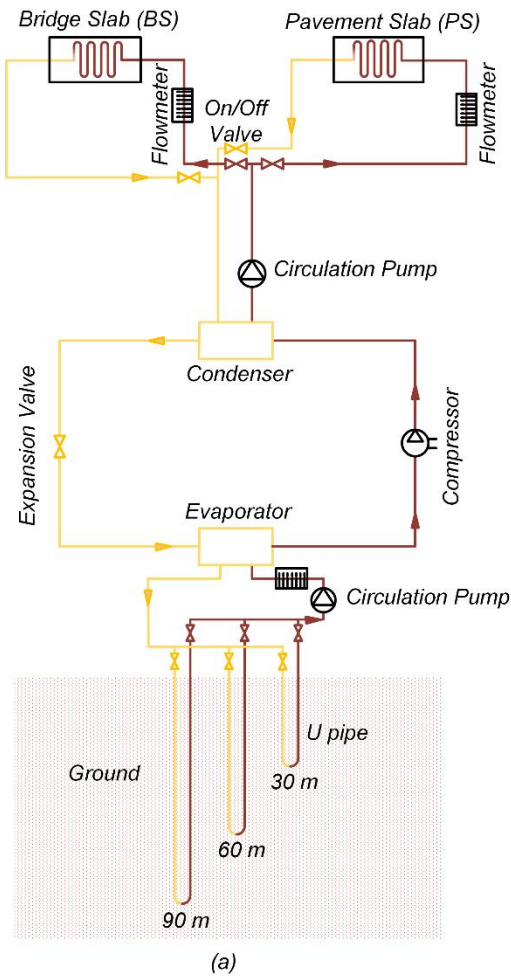
Borehole Depth in Primary Unit

Balbay and Esen (2010) evaluated the performance of a ground source heat pump (GSHP) system for snow melting on a pavement slab (PS) and a bridge slab (BS), as illustrated in Figure 41. The experimental setup included vertical boreholes at three different depths, two concrete slabs, two circulation pumps, and a heat pump. During testing, ambient air temperatures ranged from -8°C (18°F) to -6°C (21°F). High-density polyethylene (HDPE) pipes with a nominal diameter of 40 mm (1.6 in.) were installed in boreholes with a diameter of 150 mm (5.9 in.). A U-loop configuration was used for heat extraction, and the boreholes were grouted with bentonite to ensure good thermal conductivity. The circulating fluid consisted of a 25% water-antifreeze solution. Designed flow rates varied by borehole depth: 0.43 L/s (0.11 gal/s) for 30 m (100 ft), 0.40 L/s (0.10 gal/s) for 60 m (197 ft), and 0.36 L/s (0.09 gal/s) for 90 m (295 ft). Figure 41(a) presents a schematic of the test setup. The prototype slabs were 1.7 m (5.6 ft) long, 1.2 m (3.9 ft) wide, and 20 cm (7.9 in.) thick. The hydronic system embedded in the slabs consisted of eight parallel pipe lines spaced at 20 cm (7.9 in.) intervals. The slab pipes, made of polyethylene, had an inner diameter of 16 mm (0.06 in.) and a wall thickness of 2.4 mm (0.09 in.). The circulating fluid flow rate within the hydronic system was maintained at 0.056 L/s (0.0148 gal/s). The system's operation was monitored using multiple temperature sensors installed throughout the slabs. The GSHP system extracted between 7.91 kW and 10.5 kW of heat from the ground, demonstrating its capability to maintain slab temperatures above freezing during snow events.

Figure 41 illustrates the pavement and bridge slabs before (Figure 41(b)) and after 30 minutes (Figure 41(c)) of operating the ground source heat pump (GSHP) system. The measured air and surface temperatures of the bridge deck and pavement slab for borehole depths of 30 m (98.4 ft) and 90 m (295 ft) are presented in Figure 42(a) and (b), respectively. Overall, surface temperatures increased with greater borehole depth. At an average ambient air temperature of 7°C (45°F), the bridge deck and pavement slab heated by a 30 m borehole reached average surface temperatures of 2°C (35.6°F) and 0.2°C (32.4°F), respectively. When using a 90 m borehole, the average surface temperatures rose to 3°C (37.4°F) for the bridge slab and 0.5°C (32.9°F) for the pavement slab. These results demonstrate that the GSHP system was able to maintain surface temperatures above freezing throughout the winter season in Elazığ, Turkey.

Preheating the deck

A hydronic bridge deicing system was experimentally investigated by Liu (2005) at Oklahoma State University. The test setup consisted of a model bridge deck measuring 18.3 m (60 ft) in length and 6.1 m (20 ft) in width. The heat distribution system used cross-linked polyethylene pipes with an inner diameter of 19 mm (0.75 in.). The circulating fluid was a 39% propylene glycol–water mixture. A ground source heat pump was used to elevate the temperature of the circulating fluid, with a maximum inlet temperature of 54°C (129°F) recorded during the test. The objective of the experiment was to maintain an average deck surface temperature of 4.4°C (39.9°F) to prevent snow accumulation and ice bonding. Thermistor probes were installed to monitor the inlet fluid temperature, and a flow meter was used to measure the volume flow rate. In addition, the snow-free area ratio was evaluated through digital images captured by a video system throughout the test, allowing visual assessment of snow melting performance on the deck surface.



(b)



(c)

Figure 41. (a) The layout of experimental set-up (b) initial stage of snow melting process (c) after 30 min operation of snow melt system (Balbay & Esen, 2010)

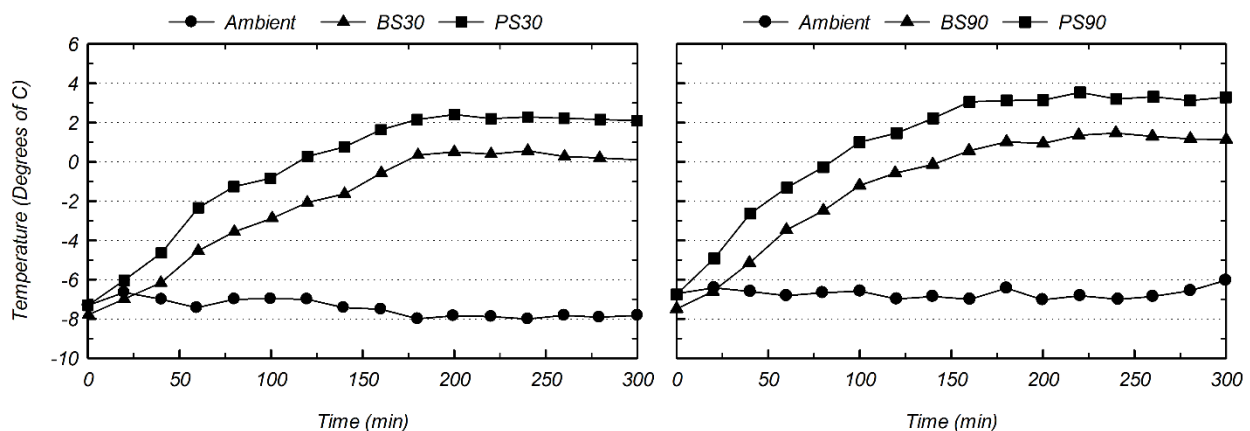


Figure 42. Variation of top surface temperatures of bridge deck and pavement slab, and air temperatures (a) borehole depth 30 m (100 ft) (b) borehole depth 90 m (295 ft) (Balbay & Esen, 2010)

Figure 43 illustrates the bridge surface conditions during the experiment, while Figure 44 presents the recorded average surface temperatures over time. The results indicate that the deck surface

temperature dropped rapidly to approximately 2 °C (35.6 °F) upon the onset of snowfall, allowing snow to accumulate on the bridge deck. After 3 hours and 38 minutes of continuous heating system operation, the average surface temperature began to rise, initiating snow melting (Figure 43(a)). As deicing progressed (Figure 43(b) and (c)), the surface temperature continued to increase, with the rate of temperature rise accelerating as more of the deck became snow-free. The entire bridge deck was cleared of snow after 8 hours of heating system operation (Figure 43(d)). Following the experiment, a transient numerical model of the snow melting process on a heated deck surface was developed and calibrated using the experimental data. As shown in Figure 44, the predicted surface temperatures closely matched the measured values, demonstrating good agreement. The simulation results also suggested that preheating the deck 3–5 hours prior to a snow event, using the system's full heating capacity, can significantly enhance the efficiency of the snow melting process. The full heating capacity was determined based on surface heat flux requirements outlined in the *ASHRAE Handbook – HVAC Applications Volume* (American Society of Heating & Engineers, 2003).

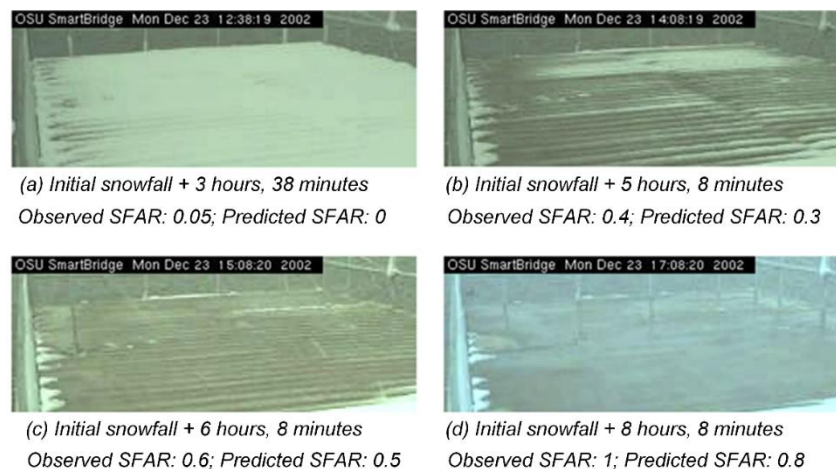


Figure 43. Photo of bridge surface condition during the test (SFAR: Snow Free Area Ratio) (Liu, 2005)

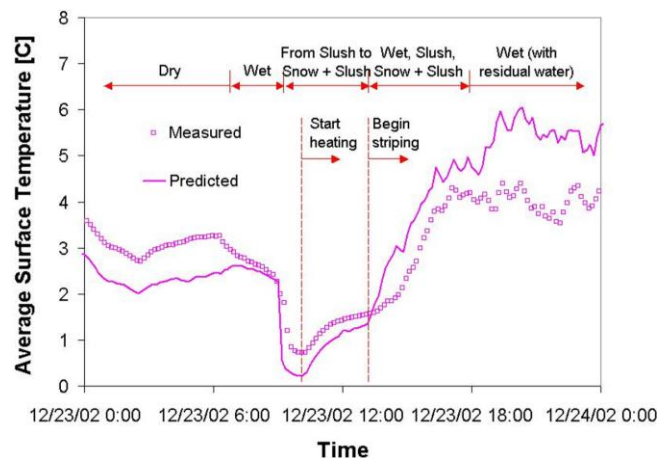


Figure 44. Recorded average surface temperature of the bridge (Liu, 2005)

External Heating Systems

Yu et al. (2020) experimentally investigated the feasibility of an attached external hydronic heating system for bridge deck deicing. The model bridge deck measured 1.83 m (6 ft) in length, 1.22 m (4 ft) in width, and 10.16 cm (4 in.) in thickness. The heating system consisted of 10 parallel lines of cross-linked polyethylene (PEX) pipes, each with an inner diameter of 13 mm (0.5 in.), a wall thickness of 3 mm (0.12 in.), and a spacing of 150 mm (5.9 in.) between lines. Geofoam and polyurethane foam were used as insulation layers to minimize heat loss. A 95-liter (25-gallon) water tank connected to a hydraulic pump was used to simulate the warm fluid supply from a ground source heat pump (GSHP) system. The tank temperature was regulated using heating coils, and the system was designed to operate within a temperature range of 21 °C (69.8 °F) to 40 °C (104 °F). Figure 45(a) and (b) show the schematic layout of the test setup and a photo of the experimental configuration, respectively. During the experiment, ambient air temperatures ranged from 4.3 °C (39.7 °F) to 17.1 °C (62.8 °F). To monitor the thermal performance, 12 Type-T thermocouples were embedded within the concrete deck, while additional thermocouples were installed inside the insulation foam and at the inlet and outlet of the piping system. Fluid flow was measured using a high-pressure flowmeter. Test results showed a gradual increase in deck temperature with the circulation of warm fluid. Thermocouple readings near the outer layer of the geofoam were close to ambient air temperatures, confirming the insulation's effectiveness in minimizing heat loss. However, temperature within the geofoam dropped rapidly with either increased time intervals between heat supply or increased distance from the heat source.

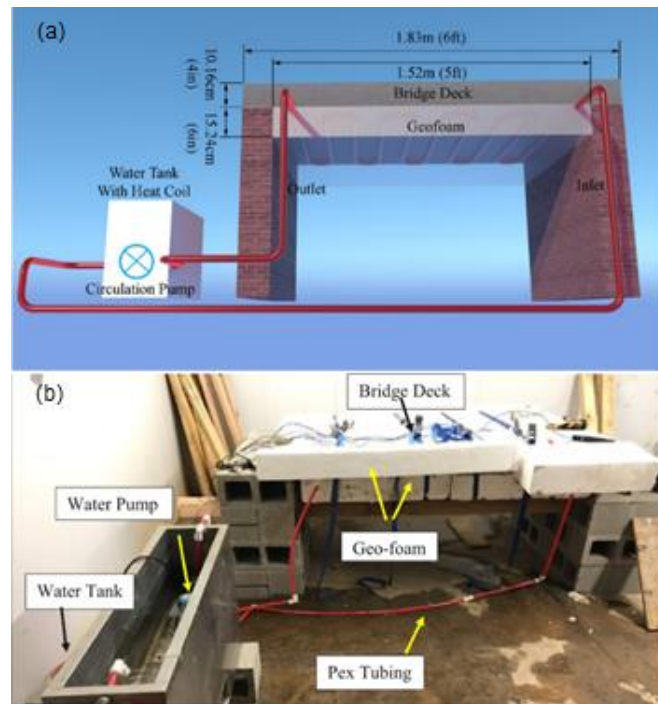


Figure 45. (a) The schematic of experimental set-up (b) laboratory setup (Yu et al., 2020)

Heat flux analyses revealed that the heat flux within the bridge deck was directly proportional to the temperature difference between the inlet fluid and the ambient air. The efficiency of heat transfer was influenced by several factors, including the thermal conductivity of the concrete, the presence and quality of thermal insulation, boundary conditions, pipe spacing, the void ratio of the geofoam, the contact area between the pipes and geofoam, and the pipe diameter. Experimental results indicated that approximately 60% of the supplied heat was successfully transferred to the bridge deck surface, with a uniform temperature distribution observed across the deck. These findings suggest that a surface-attached hydronic heating system is effective for deicing bridge decks within the temperature ranges studied.

Inlet Flow Rate and Temperature

Ghasemi-Fare et al. (2015) investigated the feasibility of using geothermal energy for bridge deck snow melting through experimental studies conducted at the Civil Infrastructure Testing and Evaluation Laboratory (CITEL) at Pennsylvania State University (PSU). A model-scale energy pile system was constructed to evaluate the influence of various design parameters, such as inlet fluid temperature and flow rate, on heat extraction and transfer efficiency (Figure 46). The experimental setup included a concrete pile with a diameter of 100 mm (4 in.) and a length of 1.38 m (4.5 ft), embedded in a $1.83 \text{ m} \times 1.83 \text{ m} \times 2.13 \text{ m}$ ($6 \text{ ft} \times 6 \text{ ft} \times 7 \text{ ft}$) soil bed. A U-loop heat exchanger, made of polyvinyl chloride (PVC) with an inner diameter of 9.5 mm (0.4 in.) and a wall thickness of 3 mm (0.12 in.), was embedded within the pile. To improve workability, a water-reducing concrete admixture was added at a dosage of 722 mL/m^3 . The resulting fresh concrete mix had a slump of 140 mm (5.5 in.), and the cured concrete achieved a compressive strength of 40.94 MPa (20,305 psi) with the embedded U-loop. Temperature monitoring was conducted using 94 Type-T thermocouples strategically placed within the soil bed. Figure 46(a) illustrates the experimental setup and data acquisition system. During testing, the ambient temperature was maintained at 19°C (66°F). For heating scenarios, the inlet fluid temperatures were 39°C (102°F) and 34°C (93°F), while for cooling cases, it was -9°C (16°F). The average linear flow velocity of the circulating fluid varied between 0.11 m/s (0.36 ft/s) and 0.66 m/s (2.16 ft/s) to study its impact on system performance.

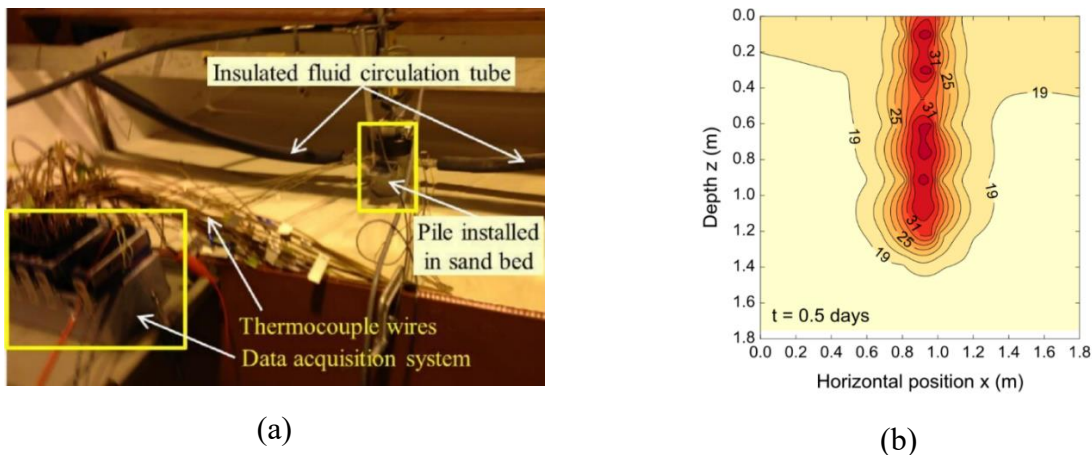


Figure 46. (a) Experimental set up (b) temperature contours after 0.5 day (Ghasemi-Fare et al., 2015)

The temperature contour results revealed that the majority of heat transfer occurs in the radial direction. As shown in Figure 46(b) after 12 hours of operation, the thermal influence zones around the piles became clearly defined. This thermal influence zone is a critical consideration in the design of pile groups, as overlapping zones between adjacent piles can reduce the overall thermal efficiency of the system. Additionally, the results indicated that the energy transfer rate increased with higher flow rates of the circulating fluid, suggesting that flow rate is a key parameter for optimizing heat extraction in geothermal systems.

Soil Thermal Properties

In shallow geothermal foundations, heat exchange occurs as a result of the temperature difference between the pipe network embedded within the foundation piles and the surrounding soil. Heat

transfer in thermo-active foundations and boreholes primarily occurs through several mechanisms: (1) forced convection within the pipes, driven by the circulation of a heat carrier fluid; (2) conduction through the pipe walls; (3) conduction through the pile material, typically concrete; and (4) a combination of conduction and natural convection within the surrounding soil. These mechanisms work together to facilitate thermal energy exchange between the geothermal system and the ground. Figure 47 illustrates the primary heat transfer pathways between the circulating fluid, the concrete pile, and the surrounding soil.

Ghasemi-Fare and Basu (2016) conducted laboratory experiments and finite difference analyses to evaluate the performance of geothermal energy piles equipped with a single U-shaped circulation pipe. Their findings indicated that the thermal efficiency of heat exchanger piles, under both short-term and long-term operation, is highly sensitive to the thermal properties of the surrounding soil. Heat transfer in soils is complex and involves multiple interacting mechanisms. The primary modes of heat transfer are: (1) conduction, (2) convection, and (3) radiation. In addition, several other mechanisms play a significant role in heat transfer within soils, including (4) vaporization and condensation, (5) freezing and thawing, and (6) ion exchange (Brandl, 2006). Figure 48 illustrates these key heat transfer mechanisms. Among these, heat transfer occurs most effectively through the solid particles of the soil matrix, which serve as the preferred conduction pathway.

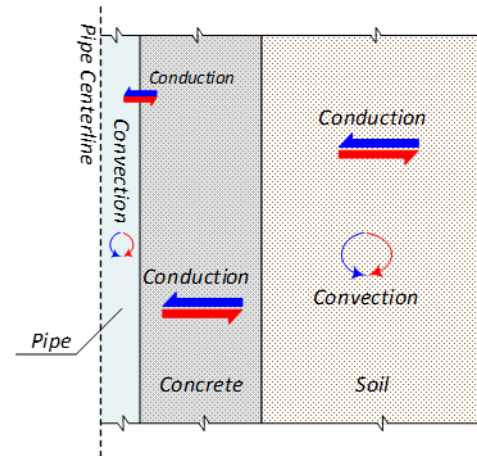
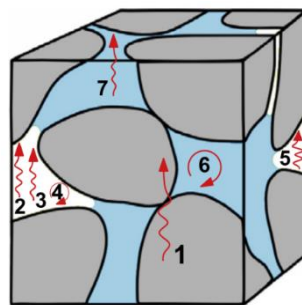


Figure 47. Primary heat transfer mechanisms in a thermo-active foundation with heat exchanger pipe embedded in a concrete pile and surrounded by soil (not to scale) (Atalay, 2019)



- 1 - Conduction in particle
- 2 - Conduction in air
- 3 - Radiation in air
- 4 - Convection in pore air
- 5 - Vapour diffusion
- 6 - Convection in liquid
- 7 - Conduction in liquid

Figure 48. Heat transfer paths in soil (Alrtimi et al., 2016)

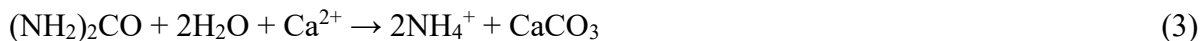
Heat transfer by conduction, the dominant heat flow mechanism in soils, refers to the transfer of thermal energy within solids and fluids (Dawoud et al., 2007). In contrast, convective heat transfer occurs through the movement of a fluid and is driven by the fluid's bulk motion (Brandl, 2006). Convection can be either natural or forced. Natural convection arises from density differences caused by temperature gradients, leading to the migration of air or water molecules within the soil. Forced convection, on the other hand, is driven by external forces, such as groundwater flow. However, in soils with grain sizes smaller than sand, convective heat transfer is generally negligible (Farouki, 1981). Radiative heat transfer occurs in the pore spaces of soil through

electromagnetic waves or photons. This mechanism contributes minimally to overall heat flow in natural soils, typically less than 2% (Rees et al., 2000) but may account for up to 10% of total heat transfer in coarse aggregates with particle sizes around 20 mm (Farouki, 1981). Therefore, radiation is only a significant factor in dry, coarse-grained materials such as gravel.

One of the objectives of this research is to comprehensively investigate the effects of bio-cementation on the thermal properties of soil, particularly thermal conductivity and heat capacity. Heat transfer in soils is influenced by several factors, including grain size, composition, density, and moisture content. Among these, grain size plays a key role by affecting secondary parameters such as porosity, permeability, fabric, and specific surface area, all of which impact thermal conductivity. Therefore, while grain size is not a direct driver, it must be considered in the evaluation of primary thermal parameters (Midttomme & Roaldset, 1998). Another critical structural factor is the nature and number of contacts between soil particles. Studies have shown that bio-cementation, particularly through Microbially Induced Calcite Precipitation (MICP), enhances these particle contacts by depositing calcite crystals at interparticle boundaries. This process forms 'thermal bridges' that significantly improve thermal conductivity (Venuleo et al., 2016). In fact, MICP treatment has been reported to increase the thermal conductivity of sand by as much as 250%, highlighting its potential to improve the thermal behavior of treated soils.

Effect of Bio-Cementation on Thermal Properties of Soil

Microorganisms can alter their surrounding chemical environment to induce the precipitation of calcium carbonate, forming a type of bio-cement (DeJong et al., 2010; Phillips et al., 2013; van Paassen et al., 2010). One extensively studied mechanism involves the enzyme urease, produced by microbes or plants, which catalyzes the hydrolysis of urea. This reaction alters the saturation state of the environment, and in the presence of calcium ions, leads to the precipitation of calcium carbonate (Cuthbert et al., 2013; Ebigo et al., 2012; Hommel et al., 2015; Mitchell et al., 2013; Phillips et al., 2016; Phillips et al., 2013). The hydrolysis of urea by urease creates favorable conditions for CaCO_3 formation, as summarized in Equation 3.



In this process, the precipitation of calcium carbonate (CaCO_3), typically in the stable mineral form of calcite, binds porous media such as soil particles. Microbially Induced Calcite Precipitation (MICP)-treated sand has been shown to reduce soil settlement (DeJong et al., 2006; van Paassen et al., 2010), increase shear strength (Chou et al., 2011; DeJong et al., 2006; Ismail et al., 2002), and enhance stiffness (Feng & Montoya, 2015; Lin et al., 2016; Montoya & DeJong, 2015).

The Microbially Induced Calcite Precipitation (MICP) treatment primarily influences the average dry density of the soil. The precipitation of calcite increases the solids content by binding soil particles together at their contact points through the formation of calcite bridges (Whiffin et al., 2007). This process not only increases dry density but also reduces porosity, as calcite crystals grow around soil particles and fill void spaces. As porosity decreases, the number of particle-to-particle contacts increases, enhancing the pathways for heat transfer through solid particles, which have higher thermal conductivity than air. Consequently, the overall thermal conductivity of the treated soil improves. As illustrated in Figure 49, an increase in the number of MICP treatment cycles leads to greater calcite formation, resulting in a substantial enhancement in thermal conductivity, up to 120% higher after four treatment cycles compared to untreated sand.

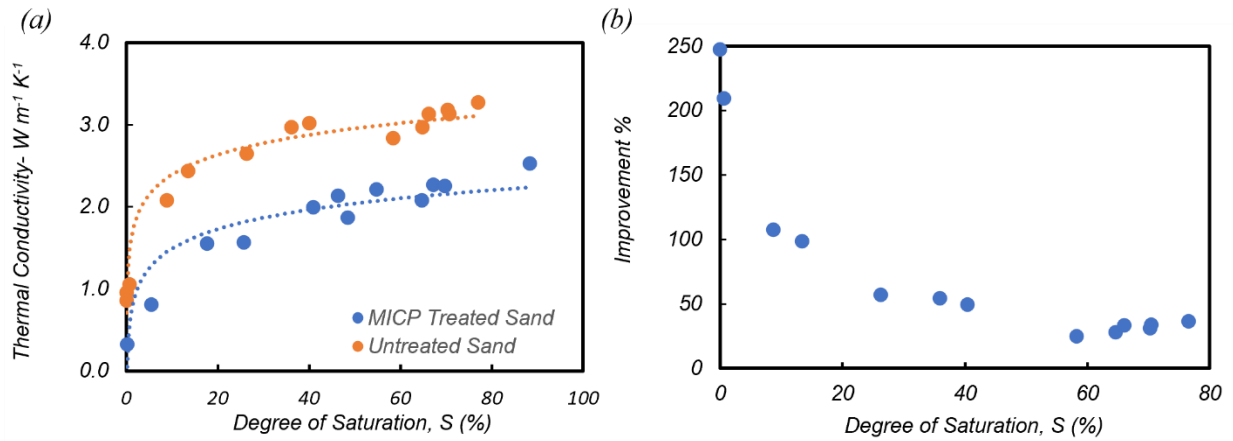


Figure 50(a) and (b) illustrate the variation in thermal conductivity across different degrees of saturation (S), ranging from 0% to 100%, for both untreated and bio-treated soil specimens. Since the thermal conductivity of water is significantly higher than that of air, an increase in water content enhances heat flow through the soil, resulting in higher overall thermal conductivity. Martinez et al. (2019) demonstrated that the thermal conductivity of a dry soil specimen ($S = 0$) increased by 860% upon full saturation. As shown in

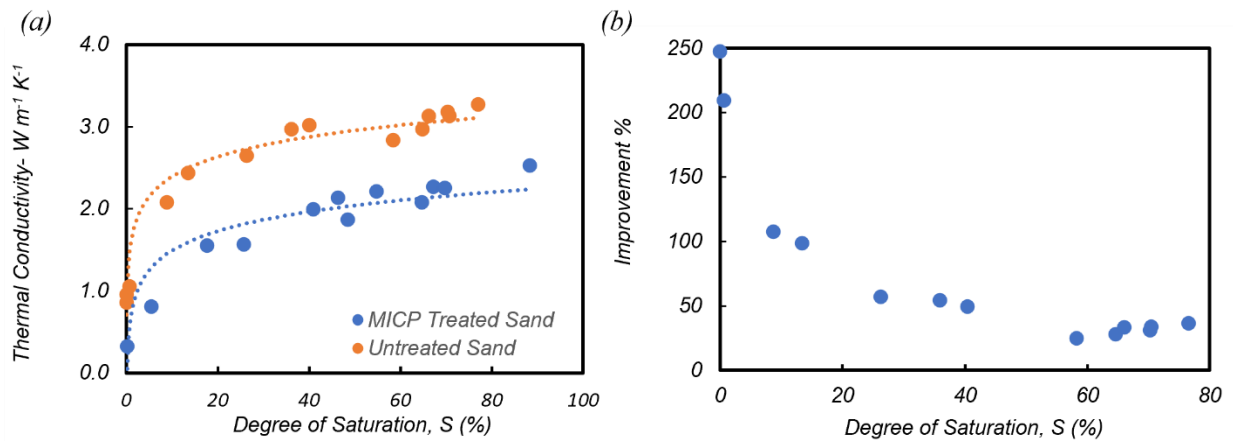


Figure 50(a), the influence of water content on thermal conductivity is most pronounced at lower saturation levels. As saturation increases, the rate of conductivity increase slows for both treated and untreated soils. At higher degrees of saturation, within the capillary and funicular regimes, thermal conductivity is primarily governed by particle-to-particle contact and the presence of continuous water films, while the influence of residual air voids becomes negligible (Likos, 2015).

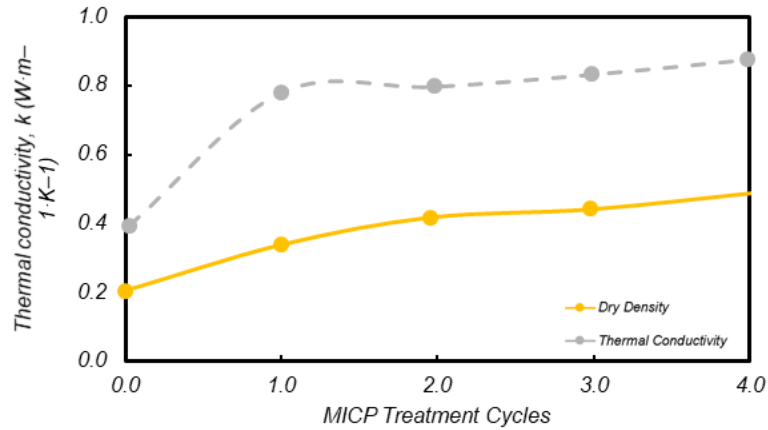


Figure 49. Thermal conductivity and dry density of MICP-treated sand versus MICP treatment cycles (Wang et al, 2019)

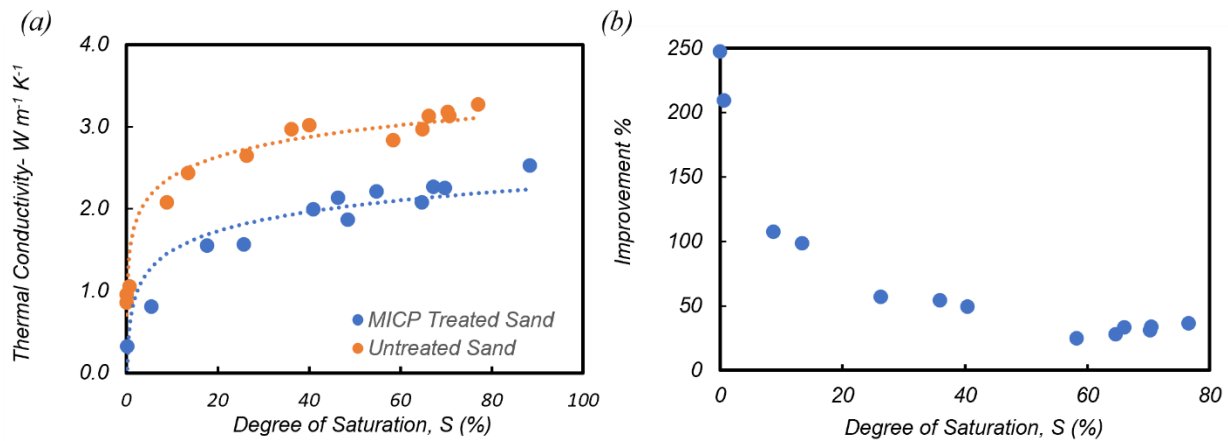


Figure 50(b) illustrates the change in thermal conductivity resulting from Microbially Induced Calcite Precipitation (MICP) treatment across varying degrees of saturation (Venuleo et al., 2016). As shown, the effect of bio-cementation is significantly more pronounced at lower saturation levels. Specifically, the enhancement in thermal conductivity due to bio-cementation decreases sharply as the degree of saturation increases. This is because the thermal conductivity of calcite is substantially higher than that of air (approximately $0.026 \text{ W}\cdot\text{m}^{-1}\cdot\text{K}^{-1}$), making its influence most notable in dry soils. In dry sand, calcite crystals replace air voids and form cementation bridges between grains, creating highly conductive heat transfer paths by increasing inter-particle contact. Under these dry conditions, MICP treatment was found to increase thermal conductivity by up to 330%. In contrast, the same increase in calcium carbonate content resulted in only a 15% improvement under fully saturated conditions, where the presence of water already facilitates higher thermal conduction.

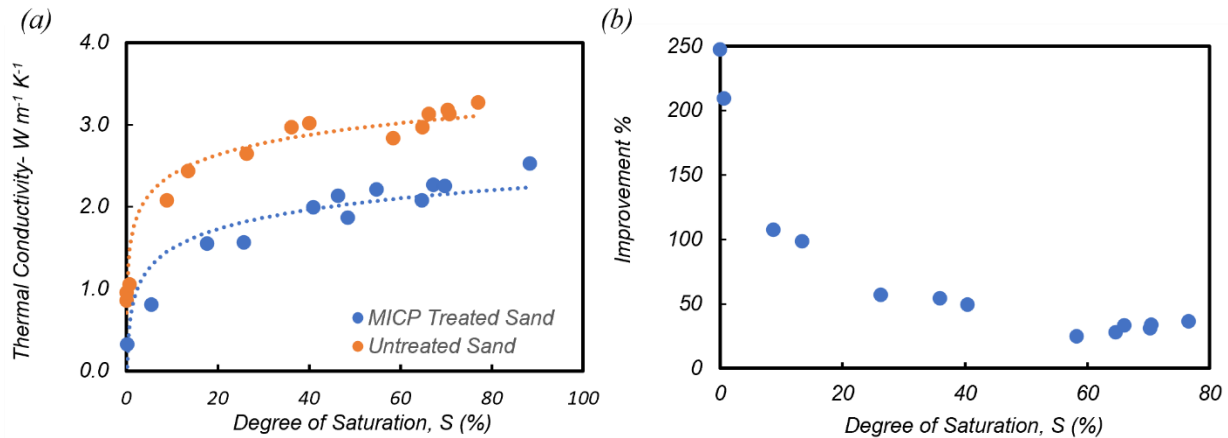


Figure 50. Effect of degree of saturation on (a) thermal conductivity of the MICP-treated and untreated sand (b) improvement in thermal conductivity of the MICP-treated soil (Venuleo et al., 2016)

Numerical Modeling Studies on the Efficiency of Shallow Geothermal Energy System

Several numerical modeling studies have been conducted to evaluate the energy performance of bridge deck deicing systems. This section highlights the key factors that directly and indirectly influence system efficiency and overall performance.

Inlet Fluid Temperature and Flow Rate

This section presents findings from previous studies examining the influence of inlet fluid temperature and flow rate on the performance of bridge deck hydronic heating systems. Key performance indicators include: (1) average bridge deck surface temperature, (2) the temperature difference between inlet and outlet fluid, (3) the time required to raise the deck temperature above the freezing point of water, and (4) overall energy consumption. Results show that increasing the inlet fluid temperature leads to a higher surface temperature, a greater temperature differential between inlet and outlet, and a shorter time to reach $0^{\circ}C$ ($32^{\circ}F$). While a high inlet flow rate has minimal effect on system performance, a low volumetric flow rate can result in excessive temperature drops and uneven surface heating, which may induce thermal stresses and surface cracking. Additionally, operating a hydronic system with unnecessarily high inlet fluid temperatures or flow rates increases energy use and operating costs. Therefore, defining an optimal relationship between inlet temperature and volumetric flow rate is essential to minimize energy consumption while maintaining effective deicing performance.

Balbay and Esen (2013) performed three-dimensional (3D) finite element modeling using the FLUENT computational fluid dynamics (CFD) software to investigate the impact of fluid inlet temperature on the performance of a ground source heat pump (GSHP) system. Their study focused on how varying borehole depths influence the surface temperature distribution of a bridge deck. The geometry of the bridge deck model used in the simulation was consistent with the experimental setup described in their earlier study Balbay and Esen (2010). Figure 51(a) presents the meshed model used for the simulations. In the model, the fluid inlet velocity was set at 0.07 m/s , and the outlet was maintained at atmospheric pressure. Boundary conditions included an open top surface exposed to ambient air and insulated side boundaries. A 1-cm (0.4-inch) thick layer of snow and/or ice was assumed to cover the top surface, with both the top and bottom surfaces

initialized at a temperature of -7°C (19.4°F). The average fluid inlet temperature was set at 36°C (96.8°F). Figure 51(b) shows a sample output illustrating the temperature distribution within the bridge deck model for a borehole depth of 90 m (295 ft). The results of the study demonstrated two key findings: (1) the fluid inlet temperature increased with deeper geothermal boreholes, and (2) higher inlet fluid temperatures led to increased average surface temperatures and larger temperature differentials between the inlet and outlet circulating fluid.

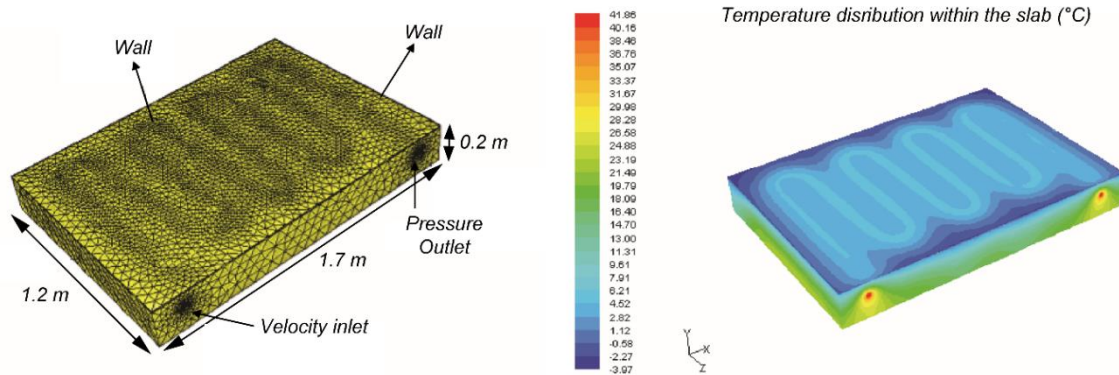


Figure 51. (a) The mesh of deck model (b) distribution of temperature within the bridge deck using boreholes depths of 90 m (295 ft) (Balbay & Esen, 2013)

Chowdhury (2019) developed a three-dimensional numerical model using the finite element software COMSOL Multiphysics to evaluate the performance of an externally heated geothermal bridge deck under varying weather conditions in the Dallas–Fort Worth area. The bridge deck geometry was based on the experimental setup used by Yu et al. (2020), as shown in Figure 45 (previous section). A meshed view of the modeled bridge deck is presented in Figure 52.

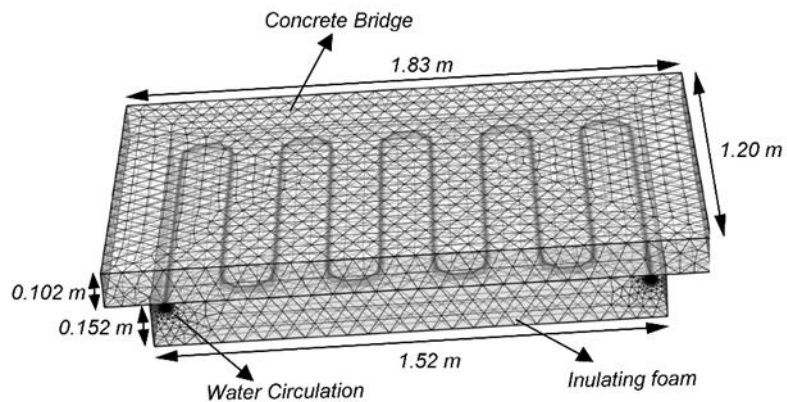


Figure 52. Meshed 3D model (Chowdhury, 2019)

A key assumption in the simulation was that the bridge deck had been pre-heated during snowfall and that no snow accumulation was present on the surface. The circulating fluid used in the model was water, with a flow rate of 7.5 L/min (2 gal/min), and an average inlet temperature maintained at approximately 22°C (71.6°F) throughout the simulation event. Weather and wind speed data for extreme cold events between 2014 and 2018 were sourced from the National Oceanic and Atmospheric Administration (NOAA). Model simulations for inlet fluid temperatures of 22°C (71.6°F) and 38°C (100.4°F) were conducted for the coldest days of 2016 (December 17–20), and results are shown in Figure 53 (a) and (b), respectively. Temperature monitoring at location T1, positioned 1.27 cm (0.5 in.) below the bridge deck surface, revealed that an inlet fluid temperature of 22°C was insufficient to maintain surface temperatures above freezing. The simulation concluded that,

under these conditions, an inlet fluid temperature of approximately 38 °C (100.4 °F) was necessary to keep the deck surface above freezing and ensure effective deicing.

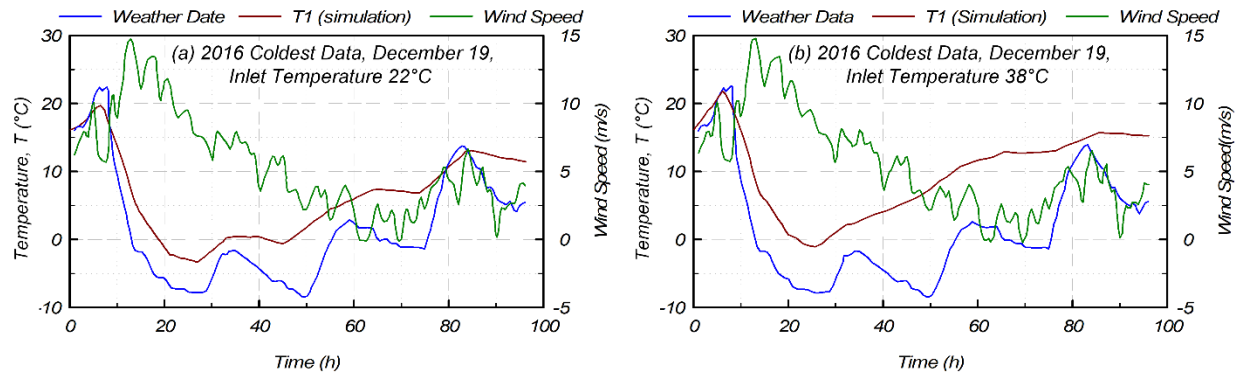


Figure 53. Weather data and numerical model results in the coldest day of 2016, December 19, 2016, for inlet fluid temperatures of (a) 22 °C (b) 38 °C (Chowdhury, 2019)

Yu et al. (2017) conducted a series of three-dimensional numerical simulations using the finite element software COMSOL Multiphysics to investigate the effects of flow rate and inlet fluid temperature on the performance of a bridge deck deicing system. The baseline model configuration is shown in Figure 54. The model dimensions were 3.5 m (11.5 ft) \times (2 \times pipe spacing in meters) \times 0.25 m (10 in.). Both the pipe spacing and the embedded depth were set to 20 cm. The circulating fluid, water mixed with 25% propylene glycol, was transported through pipes with an inner diameter of 14 mm (0.55 in.) and a wall thickness of 3 mm (0.12 in.). The study did not consider the snow melting process; instead, it assumed that the bridge deck was preheated before snowfall and no snow accumulation occurred. The initial temperature of the bridge deck was set at -2 °C (28.4 °F), with the baseline inlet fluid temperature and flow rate set at 12 °C (53.6 °F) and 0.6 m/s, respectively. Simulations were run for a range of inlet temperatures (6 °C to 20 °C or 42.8 °F to 68 °F) and flow rates (0.3 m/s to 1.5 m/s or 1.0 ft/s to 4.9 ft/s). Figure 55 and Figure 56 illustrate the influence of inlet temperature (Figure 55) and flow rate (Figure 56) on the average bridge deck surface temperature and the time required for the surface to rise above the freezing point. The results showed that increasing the inlet fluid temperature significantly elevated the deck surface temperature and reduced the time needed to reach above-freezing conditions. While the flow rate had a less pronounced effect on surface temperature, it did contribute to a reduction in the time required to exceed the freezing threshold.

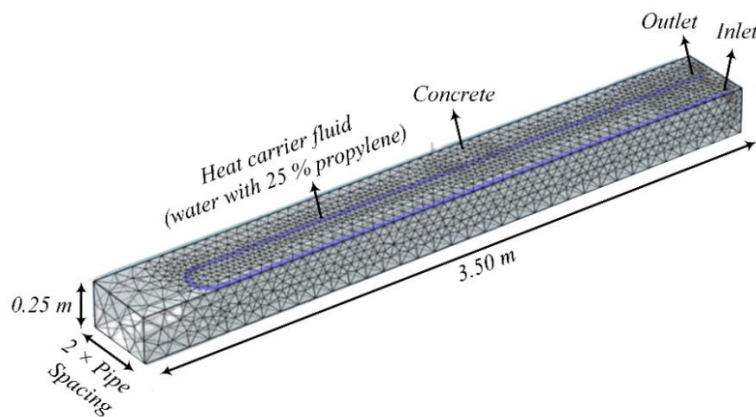


Figure 54. Numerical baseline model configuration of the bridge deck (Yu et al., 2017)

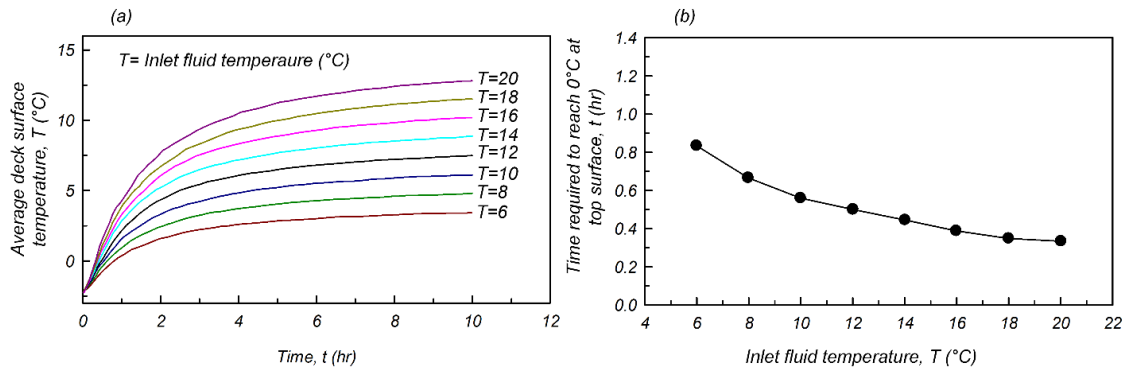


Figure 55. Effect of inlet fluid temperature on (a) average deck surface temperature (b) time required to reach above-freezing point (Yu et al., 2017)

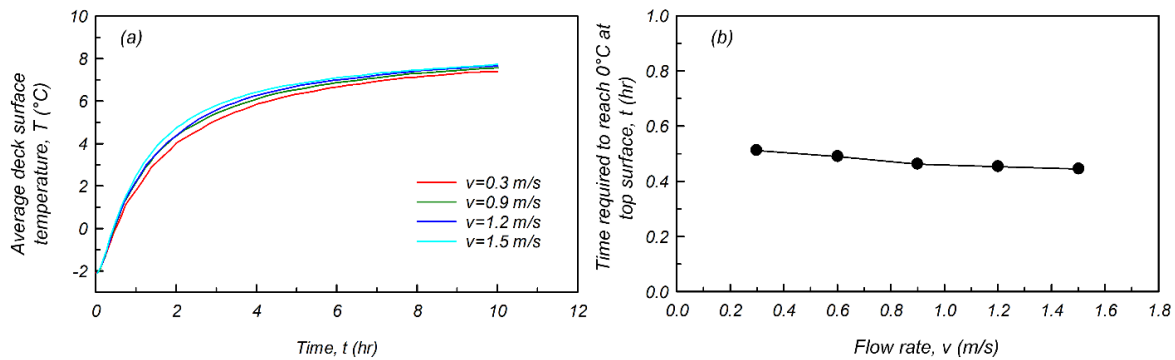


Figure 56. Effect of flow rate on (a) average deck surface temperature (b) time required to reach above-freezing point (Yu et al., 2017)

Feng and Yin (2019) conducted a three-dimensional numerical simulation of fluid flow and heat transfer in a bridge deck using ANSYS, employing a thermal-fluid hydraulic coupling method to evaluate the performance of a bridge deck deicing system. This coupling method accounts for temperature variations of the circulating fluid along the pipe network, providing a more realistic representation of system behavior. The numerical model configuration is shown in Figure 57. Adiabatic boundary conditions were applied to the sides of the bridge deck model, meaning that no heat transfer was allowed through these boundaries. The inlet fluid temperature was set at 15 °C (59 °F), and the flow velocity was varied between 0.6 m/s (2 ft/s) and 2 m/s (6.6 ft/s) to analyze system performance under different operational scenarios.

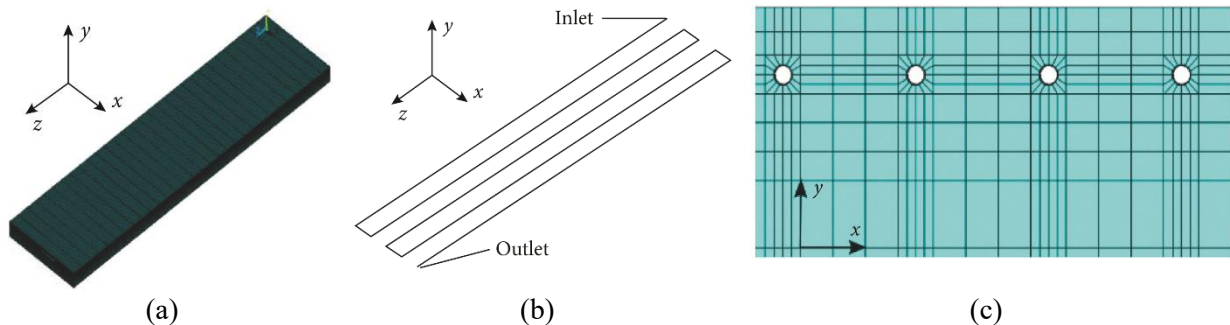


Figure 57. 3D Finite Element model meshing for: (a) whole model, (b) serpentine pipes, and (c) pipes and surrounding concrete (Feng & Yin, 2019)

The time histories of deck surface temperatures for varying inlet fluid temperatures are shown in Figure 58. The results indicate that surface temperature exhibited only minor changes with varying flow rates, suggesting that the influence of flow rate on surface temperature is negligible. Consequently, increasing the circulating fluid flow rate does not significantly enhance the system's heat transfer efficiency.

Ho et al. (2019) investigated the effects of inlet fluid temperature and flow rate on the performance of a hydronic heating system under the extreme continental climate of western and central North Dakota, using COMSOL Multiphysics software. With an average winter ambient temperature of -12.4°C (9.7°F), North Dakota experiences significantly higher heat demand during winter compared to many other regions in the United States (Ho & Dickson, 2017). The simulated concrete panel had dimensions of 7.31 m (24 ft) \times 7.16 m (23.5 ft) \times 0.61 m (2 ft), with heating pipes embedded at a depth of 7.6 cm (3 in.) and spaced 15.2 cm (6 in.) apart horizontally. The model assumed insulated sidewall boundaries, while heat transfer was permitted through the top and bottom surfaces. The simulation coupled heat transfer between the circulating fluid and the pipe wall, as well as between the pipe wall and the surrounding concrete. The model also included the snow melting process to capture realistic surface conditions. The study examined a wide range of operating parameters. Inlet fluid temperatures varied from -30°C (-22°F) to 60°C (140°F), while ambient air temperatures ranged from -25°C (-13°F) to -5°C (23°F). Fluid flow rates were tested between $0.0002\text{ m}^3/\text{s}$ ($0.007\text{ ft}^3/\text{s}$) and $0.001\text{ m}^3/\text{s}$ ($0.035\text{ ft}^3/\text{s}$), allowing the researchers to evaluate the sensitivity of system performance to both thermal and hydraulic inputs.

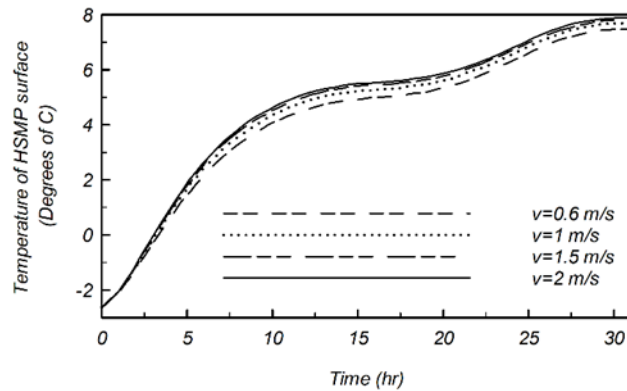


Figure 58. Surface temperature with variation of inlet flow rate (Feng & Yin, 2019)

Figure 59 presents the surface temperature distribution and circulating fluid temperature variation for a fluid inlet temperature of 30°C (86°F), an ambient temperature of -25°C (-13°F), and a flow rate of 0.21 L/s (0.05 gal/s). As shown in Figure 59(a), the pavement surface temperature remained mostly below the freezing point. Figure 59(b) indicates a significant temperature drop between the inlet and outlet fluid temperatures, highlighting substantial heat loss to the surrounding environment. Figure 60(a) illustrates the influence of inlet fluid temperature on pavement surface temperature at the same ambient air temperature of -25°C (-13°F). The results show that an inlet fluid temperature of 60°C (140°F) was sufficient to maintain the pavement surface temperature above freezing, regardless of the volumetric flow rate. In contrast, with an inlet fluid temperature of 30°C (86°F), surface temperatures ranged between 3.2°C (38°F) and -1.4°C (29.5°F), depending on the flow rate. These findings emphasize that both inlet fluid temperature and flow rate are critical parameters influenced by ambient air temperature. As shown in Figure 60(b) increasing the flow rate led to higher surface temperatures, while lower flow rates resulted in greater temperature gradients across the pavement surface. This non-uniform thermal distribution

may cause uneven stress along the surface, potentially leading to cracking and long-term durability issues.

Pipe Spacing and Embedded Depth

The pipe embedment depth refers to the vertical distance from the pipe to the bridge deck surface, while pipe spacing denotes the horizontal distance between adjacent pipes. Both parameters play a critical role in determining heat transfer efficiency through the bridge deck and, consequently, the overall performance of the hydronic heating or cooling system. Findings from previous studies indicate that increasing the pipe spacing or embedment depth results in a lower average surface temperature and a longer time required to raise the deck surface above freezing. These effects highlight the importance of optimizing pipe layout to ensure effective and energy-efficient deicing performance.

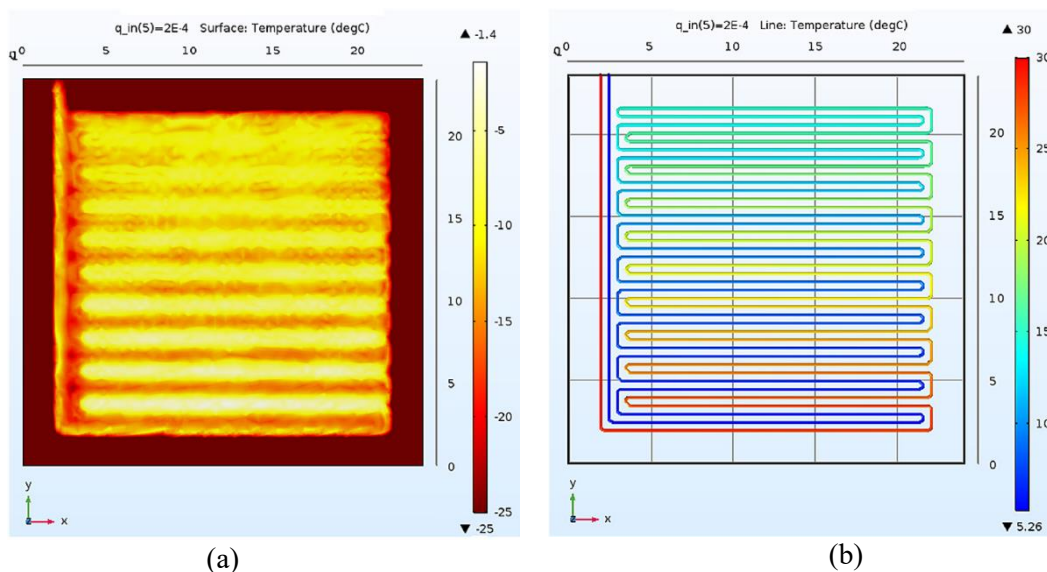


Figure 59. Contours of (a) surface temperature of heated deck (b) circulating fluid temperature variation, inlet fluid temperature 30°C (86°F), ambient temperature of -25°C (-13°F), and flow rate of 0.21 l/s (0.05 gal/s) (Ho et al., 2019)

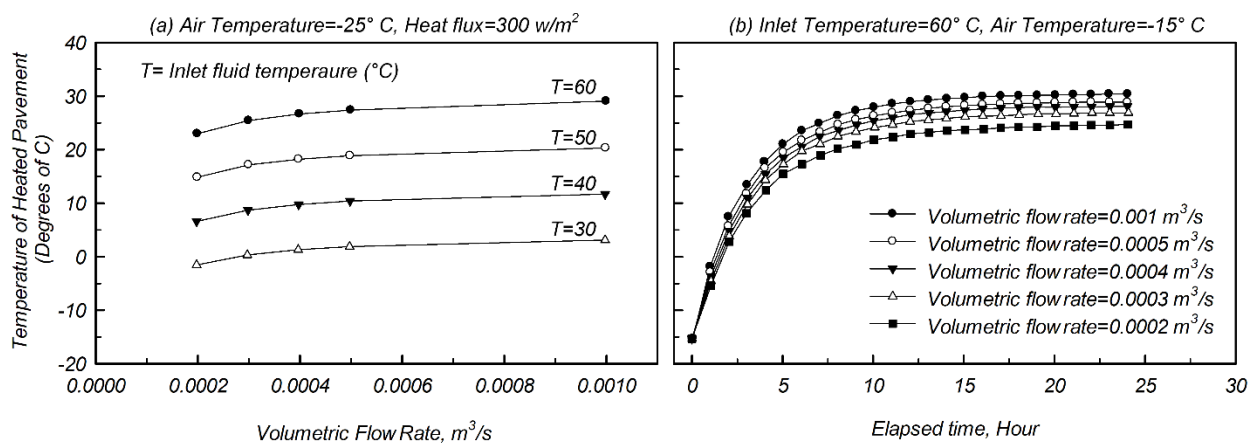


Figure 60. Temperature of heated pavement versus volumetric flow rate for ambient temperature of (a) -25°C (-13°F) (b) -15°C (5°F) (Ho et al., 2019)

Feng and Yin (2019) conducted a numerical study to investigate the effects of pipe embedment depth and pipe spacing on the performance of a bridge deck snow melting system. Figure 61(a) illustrates the surface temperature distribution after 4.25 hours of heating for a constant pipe spacing of 15 cm (5.9 in.) and three different embedment depths: 9 cm (3.5 in.), 10 cm (3.9 in.), and 11 cm (4.3 in.). The results show that as the embedment depth increases, more time is required for heat to reach the surface, resulting in lower surface temperatures. Figure 61(b) presents the surface temperature distribution for a fixed embedment depth of 11 cm (4.3 in.) and varying pipe spacings of 10 cm (3.9 in.), 15 cm (5.9 in.), and 20 cm (7.9 in.). The results indicate that the surface temperature decreases as pipe spacing increases. Specifically, increasing the pipe spacing from 10 cm to 20 cm led to a reduction in maximum surface temperature ranging from 1.4 °C (34.5 °F) to 1.7 °C (35 °F). As shown in Figure 50, wider pipe spacing also resulted in a steeper temperature gradient across the surface, indicating less uniform heat distribution.

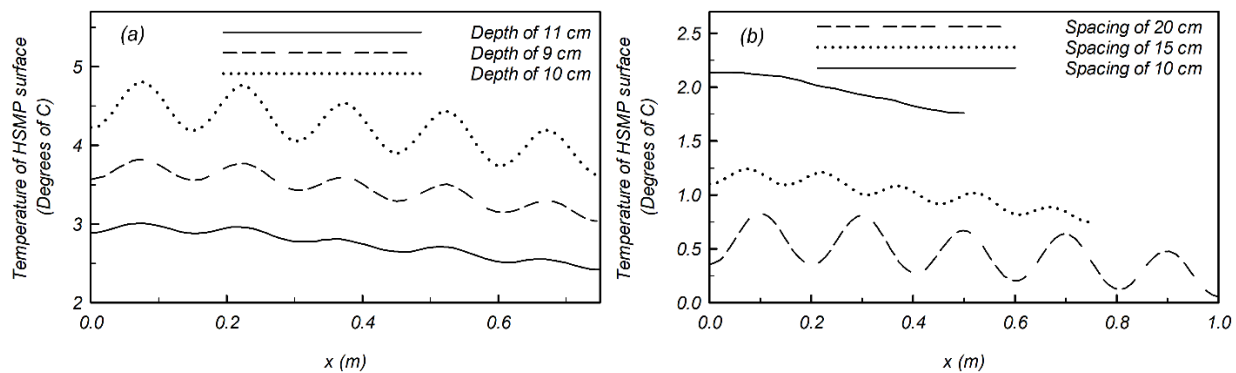


Figure 61. Comparison of surface temperature difference with (a) different pipe embedded depth in terms of pipe spacing of 15 cm (b) different pipe spacing in terms of pipe embedded depth of 15 cm (5.9 inch) (Feng & Yin, 2019)

Bowers Jr (2016) conducted a 3D finite element analysis of a shallow geothermal energy bridge deck deicing system using COMSOL Multiphysics to evaluate performance across different geometric configurations. The modeled bridge deck measured 3.7 m (12.1 ft) in width, with a length equal to four times the pipe spacing, and a thickness of 25.4 cm (10 in.). In the baseline model, the heat exchanger pipes were embedded at a depth of 7.45 cm (2.9 in.) with a pipe spacing of 20 cm (7.9 in.). The inlet fluid temperature was set at 12 °C (53.6 °F). Figure 62 illustrates both the model geometry and the mesh configuration. The study investigated four different pipe spacing scenarios: 15 cm (5.9 in.), 20 cm (7.9 in.), 25 cm (10 in.), and 30 cm (12 in.). Boundary conditions were applied such that the side walls of the bridge deck were insulated, allowing heat transfer only through the top and bottom surfaces. Figure 63 shows the contours of average surface temperatures for the various pipe spacing cases. Results indicated that both the average surface temperature and the time required to raise the surface above freezing increased as pipe spacing widened, due to reduced heat coverage between pipes. Models with narrower pipe spacing (e.g., 15 cm) delivered more energy per unit pipe length than those with wider spacing, such as 25 cm and 30 cm. Wider spacing resulted in slower heating of the deck surface between pipes, as heat took longer to reach midpoints between loops. Although models with wider spacing had greater deck volume to heat per unit pipe length, they exhibited slightly lower energy loss compared to narrower configurations. Overall, the study concluded that systems with wider pipe spacing may be marginally more efficient in terms of energy use, though at the cost of slower surface heating performance.

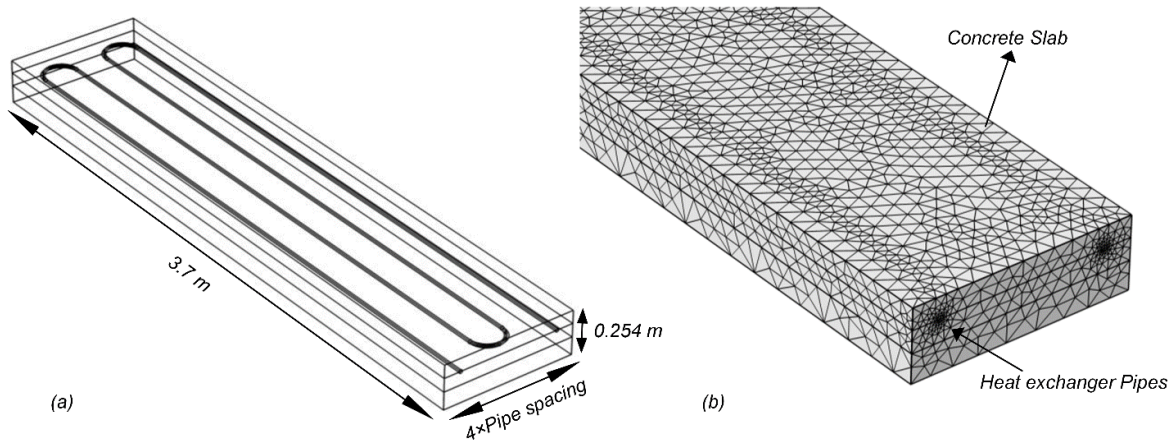


Figure 62. (a) Numerical baseline model configuration, (b) Numerical modeling mesh (Bowers Jr, 2016)

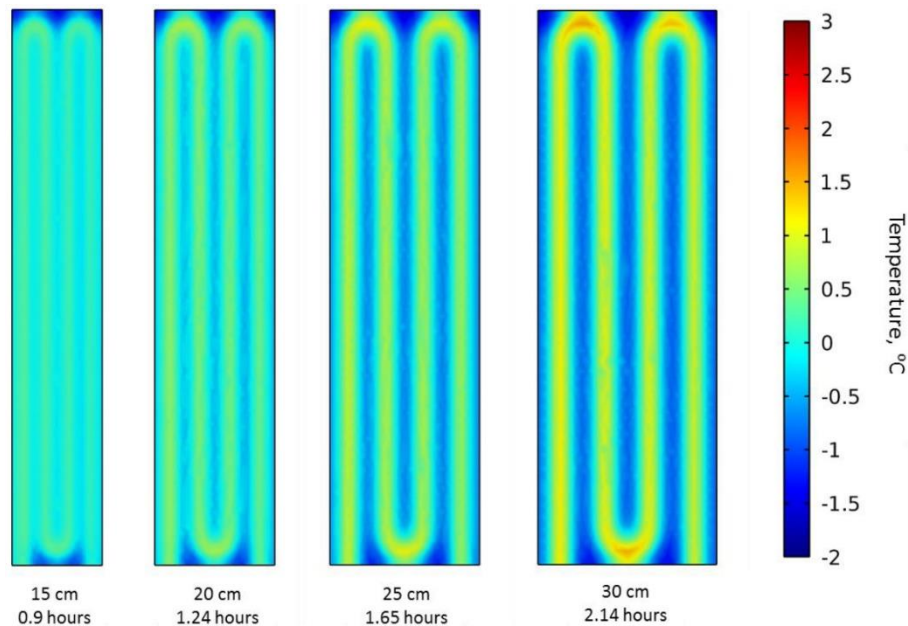


Figure 63. Contours of deck surface temperature for different pipe spacing when the average surface temperature reached above freezing point (Bowers Jr, 2016)

A parametric study by Yu et al. (2017) investigated the effect of pipe embedment depth on the performance of a geothermal bridge deck deicing system and identified it as a critical design parameter. As shown previously in Figure 54, the baseline model used a pipe spacing of 20 cm (7.9 in.), while the embedment depth of the pipes varied from 4 cm (1.6 in.) to 12 cm (4.7 in.). The system circulated fluid with an inlet temperature of 12 °C (53.6 °F) at a flow rate of 0.6 m/s. The ambient temperature was held constant at -2 °C (28.4 °F), and wind effects were excluded from the simulation. Figure 64(a) illustrates that the average bridge deck surface temperature decreased as the pipe embedment depth increased, due to the greater distance between the heat source and the deck surface. Similarly, Figure 64(b) shows that the time required for the surface temperature to rise above freezing increased significantly with deeper pipe embedment. These findings highlight the importance of optimizing pipe placement to improve thermal efficiency in geothermal bridge deck heating systems.

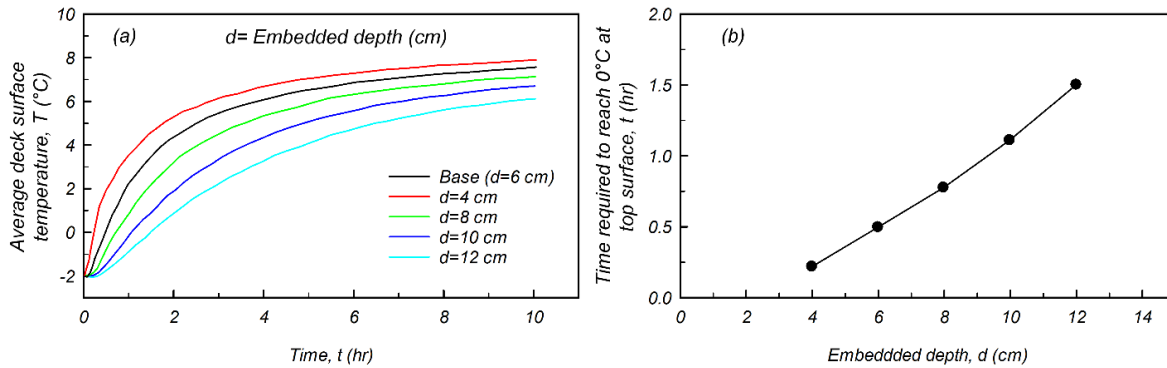


Figure 64. (a) Average deck surface temperature, and (b) time required to reach above-freezing point at top surface of bridge deck (Yu et al., 2017)

Weather Condition (Snowfall Rate, Wind Speed, and Ambient Temperature)

Bowers Jr (2016) evaluated the performance of a baseline shallow geothermal bridge deck deicing system under varying ambient air temperatures, ranging from -10°C (14°F) to -0.5°C (31°F). Figure 65(a) illustrates how both the average surface temperature and the proportion of the deck area maintained above 0°C (32°F) changed over time at different ambient conditions. The results showed that lower ambient temperatures significantly increased the time required to raise the deck surface above the freezing point. For example, at an ambient temperature of -10°C (14°F), it took approximately four hours for the deck surface to reach above 0°C , whereas much less time was needed at higher ambient temperatures. Figure 65(b) presents the cumulative energy input required for deck heating at each ambient temperature relative to the baseline model. The findings indicated that as ambient temperatures decreased, the amount of energy injected into the deck increased accordingly. This is attributed to the greater thermal loss to the environment at lower temperatures, which necessitates more energy to maintain a safe surface temperature. Overall, the study confirmed that colder air temperatures substantially increase the energy demand and heat loss associated with geothermal bridge deck deicing systems.

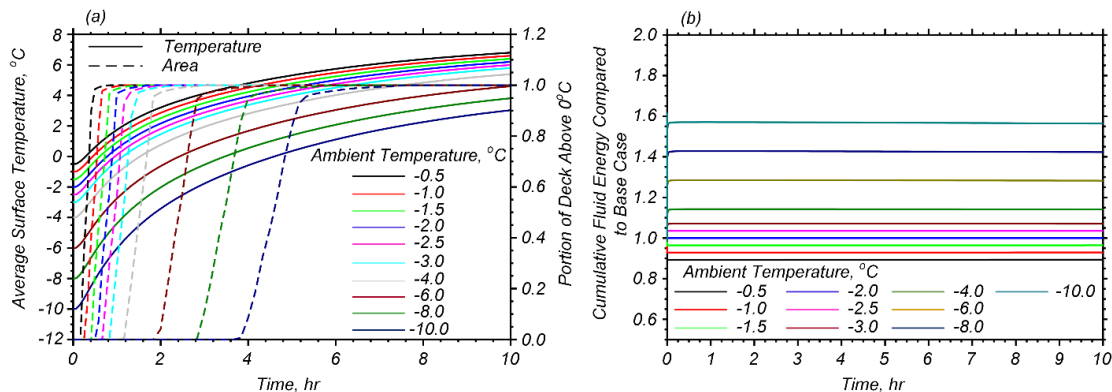


Figure 65. (a) Average deck surface temperature and area of deck surface above 0°C (32°F) for different ambient temperatures (b) Distribution of injected energy to the deck and lost energy for different air temperatures (Bowers Jr, 2016)

Bowers Jr. (2016) investigated the impact of wind speed on the performance of a bridge deck deicing system. The study analyzed average deck surface temperatures and the area of the deck maintained above 0°C (32°F) under varying wind speeds, ranging from 2 m/s (6.6 ft/s) to 20 m/s

(65.6 ft/s), as shown in Figure 66(a). Results indicated that as wind speed increased, the average surface temperature decreased, and it took longer for the deck to reach temperatures above freezing. Figure 66(b). presents the distribution of energy input used to heat the deck versus the energy lost to the surrounding environment at different wind speeds. The findings show that higher wind speeds lead to significantly greater energy losses. At a wind speed of 20 m/s (65.6 ft/s), more than 75% of the input energy was lost to the environment, an amount 50% greater than the loss at 2 m/s (6.6 ft/s). Additionally, the mode of heat loss shifted with increasing wind speed: at speeds above 15 m/s (49 ft/s), over 90% of the energy loss occurred through convection, whereas at 2 m/s, convection accounted for approximately 70% of the total energy loss. These results emphasize the critical role of wind speed in determining the energy efficiency of bridge deck deicing systems.

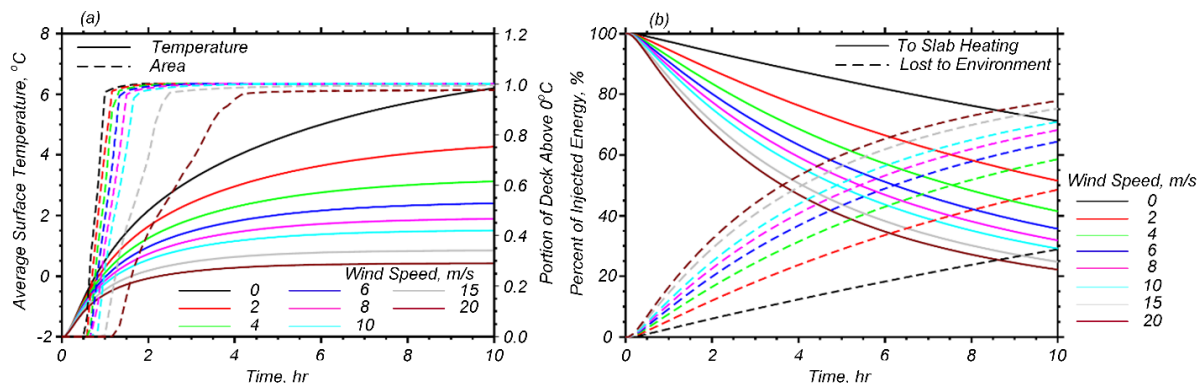


Figure 66. (a) Average deck surface temperature and area of deck surface above 0°C (32°F) for different wind speeds (b) Distribution of injected energy to the deck and lost energy for different wind speeds (Bowers Jr, 2016)

Yu et al. (2017) Yu et al. (2017) investigated the impact of wind speed on the bridge deck heating process. Wind speeds ranging from 1 m/s (3.3 ft/s) to 6 m/s (20 ft/s) were analyzed. The effects of wind speed on both the average surface temperature and the time required for the deck surface to exceed 0 °C (32 °F) are shown in Figure 67(a) and (b), respectively. The results indicated that as wind speed increased, the average surface temperature decreased, and the time required for the surface to rise above freezing increased. Notably, the influence of wind speed became more significant at speeds above 2 m/s (6.6 ft/s), while it remained negligible at lower speeds. However, at wind speeds of 4 m/s (13.1 ft/s) or higher, the reduction in surface temperature plateaued, suggesting a threshold beyond which further increases in wind speed have diminishing effects.

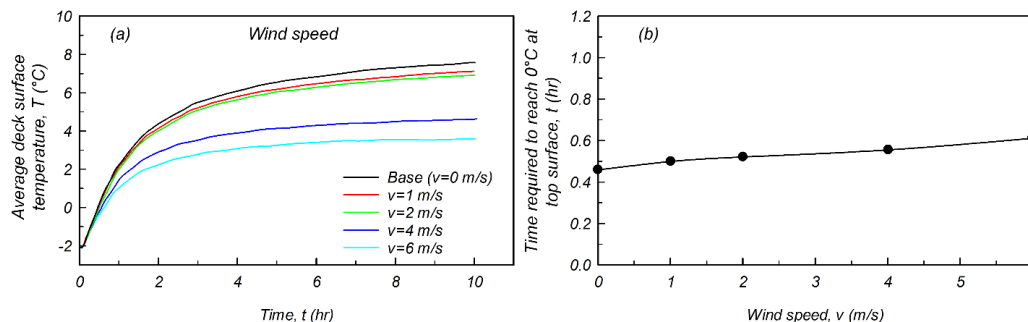


Figure 67. (a) Average deck surface temperature (b) time required to reach above-freezing point at bridge deck surface (Yu et al., 2017)

Bowers Jr (2016) evaluated the performance of a bridge deck deicing system under three different snowfall rates: 2 cm/hr (0.79 in/hr) representing mild conditions, 5 cm/hr (1.97 in/hr) for moderate conditions, and 10 cm/hr (3.94 in/hr) for severe conditions. Figure 68(a) illustrates the average deck surface temperatures corresponding to each snowfall rate. The results showed that the rate of surface temperature decrease during snowfall was directly influenced by the snowfall intensity, the higher the snowfall rate, the greater the initial surface temperature drop. However, after the initial decrease, surface temperatures gradually increased due to system operation. Figure 68(b) compares the deck heating flux per unit surface area for the different snowfall rates. Deck heating flux is defined as the rate of energy transferred to the deck per unit area. As shown, higher snowfall rates required greater heating fluxes to maintain surface temperature, highlighting the increased energy demand under severe snow conditions.

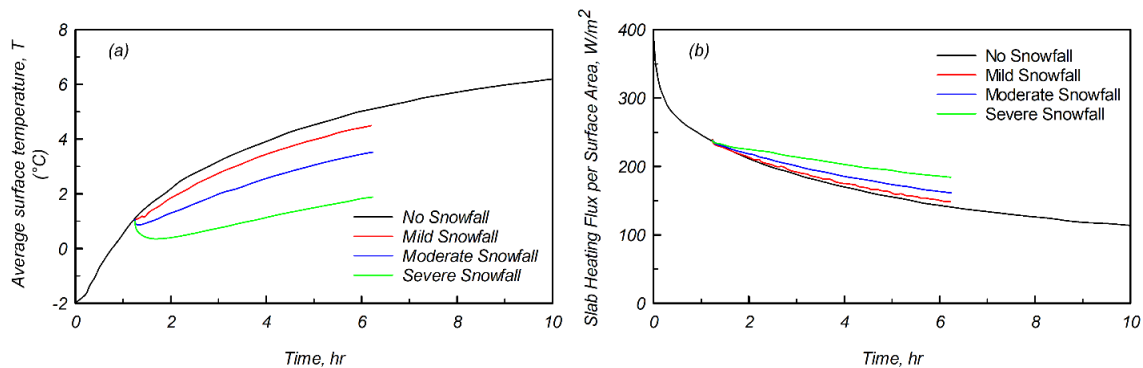


Figure 68. (a) Average deck surface temperature with different snowfall rate (b) deck heating flux per surface area for different snowfall rates (Bowers Jr, 2016)

Liu et al. (2019) conducted a sensitivity analysis to examine the impact of snowfall rate on the optimal design of a hydronic snow melting system. In their study, the bridge deck model measured 4 m (13 ft) in length, 7 m (23 ft) in width, and 0.2 m (8 in.) in thickness. The horizontal pipe spacing was 5 cm (2 in.), with pipes embedded 20 cm (8 in.) below the surface. The 3D configuration of the numerical model is shown in Figure 69(a). Inlet fluid temperature and flow rate were optimized using the Nelder-Mead algorithm to minimize energy consumption for snow melting. The circulating fluid flow rate was set at 1 m/s (3.3 ft/s), and the optimal hourly inlet temperature was determined accordingly. The model assumed insulated bottom and side boundaries (no heat flow), and a complete energy balance approach was used to calculate the required heat flux. Because surface heat flux is influenced by several climate-related factors, including snowfall rate, ambient temperature, and wind speed, two snowfall rates were analyzed: (1) a base case of 0.3 cm/h (0.12 in./h) and (2) an elevated rate of 0.39 cm/h (0.15 in./h), representing a 30% increase. Figure 69(b) compares the cumulative energy consumption for both scenarios. The analysis revealed that increasing the snowfall rate by 30% resulted in a 35% rise in energy consumption, indicating that the energy required to melt snow, particularly during the phase change, is substantial. These findings underscore the importance of accurately accounting for snowfall rates in the design of efficient hydronic heating systems for snow melting applications.

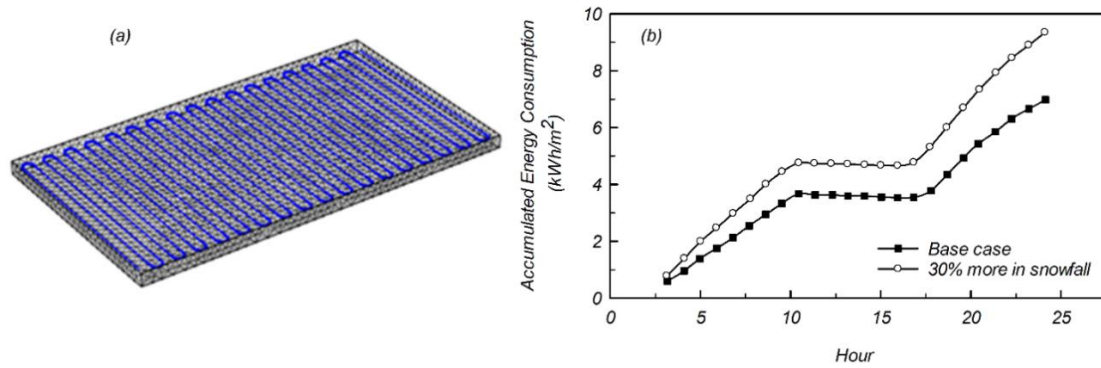


Figure 69. (a) Mesh of bridge deck model and snow melting system (b) accumulated energy consumption with various snowfall rate (Liu et al., 2019)

Ghasemi-Fare & Basu, (2016) employed a finite difference analysis to evaluate the thermal performance of geothermal energy piles equipped with a single U-shaped circulation pipe. Figure 70 illustrates how key parameters influence the efficiency of geothermal piles after 12 hours and 60 days of operation. Their analysis identified three primary factors affecting the snow and ice melting capacity of hydronic heating systems: (1) the initial temperature difference, θ ($\theta = T_{\text{inlet}} - T_{\text{initial}}$), 2) the thermal conductivities of surrounding soil, k_s , and concrete, k_c , and 3) circulation system design parameters such as the radius of the pipe, r_i , pipe depth, and pipe spacing. The study concluded that system efficiency improves with higher fluid inlet temperatures and greater concrete thermal conductivity. However, increased pipe embedment depth and wider spacing negatively impact system performance. In the short term, efficiency was most sensitive to the pipe radius, while over longer periods, soil thermal conductivity became the dominant factor. Additionally, ambient air temperature, the temperature gradient between the ground and the circulating fluid, and the depth to the groundwater table were found to significantly influence GSHP system performance. For regions in Montana where the groundwater level is relatively shallow, GSHP systems are expected to operate more efficiently.

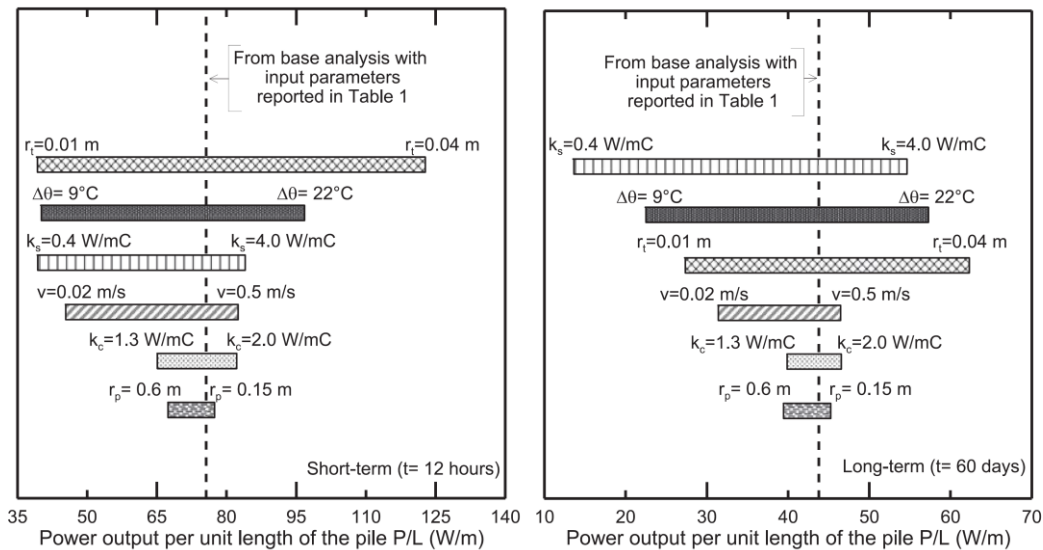


Figure 70. Effects of key parameters on the efficiency of a geothermal piles after 12 hrs and 60 days of operation (Ghasemi-Fare & Basu, 2016)

Optimization of Heat Extraction/Injection in Primary Unit

One of the primary challenges in the design and long-term operation of ground source heat pump (GSHP) systems is the gradual change in subsurface temperature resulting from continuous heat extraction and injection. These temperature shifts can significantly affect system efficiency and overall performance. The configuration of the heat exchange system, particularly the spatial arrangement and sequencing of energy piles or wells, plays a critical role in how the ground temperature evolves over time. Several studies have examined the strategic use of selected piles or wells within a grid to reduce thermal interference, minimize energy loss to the ground, and enhance heat pump efficiency. This section reviews key findings from prior research to evaluate how geometric layout and operational strategies influence the thermal behavior and effectiveness of GSHP systems with multiple heat exchangers. Optimization of energy extraction in shallow geothermal systems has been explored by de Paly et al. (2012), Beck et al. (2013), and Bowers Jr. and Olgun (2020). In particular, Bowers Jr. and Olgun (2020) developed a numerical model using COMSOL Multiphysics™ to simulate vertical heat exchangers and investigate various heat injection and extraction scenarios, along with their impacts on the efficiency of shallow geothermal energy (SGE) systems. Their model was based on the approach developed and calibrated by Ozudogru et al. (2015) and incorporated the full borehole-soil system. Key components included fluid circulation pipes, a one-dimensional line element centered within the fluid pipes, thermal grout, and the surrounding soil. To improve computational efficiency, the authors applied two major simplifications: symmetry and domain discretization. The model featured a 6×6 grid of energy piles, each with a diameter of 15 cm (5.9 in.) and a center-to-center spacing of 8 m (26 ft), as shown in Figure 71(a). Quadrilateral symmetry with zero heat flux at the symmetry boundaries was applied to reduce computational demands. A constant temperature equal to the initial ground temperature was assigned to the outer model boundaries. Inside each energy pile, a single U-shaped heat exchanger pipe with an inner diameter of 3.4 cm (1.34 in.) and a wall thickness of 3.8 mm (0.15 in.) was modeled. The meshed domain around the geothermal boreholes is illustrated in Figure 71(b).

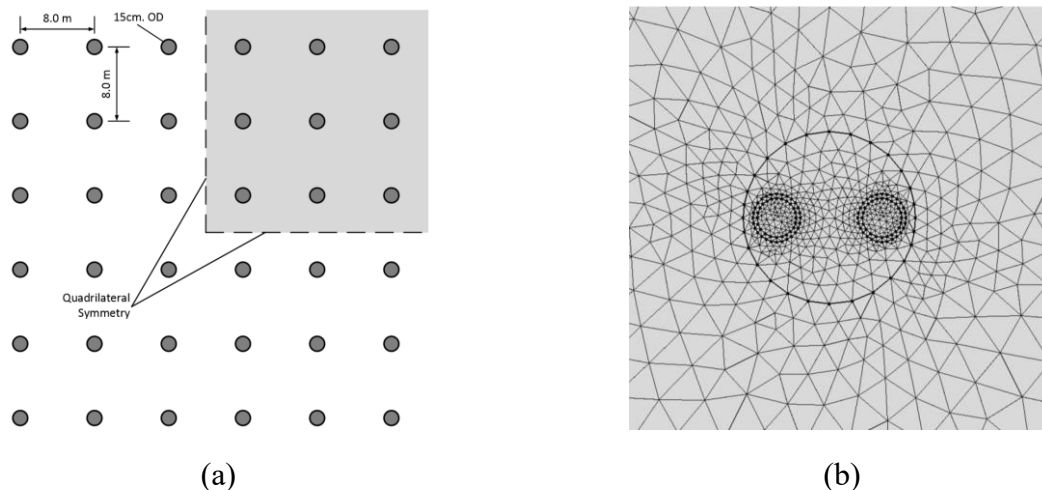


Figure 71. (a) Grid arrangement of boreholes (b) the Meshing of the pile and heat exchanger pipes (Bowers Jr & Olgun, 2020)

The results of this study indicated that the arrangement of geothermal energy piles significantly influences energy loss within the system and, consequently, its long-term efficiency. As illustrated

in Figure 72, the energy piles in the grid were categorized into three groups, inner, middle, and outer, and various heat extraction and injection scenarios were analyzed. In the first scenario, referred to as the “Base” scenario, all three groups of energy piles operated simultaneously over a five-month period with a uniform extraction rate of 20 W/m (6 W/ft) per pile. The second scenario, called the “Outside-Inside” scenario, involved staged operation: for the first 75 days, only the outer piles were used for heat extraction at a rate of 36 W/m (11 W/ft), followed by the activation of the inner and middle piles for the remaining 75 days at a higher extraction rate of 45 W/m (14 W/ft). The final scenario, termed “Different Rates,” assigned variable extraction rates to each group over the entire five-month period. In this case, all piles operated continuously, but with differing extraction rates: 25 W/m (7.6 W/ft) for the outer group, 16 W/m (5 W/ft) for the middle group, and 7 W/m (2.1 W/ft) for the inner group..

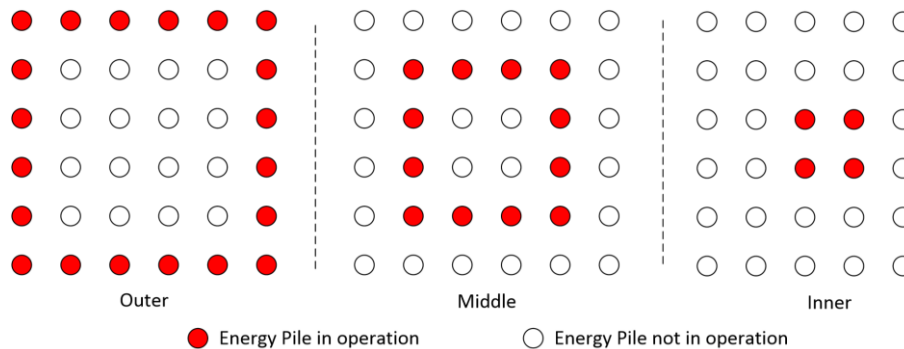


Figure 72. Different extraction strategies (Bowers Jr & Olgun, 2020)

Several metrics were used to evaluate the performance of each scenario, including temperature measurements at selected locations and the net change in energy within the geothermal footprint area (Bowers, 2016). The net energy change is influenced by the volumetric heat capacity of the surrounding soil and variations in average air temperature. Figure 73 compares the net change in energy within a grid of energy piles at two time points: the end of the five-month extraction period and after one full year. At the end of the extraction period, none of the scenarios showed a net positive energy balance (Figure 73). However, by the end of one operational year, Scenario 3, featuring variable extraction rates, achieved a positive net energy change of 8 MJ. In contrast, Scenario 2 and the base case showed energy losses of 13 MJ and 17 MJ, respectively. The results suggest that extracting energy from the outer group of piles either earlier or at a higher rate helps retain more energy within the geothermal footprint. Among the three configurations tested, Scenarios 2 and 3 were more effective than the base case in preserving subsurface thermal energy. Moreover, the greater disparity in extraction rates used in Scenario 3 contributed to its higher efficiency.

de Paly et al. (2012) developed an optimization algorithm based on linear programming to enhance energy extraction efficiency in a borehole heat exchanger (BHE) system. Leveraging the linear relationship between the heat loads of individual boreholes and the resulting ground temperature change, they formulated a linear optimization problem. The objective of the study was to minimize the overall temperature drop in the ground by adjusting the heat extraction rates at each borehole. The model assumed a 30-year operational period and employed the analytical line heat source equation to represent thermal interactions for each borehole. Using the superposition principle, the researchers estimated the cumulative ground temperature change resulting from multiple boreholes operating with time-varying loads. The system geometry, shown in Figure 74, consisted of a $5 \times$

5 array of boreholes, each 100 m (328 ft) deep and spaced 10 m (32.8 ft) apart. The optimized scenario was compared to a baseline case in which equal energy was extracted from all boreholes. The results demonstrated that variable, optimized extraction rates significantly reduced ground temperature depletion compared to uniform loading, highlighting the potential benefits of load distribution optimization in BHE system design.

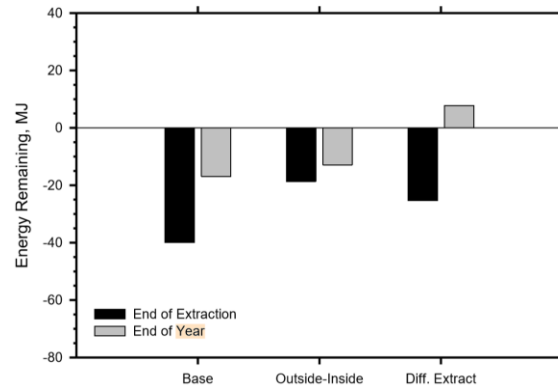


Figure 73. Comparison of the net energy remaining within the energy pile grids at the end of extraction and end of operational year for three scenarios (Bowers Jr & Olgun, 2020)

Figure 74 presents the temperature distribution and borehole heat exchanger (BHE) workloads for an optimized geothermal system case. During winter, when energy demand is highest, heat extraction was initiated from the boreholes located at the outer edge of the field and progressively shifted inward. The results demonstrated that the inner boreholes were thermally insulated by the surrounding outer boreholes, limiting their ability to receive conductive heat from the ambient ground. Over a 30-year operation period, for the same annual energy extraction, the optimized configuration resulted in an 18% reduction in subsurface temperature decline. This indicates that the optimization strategy produced a more uniform ground temperature distribution and improved energy extraction efficiency without increasing environmental impact. However, successful implementation of such a system requires an advanced control framework capable of continuously monitoring and dynamically adjusting the heat extraction rates for each borehole.

Beck et al. (2013) utilized a similar modeling approach to optimize a borehole heat exchanger (BHE) system by focusing on the geometric arrangement of boreholes and the distribution of energy extraction to minimize surface temperature decline. As in the study by de Paly et al. (2012), boreholes were modeled using an analytical line source approach. The optimization was conducted over a 50 m × 50 m (164 ft × 164 ft) field containing 36 boreholes, each 100 m (328 ft) deep and spaced 10 m (32.8 ft) apart center-to-center. The study examined various optimization scenarios, including a base case where all boreholes extracted energy at equal rates, as well as configurations with varied extraction rates. The results, illustrated in Figure 75, highlight how strategic arrangement and energy distribution can improve thermal performance and reduce surface temperature impacts.

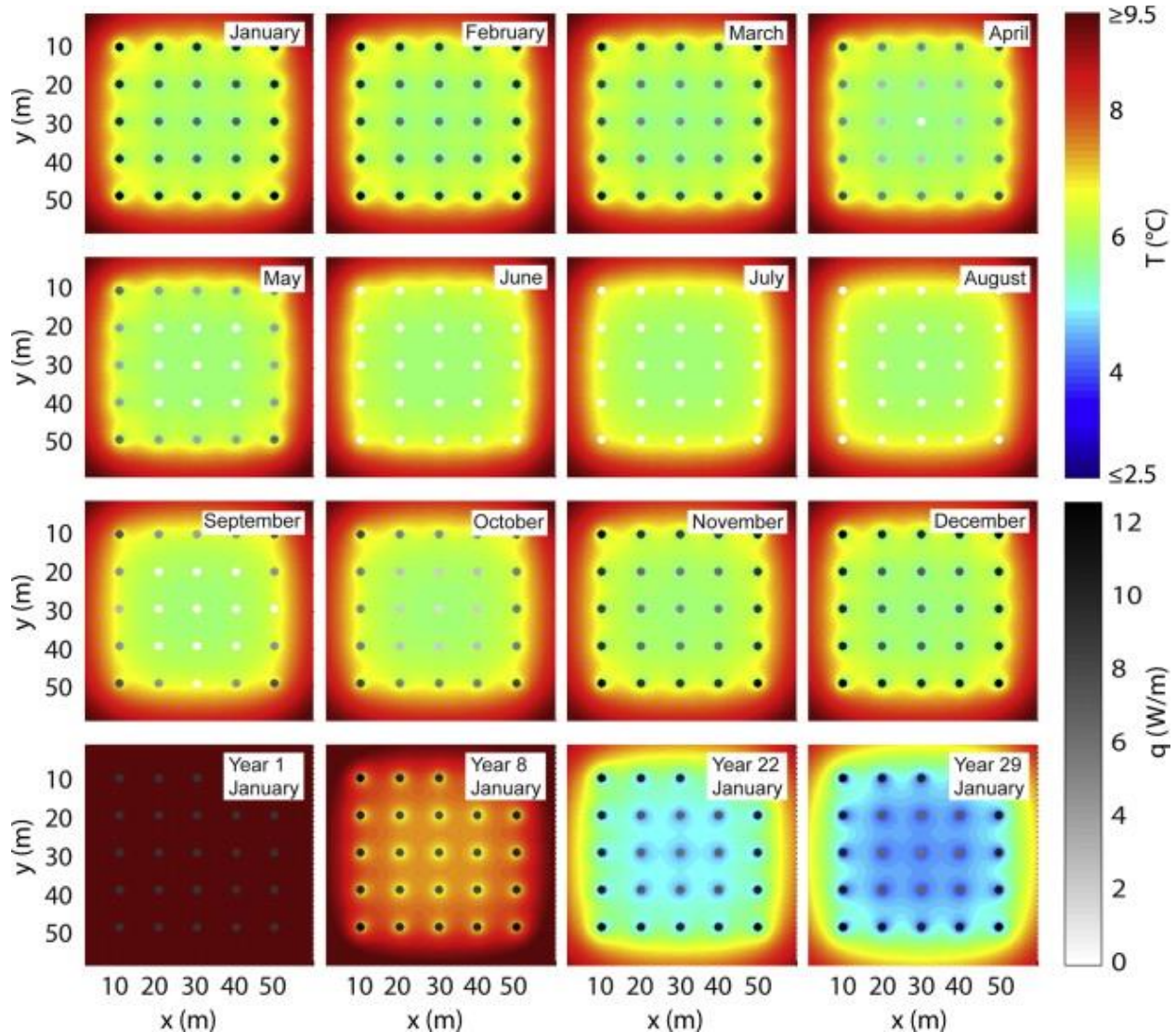


Figure 74. Temperature distribution and BHE workloads for the optimized case. Each circle represents a BHE with its corresponding load in grayscale. Darker color shades illustrate higher BHE loads. The subsurface temperature distribution at a depth of 50 m (164 ft) is shown by colors, where high absolute temperatures appear in red and lower temperatures in blue (de Paly et al., 2012).

Figure 75 presents the temperature distribution at a depth of 50 m (164 ft) after 30 years of simulation for both the optimized and base case scenarios. The results indicated greater temperature variation in the optimized system (Figure 75(g)). However, the study concluded that incorporating seasonally variable heat demand into the geometric optimization of borehole arrangements reduced the maximum ground temperature by approximately 10–15%. The optimization results further showed that placing boreholes away from the central square region was advantageous. This configuration enhanced conductive heat transfer from the surrounding ground toward the borehole field. Additionally, the study found that well-designed energy extraction strategies could partially offset the limitations of suboptimal borehole arrangements. When the geometric layout was optimized, load optimization had minimal additional impact, suggesting that proper borehole placement alone significantly improves long-term thermal performance.

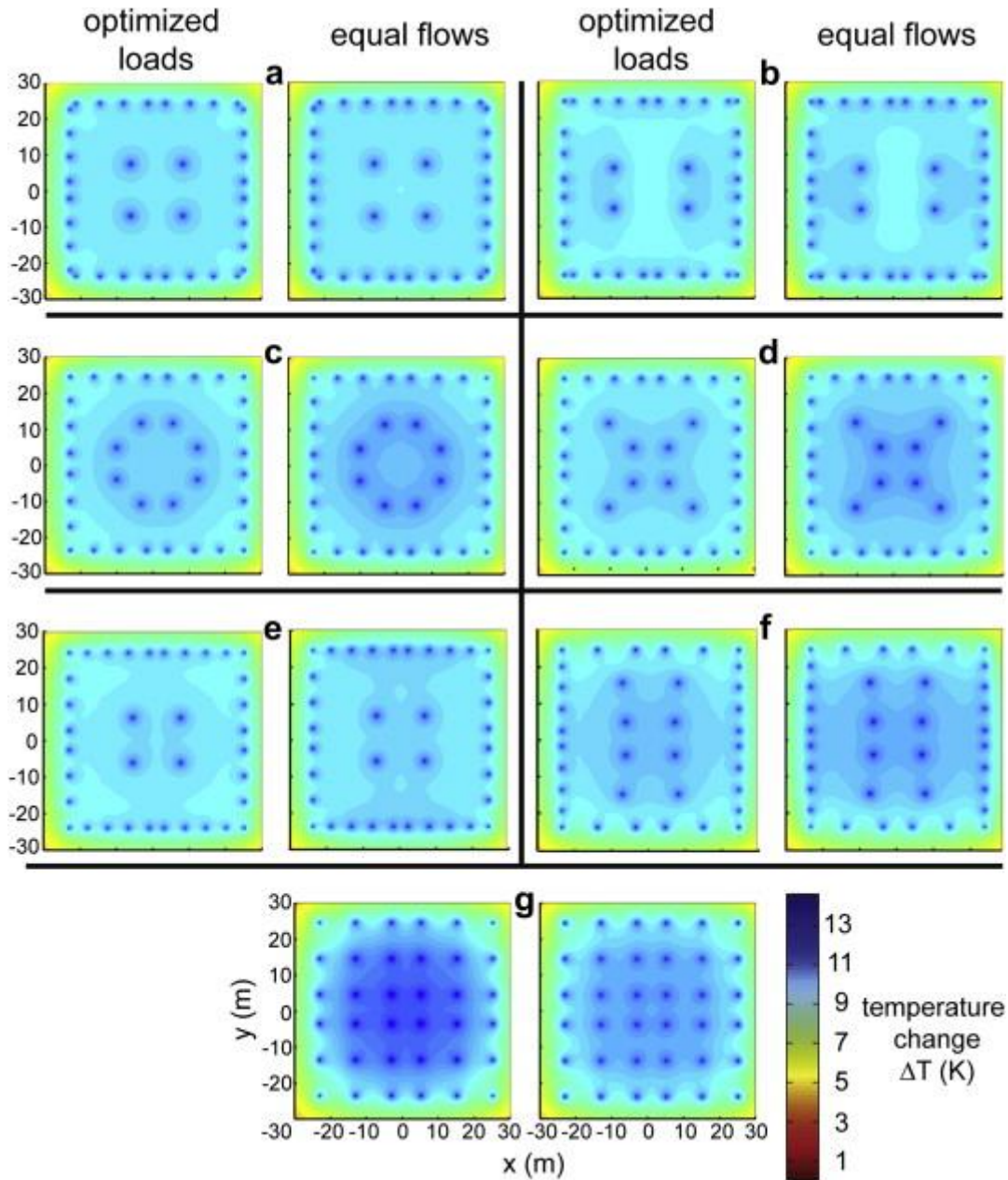


Figure 75. The subsurface temperature distribution at depth of 50 m for the optimized case and the equal heat extraction case (Beck et al., 2013)

CHAPTER 4: BRIDGE DECK MODEL DESIGN AND CONSTRUCTION

This chapter outlines the construction procedure for a physical bridge deck model developed to assess the feasibility of using geothermal energy for bridge deck deicing in Montana. It begins with a presentation of the concrete mix design used in the model, followed by the development and validation of a numerical simulation of the geothermal bridge deck system. Sensitivity analyses were conducted to evaluate the effects of key design parameters on system performance. The chapter then presents the finalized design of the physical model and provides a detailed description of its construction and instrumentation setup. Finally, relevant Montana weather data obtained from Road Weather Information System (RWIS) stations are introduced to support the experimental design and analysis.

Concrete Mix Design

Concrete is a composite material composed of water, cement, fly ash, slag (ground granulated blast-furnace slag, GGBFS), and other cementitious materials (CMs). CMs are essential components of concrete mixtures, commonly used alongside Portland cement to reduce the heat of hydration, improve workability, and minimize thermal cracking in structural applications. The most widely used cementitious materials include fly ash, slag, and silica fume. Fly ash offers multiple benefits in both the fresh and hardened states of concrete. It is cost-effective by reducing the required amount of cement, while also improving the workability, strength, and long-term durability of the concrete. Slag is another commonly used CM, either as part of blended cements or as a separate additive. It enhances concrete's resistance to chemical attack, reduces permeability, and mitigates reinforcement corrosion when used in combination with Portland cement. Silica fume, a highly reactive pozzolanic material, contributes to early-age high compressive strength, increased tensile strength, durability, toughness, abrasion resistance, and high electrical resistivity, while significantly reducing permeability. The objective of this section is to evaluate the mechanical and thermal properties of the concrete mixtures used in this study. To develop an appropriate mix for the model-scale bridge deck and culvert experiments, a series of MDT-approved concrete mix designs was compiled. This section provides a summary of the collected data and outlines the methodology used to formulate the concrete mixture for experimental testing conducted in the Subzero Research Lab (SRL) at Montana State University.

An Overview of the Collected Mix Designs

Table 9 presents the quantities and percentages of concrete aggregates used in MDT-approved concrete mix designs, along with the gradation type associated with each mixture. The aggregate components include sand, which ranges from 36.5% to 44.2%; coarse aggregate (CA), ranging from 49.2% to 56.7%; and manufactured (fine) aggregate (MA), which appears in mixtures 1811DECK04 and 2022STRUCTURE02 at proportions between 10.1% and 14.3%.

Cementitious Materials

Table 10 summarizes the weights and proportions of the cementitious materials used in the concrete mix designs approved by MDT. The specific gravity of cement is typically assumed to be 3.15. As shown in the table, in addition to ordinary Portland cement, supplementary cementitious materials such as slag (used in mix 1811DECK04) and fly ash (used in mixes 1931DECK01, 1943DECK01, and 2031DECK01) were incorporated at replacement levels

ranging from 15% to 20%. Silica Fume Type 100 was also included in most mixtures, except for 2022STRUCTURE02, at dosage rates between 4% and 5%.

Table 9. Gradation and Gradation Properties of Concrete Mix Designs' Aggregates

<i>Sample ID</i>	<i>Unit</i>	<i>Sand #1</i>	<i>Sand #2</i>	<i>CA #1</i>	<i>CA #2</i>	<i>CA #3</i>	<i>MA #1</i>	<i>Gradation Type</i>
<i>1811DECK04</i>	<i>lbs.</i>	1100	-	-	1480	-	430	Optimized
	<i>%</i>	36.5%	-	-	49.2%	-	14.3%	
<i>1931DECK01</i>	<i>lbs.</i>	1320	-	1730	-	-	-	Conventional
	<i>%</i>	43.3%	-	56.7%	-	-	-	
<i>1943DECK01</i>	<i>lbs.</i>	1380	-	1740	-	-	-	Conventional
	<i>%</i>	44.2%	-	55.8%	-	-	-	
<i>2022STRUCTURE02</i>	<i>lbs.</i>	1220	-	1527	-	-	310	Optimized
	<i>%</i>	39.9%	-	50.0%	-	-	10.1%	
<i>2031DECK01</i>	<i>lbs.</i>	1320	-	1730	-	-	-	Conventional
	<i>%</i>	43.3%	-	56.7%	-	-	-	

CA: coarse aggregate, MA: fine aggregate.

Table 10. Ingredients of the Collected Concrete Mix Designs

<i>Sample ID</i>		<i>Cement</i>	<i>Fly Ash</i>	<i>GGBFS</i>	<i>Other CM</i>	<i>Water (lb)</i>	<i>W/C</i>
<i>1811DECK04</i>	<i>lbs.</i>	426	-	113	25	242	0.43
	<i>%</i>	78.0%	-	20.0%	5.0%		
<i>1931DECK01</i>	<i>lbs.</i>	430	90	-	30	231	0.42
	<i>%</i>	78.0%	16.0%	-	5.0%		
<i>1943DECK01</i>	<i>lbs.</i>	454	85	-	25	235	0.42
	<i>%</i>	80.0%	15.0%	-	4.0%		
<i>2022STRUCTURE02</i>	<i>lbs.</i>	580	-	-	-	217	0.37
	<i>%</i>	100.0%	-	-	-		
<i>2031DECK01</i>	<i>lbs.</i>	430	90	-	30	231	0.42
	<i>%</i>	78.0%	16.0%	-	5.0%		

GGBFS: ground granulated blast-furnace slag, CM: cementitious material, W/CM: water/cement

Admixtures

Table 11 presents the target air content, slump height, and the volume of admixtures used in the MDT-approved concrete mixtures. Admixtures are incorporated into concrete to achieve specific performance characteristics, such as reducing water content, adjusting slump, delaying setting time while maintaining workability, accelerating early strength gain, minimizing air bubbles to enhance cohesion, and improving resistance to freeze-thaw damage. All concrete mixtures included mid- to high-range air-entraining agents (Admixture #1) and mid- to high-range water-reducing agents (Admixture #2). Additionally, high-range water-reducing agents (Admixture #3) were used in mixtures 1811DECK04, 1931DECK01, and 2031DECK01. A workability-retaining agent (Admixture #4), intended to maintain slump over time, was used in 1811DECK04 and 1931DECK01. Finally, a hydration-controlling agent (Admixture #5) was used exclusively in mixture 1811DECK04.

Base Mix Design

Two candidate concrete mixtures were proposed for the model-scale experiments conducted in the Subzero Research Laboratory (SRL). The first mixture consisted of 100% Portland cement, similar to mixture 2022STRUCTURE02. The second mixture included a blend of 85% Portland cement and 15% fly ash, following proportions similar to mixtures 1931DECK01, 1943DECK01, and 2031DECK01. The water-to-cement ratio was 0.43 for the fly ash mixture and 0.37 for the mixture without fly ash. Mix proportions for a 2.5 ft³ batch are presented in Table 12. All cement used in the mixes was sourced from the Trident Cement Plant, and the fly ash was obtained from the Genesee Generating Station. No chemical admixtures were incorporated into the concrete mix designs for this study.

Table 11. Aim of Air Contents, and Admixtures' Dosages of the Collected Mix Designs

Sample ID	Admix #1 Dosage	Admix #2 Dosage	Admix #3 Dosage	Admix #4 Dosage	Admix #5 Dosage	% Air Content
1811DECK04	0.8 oz/100# CM	5 oz/100# CM	8 oz/cy	2 oz/cy	45 oz/cy	6
1931DECK01	1-2 oz/100# CM	5-6 oz/100# CM	4-8 oz/100# CM	2-6 oz/100# CM		5.0-8.5
1943DECK01	0.8 oz/100# CM	6 oz/100# CM				6
2022STRUCTURE02	3.2 oz/cy	46 oz/cy				7.1
2031DECK01	1-2 oz/100# CM	6 oz/100# CM	6 oz/100# CM			7

Table 12. Mix Proportions for 2.5 cu. ft. Mix

Item	Item Type	Amount (lbs)	
		W/O Fly Ash	With Fly Ash
Water	-	19.8	21.4
Portland Cement	Type I/II Trident	52.9	41.4
Fly Ash	Trident Genesee	-	7.7
Fine Aggregate	O.D. BBB&T Concrete Sand	111.2	125.8
Coarse Aggregate		139.2	158.6
W/C ratio (%)	-	37	43

Two different concrete aggregates, sourced from Bozeman Brick and Tile and Bekaert Steel Fibers, were used in the mix designs. For each aggregate type, a representative gradation analysis was conducted, and the resulting grain size distribution curves are shown in Figure 76. In the mixtures 1931DECK01, 1943DECK01, and 2031DECK01, a conventional gradation type was employed using a combined aggregate ratio. As shown in Table 10, these mixtures contained 56% coarse aggregate and 44% fine aggregate by weight.

Concrete Aggregate Combined Gradation

Three optimization charts are required for developing an optimized concrete mix design: (1) the Coarseness Factor Chart, (2) the 0.45 Power Chart, and (3) the Percent Retained Chart. Each chart addresses a different aspect of aggregate gradation and its influence on concrete performance. The Coarseness Factor Chart, also known as the Shilstone Chart, is used to evaluate whether a

combined aggregate gradation falls within an optimized range. This chart illustrates the relationship between the coarseness factor (x-axis) and the workability factor (y-axis), both expressed as percentages. These factors can be calculated using defined aggregate properties and proportions, providing insights into the expected workability and packing characteristics of the mix.

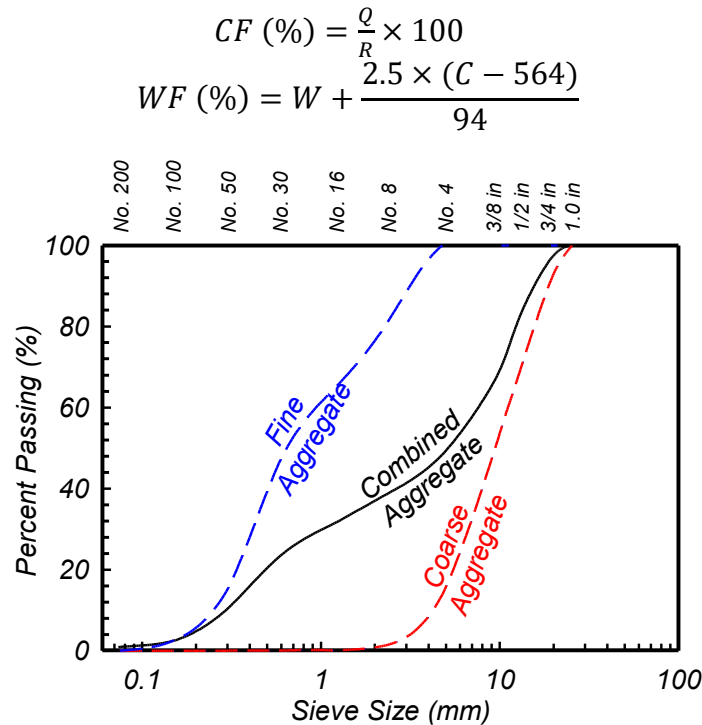


Figure 76. Individual Grain Size Distribution Curves

Where Q is the cumulative percentage retained on a 3/8-inch sieve, R is the cumulative percentage retained on the No. 8 sieve, W is the percentage passing the No. 8 sieve, and C is the cementitious material content in lb/yd³. Figure 77 illustrates the coarseness factor chart for the proposed concrete mix designs. Zone II is generally considered the region representing workable and durable mixes. Aggregate combinations that plot near the boundaries of, or outside, Zone II are more susceptible to placement challenges or long-term durability issues. As shown in the figure, both combined aggregates fall within Zone II. However, the concrete mix containing fly ash plots on the edge of the workability box, whereas the mix without fly ash falls outside the box, indicating that the fly ash-enhanced mix is likely to exhibit better workability.

The 0.45 power line method is commonly used to evaluate the gradation of combined aggregates and predict the potential for voids in concrete mixtures. In Figure 78(a), the 0.45 power line is plotted based on the nominal maximum aggregate size. A gradation curve that falls above the power line typically indicates a finer aggregate blend, while a curve below the line indicates a coarser blend. As shown in Figure 78(a), the grain size distribution of the combined aggregates generally follows the power line, with the portion passing the No. 30 sieve falling below the line. This allows space for cementitious materials within the mix, contributing to a denser and more workable concrete. The overall combined grading remains within ± 7 percentage points of the 0.45 power line, indicating a well-graded aggregate blend suitable for concrete production.

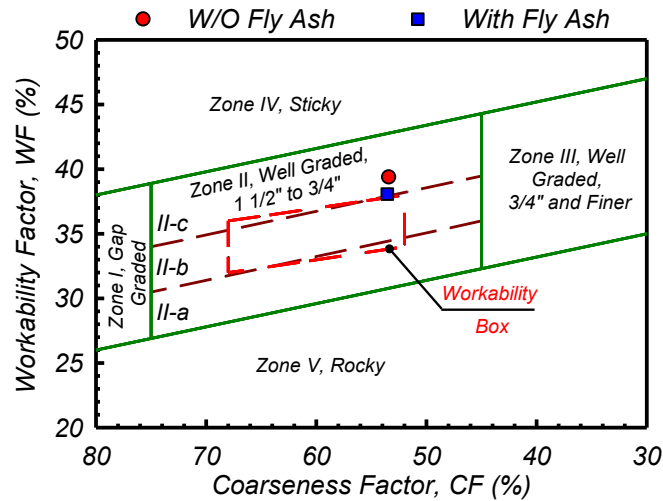


Figure 77. Coarseness Factor Chart of Concrete Mix Designs

The Individual Percent Retained chart, commonly referred to as a Haystack Plot, is used to evaluate the adequacy of combined aggregate sizes in a concrete mix. This method helps identify whether a mix is well-graded, highlighting potential deficiencies or excesses in specific size fractions. It also serves as an indicator of workability and water demand; mixes falling within an optimal range are typically associated with lower water requirements and improved performance. The chart is bounded by “High” and “Low” limit lines, which generally range between 18–22% and 5–12% retained, respectively. To minimize the risk of segregation, it is generally recommended that at least 13% of the combined aggregate be retained on any two adjacent sieves. Figure 78(b) illustrates the percent retained (y-axis) for each sieve size in the evaluated concrete mix. In this case, the upper and lower boundaries were set at 20% and 8%, respectively. As shown, the mix falls between these limits across all sieve sizes, indicating a well-graded aggregate structure. This suggests that the mix is likely to be workable and exhibit relatively low water demand.

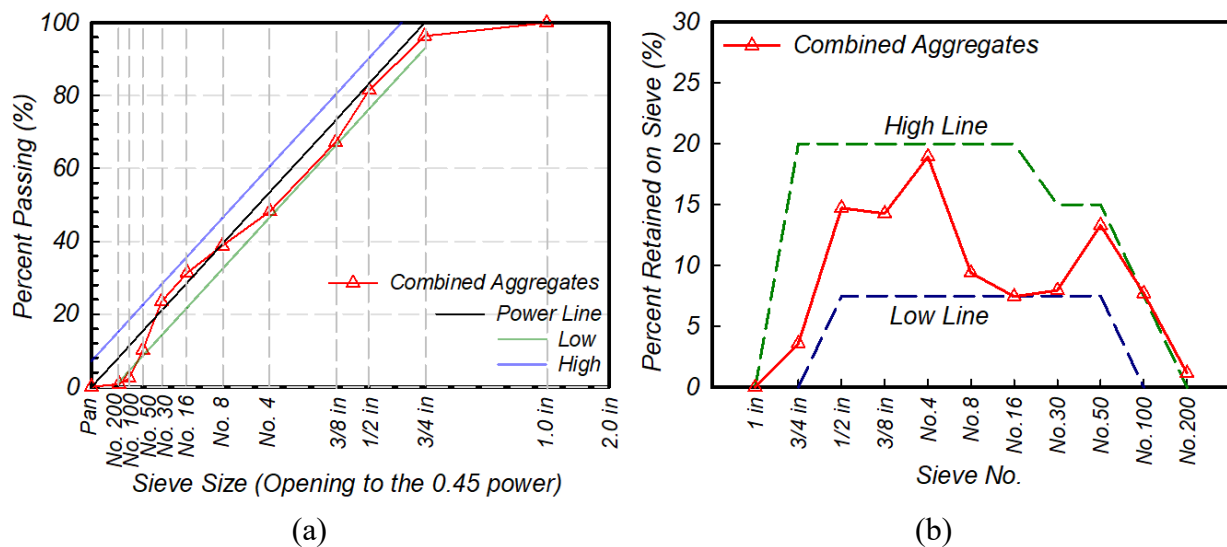


Figure 78. a) 0.45 Power Chart, and b) Percent Retained Chart of the Collected Mix Designs

Average 7- and 28-day compressive strengths are summarized in Table 13. Compressive strength tests were conducted in accordance with ASTM D-1633. The compressive strength of the MDT concrete mix designs were in the range of 3200 to 4200 psi for the 7-day curing time and 4990 to 5500 psi for the 28-day curing time. For the recommended concrete mixtures, a 7-day strength in the range of 2600 psi to 4000 psi was obtained, while the 28-day strength was in the range of 3400 psi to 4700 psi. The results were comparable to those approved by MDT. The results suggested that using fly ash as cementitious material could result in a lower strength, therefore, the mixture without fly ash will be used for the model-scale experiments. Figure 79 shows the concrete samples after failure.

Table 13. Average Compressive Strengths of the Collected and Proposed Concrete Mix Designs

Sample ID		Fly Ash (%)	Compressive Strength (psi)	
			7-day	28-day
<i>Collected</i>	<i>1811DECK04</i>	<i>0.0</i>	<i>3457</i>	<i>4990</i>
	<i>1931DECK01</i>	<i>16.0</i>	<i>4110</i>	<i>5547</i>
	<i>1943DECK01</i>	<i>15.0</i>	<i>3233</i>	<i>5237</i>
	<i>2022STRUCTURE02</i>	<i>0.0</i>	<i>4140</i>	<i>5440</i>
	<i>2031DECK01</i>	<i>16.0</i>	<i>4150</i>	<i>5210</i>
<i>Proposed</i>	<i>W/O Fly Ash</i>	<i>0.0</i>	<i>3967</i>	<i>4659</i>
	<i>With Fly Ash</i>	<i>15.0</i>	<i>2666</i>	<i>3471</i>



Figure 79. Two proposed Concrete Mixtures after 28-day Strength Test

Slump Test

Table 14 summarizes the results of the slump tests, which were conducted to evaluate the workability and consistency of the fresh concrete mixture. The tests were performed in accordance with ASTM C143, and the results are reported alongside corresponding measurements of concrete temperature, air content, unit weight, and yield.

Table 14. Properties of Proposed Concrete Mixture Designs

Sample ID	Fly Ash (%)	Slump (in)	Air (%)	Temperature (°F)	Unit Weight (pcf)	Yield (yd³)
<i>1811DECK04</i>	<i>0.0</i>	<i>5.0</i>	<i>6.1</i>	<i>63</i>	<i>141.1</i>	<i>27.2</i>
<i>1931DECK01</i>	<i>16.0</i>	<i>5.0</i>	<i>7.1</i>	<i>60</i>	<i>141.1</i>	<i>27.1</i>
<i>1943DECK01</i>	<i>15.0</i>	<i>4.0</i>	<i>8.5</i>	<i>70</i>	<i>139.7</i>	<i>-</i>
<i>2022STRUCTURE02</i>	<i>0.0</i>	<i>4.0</i>	<i>6</i>	<i>60</i>	<i>143.1</i>	<i>27.1</i>
<i>2031DECK01</i>	<i>16.0</i>	<i>3.5</i>	<i>7.3</i>	<i>68</i>	<i>140.1</i>	<i>27.8</i>
<i>W/O Fly Ash</i>	<i>0.0</i>	<i>5.0</i>	<i>-</i>	<i>-</i>	<i>-</i>	<i>-</i>
<i>With Fly Ash</i>	<i>15.0</i>	<i>1.7</i>	<i>-</i>	<i>-</i>	<i>-</i>	<i>-</i>

Thermal Conductivity and Resistivity

The thermal properties of the tested concrete were measured using a portable, battery-operated TEMPOS Thermal Properties Analyzer with a TR-3 sensor, which features a 100 mm-long, 2.4 mm-diameter needle (Figure 80 **Error! Reference source not found.**). The analyzer and sensor comply with ASTM D5334 and IEEE 442 standards. Concrete specimens were cylindrical, with a diameter of 100 mm (4 in.) and a height of 200 mm (8 in.). According to the equipment manual, a minimum of 10 mm of concrete surrounding the sensor in all directions is required to ensure accurate measurements. Thermal properties were measured under two conditions: (1) in the fresh state and (2) after seven days of curing. For the cured samples, a 4 mm (5/32 in.) hole was drilled into the concrete using a rotary hammer. The hole was cleaned with compressed air and filled with thermal grease (Arctic Silver 5 AS55-3.5G) to improve heat dissipation and ensure good thermal contact between the sensor and the concrete. The sensor needle was then inserted into the prepared hole for measurement. Thermal properties were not measured at 28 days of curing due to the difficulty of drilling into the fully cured concrete. Table 15 summarizes the thermal properties of the concrete mixtures in both fresh and cured states.



Figure 80. Thermal Test Setup

Table 15. Thermal Conductivity of Proposed Concrete Mix Designs

<i>Sample ID</i>	<i>Fly Ash (%)</i>	<i>Thermal Conductivity (W/m·K)</i>	
		<i>Fresh concrete</i>	<i>7-day curing</i>
<i>W/O Fly Ash</i>	<i>0.0</i>	<i>1.489</i>	<i>1.927</i>
<i>With Fly Ash</i>	<i>15.0</i>	<i>-</i>	<i>1.796</i>

The thermal conductivity of concrete depends on its water content, aggregate type and size, and overall material density. For saturated concrete, thermal conductivity typically ranges from 1.4 to 3.4 W/m·K.

Numerical Model Development and Validation

Experimental data from [Bowers \(2016\)](#), collected at the Virginia Tech Geotechnical Research Facility, was used to develop and validate a numerical simulation in COMSOL Multiphysics. After successful validation, the model was employed to conduct parametric studies aimed at identifying the most influential design parameters for a geothermal bridge deck system.

Overview of the Experiments (Bowers, 2016)

The thermal performance of a small-scale bridge deck deicing system was investigated by Bowers (2016) at the Virginia Tech Geotechnical Research Facility. Two experimental bridge deck models were constructed, each measuring 1.3 m (4.3 ft) in width, 3.05 m (10 ft) in length, and 0.254 m (10.4 in.) in depth. The experimental setup is shown in Figure 81(a). Heat exchanger pipes were embedded within the decks, with spacing of 30 cm (12 in.) on the left side and 20 cm (8 in.) on the right side of the model. The pipes had an inner diameter of 16 mm (0.62 in.) and an outer diameter of 22 mm (0.87 in.). A 20% glycol solution served as the circulating fluid, flowing at a rate of 15.1 L/m (1.2 gal/ft). System performance was monitored using multiple thermistors installed

within the deck to measure internal temperature distributions. The plan and cross-sectional layouts of the sensor placements are shown in Figure 81(b) and (c). The bridge deck models were cast using Virginia Department of Transportation (VDOT) Class A4 concrete, which has a minimum 28-day compressive strength of 27.6 MPa (4000 psi) and a maximum allowable permeability of 2500 coulombs. Figure 82 depicts the completed deck models after the concrete was poured into the two halves of the test specimens.

Weather Scenarios

In the study by Bowers (2016), various weather conditions were tested to evaluate the thermal performance of a geothermal bridge deck system. Two primary scenarios were examined: (1) a severe winter event designed to assess the impact of material properties and lower surface boundary conditions on the deck's heating behavior, and (2) a cold weather period followed by snowfall. The second scenario served a dual purpose: first, to evaluate the boundary conditions of the thermal model when the deck was initially clear and exposed to environmental radiation and convection; and second, to analyze the snowmelt process as snowfall occurred. These test conditions were selected to reflect the climate patterns typical of both the project site in Blacksburg, Virginia, and Montana. Table 16 summarizes the selected weather parameters and the experimental snow melting results under these conditions.

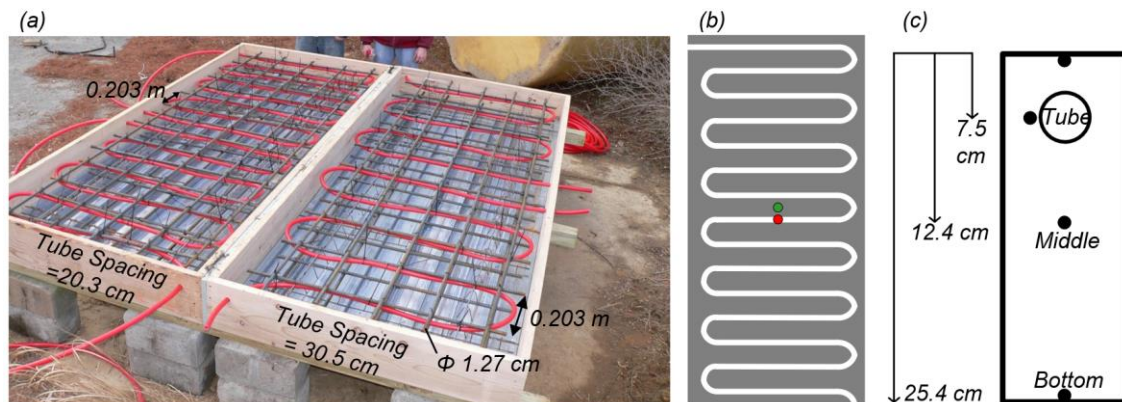


Figure 81. (a) Layers of reinforcement and the configuration of heat exchanger pipes, (b) Location of studied temperature sensors (plan view), and (c) Location of studied temperature sensors deck (cross section) (Bowers, 2016)

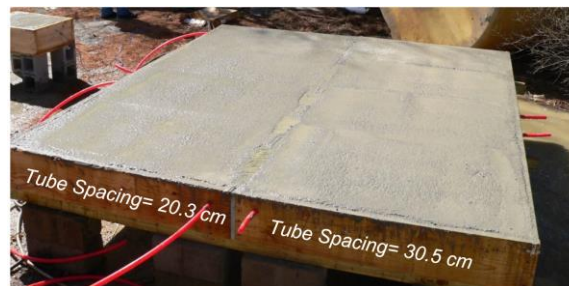


Figure 82. Photograph showing the poured concrete into the deck frame works (Bowers, 2016)

Severe Winter Weather (February 20-22, 2015)

On February 16–17, 2015, a snowstorm impacted Blacksburg, Virginia, during which the geothermal heating system was not operational. As a result, approximately 20 cm (7.87 in.) of snow accumulated on the bridge deck surface.

Table 16. Selected weather parameters and experimental test results of snow melting

<i>Cold event (time)</i>	<i>Severe winter event (20-23 February 2015)</i>	<i>Moderate winter event (25-27 February 2015)</i>
<i>Ambient temperature (°C)</i>	-18 to 10 (-0.4 °F to 50 °F)	-7 to 6 (19.4 °F to 42.8 °F)
<i>Depth of snow (cm)</i>	20 (7.87 inches)	7.6 (3 inches)
<i>Starting time of operation</i>	14:30, 2/20/2015	In operation
<i>Circulating fluid temperature (°C)</i>	3.8 to 7.2 (38.8 °F to 45.0 °F)	6 to 9.6 (42.8 °F to 49.3 °F)
<i>Melting time (Hours)</i>	48.5	31.5

Figure 83 presents the variation of top surface temperatures for both heated and non-heated decks, along with air temperature, cumulative snowfall, and surface conditions during the heating operation. The heating system was activated at 14:30 on February 20, 2015, following the storm. At the time of activation, the deck surface temperature was -18 °C (-0.4 °F). Figure 83(a) taken at 17:00 (2.5 hours after heating began and prior to further snowfall), shows a remaining snow depth of 16.5 cm. After 9 hours of continuous heating, the average surface temperature of the heated deck exceeded the freezing point, despite a 15 °C (59 °F) drop in ambient temperature. By 10:00 on February 21, 19.5 hours into system operation, Figure 83(b) shows that the heated deck surface remained above freezing throughout the storm. At that time, snow depths on the non-heated and heated decks were 22.9 cm (9 in.) and 20.3 cm (8 in.), respectively. One hour later, the non-heated deck accumulated up to 24.1 cm (9.5 in.) of snow, whereas the heated deck maintained a reduced depth of 19.7 cm (7.7 in.), indicating that the snow melt rate exceeded the accumulation rate. After 24.5 hours of operation (15:00, February 21), snow depths were measured at 29.8 cm (11.7 in.) on the heated deck and 24.1 cm (9.5 in.) on the non-heated deck, as shown in Figure 83(c). By 19:30 (29 hours of operation), snow depths reached 30.5 cm (12 in.) on the non-heated side and 21.6 cm (8.5 in.) on the heated side. These results suggest improved melting performance as ambient temperatures rose. Figure 83(d), taken at 7:30 on February 22 (after 41 hours of heating), shows a snow depth of 11.4 cm (4.5 in.) on the heated deck. Finally, Figure 83(e) captured after 48.5 hours of heating at 15:00, reveals a snow-free surface, confirming the system's ability to clear the deck. Notably, the deck surface temperature increased rapidly once the snow was fully removed.

Moderate Winter Event (February 25-26, 2015)

Bowers (2016) evaluated the performance of a bridge deck deicing system during a moderate snowstorm that occurred on February 25–26, 2015. Figure 84. presents data collected during the event, including surface temperatures of both heated and unheated bridge decks, ambient air temperature, cumulative snowfall, and surface conditions of the test deck. The geothermal heating system on the treated side was activated prior to the onset of the cold weather. During the period of system operation, ambient temperatures ranged from -7 °C (19.4 °F) to 6 °C (42.8 °F). As shown in Figure 84, approximately 7.6 cm (3 inches) of snow accumulated during the event, with an average ambient temperature of -2.5 °C (27.5 °F).

Figure 84(a) was taken 2.5 hours after the onset of a snowstorm, at 2:30 AM on February 26, 2015. The results indicated that the geothermal system successfully maintained the bridge deck surface temperature above the freezing point (0°C or 32°F) throughout the storm. As reported by Bowers (2016), at this time, approximately 60% of the heated deck surface remained free of snow, demonstrating the system's ability to prevent snow accumulation. Further inspection revealed that roughly half of the residual snow was due to wind-blown debris landing on the deck, while the other half accumulated in areas between the heat exchanger pipes where localized heating was less effective. In contrast, the surface temperature of the non-heated deck dropped below freezing, leading to significant snow accumulation. Figure 84(b) taken at 7:30 AM on the same day, 7.5 hours after the storm began, shows that the heated side of the bridge remained entirely free of snow, while the non-heated side was fully covered. The recorded snow depth on the non-heated deck at that time was 7.6 cm.

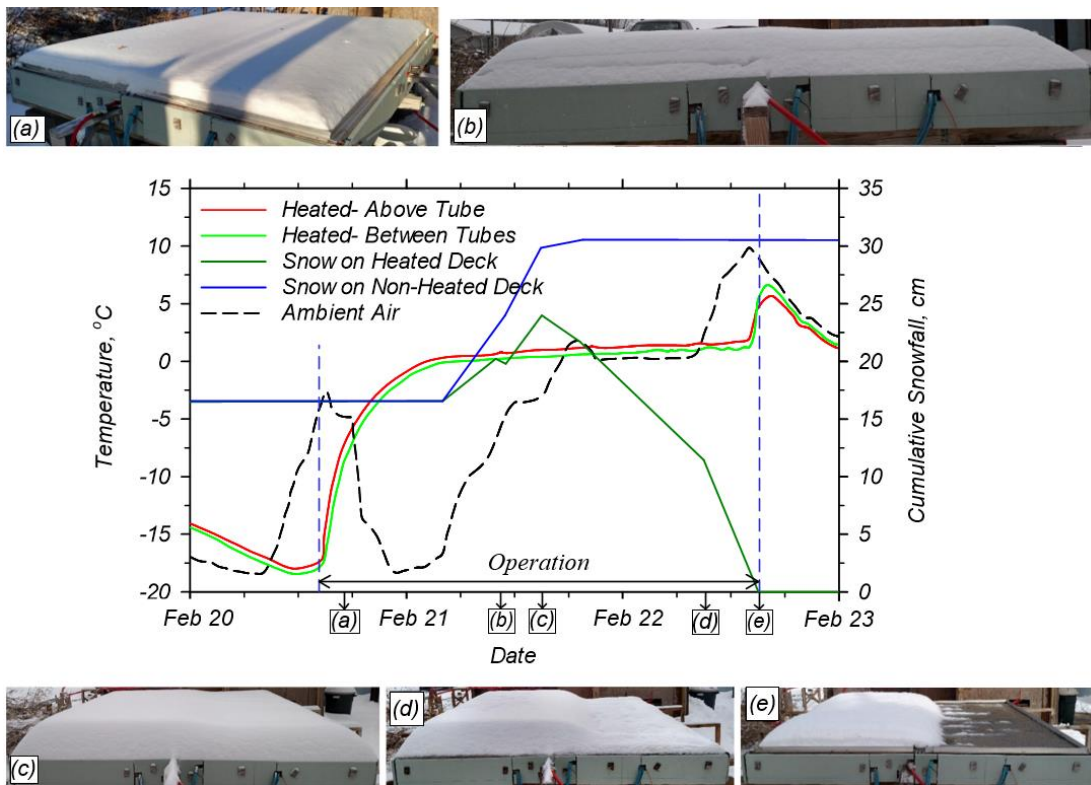


Figure 83. Recorded surface temperature of the heated and non-heated decks, ambient temperature, cumulative snowfall, and photo of the deck model surface during the storm after: (a) 2.5 hours (b) 19.5 hours, (c) 24.5 hours, (d) 41 hours, (e) 48.5 hours of heating system operation (Bowers, 2016)

Numerical Simulation of Bridge Deck Snow Melting/De-icing System

Modeling the bridge deck deicing process is inherently complex due to the interplay of multiple heat transfer mechanisms and variable weather conditions. A ground-source bridge deck deicing system involves conduction, convection, solar and thermal radiation, as well as the latent heat associated with snow melting. This section presents the results of a three-dimensional numerical model developed to evaluate the performance of a geothermal bridge deck deicing system. The model was first validated using experimental data from bridge deck heating tests conducted by

Bowers (2016). Upon validation, the model was applied to assess the performance and feasibility of using geothermal energy for bridge deck deicing under typical Montana winter conditions.

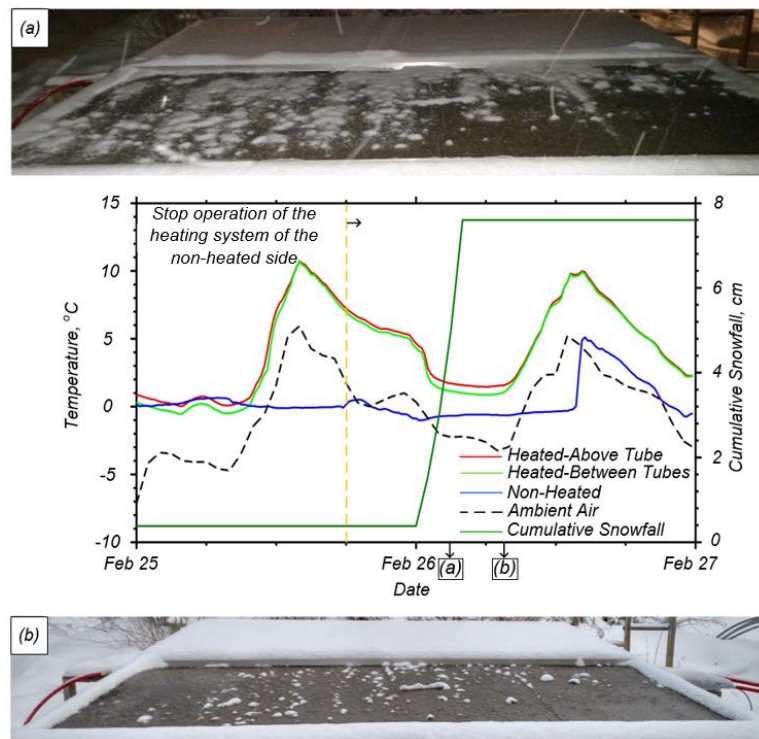


Figure 84. Recorded surface temperature of the heated and non-heated decks, ambient temperature, cumulative snowfall, and photo of the deck surface condition during the test: (a) 2.5 hours, and (b) 7.5 hours after the storm began (Bowers, 2016).

Bridge Deck Heating and Snow Melting Process

Modeling the bridge deck deicing process is complex due to the interaction of multiple heat transfer mechanisms and the variability of weather conditions during system operation. As illustrated in Figure 85, several key heat transfer processes contribute to the thermal performance of geothermal bridge deck systems. Heat exchange between the bridge deck and its surroundings occurs through four primary mechanisms: conduction (within the concrete and embedded heating elements), convection (with ambient air and wind), radiation (including both solar and thermal radiation), and precipitation heat flux (associated with snow, rain, or ice interacting with the surface). Accurately capturing these dynamic interactions is essential for reliable modeling and performance prediction of geothermal deicing systems.

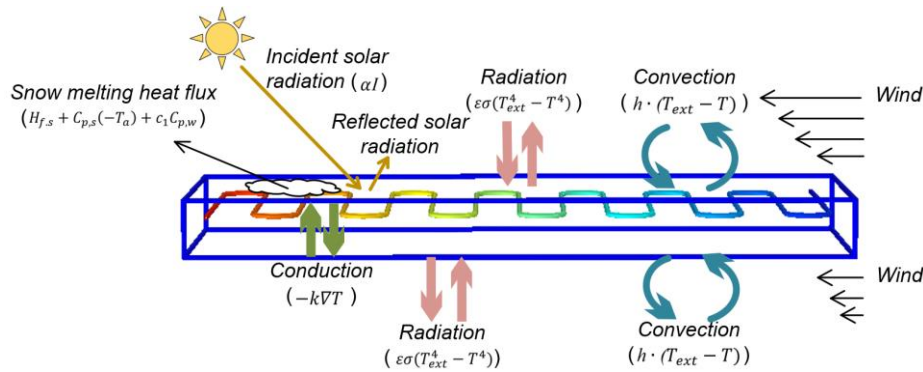


Figure 85. Heat transfer mechanisms involved in bridge heating and snow melting process

Conductive Heat Transfer: Heat transfer by conduction involves the transfer of thermal energy from regions of higher temperature to regions of lower temperature due to molecular interactions, driven by a temperature gradient (Thompson, 2013). In a bridge deck deicing system, conduction primarily occurs between the circulating heat exchanger fluid and the inner pipe walls, and subsequently between the pipe surface and the surrounding concrete. This mechanism is critical for distributing heat uniformly across the deck. The governing differential equation for heat conduction in solids is presented below.

$$\rho C_p \frac{\partial T}{\partial t} + \nabla \cdot q = Q = -k \nabla T \quad (4)$$

where ρ is the density (kg/m^3), C_p is the heat capacity at constant pressure (J/(kg.K)), T is the absolute temperature (K), $\frac{\partial}{\partial t}$ is time derivatives operator, q is conductive heat flux vector (W/m^2), k is the thermal conductivity coefficient (W/m.K), ∇T is the temperature gradient, and Q is the heat source (or sink) (W/m^3). The relationship between the heat flux vector and temperature gradient is defined by the thermal conductivity coefficient in $q = -k \nabla T$, which is Fourier's law of heat conduction. For insulated boundary conditions, such as those caused by snow accumulation acting as a thermal barrier on the bridge deck surface, the heat flux at the surface is considered to be zero, meaning no heat is lost through the boundary. Under these assumptions, the governing heat transfer equation is defined as follows:

$$q = (-k \nabla T) = 0 \quad (5)$$

Convective Heat Transfer: Convective heat transfer occurs through the bulk motion of a fluid and can be classified as either natural or forced convection (Brandl, 2006). Natural convection arises from temperature or concentration gradients within the fluid, causing motion without the influence of external forces. In contrast, forced convection results from external influences such as wind or groundwater flow, which enhance fluid motion and thus heat transfer. In the context of bridge deck de-icing systems, convective heat transfer can occur on surfaces exposed to the atmosphere and between the circulating fluid and the inner walls of the heat exchanger pipes. This process is governed by Newton's law of cooling, which is expressed as:

$$-n \cdot q = h \cdot (T_{ext} - T_s)$$

where n is the normal vector on the boundary, h is the convective heat transfer coefficient ($\text{W/m}^2 \cdot \text{K}$), T_s is the surface temperature (K), and T_{ext} is the external temperature. T_{ext} for the top and bottom surfaces is either ambient temperature or mean radiant temperature (K). The

convective heat transfer coefficient, h , depends on several factors including boundary layer characteristics (e.g., wind speed and ambient temperature), the nature of fluid motion, and fluid properties (Chowdhury, 2019). According to William (1973), appropriate adjustment of h is essential based on the heat transfer area's size, wind exposure, and the height at which wind speed is measured.

Radiative Heat Transfer: Radiative heat transfer occurs within pore spaces through the movement of electromagnetic waves, or equivalently, photons. In the context of bridge heating, radiative transfer plays a significant role in overall thermal behavior. The amount of heat transferred via radiation in a hydronic heating system can be influenced by various factors, including ambient temperature, cloud cover, surface emissivity, geographic location (latitude and longitude), time of day, and time of year. These parameters collectively determine the energy that is emitted or absorbed by the bridge deck through radiation. The radiative out-of-plane heat flux can be calculated using the following equation:

$$-n \cdot q = \varepsilon \sigma (T_{ext}^4 - T_s^4)$$

where ε is the surface emissivity, σ is the Stefan-Boltzmann constant (a predefined physical constant, $5.67 \times 10^{-8} \text{ (W} \cdot \text{m}^2/\text{K}^4)$), T_{ext} for the top and bottom surfaces is either ambient temperature or mean radiant temperature (K). To compute the longwave thermal radiation, an accurate determination of T_{ext} is necessary. The conditions that need to be considered in calculating T_{ext} are described in subsequent sections.

Snow Melting Heat Flux: Various mathematical models have been developed to describe the snow melting process, encompassing both steady-state and transient conditions (e.g., Chapman et al., 1952; Rees et al., 2002; Liu, 2005; Wang and Chen, 2009). Chapman et al. (1952) proposed a one-dimensional steady-state model to calculate the amount of heat required for snow melting. More recent studies have shifted toward transient models to better capture the dynamic behavior of snow melting under realistic operating conditions for bridge decks. Rees et al. (2002) introduced a two-dimensional transient model that couples heat and mass transfer processes during snowmelt. Their model dynamically determines the surface condition at each time step by calculating the mass distribution of snow, ice, and liquid water. However, due to the computational complexity of modeling surface conditions in detail, Liu (2005) refined Rees's approach by developing a more efficient model capable of accounting for a broader range of weather scenarios. Additionally, Wang and Chen (2009) proposed a theoretical model that incorporates capillary effects within the snow layer, improving the accuracy of thermal conductivity estimates as snow transitions through melting phases.

In this study, the approach proposed by Chapman et al. (1952) was employed to estimate the heat flux required for snow melting. While the model may not capture the full complexity of all snow melting processes, it offers a reasonable approximation of the heat demand needed to melt falling or accumulated snow on the bridge deck surface. The total heat flux (q_0) required at the deck's top surface is mathematically formulated as follows:

$$q_0 = q_s + q_m + A_r(q_h + q_e)$$

where q_s is the total sensible heat flux (W/m^2), q_m is the latent heat of fusion of snow (W/m^2); A_r is snow free area ratio; q_h is the sum of convective and radiative heat flux (W/m^2); and q_e is the evaporative heat flux (W/m^2).

The sensible heat flux refers to the energy required to raise the temperature of snow, assumed to fall at ambient temperature, to the freezing point, and subsequently increase the temperature of the resulting meltwater to a specified liquid film temperature. The corresponding sensible heat flux (q_s) can be obtained as follows:

$$q_s = \rho_{water} s [c_{p,snow} (t_s - T_a) + c_{p,water} (t_f - t_s)]$$

where ρ_{water} is the density of water (kg/m³), s is the snowfall rate in expressed in water equivalent (m/s), $c_{p,snow}$ is the specific heat capacity of snow (J/(kg.K)), t_s is the melting temperature (0 °C), T_a is the ambient temperature (°C), $c_{p,water}$ is the specific heat capacity of water (J/(kg.K)), and t_f is the liquid film temperature (°C). According to ASHRAE 1999, the temperature of the liquid film is usually taken as 0.56 °C (33 °F).

The heat flux required to be absorbed during the phase change, latent heat of fusion of snow (q_m), is expressed by the following equation:

$$q_m = \rho_{water} s h_{if}$$

where h_{if} is the heat of fusion of the snow, usually taken as 3.3×10^5 J/kg.

Under snow-free conditions, the heat is being transferred from the surface to the atmosphere through convection and radiation (q_h) mechanisms. These terms have been previously described in detail. The energy required to evaporate water from the surface (q_e) is defined as follows:

$$q_e = (530.84V + 649.61)(P_{wv} - P_{av}) h_{fg}$$

where V is the wind speed (m/s), P_{wv} is partial pressure of water vapor in ambient conditions (Pa), taken as 636.6 kPa, P_{av} is partial pressure of water vapor in saturated air film on the surface (Pa), taken as 613.28 kPa, and h_{fg} is the heat of vaporization (J/kg) (enthalpy difference between saturated water vapor and saturated liquid water), taken as 2.257 J/kg.

The snow free area ratio (A_r) in the equation presented by Chapman et al, (1952) represents the ratio of the uncovered, or free, area to the total pavement area. $A_r=1$ represents a snow-free surface condition, and $A_r=0$ means the entire surface is covered with the snow.

A few assumptions must be considered to use the Chapman et al, (1952) equation. The assumptions applied by Bowers (2016) in the use of the Chapman et al, (1952) equation are as follows. A description of the errors that resulted from these assumptions in the calculation of snow melting heat flux and the related correction methods can be found in the study by Bowers (2016).

- 1) All three processes of snow melting, heating the snow to freezing, melting, and heating the liquid film, happen instantaneously.
- 2) The melted snow will be heated to a specific point and will then disappear (perfect drainage).
- 3) Material and thermal properties of snow are independent of time and space.

Bowers (2016) evaluated the performance of a snow melting system during a snowstorm and described how varying conditions relate to the applied heat flux at the bridge deck surface. Three distinct operational conditions were identified based on the balance between heat input and

snowfall rate. In Condition 1, if the energy transferred to the deck surface is sufficient to melt the snow immediately upon contact, snow does not accumulate. The required surface heat flux in this case is calculated by multiplying the snowfall mass rate by the latent heat of fusion of snow. However, convective and radiative heat losses still occur and must be accounted for in the overall energy balance. In Condition 2, although the heat input is enough to melt snow, the melting rate does not keep pace with the snowfall rate, resulting in gradual snow accumulation. Here, the total snow melting flux includes both the latent heat required for melting and the conductive heat transferred into the accumulating snow layer. In Condition 3, the energy supplied to the surface is insufficient to melt the incoming snow, and snow begins to accumulate and cover the deck. Under this scenario, the heat flux at the surface is effectively zero, corresponding to a Neumann boundary condition.

The methodology employed by Bowers (2016) for interpreting numerically obtained results when applying the snow melting heat flux equation to the top surface of a bridge deck model is illustrated in Figure 86. When the snow melting flux is applied, any portion of the deck with a surface temperature above 0 °C (32 °F) initiates snow melting. Conversely, areas with surface temperatures below freezing are expected to accumulate snow. In such cases, the model can be rerun under the assumption that the heat transfer rate is insufficient to melt snow, and the boundary heat flux is therefore set to zero. If the deck surface temperature remains below 0 °C (32 °F) under a Neumann boundary condition, this corresponds to Condition 3, in which no snow melting occurs. When the surface temperature is above freezing, Condition 2 applies, indicating that snow melting is occurring, but the surface is not completely cleared of snow. Under Conditions 1 or 3, the model provides accurate predictions for both temperature and energy values. For Condition 2, the results remain valid until the surface temperature drops below freezing again, at which point snow begins to accumulate and the actual heat flux declines toward 0 W/m². If the surface temperature remains above 0 °C (32 °F) after applying the Neumann boundary condition, the model suggests that snow is melting, but at a rate slower than the snowfall accumulation rate.

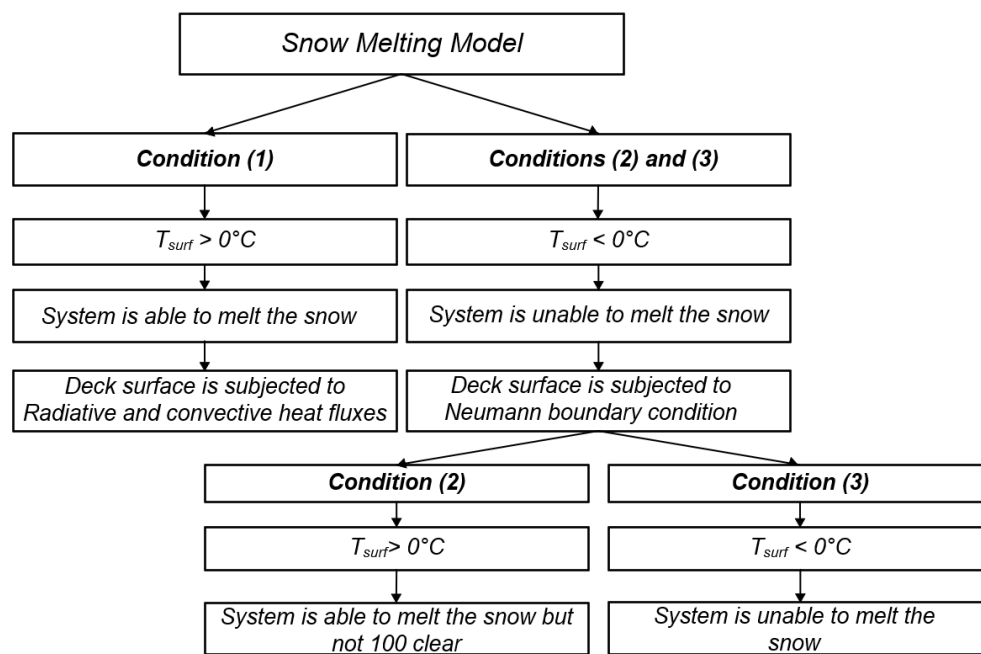


Figure 86. Interpretation of snow melting model proposed by Bowers (2016)

Boundary Conditions

The numerical model was developed using boundary and initial conditions that mirrored the experimental setup described by Bowers (2016). Initial conditions across all domains of the model were defined based on the two previously described weather scenarios. Distinct boundary conditions were applied to the top and bottom surfaces of the bridge deck model, depending on the specific heating scenario being simulated. This section outlines the key boundary condition variables that significantly influenced the simulation outcomes.

Thermal Radiation: For modeling thermal radiation from the bridge deck surface, two critical parameters must be defined: the surface emissivity constant (ε) and the external temperature (T_{ext}). Emissivity quantifies the efficiency of a surface in emitting thermal radiation compared to a perfect black body at the same temperature (Howell et al., 2020). According to a study by Sen and Roesler (2019), the emissivity of concrete ranges from 0.70 to 0.90, depending on surface properties and condition.

T_{ext} needs to be pre-computed and specified as a time-varying, or unsteady, parameter. Also, the external temperature is not necessarily equal to the ambient temperature (ASHRAE, 2013). According to ASHRAE (2013), the external temperature is equal to the mean radiant temperature (TMR) which is defined as the equivalent black body temperature of the surroundings of the snow melting system. Different models have been proposed for mean radiant temperature (T_{MR}) (e.g., Ramsey et al. 1982; Martin and Berdahl 1984). The proposed model by Ramsey et al. (1982) is as follows:

$$T_{MR} = [T_{cloud}^4 - F_{sc} + T_{sky\ clear}^4(1 - F_{sc})]^{1/4}$$

where F_{sc} is the cloud coverage, $T_{sky\ clear}$ is the equivalent blackbody temperature of the clear sky, and T_{cloud} is the cloud temperature. The variable $T_{sky\ clear}$ is obtained using the following:

$$T_{skyclear} = T_a - [1.1058 \times 10^3 - 7.562(T_a) + 1.333 \times 10^{-2}(T_a)^2 - 31.292\phi + 14.58\phi^2]$$

where T_a is the ambient temperature (K) and ϕ is relative humidity of the air.

The part of the sky that is covered with clouds is assumed be at T_{cloud} (K), the temperature at the base of the clouds. The cloud base height is assumed to be 3048 m (10000 ft), and according to altitude, the temperature decreases 6.38k per 1000 m (3281 ft). Thus, the temperature of the clouds at 3048 m (10000 ft) is computed as follows:

$$T_{cloud} = T_a - 19.4,$$

To estimate the sky temperature (T_{sky}) using Martin and Berdahl's (1984) model, a set of equations for monthly average clear sky emissivity ($\varepsilon_{skyclear}$), cloud emissivity (ε_{cloud}), and cloud factor (I_i) must be set. The monthly average clear sky emissivity ($\varepsilon_{skyclear}$) is calculated based on the following equation:

$$\varepsilon_{skyclear} = 0.711 + 0.56\left(\frac{T_{dp}}{100}\right) + 0.73\left(\frac{T_{dp}}{100}\right)^2 + 0.013 \cos\left[2\pi \frac{t_h}{24}\right] + 0.00012(P - 1000)$$

where T_{dp} is the dew point temperature, °F or °C, t_h is the hour of the day, and P is the station pressure in millibar. The cloud emissivity (ε_{cloud}) is calculated by:

$$\varepsilon_{cloud} = \varepsilon_{skyclclear} + (1 - \varepsilon_{skyclclear}) \sum_i n_i \varepsilon_{c,i} \Gamma_i$$

where n_i is the fractional area of the sky covered at the i^{th} level, $\varepsilon_{c,i}$ is the hemispherical emissivity of the cloud at the i^{th} level, and Γ_i is the cloud factor at i^{th} level. According to Bowers (2016), the low and mid-level clouds are generally opaque and have an emissivity value of 1, whereas the emissivity values for high-level clouds are around 0.4. The cloud factor (Γ_i) is defined by the following equation:

$$\Gamma_i = e^{-h_i/h_o}$$

where h_i is the cloud base height, and h_o is the reference base height (8.2 km).

Finally, the sky temperature (T_{sky}) is calculated by the following equation:

$$T_{sky} = T_a \cdot \varepsilon_{cloud}^{1/4}$$

Liu (2005) compared two sky temperature prediction models, those proposed by Ramsey et al. (1982) and Martin and Berdahl (1984), and found that the model by Martin and Berdahl provided more accurate estimations. According to ASHRAE (1999), the Ramsey et al. model significantly underestimates sky temperature, particularly under conditions of high relative humidity.

Solar Radiation: Solar radiation from the sun can be estimated by calculating the total direct incident radiation on a horizontal surface (I) and accounting for the surface's solar absorptance (α). Based on the sun's position in the sky throughout the year, the intensity of direct solar radiation on a given surface can be determined. The equation below provides the formula used to estimate solar radiation received by the surface.

$$-n \cdot q = \alpha I \quad (6)$$

The direct component of solar radiation can be calculated theoretically based on the Air Mass (AM) value at a given location using the following equation (Duffie and Beckman, 1994):

$$I = 1.353 \times 0.7^{(AM^{0.678})} \quad (7)$$

where the Air Mass can be determined using the cosine of solar zenith angle (θ):

$$AM = \frac{1}{\cos \theta} \quad (8)$$

The absorptivity coefficient (α) used in solar radiation calculations depends on the surface condition. According to Levinson and Akbari (2001), the solar absorptance of concrete ranges from 0.23 to 0.59. They also noted that concrete exhibits maximum solar reflectance immediately following a fresh snowfall.

Convection: As previously discussed, convective heat transfer occurs through two primary mechanisms: forced convection and free (or natural) convection. The impact of each mechanism is closely linked to the convective heat transfer coefficient. According to Bergman et al. (2011), the range of convective coefficients for free convection is significantly lower than that for forced convection. In the absence of wind, the effects of natural convection were incorporated into the

numerical model developed by Liu (2005). Numerous laboratory experiments have been conducted to determine heat transfer coefficients under both forced and natural convection conditions. Generally, the following equation is used to calculate the convective heat transfer coefficient (h_c) for both the top and bottom surfaces of the bridge deck model:

$$h_c = N_u \frac{k_f}{L} \quad (9)$$

where the N_u is the Nusselt number, k_f is the thermal conductivity of the fluid, and L is the characteristic length. In the study by Bejan (2013), the characteristic length was defined as the ratio of surface area to perimeter. As noted by Bowers (2016), a conservative approach is to use the shortest dimension of the deck model as the characteristic length when the airflow direction is unknown. Incropera et al. (2006) presented the following equations for calculating the free convection heat transfer coefficient (h):

$$h = \begin{cases} \frac{k_a}{L} 0.54 Re_L^{1/4} & \text{if } T > T_{ext} \text{ and } 10^4 \leq Re_L \leq 10^7 (\text{laminar flow}) \\ \frac{k_a}{L} 0.15 Re_L^{1/3} & \text{if } T > T_{ext} \text{ and } 10^7 \leq Re_L \leq 10^{11} (\text{turbulent flow}) \\ \frac{k_a}{L} 0.27 Re_L^{1/4} & \text{if } T \leq T_{ext} \text{ and } 10^5 \leq Re_L \leq 10^{10} (\text{turbulent flow}) \end{cases} \quad (10)$$

where the Re_L is the Reynolds number.

The average convective heat transfer coefficient for external forced convection on a horizontal surface can be computed by the following equations (Wetty et al., 2014):

$$h = \begin{cases} 2 \frac{k_a}{L} \frac{0.338 P_r^{1/3} Re_L^{1/2}}{(1 + (\frac{0.0468}{P_r})^{2/3})^{1/4}} & \text{if } Re_L \leq 5 \times 10^5 (\text{laminar flow}) \\ 2 \frac{k_a}{L} P_r^{1/3} (0.037 Re_L^{4/5} - 871) & \text{if } Re_L > 5 \times 10^5 (\text{turbulent flow}) \end{cases} \quad (11)$$

where P_r is the Prandtl number of air which according to ASHRAE (2013) can be considered to be 0.7.

Model Development

A series of three-dimensional numerical simulations of a bridge deck deicing system were conducted using the finite element software COMSOL Multiphysics. The experiments performed by Bowers (2016) were used to validate the numerical model. Key components of the deicing system, including the circulating fluid, heat exchanger pipes, and concrete deck, were explicitly represented in the simulation. One-dimensional (1D) linear elements were used to model fluid flow and heat transfer within the heat exchanger pipes. Flow rate, pressure, and temperature were modeled as average cross-sectional values, varying only along the pipe length. Pressure losses in the piping system were calculated using friction factors, and pipe wall thickness and thermal conductivity were incorporated by assigning external wall resistance.

Model Geometry and Material Properties: The baseline configuration and meshed model geometry of the bridge deck are shown in Figure 87(a) and (b), respectively. The geometric dimensions and material properties used in the simulation are summarized in Table 17, based on data from Bowers (2016). The heat exchanger pipes were modeled using 1D linear elements with non-isothermal flow and heat transfer modules applied. Although rebar was not explicitly modeled, its influence

was accounted for by dividing the concrete deck into three vertical zones. The top and bottom zones represented rebar-reinforced concrete, while the middle zone represented plain concrete. The material properties for each zone were calculated as volumetric averages of concrete and steel reinforcement, as presented in Table 17. **Error! Reference source not found..**

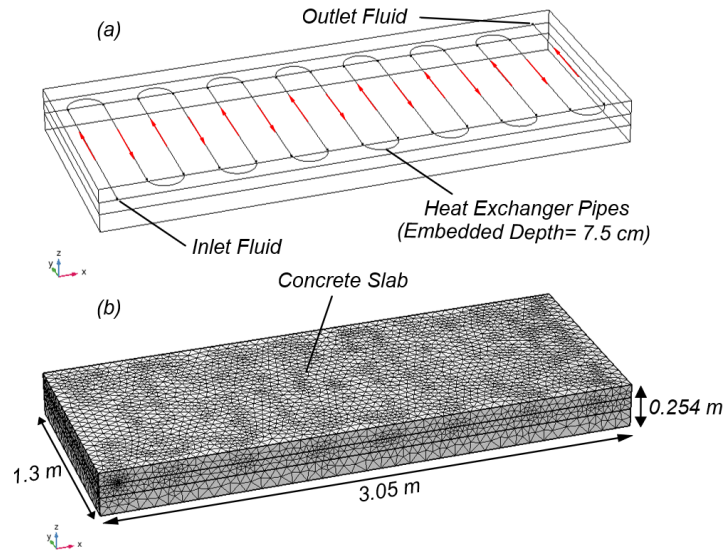


Figure 87. (a) The bridge deck model configuration, (b) Meshed 3D model

Table 17. List of the material properties of the experimental and numerical models (Bowers, 2016)

Parameter	Experimental	Numerical
<i>Bridge Deck Dimensions</i>		
Length (m)	3.0	3.0
Width (m)	1.3	1.3
Height (cm)	25.4	25.4
Depth of circulation pipes (cm)	7.4	7.4
<i>Circulation Fluid (20% Glycole)</i>		
Flow rate (L/m)	15.1	15.1
Dyncamic Viscosity (mPa.s)	4.8	4.8
Thermal conductivity (W/m.k)	0.4	0.4
Specific heat capacity (J/kg.k)	3538.0	3538.0
Density (Kg/m ³)	1070.0	1070.0
<i>Concrete</i>		
Thermal conductivity (W/m.k)	3.0	3.0
Specific heat capacity (J/kg.k)	880.0	880.0
Density (Kg/m ³)	2360.0	2360.0
<i>Concrete/Rebar Zones</i>		
Top height (cm)	-	7.40
Bottom height (cm)	-	10.20
Top thermal conductivity (W/m.k)	-	3.65
Top specific heat capacity (J/kg.k)	-	873.82
Top density (Kg/m ³)	-	2443.80
Bottom thermal conductivity (W/m.k)	-	3.48
Bottom specific heat capacity (J/kg.k)	-	875.42
Bottom density (Kg/m ³)	-	2422.10

Model Validation

Two experimental test conditions were selected for model validation, each designed to isolate and evaluate specific boundary conditions: (1) a bridge deck with accumulated snow on the surface, and (2) a bridge deck exposed to cold weather conditions (with no initial snow) followed by a snowfall event. Given snow's extremely low thermal conductivity and strong insulating properties, the first model simulated a fully insulated bridge deck, with both top and side surfaces insulated. This configuration was used to assess the influence of material properties and surface boundary conditions on the heating process, without considering the snow melting process. The second model was developed to simulate a more dynamic condition: initially, the bridge deck was exposed to cold ambient temperatures without snow, allowing for direct interaction with environmental factors such as radiation and convection. Snowfall was then introduced during the later stage of the simulation. This scenario served two purposes: (1) to validate the model's treatment of thermal boundary conditions during snow-free conditions, and (2) to assess the model's performance in simulating the snowmelt process as snow accumulated on the deck.

First Scenario - Severe Winter Event

The accuracy of the numerical model was validated against measured data collected during a severe winter event. As previously described, nearly 20 cm of snow accumulated on the bridge deck surface during this period. Due to the insulating effect of the snow, the top surface and the edges of the bridge deck model were treated as insulated boundaries, with no heat flow, modeled using Neumann boundary conditions. Additionally, the bottom surface of the deck was exposed to thermal radiation effects by applying the ambient air temperature as the boundary condition.

Figure 88 compares the measured and predicted variations of inlet and outlet fluid temperatures during system operation. The temperature trends observed in the numerical simulations closely matched the experimental results reported by Bowers (2016), demonstrating good model validation. The difference between the inlet and outlet fluid temperatures reflects the system's heat absorption capability. The amount of thermal energy transferred to the bridge deck can be calculated by multiplying the circulating fluid's density, specific heat capacity, volumetric flow rate, and the temperature differential between the inlet and outlet. As shown in the figure, the temperature difference between the inlet and outlet decreased over time, indicating a corresponding reduction in the rate of heat transfer to the deck. The maximum and minimum observed temperature differentials were 2.08 °C (35.7 °F) and 0.33 °C (32.6 °F), respectively. The largest deviation between the predicted and measured values occurred between minutes 10 and 80, likely due to uncertainties in assumed material properties, such as the volumetric averages of concrete and reinforcing steel, and the boundary conditions applied to the bottom surface of the model.

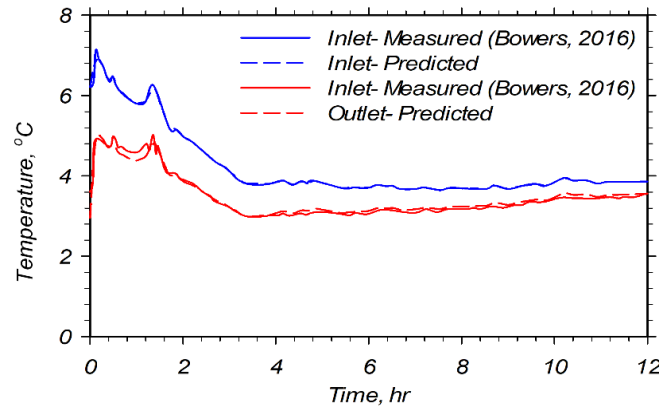


Figure 88. Experimentally recorded and predicted time histories of inlet and outlet fluid temperature

Figure 89 compares the variation of measured and predicted temperatures at different locations along two cross-sections near the mid-span of the bridge deck. The measured temperatures correspond to thermal sensors installed at a cross-section containing a heat exchanger pipe (Figure 89(a)) and a cross-section without a heat exchanger pipe (Figure 89(b)). simulation results showed good agreement with the experimental data. Accurate prediction of the top surface temperature was particularly important, as system performance, success or failure, can be evaluated based on surface temperature behavior (Bowers, 2016). The results indicated that the surface temperature was consistently higher above the heat exchanger pipe than in the region between the pipes throughout the system's operation. Additionally, the rate of temperature change was more rapid during the initial hours of testing. This behavior is attributed to elevated ambient and inlet fluid temperatures at the beginning of the test period, which accelerated heat transfer to the deck surface.

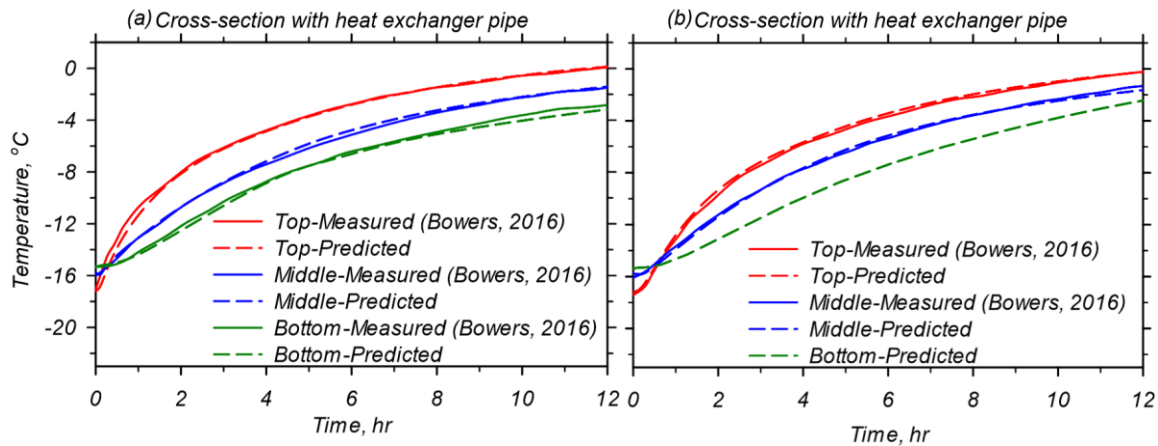


Figure 89. Comparison between experimental results and numerically predicted values of temperature at the top, middle, and bottom location within the bridge deck at (a) cross-section with heat exchanger pipes, (b) cross-section without heat exchanger pipes

Figure 90 illustrates the cross-sectional and top surface temperature contours of the bridge deck at various stages of the simulation. At the onset of heating, the temperature distribution across both the cross-section and top surface was relatively uniform, ranging between -15°C (5°F) and -17°C (1.4°F), as shown in Figure 90a. After 4 hours of heating, the surface temperature above and between the heat exchanger pipes increased to approximately -4.8°C (23.4°F) and -5.9°C (21.4°F), respectively. A pronounced thermal gradient developed within the deck at this stage (Figure 90b), with cross-sectional temperatures varying from -3°C (26.6°F) near the pipes to -

10 °C (14 °F) near the bottom surface. The highest temperatures were observed adjacent to the heat exchange pipes, while the lowest were recorded at the bottom of the deck. After 8 hours of heating, the surface temperature distribution became more uniform, averaging around -2 °C (28.4 °F), as shown in Figure 90c. Within the deck, temperatures ranged from -1 °C (30.2 °F) near the pipes to -5.8 °C (21.6 °F) at the bottom. The thermal pattern remained consistent with earlier observations, with warmer zones surrounding the heat exchanger pipes and colder regions concentrated at the deck's underside. By 12 hours of continuous heating, the average surface temperature of the deck reached the freezing point (0 °C or 32 °F), as depicted in Figure 90d. The bottom of the deck remained the coldest region, but the overall temperature gradient had diminished significantly, with a maximum difference of approximately 3 °C (37.4 °F). These results suggest that while surface temperatures respond relatively quickly to heating, it takes sustained operation to achieve a uniform thermal profile throughout the deck's thickness.

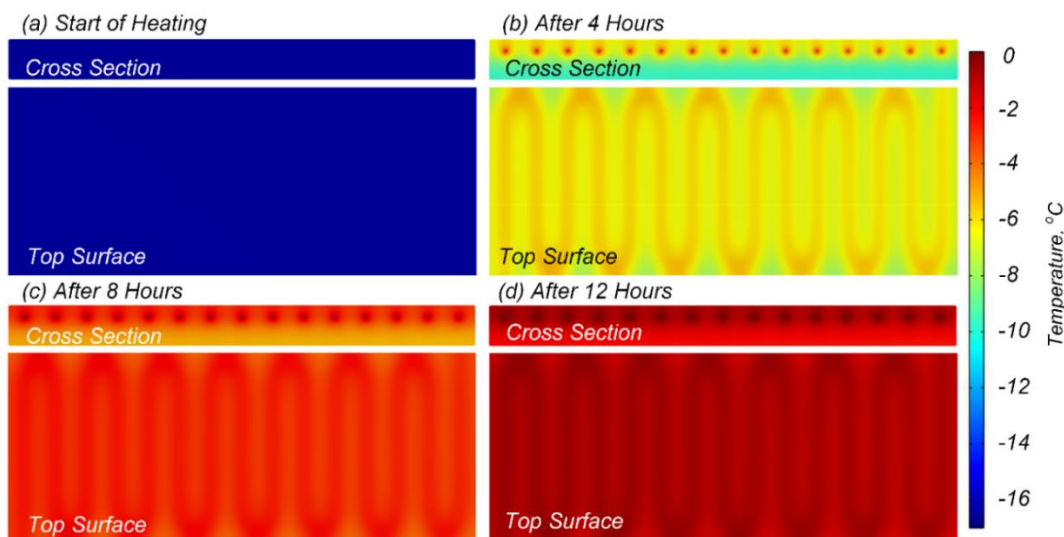


Figure 90. The progression of the cross-sectional temperature and the top surface temperature over time obtained in this study

Second Scenario- Moderate Winter Event

Validation of the numerical model was performed using experimental data from Bowers (2016), based on a moderate winter event that occurred on February 25–26, 2015. During this event, approximately 7.6 cm (3 in.) of snow accumulated over a five-hour period. The model incorporated various weather conditions, including sunny, partially cloudy, cloudy, and snowy scenarios. Since the bridge deck surface was initially snow-free, the top surface was subjected to both convective and radiative heat fluxes. A Neumann boundary condition was applied to the edges of the bridge deck model, while heat transfer from the bottom surface occurred through natural convection and radiation. For the radiant and convective boundary conditions, the external temperatures were defined as the sky temperature, T_{sky} , for the top surface and the ambient air temperature for the bottom surface. Figure 91 presents the time-dependent inputs used in the simulation, including ambient temperature, sky temperature, solar radiation, and snow melt heat flux.

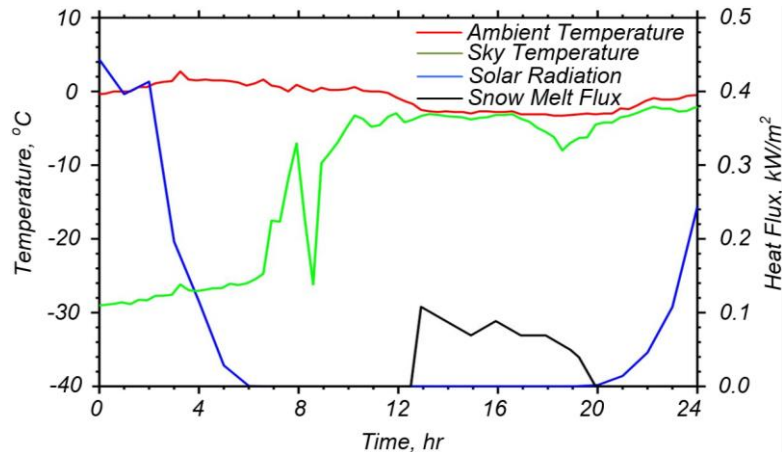


Figure 91. Variation of ambient and sky temperature during the experimental test and input heat fluxes to the numerical model (Bowers, 2016)

The predicted and measured inlet and outlet fluid temperatures are compared in Figure 92. As previously noted, the temperature difference between the inlet and outlet heating fluid is a key indicator for analyzing the energy required for snow melting. Experimental results showed a significant discrepancy between the measured and predicted fluid temperatures after four hours of system operation. Specifically, the measured outlet temperature was lower than predicted, suggesting higher energy loss or lower heat transfer to the deck than anticipated. After this initial period, the measured temperature difference decreased, indicating a reduction in heat transfer, consistent with the conservation of energy. As shown in Figure 92, the discrepancy between measured and predicted outlet temperatures was notable. Similar discrepancies were reported by Bowers (2016), who attributed them to uncertainties in weather parameters, boundary conditions, and material properties used in the numerical model. The results also revealed that the temperature differential, and thus the energy delivered to the deck, increased when the snow melting heat flux mode was activated (between hours 12.5 and 20), and began to decline once the snow had been removed from the deck surface (between hours 12 and 24). During this latter period, the predicted temperature changes closely matched the experimental data, supporting the accuracy of the model under snow-free conditions.

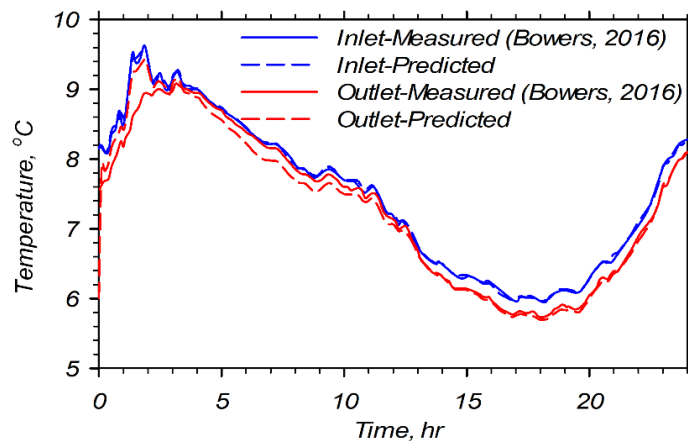


Figure 92. Experimentally recorded and predicted time histories of inlet and outlet fluid temperature

Figure 93 illustrates the measured and predicted temperature variations over time at various locations along a cross-section through the middle of the bridge deck that included a heat exchanger pipe. The corresponding results for a cross-section located between the heat exchanger pipes are shown in Figure 94. The measurement points for both sections are indicated in Figure 81(b). The numerical simulation results closely matched the experimental temperature data, especially in capturing general trends and peak values. The highest surface temperature was recorded during the daytime after approximately 2.5 hours of system operation. This peak is likely attributed to the combined influence of elevated inlet fluid temperatures (Figure 92), and solar radiation (Figure 91). The largest discrepancies between measured and predicted values occurred between 4 and 12 hours of operation. One likely cause of this deviation is the use of average ambient temperature as a proxy for sky temperature, T_{sky} , the simulation. As reported by Bowers (2016), the bridge site was surrounded by a maintenance shed, a soil mound, and buildings and trees located approximately 7 m (23 ft) away, all of which affect the mean radiant temperature, T_{MR} . This makes T_{MR} potentially different from T_{sky} , introducing error into the simulation. Additional sources of uncertainty stem from material property assumptions. Bowers (2016) did not experimentally measure the thermal conductivity or specific heat capacity of the concrete used. Previous studies (e.g., Liu, 2005) have shown that deck surface temperature is sensitive to the thermal properties of the concrete, which can vary with admixture type, density, and moisture content (Kim et al., 2003). Therefore, using estimated or literature-based values for these properties could introduce error into the model. Another modeling simplification involved the omission of rebar. Instead, the material properties of the reinforced concrete were approximated using a volumetric average of concrete and steel. This assumption may also contribute to discrepancies between measured and predicted temperatures. Weather data input posed additional limitations. Two weather stations were used: one at Virginia Tech Airport (6.76 km or 4.2 mi from the site) and another at Kentland Farm (approximately 6.4 km or 4 mi in the opposite direction). The Virginia Tech station provided data every 20 minutes, while Kentland Farm reported hourly. Sky temperature was calculated using the Virginia Tech data due to its higher temporal resolution, whereas solar radiation and precipitation were derived from Kentland Farm data. As Bowers (2016) noted, these data sources may not accurately represent the actual site conditions, particularly cloud cover, which affects sky temperature calculations and thus influences simulation results. Interestingly, the predicted and measured temperatures aligned more closely between 12 and 24 hours of operation, a period during which increased cloud cover likely caused the sky temperature to converge with ambient air temperature. This improved alignment was consistent across different locations within the bridge deck, as shown in both Figure 93 and Figure 94.

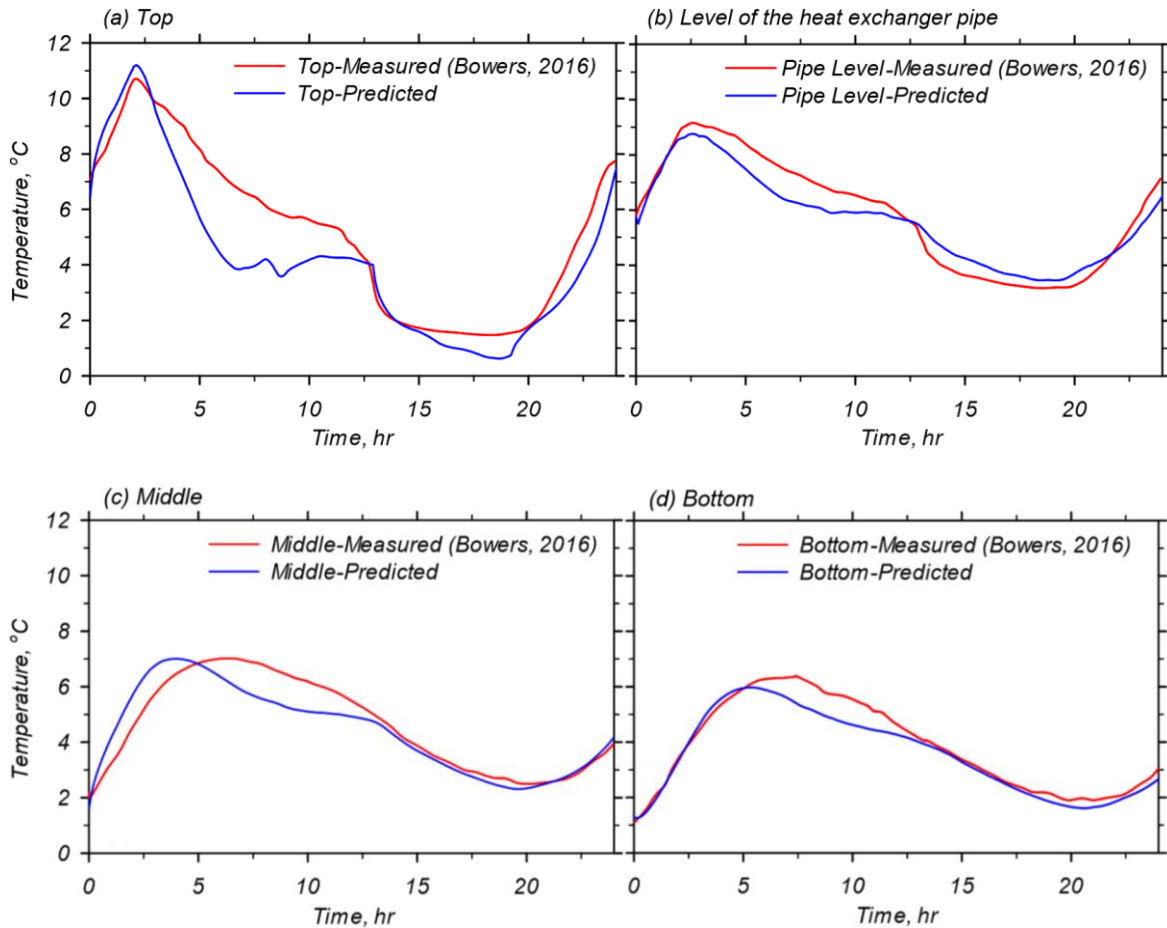


Figure 93. Comparison between experimental results and numerically predicted values of temperature at the top, pipes, middle, and bottom locations within the deck at cross-section with heat exchanger pipes

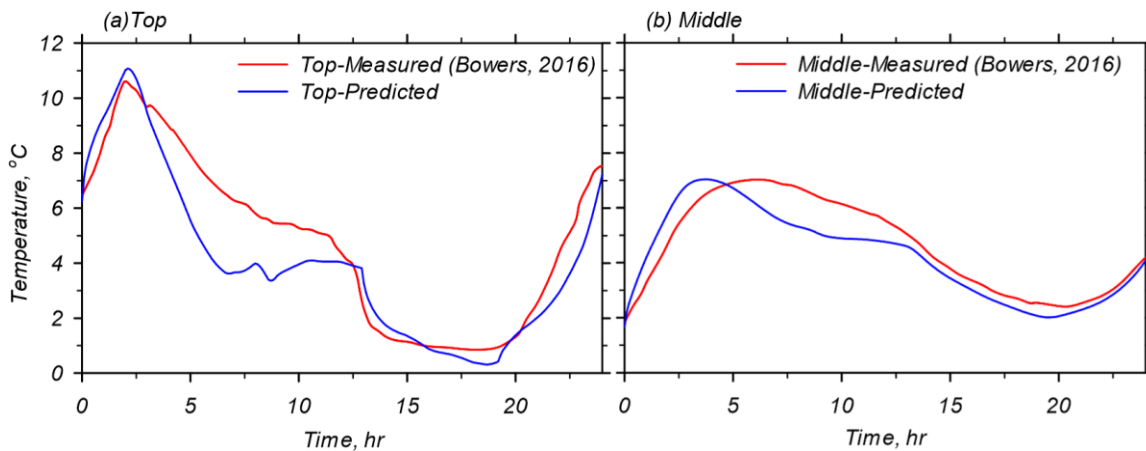


Figure 94. Comparison between experimental results and numerically predicted values of temperature at the top and middle locations within the deck at cross-section without heat exchanger pipes

Figure 95 illustrates the evolution of temperature distribution across the top surface and cross-section of the bridge deck model over time. At the initial condition, when the geothermal system was turned on, the top surface temperature was uniformly 6.7 °C (44.1 °F), with a visible vertical temperature gradient through the deck depth (Figure 95a). After 3 hours of heating, the surface

temperature increased to a uniform value of 9.5°C (49.1°F) (Figure 95b). The temperature contours indicate that the top surface experienced higher temperatures than the interior of the deck, which can be attributed to both the elevated inlet fluid temperature and solar exposure. After 12 hours of heating, immediately before the simulated storm event, the average surface temperature reached approximately 4.25°C (39.65°F) (Figure 95c). The highest temperatures were observed near the heat exchanger pipes, while the average temperatures of the top and bottom surfaces were lower than those in the core region of the model. Following 16 hours of simulation, the surface temperature remained above the freezing point at 0°C (32°F), as shown in Figure 95d. As expected, the top surface exhibited the lowest temperature at this stage, due to the application of a snowmelt heat flux simulating active deicing conditions.

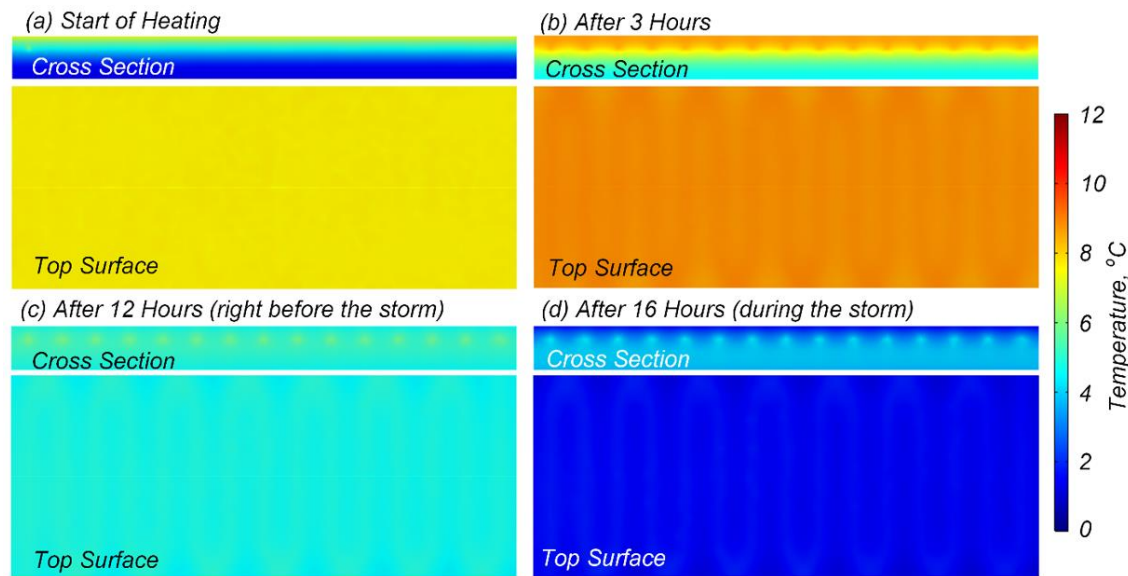


Figure 95. Progression of the cross-sectional temperature and top surface temperature over time obtained in this study

Parametric Study

A parametric study was conducted to evaluate the influence of key design and environmental factors on the performance of a geothermal bridge deck deicing system. Specifically, the study examined the effects of ambient temperature, deck dimensions, top reinforcement cover, inlet flow rate, heat exchanger tube spacing, and inlet fluid temperature on the system's ability to raise the top surface temperature above 0°C . The findings from this study informed the design and configuration of the physical bridge deck model used in subsequent experiments.

Ambient Temperature

The influence of ambient temperature on the top surface temperature of a geothermally heated bridge deck was investigated to assess its significance in the system's design and operation. All other test variables were held constant, including an inlet fluid temperature of 6°C . Nine different ambient temperatures were evaluated, ranging from -17°C to -0.5°C . In the test conducted at an ambient temperature of -0.5°C , the deck surface reached 0°C in approximately 0.6 hours. In contrast, at -17°C , it took about 9.2 hours for the surface to reach the same temperature. Figure 96 presents the top surface temperature profiles for all tests, including those conducted at intermediate

ambient temperatures. As expected, the results demonstrate a clear trend: higher ambient temperatures significantly reduce the time required for the geothermal system to raise the bridge deck surface temperature above freezing.

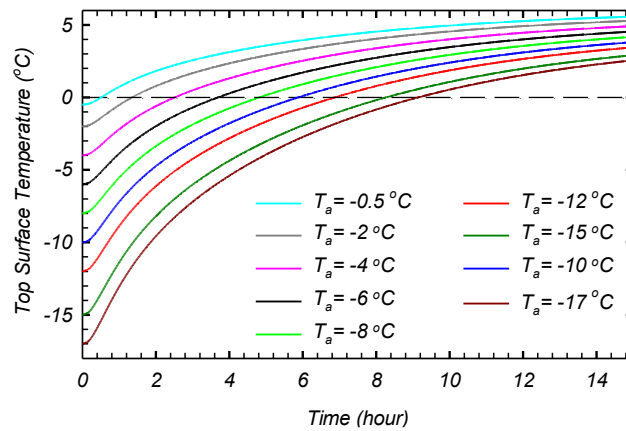


Figure 96. Parametric study results for ambient temperature

Bridge Deck Dimensions

A parametric study on bridge deck dimensions was conducted because the base model, measuring 3.05 m in length, 1.30 m in width, and 0.25 m in depth, was too large to be tested within the Subzero Research Laboratory (SRL). To address this limitation, a smaller model was developed to evaluate whether it could yield comparable thermal performance to the base model under ambient temperature conditions. The smaller model measured 1.50 m in length, 1.20 m in width, and 0.20 m in depth.

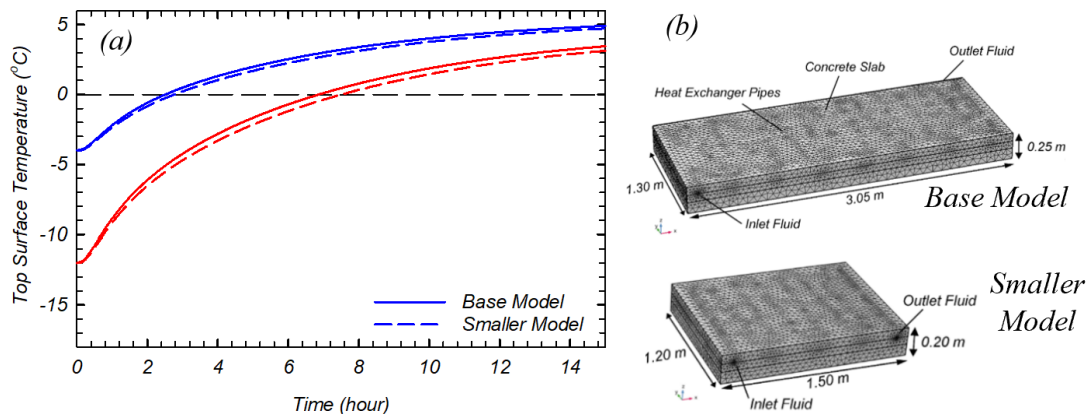


Figure 97(b) presents schematics of both models. The smaller model was tested at ambient temperatures of -4 °C and -12 °C. At -4 °C, the top surface temperature of the smaller model reached 0 °C in 2.8 hours, compared to 2.6 hours for the base model. At -12 °C, the time required for the smaller model to reach 0 °C was 7.5 hours, while the base model required 6.9 hours.

These results are illustrated in

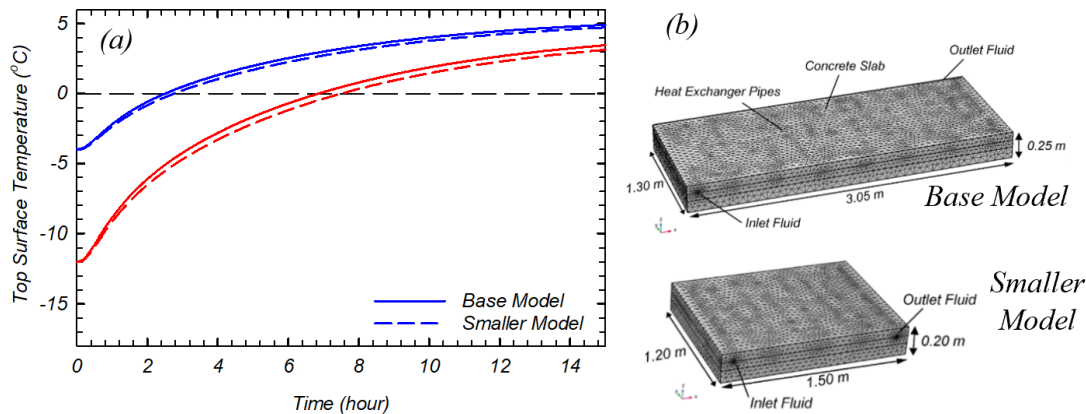


Figure 97(a), which shows the surface temperature profiles of both models under the two ambient temperature scenarios. The findings indicate that the smaller model produces surface temperature responses similar to those of the base model, suggesting it is a viable alternative for testing within the SRL's spatial constraints.

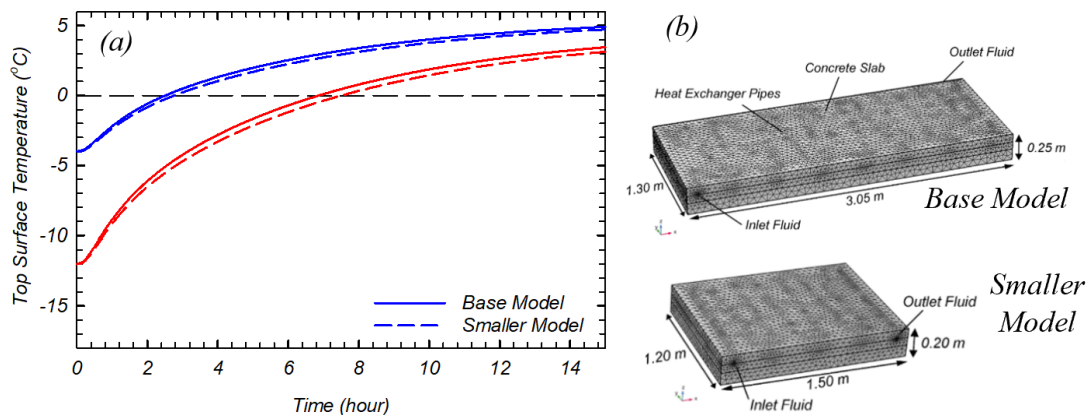


Figure 97. a) Parametric study results for Base Model and Smaller Model and b) schematic of Base Model and Smaller Model

Top Reinforcement Cover

In the physical bridge deck model, heat exchanger tubes were typically attached to the bottom of the top reinforcement layer. To evaluate the influence of tube placement depth on geothermal system performance, tests were conducted with varying top reinforcement covers of 4.5 cm, 5.5 cm, and 6.0 cm, while keeping all other parameters constant. The ambient and inlet fluid temperatures were maintained at -17°C and 6°C , respectively. The time required for the top surface temperature to reach 0°C was 8.2 hours for the 4.5 cm cover, 8.5 hours for the 5.5 cm cover, and 8.8 hours for the 6.0 cm cover. These results are illustrated in Figure 98(a). As expected, decreasing the cover depth improved heat transfer efficiency, reducing the time needed for the surface to reach freezing point. However, the differences among the three cover depths were relatively small, suggesting that the impact of top reinforcement cover thickness, within this tested range, on surface temperature response is minimal.

Inlet Fluid Flow Rate

The effect of inlet fluid flow rate was investigated because the calibrated numerical model employed a flow rate higher than the maximum achievable in the Subzero Research Lab (SRL). To evaluate this parameter, the top surface temperature of the bridge deck was monitored at four different inlet flow rates: 10 L/min, 15 L/min, 20 L/min, and 25 L/min. All other test conditions were held constant, with an ambient temperature of -17°C and an inlet fluid temperature of 6°C . The time required for the deck surface to reach 0°C was 8.9 hours for 10 L/min, 8.2 hours for 15 L/min, 8.0 hours for 20 L/min, and 7.9 hours for 25 L/min. These temperature trends are shown in Figure 98(b). The results indicate that increasing the inlet flow rate reduces the time required to raise the surface temperature above freezing. However, the improvement in heating performance between 10 L/min and 25 L/min is relatively small, suggesting diminishing returns beyond a certain flow rate.

Heat Exchanger Tube Spacing

The effect of heat exchanger tube spacing was evaluated to determine its influence on the performance of a geothermal bridge deck system. Simulations were conducted to model the top surface temperature of the deck using tube spacings of 15 cm, 20 cm, and 30 cm, while keeping all other parameters constant. The ambient temperature and inlet fluid temperature were set at -17°C and 6°C , respectively. The time required for the deck surface to reach 0°C was 5.5 hours for the 15 cm spacing, 8.2 hours for the 20 cm spacing, and 14.2 hours for the 30 cm spacing. Figure 99(a) illustrates the surface temperature evolution for each spacing condition. These results indicate that reducing the spacing between heat exchanger tubes significantly improves thermal efficiency by accelerating surface heating.

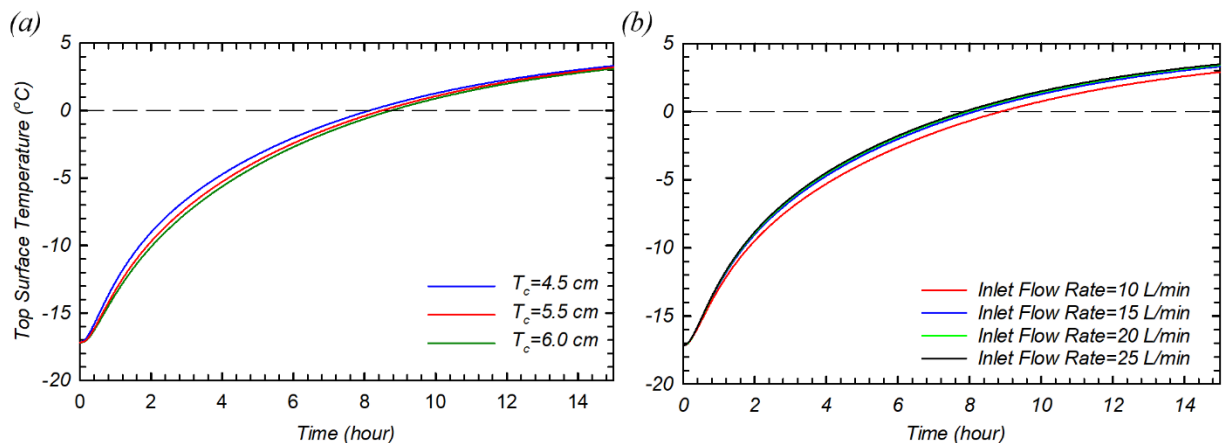


Figure 98. Parametric study results for a) top reinforcement cover and b) inlet fluid flow rate

Inlet Fluid Temperature

The effect of inlet fluid temperature was evaluated to determine its influence on the performance of a geothermal bridge deck system. Nine different inlet fluid temperatures were modeled, ranging from 6.0°C to 10.0°C , while all other parameters were held constant. The ambient temperature was fixed at -17°C across all simulations. The results showed that with an inlet temperature of 10.0°C , the bridge deck surface reached 0°C in approximately 6.2 hours, whereas at 6.0°C , it

required 9.1 hours to reach the same temperature. As shown in Figure 99(b), surface temperature response improved with higher inlet fluid temperatures. These findings indicate that increasing the inlet fluid temperature significantly reduces the time required for the geothermal system to bring the bridge deck surface above freezing.

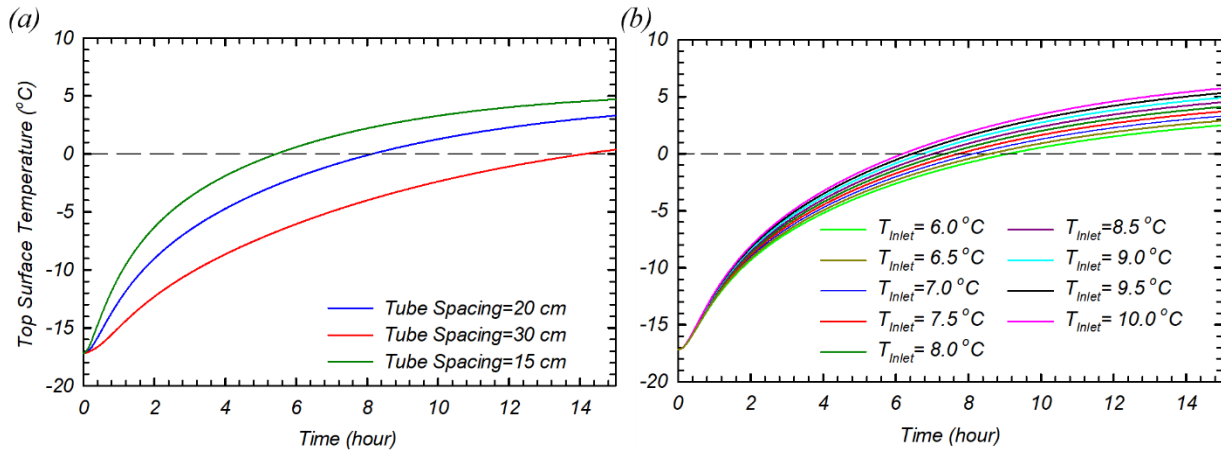


Figure 99. Parametric study of a) heat exchanger pipe spacing and b) inlet fluid temperature

Summary of Parametric Study

The effects of bridge deck dimensions, top reinforcement cover, and inlet fluid flow rate were found to be negligible in the design of a geothermal bridge deck model. Therefore, any discrepancies between Montana's design codes for reinforcement cover or the CHC's constraints related to bridge deck dimensions and fluid flow rates will not significantly impact the validation of simulation results against past field tests. In contrast, ambient temperature, heat exchanger tube spacing, and inlet fluid temperature have a substantial influence on the performance of the geothermal system. To ensure accurate validation, the tube spacing in the model will replicate that of previous field implementations. Additionally, ambient and inlet fluid temperatures will be aligned with Montana-specific weather and geothermal conditions to reliably assess the feasibility of geothermal bridge deck deicing in the state.

Experimental Models

A series of experiments was conducted in the Cold Hydrodynamics Chamber (CHC) of the Subzero Research Laboratory at Montana State University to evaluate the feasibility of using geothermal energy for bridge deck deicing in Montana and to investigate its potential to mitigate thermally induced concrete deterioration. The CHC is capable of controlling ambient temperatures between -25°C and 10°C and is equipped with a temperature-controlled water reservoir that can circulate a steady flow of water into and out of the chamber. Additionally, the chamber features a solar simulator with a maximum intensity of 490 W/m^2 , measured at the bridge deck surface, to replicate solar radiation. While the chamber lacks an adjustable wind mechanism to simulate forced convection, wind velocity around the specimen was measured during testing. These measurements were later used to calibrate the numerical model and analyze the influence of wind speed on bridge deck thermal performance.

The experiments were performed on two physical bridge deck models. Model 1 was designed to achieve three primary objectives: (1) assess the feasibility of using geothermal energy to deice

concrete bridge decks, (2) evaluate its effectiveness in melting snow accumulation, and (3) investigate its potential to mitigate thermal stresses and frost action. The design and dimensions of Model 1, shown schematically in Figure 100, were informed by prior numerical simulations (Turner et al., 2023) and constrained by the available space within the Cold Hydrodynamics Chamber (CHC). The bridge deck dimensions were 160 cm long, 100 cm wide, and 20 cm thick, aligning with the minimum thickness for new bridge decks specified in Montana (Barnes, 2017). Model 2 was designed as a quarter-scale replica of Model 1 (Figure 101) to evaluate the effects of geothermal heating on early-age cracking. All key design parameters, including materials and reinforcement configuration, were consistent with those of Model 1. Additionally, a control model (Model 2c) was constructed to replicate Model 2 but without embedded heat exchanger tubes, serving as a baseline for comparison. Reinforcement details for the 20 cm thick decks were selected based on the MDT Structures Manual (2002). To thermally isolate the test specimens, rigid insulation was applied to the deck sides, while corrugated steel sheeting served as a permanent bottom form. Given steel's high thermal conductivity, the bottom was not insulated. The concrete mix design used in both models was developed through a series of preliminary experiments evaluating MDT-approved mix formulations, as described by Pourakbar et al. (2021).

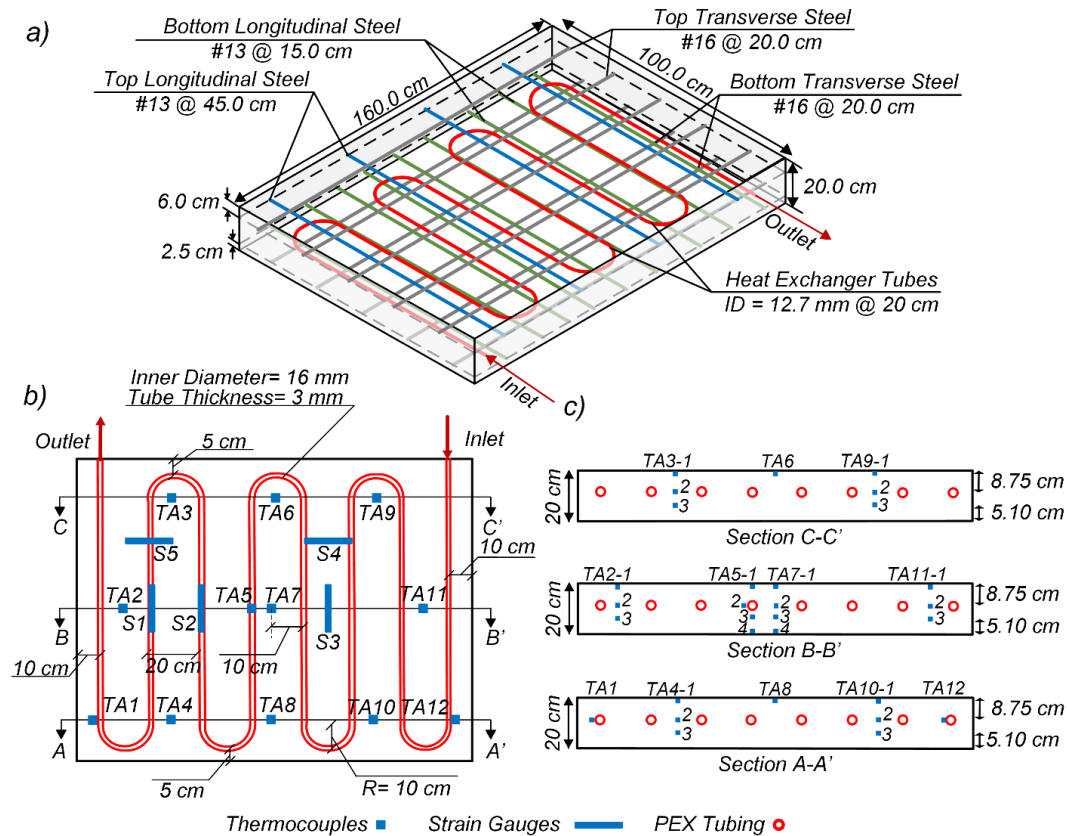


Figure 100. Model 1 design: a) 3D view, b) plan view with surface locations of sensors, and c) section views with depth location of sensors.

For the heat exchanger system, 12.7 mm cross-linked polyethylene (PEX) tubing was used with a center-to-center spacing of 20 cm. The tubes were embedded 8.75 cm below the top surface of the bridge deck. A 30% glycol mixture was circulated through the tubing at the maximum flow rate allowed by the Cold Hydrodynamics Chamber (CHC), which was 5.5 L/min. According to a

computational parametric study by Turner et al. (2023), fluid flow rate had a negligible effect on the efficiency of the deicing system for the dimensions of the experimental bridge deck. Therefore, this flow rate was maintained across all tests. An inlet fluid temperature of 8 °C was selected for all experiments, based on findings by Kusuda and Achenbach (1965), which showed that seasonal ground temperature variations are minimal. To monitor thermal performance, Models 1 and 2/2c were instrumented with Type-T thermocouples placed at various locations throughout the concrete. The thermocouple layouts for these models are shown in Figure 100 and Figure 101, respectively. Additionally, Model 1 was equipped with five vibrating wire strain gauges on the top surface to measure concrete strain. The strain gauge configuration is illustrated in Figure 100b.

Model Construction

The bridge deck model was constructed in the Bulk Materials Laboratory at Montana State University. The formwork was built using Douglas-fir 2×10 lumber and corrugated steel. To satisfy the experimental boundary conditions, which required both the top and bottom surfaces of the concrete to remain uninsulated, the corrugated steel formwork was retained as the permanent bottom of the specimen. This approach avoided the need to remove the specimen to expose the underside. Given that concrete has a thermal conductivity of 1–3 W/m·K and steel approximately 50 W/m·K (Nagy & Szagri, 2018), the steel bottom does not provide insulation and allows for effective heat transfer. Figure 102(a) illustrates the form construction. Steel reinforcement grids were fabricated according to design specifications and tied together with rebar ties, as shown in Figure 102(b). Cross-linked polyethylene (PEX) tubing was then configured and secured to the top reinforcement grid using rebar ties to simulate a geothermal heating system.

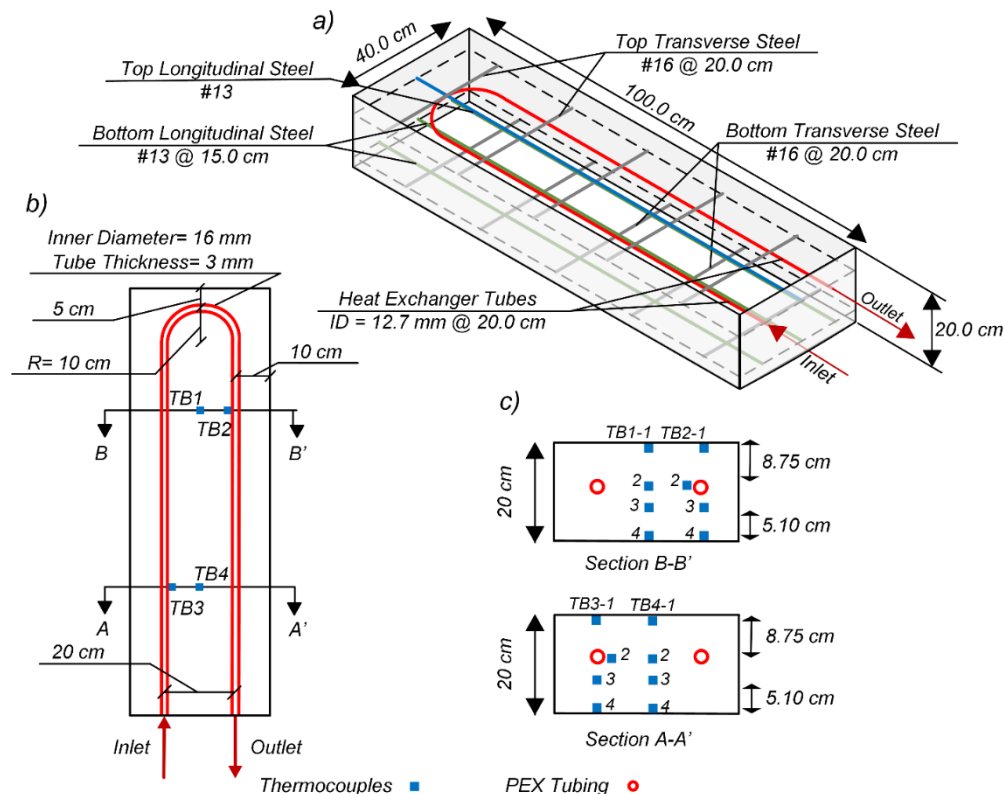


Figure 101. Model 2 Design: a) 3D view, b) plan view with surface locations of sensors, and c) section views with depth location of sensors.

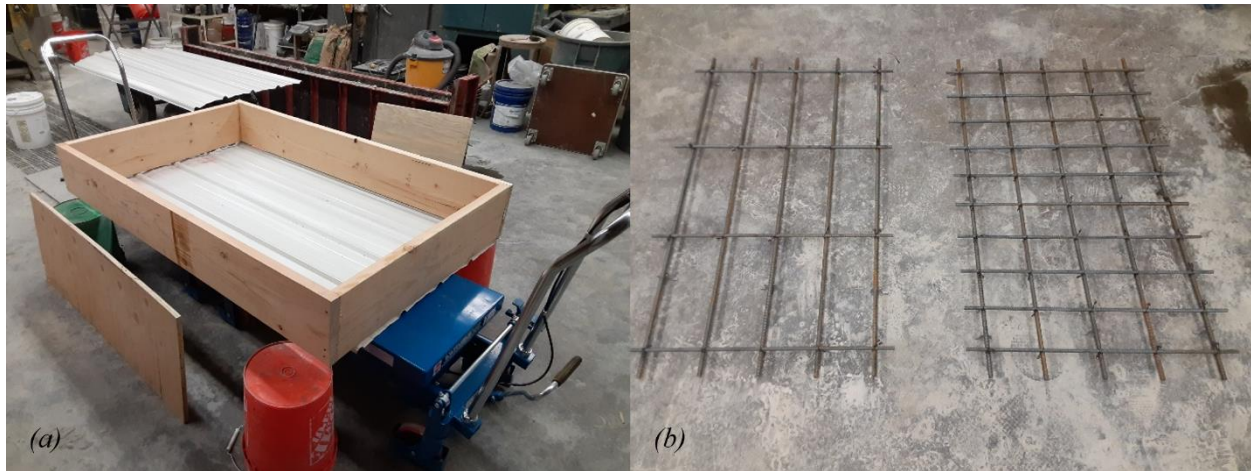


Figure 102. a) Bridge deck model form and b) finished reinforcement grids

The bottom reinforcement grid was supported on plastic rebar chairs to ensure the appropriate concrete clear cover. The top reinforcement grid was suspended using wire ties from additional steel bars placed across the top of the wooden formwork. Two 12.7 mm (0.5 in.) holes were drilled into the wood frame to allow the PEX tubing to pass through. Duct tape was applied to indicate the “fill line” for concrete placement. Figure 103 shows the completed form prior to thermocouple installation. The preparation and placement of thermocouples are discussed later in this chapter.

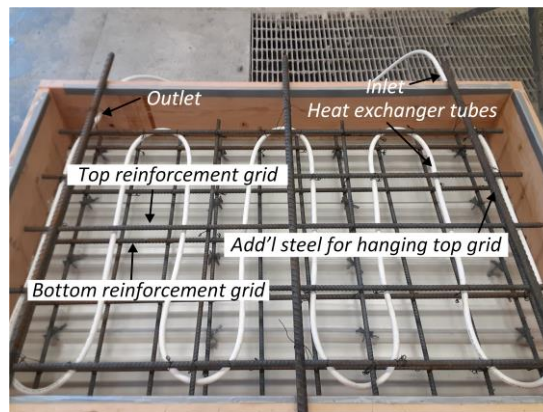


Figure 103. Completed form

Concrete Mixing, Pouring, and Curing

Four batches of concrete were required to reach the designated fill line, and a total of 32 compression cylinders were cast. After finishing the top surface, the form was covered with plastic wrap for the initial 24 hours to retain moisture. Following this period, the plastic wrap was replaced with wetted towels placed on the concrete surface, covered by a plastic tarp to help retain humidity. This process is illustrated in Figure 104(a) and (b). The towels were re-wetted every two days throughout the 28-day curing period. All curing was conducted in the laboratory, which was maintained at room temperature.

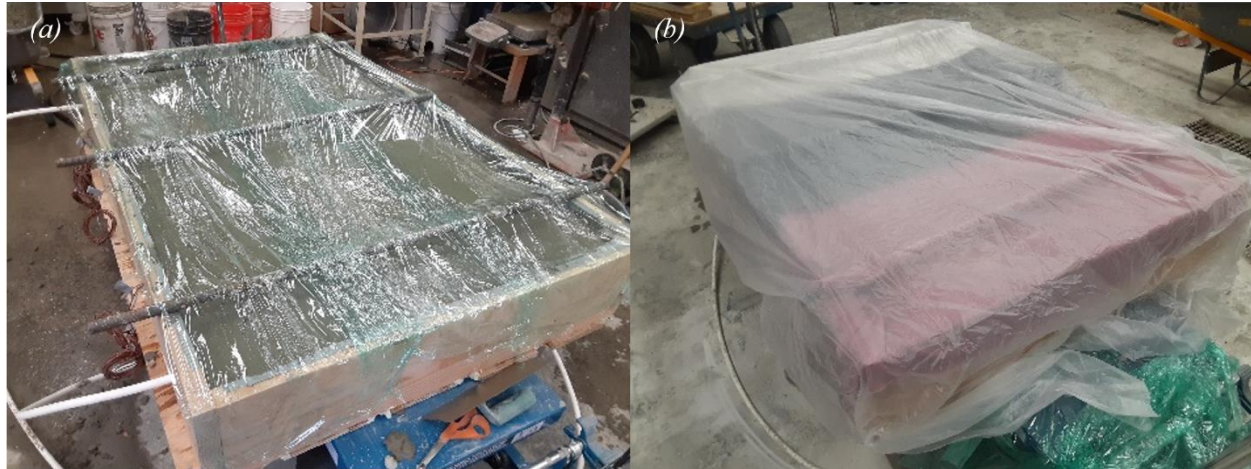


Figure 104. a) Initial 24-hour set and b) 28-day damp towel cure

Bridge Deck Test Preparation

After 28 days of curing, preparation for testing the bridge deck model began. The top steel reinforcement was removed by carefully stripping the exposed wires at the concrete surface. Following this, the wooden formwork was dismantled, with particular care taken to avoid damaging the embedded thermocouples. Minor surface imperfections were observed at six locations where wires had been used to suspend the top steel grid, causing slight finishing issues. These rough areas were smoothed using a grinder to ensure a uniform surface. Figure 105 shows the bridge deck model after the removal of the steel reinforcement and wooden frame.



Figure 105. Cured bridge deck model

After completing the initial preparation, the bridge deck model was transported from the Bulk Materials Laboratory to its final testing location in the Subzero Research Laboratory. The model was positioned on cinder blocks, as shown in Figure 106. The PEX tubing was connected to an inlet valve at one end and allowed to drain into an outlet reservoir at the other. To finalize the setup, insulation was applied to the sides of the model and to the exposed sections of the PEX tubing. Figure 106 illustrates the fully prepared bridge deck model in the SRL, ready for testing.

Instrumentation

Figure 107(a) and (b) show the general schematic of the instrumentation layout and the proposed locations of the thermocouples and strain gauges, respectively. A total of 30 embedded Type-T thermocouples were installed to monitor internal temperature distribution within the bridge deck specimen. To supplement the thermocouple data, a thermal camera was used to monitor the surface temperature of the specimen in real time. Additionally, five GEOKON vibrating wire strain gauges were installed along the x- and y-axes of the deck surface to measure thermally induced strains. To visually track snow melting over time, two GoPro cameras were deployed, one mounted directly above the specimen and the other positioned laterally. The cameras were programmed to capture images at predefined intervals, providing both top-down and side perspectives of the snowmelt progression.

Other instrumentation was used to measure the conditions in the CHC. An anemometer was used to measure the wind speed from the CHC fans and a pyranometer was used to measure the solar intensity of the solar simulator. Additional thermocouples were added to measure the ambient temperature and the inlet and outlet fluid temperatures. A McMaster flow meter was attached near the inlet to measure the flow rate.



Figure 106. Bridge deck model prepared for testing

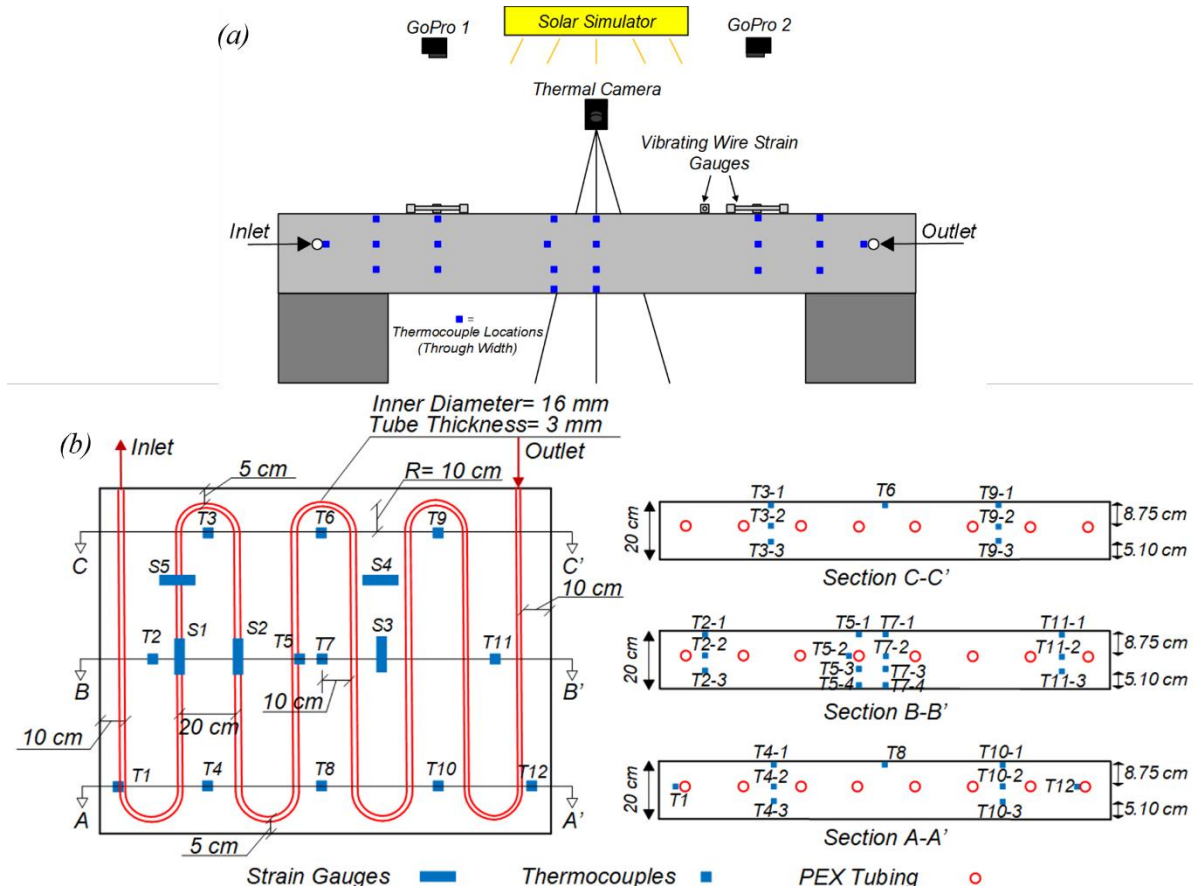


Figure 107. a) Instrumentation schematic and b) proposed locations of thermocouples and strain gauges

Thermocouple

The thermocouples were prepared using a thermocouple welder. The process includes unwelded thermocouples (Figure 108(a)) being placed in a copper holder, then inserted in the thermocouple welder (Figure 108(b)). The welded thermocouples (Figure 108(c)) were then validated using a mixture of ice and water at approximately 0 °C.

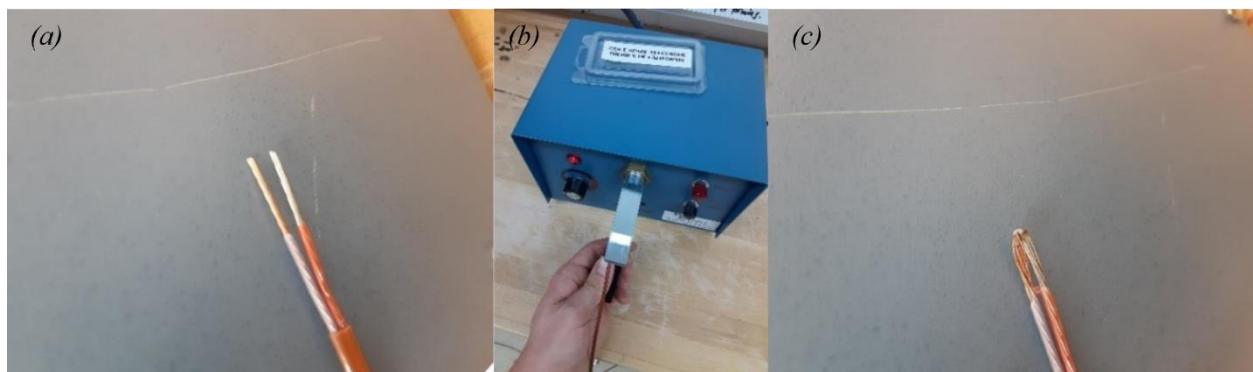


Figure 108. a) Thermocouples before welding, b) thermocouple welder, c) and welded thermocouple

Once validated, the thermocouples were placed using zip ties. Figure 109(a) and (b) shows the placed thermocouples. Holes were drilled in the wood frame for the thermocouples to be fed through.

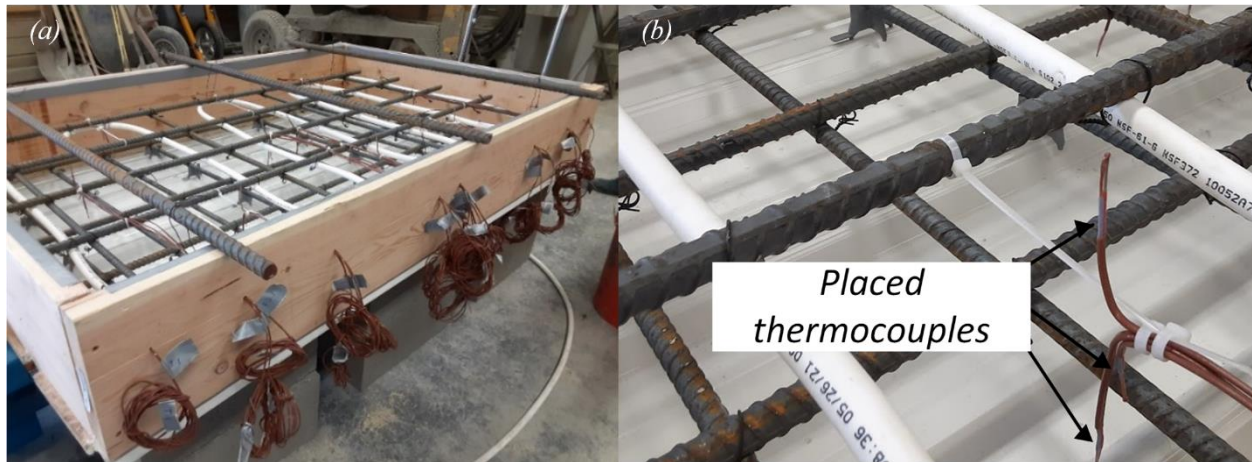


Figure 109. a) Completed form with thermocouples and b) closeup of placed thermocouple

An external temperature sensor was embedded within the snow layer to monitor the thermal behavior of the snow, as illustrated in Figure 110. Temperature data from all thermocouples, along with the snow sensor, were recorded at 3-minute intervals using the data acquisition system.



Figure 110. Temperature sensor for monitoring thermal behavior of snow

Vibrating Wire Strain Gauge Installation

The GEOKON wire strain gauges were installed by epoxying the mounting blocks into drilled holes in the top surface. Figure 111(a) and (b) shows the strain gauges and mounting blocks before and after epoxy.

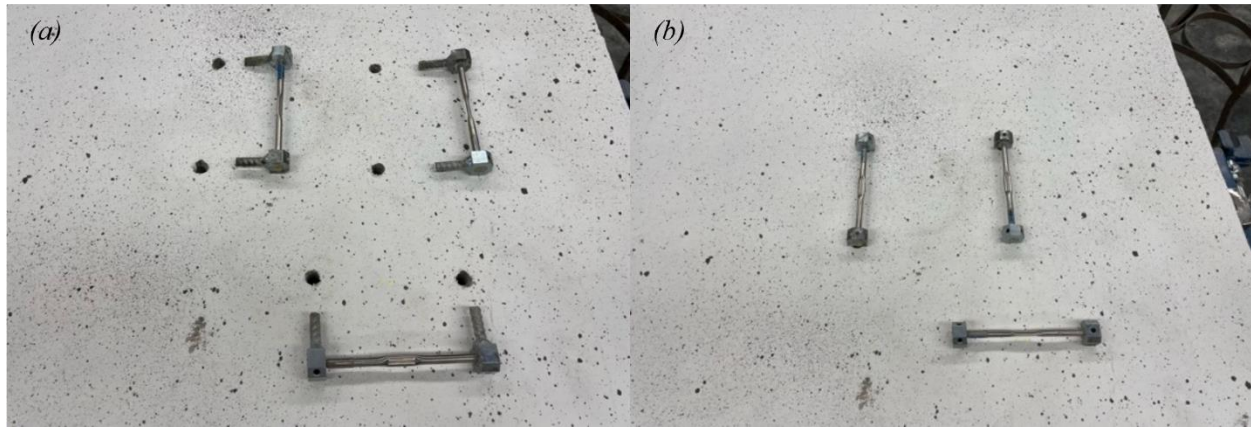


Figure 111. a) Strain gauges with mounting blocks ready for epoxy and b) installed strain gauges

Weather Scenarios and Testing Sequence

Data from Montana's Road Weather Information System (RWIS) stations were utilized to develop realistic testing scenarios for evaluating the performance of a geothermal bridge deck deicing system. To meet the experimental objectives, three weather scenarios were created for Model 1: (1) a Synthetic Weather Scenario, (2) a Daily Fluctuation Weather Scenario, and (3) a Snow Melting Scenario. These scenarios were designed to reflect a range of winter conditions commonly experienced in Montana, using historical RWIS data from 2015 to 2020 to define maximum and minimum temperatures and solar radiation levels. As shown in Figure 112, the coldest months in Montana typically span from November through February. Each experiment was conducted both with and without the geothermal deicing system in operation to facilitate direct performance comparison.

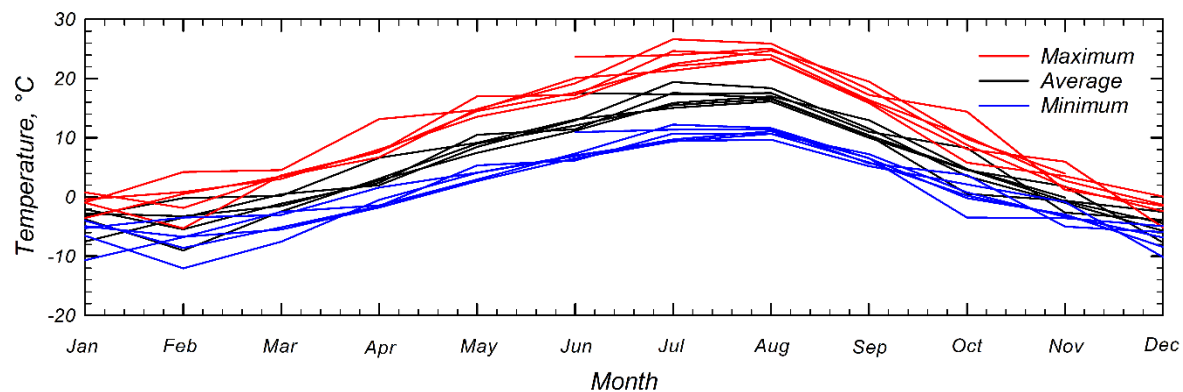


Figure 112. Montana Monthly Average Ambient Temperature for 2015-2020.

The Synthetic Weather Scenario was designed to isolate the effects of low ambient temperatures and solar radiation on the performance of the geothermal system. The test consisted of four 24-hour stages with varying ambient temperatures and solar intensities, as illustrated in Figure 113a. Prior to Stage 1, the concrete deck temperature was stabilized under an ambient temperature of 10 °C. In Stage 1, the ambient temperature was lowered to -10 °C with no solar radiation. In Stage 2, the solar simulator was activated at an intensity of 490 W/m² while maintaining the ambient temperature at -10 °C. For Stage 3, the ambient temperature was further reduced to -20 °C, with

the solar simulator remaining active at 490 W/m^2 . In the final stage, the solar simulator was turned off while the ambient temperature remained at -20°C .

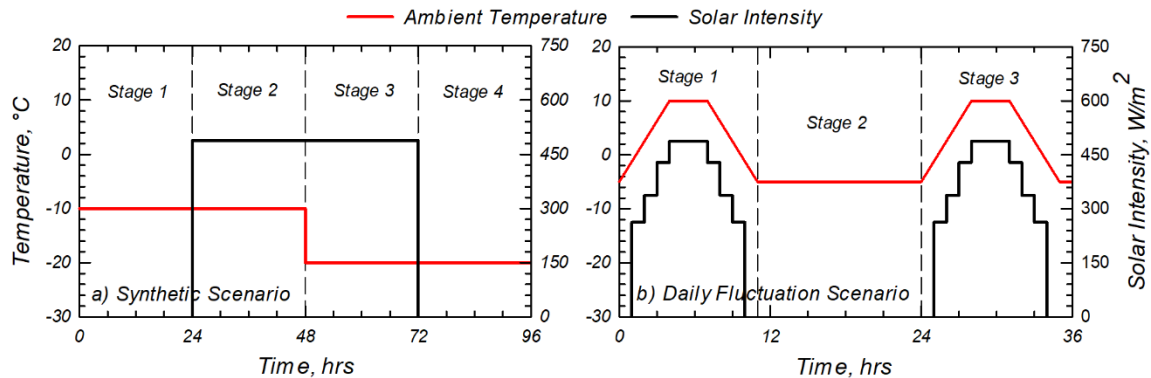


Figure 113. Ambient temperature and solar intensity of Model 1 weather scenarios: a) Synthetic and b) Daily Fluctuation.

The Daily Fluctuation Weather Scenario was designed to simulate a typical late-winter day in Montana, characterized by significant diurnal temperature swings (Figure 113b). The test consisted of three stages of varying durations. Prior to Stage 1, the concrete deck was stabilized at an ambient temperature of -5°C . During the first four hours of Stage 1, the ambient temperature increased linearly to 10°C , while the solar intensity rose in 1-hour intervals using the solar simulator's preset levels: 0%, 55%, 71%, 90%, and 100%, reaching a maximum intensity of 490 W/m^2 . After maintaining these peak conditions for three hours, the ambient temperature and solar intensity then decreased linearly back to -5°C and 0 W/m^2 , respectively, over the following four hours. Stage 2 maintained a constant ambient temperature of -5°C and zero solar radiation for 13 hours to simulate nighttime or overcast conditions. Stage 3, beginning at hour 24, repeated the same cycle as Stage 1, representing the start of a new diurnal heating cycle.

The Snow Melting Scenario was designed to evaluate the system's effectiveness in melting snow accumulation on the bridge deck. Each test consisted of three distinct 12-hour stages (Figure 114). In Stage 1, no snow was applied and the solar simulator remained off, allowing the deck to equilibrate with the ambient environment. In Stage 2, a uniform layer of fresh snow was sieved onto the deck surface while ambient conditions were held constant, enabling assessment of passive thermal interaction between the snow and deck. The snow was applied using a consistent sieving process to mimic realistic snow coverage, as shown in Figure 115(a), (b), and (c). In Stage 3, the solar simulator was activated at a constant intensity of 490 W/m^2 to evaluate the combined effect of solar radiation on snow melting. Two snow thicknesses were selected to represent typical winter events: a moderate snowfall of approximately 3 inches and a light snowfall of around 1 inch. The first test, conducted without activating the geothermal system, used the moderate snow condition, while the second test, with the geothermal system in operation, was conducted under the light snow condition. All other environmental and test parameters were held constant to enable a direct comparison of the system's thermal response and snow-melting performance under varying snow loads.

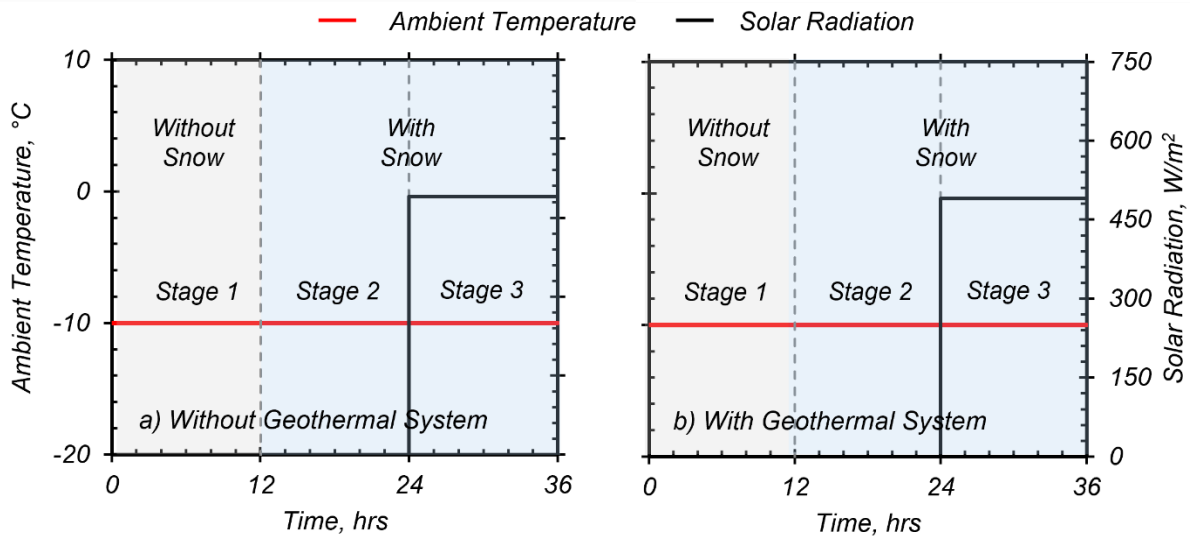


Figure 114. Experimental testing plan for snow tests showing ambient temperature and solar intensity for a) Without geothermal system in operation and b) With geothermal system in operation - Stage 1: no snow; Stage 2: with snow/no solar; Stage 3: with snow/with solar

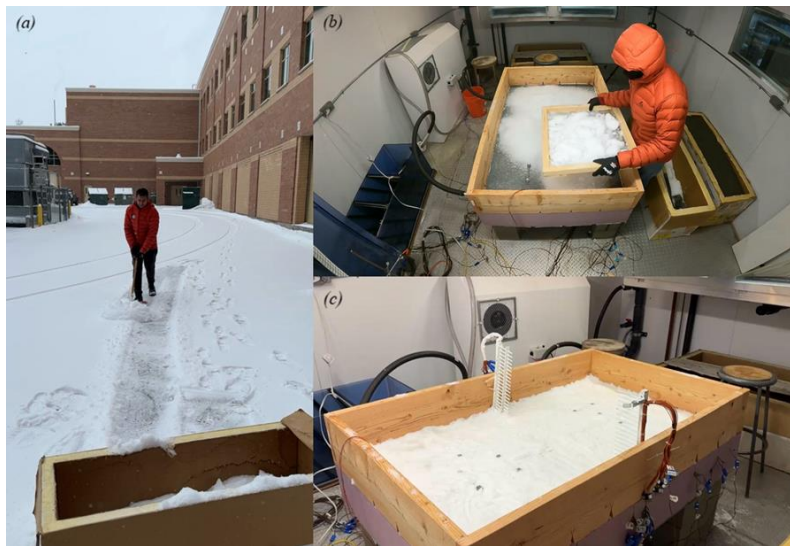


Figure 115. Collection and application of fresh snow on bridge deck surface to simulate realistic winter precipitation

An experiment was conducted using Model 2/2c to evaluate the potential for mitigating thermal shrinkage by operating the geothermal deicing system during the concrete curing process and early-age development. The Cold Hydrodynamics Chamber (CHC) was maintained at 3 °C throughout the curing period, which represents the highest ambient temperature at which the CHC could consistently sustain a fluid temperature of 8 °C. After 28 days of curing, 2-inch cores were extracted from the bridge deck specimen to measure compressive strength. These results were then compared to those from the control specimen, Model 2c, which was cured without geothermal heating.

CHAPTER 5: EXPERIMENTAL RESULTS

This chapter presents the results of physical experiments conducted to evaluate the use of geothermal energy for deicing concrete bridge decks and mitigating concrete deterioration. The content in this chapter is adapted from Turner et al. (2024), published in the *Journal of Bridge Engineering*, and is included with permission from the American Society of Civil Engineers (ASCE).

Turner, E., Khosravi, M., Matteson, K., Plymessenger, K., Toomani, P., McKittrick, L., & Jackson, J. (2024). Application of geothermal bridge deck deicing systems to mitigate concrete deterioration from temperature fluctuation: model scale experiments. *Journal of Bridge Engineering*, 29(8), 04024053.

Two scaled bridge deck models were constructed with embedded heat exchanger tubing and outfitted with thermocouples and strain gauges. The models were subjected to weather scenarios representative of winter events in Montana, both with and without the deicing system activated. The effectiveness of the system was examined for (1) deicing/snow melting capability based on surface and snow temperature data, (2) frost damage risk minimization using temperature profiles throughout the depth, (3) thermal movement and gradient reduction based on strain and internal temperature measurements, and (4) thermal shrinkage mitigation by reducing concrete curing and ambient temperature differentials. The experimental results provide insights into the potential benefits of geothermal energy for enhancing durability and extending the service life of concrete bridge decks in cold climates. Additionally, the data obtained offers a useful dataset for validating numerical modeling to further optimize the design and operation of geothermal systems in concrete bridge applications.

Application for Bridge Deck Deicing

In the absence of solar radiation, the geothermal deicing system consistently elevated the bridge deck surface temperature compared to conditions without system operation. Figure 116a and Figure 117a illustrate the Synthetic Scenario results with and without the system. Stages 1 and 4, where no solar radiation was applied, highlight this effect. In Stage 1, under an ambient temperature of -10°C , the surface temperature stabilized at -10°C without the system. When the system was active, the surface temperature rose to -3°C , demonstrating its ability to offset cold ambient conditions. Similarly, in Stage 4, with an ambient of -20°C , the system increased the surface temperature to -11°C compared to -20°C without it, a 9°C improvement. Although the system did not raise the surface temperature above freezing during these stages, it still proved effective in mitigating extreme cold exposure. Stages 2 and 3 of Figure 116 and Figure 117 include the influence of solar radiation. Early in Stage 3, a brief malfunction caused the solar simulator to deactivate; however, the issue was quickly resolved and temperatures re-stabilized within the 24-hour cycle. Data from thermocouple TA2-1, which was most affected by the incident, were removed for clarity, while data from TA7-1 and TA8 were retained and presented.

The addition of solar radiation significantly increased surface temperatures and generally enhanced the effectiveness of the geothermal system. During Stage 2 of the Synthetic Scenario, with ambient temperatures held at -10°C and solar radiation at 490 W/m^2 , the surface stabilized at 6°C with the system active, and at 3°C without it. This represents a 16°C and 13°C rise above ambient, respectively. In Stage 3, when the ambient temperature was reduced to -20°C but solar radiation

remained constant, the surface temperature reached 1 °C with the system and -6 °C without it, equivalent to increases of 21 °C and 15 °C above ambient. Notably, the combination of geothermal heating and solar radiation was required to exceed 0 °C in Stage 3, while solar radiation alone was sufficient only during Stage 2.

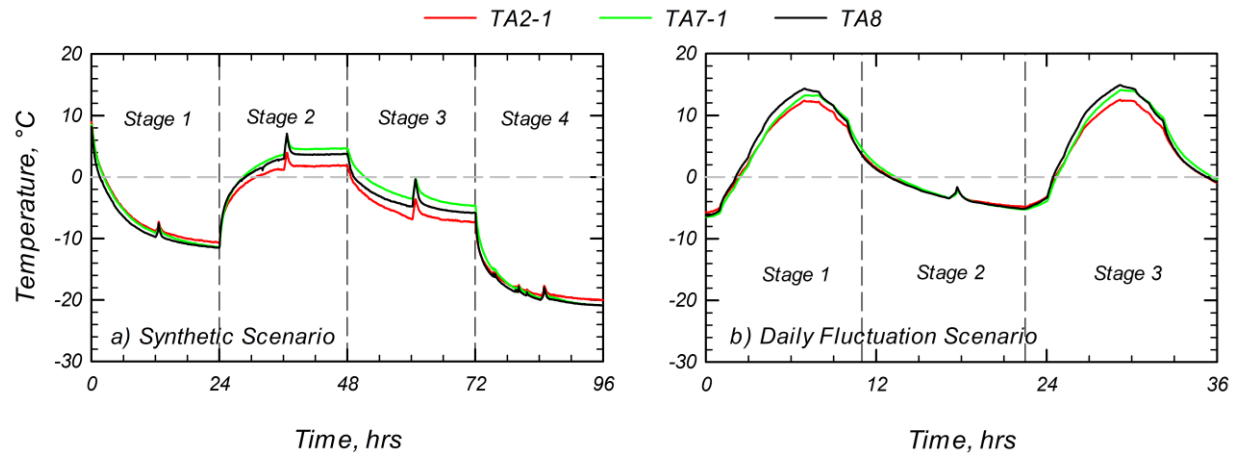


Figure 116. Top surface thermocouple results for a) Synthetic and b) Daily Fluctuation Weather Scenarios without deicing system active.

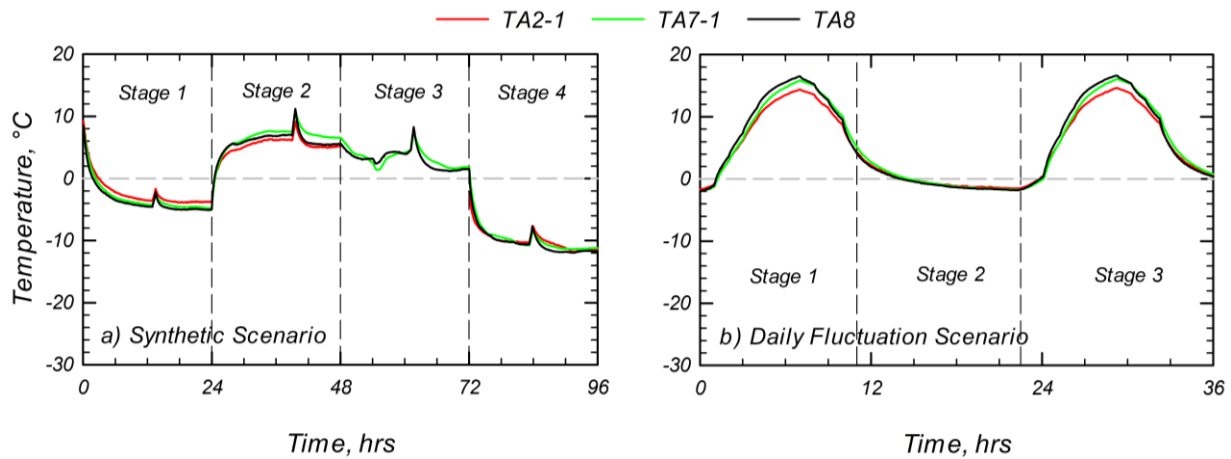


Figure 117. Top surface thermocouple results for a) Synthetic and b) Daily Fluctuation Weather Scenarios with deicing system active.

However, the relative benefit of the deicing system diminished in the presence of solar radiation. In Stage 2 (Figure 117a), the surface temperature was only 3 °C higher with the system than without it (6 °C vs. 3 °C), whereas in Stage 1 (no radiation-Figure 117a), the system resulted in a 7 °C increase (-3 °C vs. -10 °C). This reduced differential can be attributed to a smaller thermal gradient between the circulating fluid (at 8 °C) and the deck surface when solar energy was already warming the concrete. As the surface temperature neared the fluid temperature, the rate of heat transfer from the system naturally decreased. Essentially, solar radiation provided an initial thermal boost, diminishing the marginal effect of the geothermal system under those conditions.

The Daily Fluctuation Scenario was designed to replicate diurnal variations in ambient temperature and solar intensity typical of late winter in Montana. Figure 116b and Figure 117b compare results without and with the system. In the early morning, when solar intensity was minimal, the surface remained below 0 °C for the first 2.5 hours without the system. With the system active, the surface surpassed freezing after just 1.5 hours, demonstrating its ability to accelerate thawing. As solar input increased, peak surface temperatures reached 13 °C without the system and 15 °C with it, a modest 2 °C gain due to supplemental heating. Later in the evening, as solar intensity declined, the surface dropped below freezing at hour 13.5 without the system, but remained above 0 °C until hour 14.5 when the system was active. These findings illustrate the system's ability to extend above-freezing conditions during both morning warm-up and evening cool-down periods. Across the entire test duration, the surface remained above freezing for 75% of the time with the system, compared to just 62% without it.

Application for Bridge Deck Snow Melting

The temperature profiles obtained from the snow melting tests are presented in Figure 118. During Stage 1, temperatures across the bridge deck stabilized under snow-free conditions. In this phase, the snow sensor primarily recorded ambient air temperatures near the deck surface, as no snow was present. For the geothermal heating case, the system raised deck temperatures, simulating a pre-heating strategy that could be implemented prior to forecasted snow events. In Stage 2, following the application of snow, bridge deck temperatures remained largely unchanged from Stage 1. This stability is attributed to the snow being stored and applied at the same temperature as the deck, resulting in minimal thermal gradients. These findings suggest that snow placement alone does not significantly lower deck surface temperatures when thermal equilibrium exists between the snow and the structure. Stage 3 introduced solar radiation through the lab's solar simulator, during which both snow and bridge deck temperatures gradually increased. Periodic temperature spikes were observed, corresponding to defrost cycles of the environmental chiller system, which activates periodically to prevent frost buildup. The results demonstrate that the geothermal system significantly increased bridge deck surface temperatures, with both the snow and deck temperatures reaching 0 °C during operation. Moreover, the insulating properties of snow were found to limit the effectiveness of solar radiation alone, highlighting the importance of active heating systems during snowfall events when passive solar input is diminished.

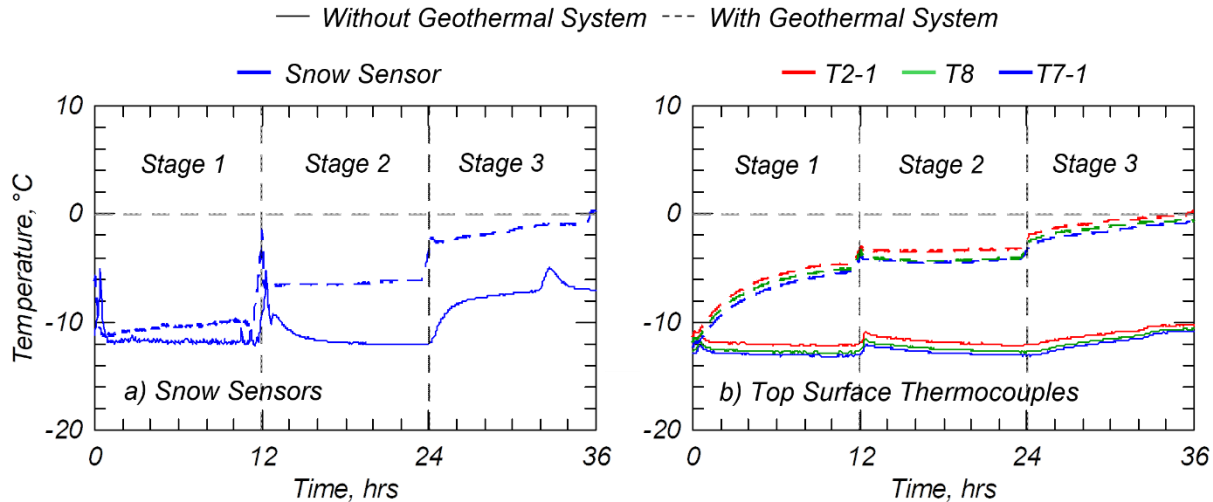


Figure 118. Temperature results for with (dashed lines) and without (solid lines) geothermal system for a) Snow sensors and b) Top surface thermocouples – dashed lines: with the geothermal systems (Stage 1: no snow; Stage 2: with 1 in snow/no solar; Stage 3: with 1 in snow/with solar); solid lines: without geothermal system (Stage 1: no snow; Stage 2: with 3 in snow/no solar; Stage 3: with 3 in snow/with solar)

Application for Mitigating Frost Action

The potential of the geothermal deicing system to mitigate damage caused by frost action was assessed by examining its ability to maintain concrete temperatures above 0 °C throughout the bridge deck depth. Thermocouples TA7-1 through TA7-4 were selected for this analysis, as they provided accurate temperature readings across the deck's depth. Figure 119a and Figure 120a display the temperature data from the TA7 thermocouples for the Synthetic Scenario without and with the deicing system in operation, respectively. Stages 1 and 4 represent periods without solar radiation. Under these conditions, the system increased not only the surface temperature but also the internal temperatures of the concrete. In Stage 1, with the system running, both the top and bottom surfaces stabilized at -5 °C, 5 °C above the ambient air temperature. The internal concrete, as measured by TA7-2 and TA7-3, stabilized at approximately -2 °C due to its proximity to the embedded heat exchanger tubes and insulation from direct ambient exposure. A similar trend occurred in Stage 4, where the top and bottom surfaces stabilized at -11 °C and the internal temperatures reached -8 °C, compared to an ambient temperature of -20 °C. These findings indicate that the surfaces, especially the top and bottom, are the most vulnerable to frost action when solar radiation is absent. Although the system could not maintain temperatures above freezing at all depths during these no-sunlight periods, it still raised the concrete temperature significantly compared to the unheated case.

With the addition of 490 W/m² of simulated solar radiation, the bridge deck's top surface became less susceptible to frost action than the bottom. Stages 2 and 3 of the Synthetic Scenario illustrate this combined effect. In Stage 2, with the system running, the top surface stabilized at 7 °C, while the bottom reached -1 °C. Without the system, all temperature readings were at least 2 °C lower. Similarly, in Stage 3, the system raised the top surface temperature to 2 °C and the bottom to -6 °C, both of which were approximately 7 °C higher than the values recorded without system operation. These results confirm that the system, when combined with solar input, can increase the temperature throughout the concrete deck more effectively than solar energy alone.

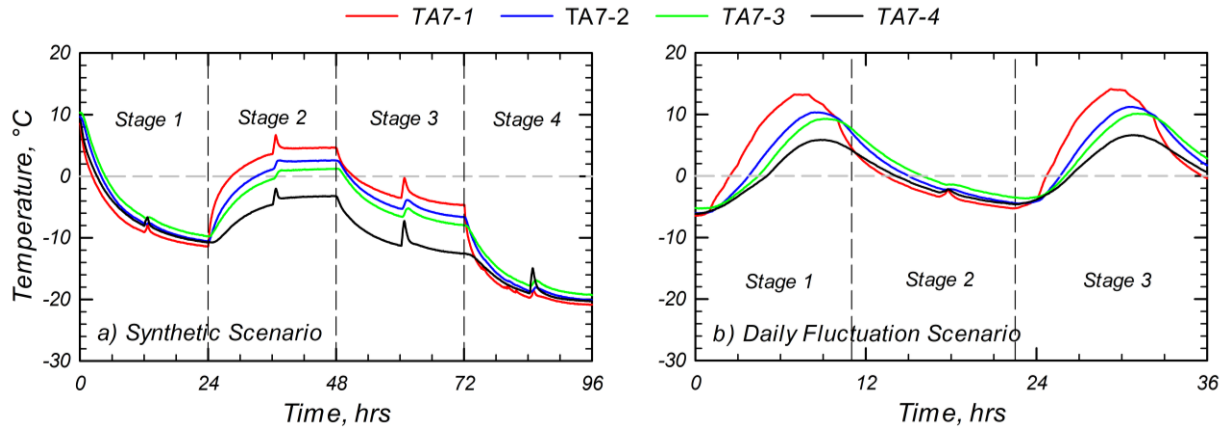


Figure 119. TA7 thermocouple results for a) Synthetic and b) Daily Fluctuation Weather Scenarios without deicing system active

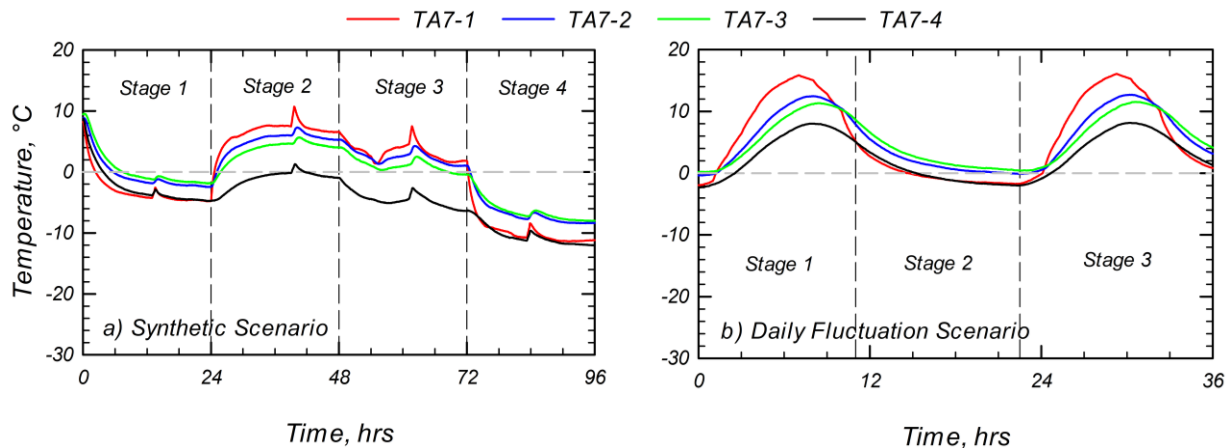


Figure 120. TA7 thermocouple results for a) Synthetic and b) Daily Fluctuation Weather Scenarios with deicing system active.

The Daily Fluctuation Scenario was designed to reflect typical late-winter freeze–thaw cycles in Montana, where ambient temperatures fluctuate above and below 0 °C, and solar intensity varies. Figure 119b and Figure 120b show temperature results for this scenario with and without the deicing system operating. In both cases, the concrete at all depths started below 0 °C, rose above freezing with rising ambient temperatures and solar input, and eventually dropped below freezing again. However, when the system was activated, the concrete warmed more quickly and remained above freezing for a longer duration. Notably, the bottom surface reached 0 °C in just 2.5 hours with the system on, compared to 5 hours without it. Additionally, the bottom surface remained above freezing for 1.5 hours longer with the system. Overall, the system maintained concrete temperatures above 0 °C for 84% of the test duration, compared to just 49% in the unheated case.

While the system did not completely prevent all frost action in the bridge deck under the tested conditions, concrete temperatures at all depths consistently trended warmer when the system was activated across various scenarios. The results indicate that, for the experimental inlet fluid temperature of 8 °C, the concrete temperature is consistently higher with the system running. This suggests that optimizing for higher inlet temperatures could provide sufficient internal warmth to mitigate freeze-thaw risks. Moreover, proactively warming concrete with hydronic circulation

could potentially reduce the severity and frequency of freezing, rather than just tolerating it once it occurs, as seen with AEAs. Preventing the initial temperature triggers proves to be more sustainable than merely enduring strains once they have begun, as is the case with air-entraining approaches.

Application for Mitigating Thermal Stresses

Thermal stresses pose a significant threat to the durability and structural performance of concrete bridge decks. These stresses arise from the combined effects of thermal movements, temperature gradients, and deck support conditions, as illustrated in Figure 121. Axial thermal movements occur when the average concrete temperature through the deck depth fluctuates, causing the entire structure to expand or contract. Temperature gradients, in contrast, represent nonuniform temperature distributions across the depth of the deck and result in differential expansion or contraction between the top and bottom surfaces.

In a simply supported bridge deck, these deformations occur freely and result in strain without stress. However, in a fully restrained system, such movements are resisted by the supports, converting strain into stress. Figure 121 illustrates three representative thermal conditions and their associated stress responses: (1) a uniform temperature profile causing uniform axial movements and, in a restrained case, uniform compressive or tensile stresses; (2) a linear temperature gradient generating both axial and bending stresses; and (3) a nonlinear profile inducing self-equilibrating stresses regardless of support conditions, driven by the requirement for plane sections to remain plane under deformation. When thermal stresses exceed the tensile strength of concrete, cracking initiates, accelerating deterioration by providing pathways for moisture and deicing chemicals, which can lead to steel corrosion. Thus, reducing thermal stresses is essential to prevent cracking, extend service life, and lower maintenance costs.

The geothermal deicing system's ability to mitigate thermally induced cracking was evaluated using Model 1 by assessing its impact on thermal movements and temperature gradients. The model was considered mostly unrestrained due to the low friction between the corrugated steel base and the supporting cinder blocks, which allowed for relatively free expansion, contraction, and bending. Strain resulting from thermal movements was computed using thermocouple data collected during tests with and without the geothermal system activated. Although the calculated strains reflect an unrestrained condition, they can be extrapolated to estimate potential stress development in restrained bridge decks. The strain at any location was calculated using the relation:

$$\varepsilon_c = \alpha_c(T - T_0) \quad (1)$$

where ε_c = the strain in the concrete, α_c = the coefficient of thermal expansion of concrete, T_0 = the reference temperature of the concrete. The relationship between the thermocouple data and strain was validated using the strain gauge results.

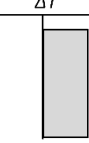
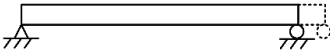


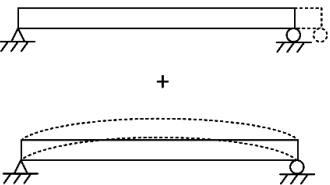
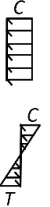
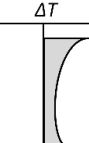
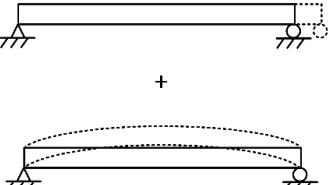


<i>Temperature Profile</i>	<i>Simply-Supported Deflected Shapes</i>	<i>Simply-Supported Stress Behavior</i>	<i>Fully Fixed Stress Behavior</i>
1) 		None	Axial Stress 
2) 		None	Axial Stress + Bending Stress 
3) 		Self-Equilibrating Stress 	Axial Stress + Bending Stress + Self-Equilibrating Stress 

Figure 121. Thermal stress mechanisms due to temperature profiles and support conditions. (regenerated based on Radolli & Green 1975)

Figure 122 compares measured top surface strain with strain estimated using the equation above, assuming a thermal expansion coefficient of $8.5 \mu\epsilon/^\circ\text{C}$, consistent with accepted values for concrete (Alungbe et al., 1992; Mehta & Monteiro, 2014). The strain values are reported relative to each experiment's initial temperature, using T7 thermocouple data. The results show strong agreement between measured and calculated strains, validating the method. Minor discrepancies were attributed to gauge sensitivity and slight restraint effects from reinforcing steel and friction with the formwork.

Figure 123 presents average strain profiles through the depth of the deck for both the Synthetic (Figure 123a) and Daily Fluctuation (Figure 123b) Scenarios, calculated by averaging the T7 thermocouple readings. These profiles capture how the concrete axially expands or contracts with temperature changes. In a restrained system, such strains would manifest as internal stresses. For the Synthetic Scenario without geothermal heating, the strain responses corresponded to temperature changes and solar radiation exposure. Notably, contraction (negative strain) intensified during colder conditions and was mitigated when solar radiation was present. Activating the geothermal system resulted in strain reductions of 41%, 36%, and 46% in Stages 1, 2, and 3, respectively. The largest contraction was observed in Stage 4, reaching $-252 \mu\epsilon$ without the system and $-155 \mu\epsilon$ with the system, representing a 39% reduction. These findings confirm that the system effectively reduces axial thermal movement, thereby lowering the risk of stress-induced cracking in restrained decks.

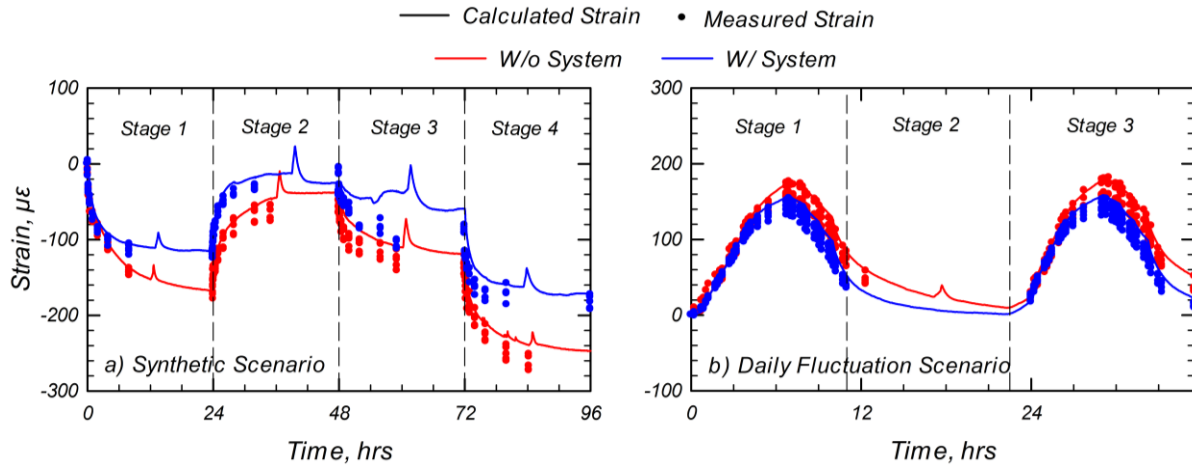


Figure 122. Top surface strains calculated from TA8 and measured from strain gauges for Model 1: a) Synthetic and b) Daily Fluctuation Scenarios

In contrast to the controlled Synthetic Scenario, the Daily Fluctuation Scenario mimicked real-world diurnal temperature variations that prevented thermal stabilization. As shown in Figure 123b, during the initial six hours of the experiment, increasing ambient temperature and solar radiation produced similar strain patterns with and without the geothermal system. However, as peak solar intensity was reached, strain values diverged. The system limited peak strain to $110 \mu\epsilon$, 17% lower than the $133 \mu\epsilon$ recorded without heating, and reached peak strain 30 minutes earlier. The strain remained 20–35 $\mu\epsilon$ lower with the system until hour 19. During the overnight cooling phase (Stage 2), strain values converged as both systems approached equilibrium. This pattern repeated during Stage 3. Throughout the daily cycle, the geothermal system consistently reduced strain amplitudes, helping to moderate thermal stress in realistic ambient conditions.

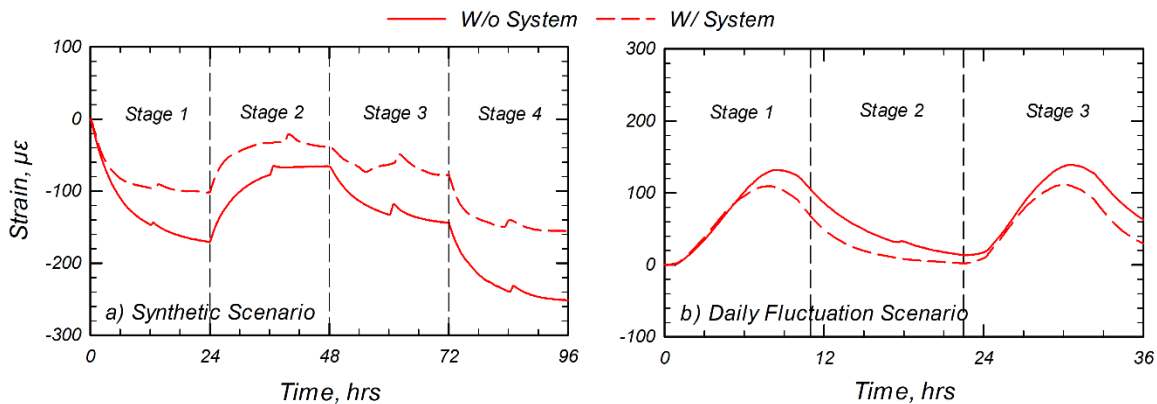


Figure 123. Average strains through depth of Model 1 calculated from TA7 thermocouples for the a) Synthetic and b) Daily Fluctuation Weather Scenarios

Thermal gradient analysis, based on T5 thermocouple readings, is shown in Figure 124 for both test scenarios. These gradients reflect temperature differentials through the deck depth that lead to bending and nonlinearity. In the Synthetic Scenario (Figure 124a), when the geothermal system was inactive, concrete temperatures remained near ambient (-10°C in Stage 1 and -20°C in Stage 4), producing negligible gradients (nearly vertical lines). When the system was active, temperatures increased, but gradients up to 5°C were introduced. Solar radiation in Stages 2 and

3 further contributed to gradients of 7–8 °C between the top and bottom surfaces. The geothermal system increased the gradients by about 1 °C in both stages. These results suggest that while the system elevates internal temperatures, it does not substantially reduce vertical gradients and may even contribute slightly to bending effects. Additionally, nonlinear gradient profiles were observed, where internal temperatures exceeded those predicted by linear interpolation.

The Daily Fluctuation Scenario resulted in more dynamic thermal gradient patterns (Figure 124b). During peak heating (hour 7), top surface temperatures produced 7 °C gradients with or without the system. By hour 9, as lower-layer temperatures peaked, gradients decreased to 5 °C across both conditions. This indicates that the geothermal system had limited influence on bending stress during peak solar loading. Overnight cooling in Stage 2 removed gradients without the system, while the system preserved a mild 2 °C gradient. These cyclical variations suggest the geothermal system maintained warmer, but still nonlinear, temperature profiles without significantly increasing bending stresses.

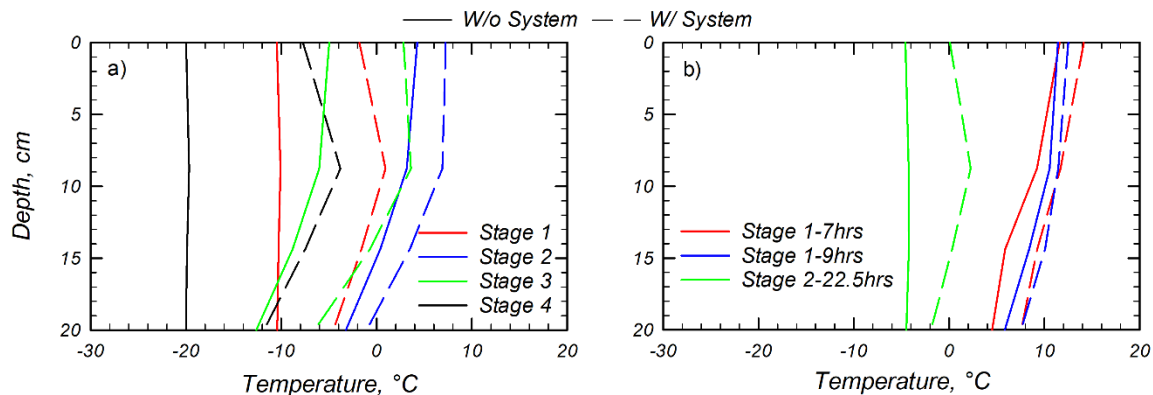


Figure 124. Temperature gradients from TA5 thermocouples for a) Synthetic and b) Daily Fluctuation Weather Scenarios.

Overall, the geothermal system proved effective at reducing axial thermal strains without introducing harmful thermal gradients. During stabilized conditions, strain reductions of approximately 40% were observed, and in fluctuating conditions, peak strain was reduced by 18%. While the system did not significantly affect bending or self-equilibrating stresses, it consistently maintained elevated internal temperatures, supporting its potential to limit freeze–thaw damage and extend service life. The influence of system design parameters, such as tube spacing, tube depth, and inlet fluid temperature, on thermal gradients is notable. Higher inlet fluid temperatures and tighter tube spacing increase heat output, which may elevate thermal gradients and associated bending stresses. Conversely, shallower tube placement can reduce gradient nonlinearity and self-equilibrating stresses but may increase vertical gradients between surface and base. Careful optimization of these variables is essential to improve thermal performance while minimizing adverse structural effects. In the current experimental setup, the system-induced gradients remained within acceptable limits and did not critically exacerbate thermal stress.

Application for Mitigating Early-Age Cracking

Early-age cracking poses a significant risk to concrete bridge decks due to its contribution to accelerated structural deterioration. One key contributor to early-age cracking is thermal shrinkage, which is particularly pronounced in cold weather conditions. As concrete cures in cold

environments, its temperature decreases from the elevated curing temperature to match the colder ambient air. This temperature drop causes the concrete to contract, and when the deck is restrained, such contraction can lead to cracking. To assess the deicing system's potential to mitigate early-age cracking, its ability to reduce thermal shrinkage is evaluated by examining the difference between the maximum concrete temperature during early curing and the final stabilized temperature. Additionally, the compressive strength of Model 2 (with the system) is compared to that of Model 2c (without the system) to determine whether the geothermal heating has any adverse impact on concrete strength.

Figure 125 presents concrete temperature measurements from representative thermocouples at various depths for both Model 2 and Model 2c. As the thermocouples located between and directly above the heat exchanger tubes in Model 2 recorded consistent results, a single thermocouple per depth was sufficient for reporting. The results demonstrate that the geothermal system effectively reduced the temperature drop between curing and stabilization. With an inlet fluid temperature of 8 °C, the concrete in Model 2 stabilized at approximately 4 °C at the top and bottom surfaces, and 5 °C within the internal layers. In contrast, all concrete layers in Model 2c stabilized around the ambient temperature of 2 °C. While the observed reduction in thermal shrinkage was modest, the findings suggest that higher inlet temperatures may further enhance the system's effectiveness in mitigating early-age thermal contraction.

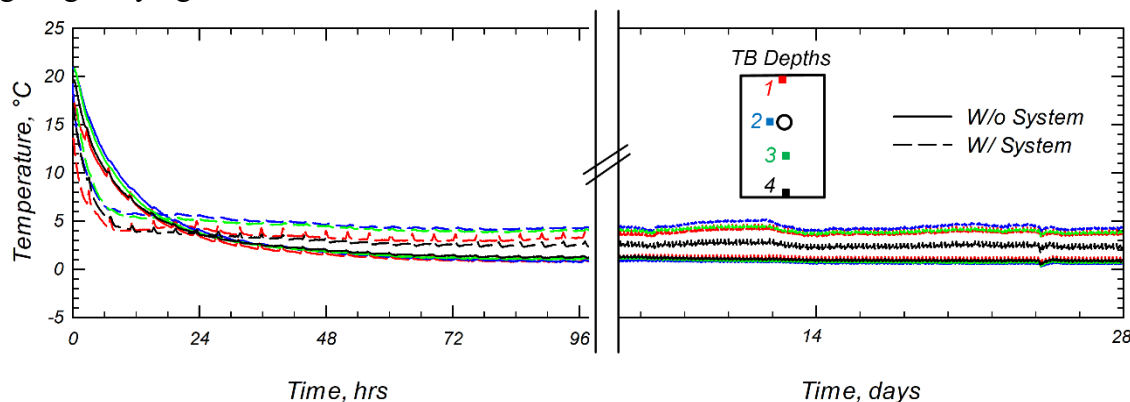


Figure 125. Model 2 (with system) and Model 2c (without system) thermocouple results at each depth.

Core samples were extracted and tested from both Model 2 and Model 2c in accordance with ASTM C42/C42M – 20 (2023). As specified in Section 7.1.2 of the standard, 50.8 mm diameter cores were used due to limited clear spacing between reinforcement. The cores were taken on day 28 and tested on day 35 to allow sufficient time for the elimination of moisture gradients. The average compressive strength of the Model 2 cores (with the geothermal system) was found to be 49% of the ideally cured 28-day compressive strength, whereas the Model 2c cores (without the system) reached 44% of the ideal strength. The lower strength development in both cases is attributed to inhibited hydration resulting from the cold temperatures and reduced moisture conditions within the Cold Hydrodynamics Chamber (CHC). The relatively higher strength observed in Model 2 may be due to the elevated concrete temperatures provided by the geothermal system. Although these initial results are encouraging, further investigation is needed to validate whether geothermal heating during curing consistently enhances concrete strength under cold weather conditions.

CHAPTER 6: NUMERICAL SIMULATION RESULTS

This chapter presents the data collected and analyzed from numerical simulations to evaluate a geothermal deicing system's effectiveness for bridge deck deicing and deterring concrete deterioration. The content in this chapter is adapted from Turner et al. (2024), published in the *Journal of Bridge Engineering*, and is included with permission from the American Society of Civil Engineers (ASCE).

Turner, E., Khosravi, M., Toomani, P., Matteson, K., Plymesser, K., McKittrick, L., & Jackson, J. (2024). Numerical evaluation of applying geothermal bridge deck deicing systems to mitigate concrete deterioration from temperature fluctuations. *Journal of Bridge Engineering*, 29(10), 04024075.

Model Development and Validation

A 3D numerical model of the bridge deck was developed in COMSOL Multiphysics to replicate experimental conditions from Turner et al. (2024a, 2024b). The model incorporated the geometry and material properties detailed in Table 18 and used volumetric averaging to represent zones containing reinforcing steel, rather than modeling the steel explicitly. Heat exchanger tubes were simulated using the Nonisothermal Pipe Flow interface, accounting for thermal conductivity, thickness, and friction losses via the Churchill model. Heat transfer processes, conduction, convection, and radiation, were modeled with the Heat Transfer in Solids interface, with insulated sides and exposed top and bottom surfaces to simulate environmental effects. To evaluate structural performance, the Solid Mechanics interface was used, with boundary conditions mimicking experimental supports. Roller supports and low-stiffness springs were applied to ensure convergence without significantly affecting strain results. Thermal properties for surface conditions are summarized in Table 18, with additional modeling assumptions detailed in the preceding sections.

The numerical model was validated using the results from two different weather scenarios, the Synthetic (Figure 113) and Daily Fluctuation Scenarios (Figure 113b), designed to evaluate system efficiency. Figure 126a and 126b compare experimental and predicted temperature results for the Synthetic and Daily Fluctuation Scenarios, respectively. Temperature results from thermocouples TA8, TA11-2, TA10-3, and TA7-4 were used for validation to provide concrete temperatures at various locations (Figure 100). In the Synthetic Scenario (Figure 126a), strong agreement was observed during Stages 1 and 4, while solar radiation in Stages 2 and 3 introduced discrepancies of up to 1.5 °C, particularly due to modeling limitations in simulating the spatial variation of solar intensity across the bridge deck. A brief solar simulator malfunction during Stage 3 also caused irregularities at the top surface but was quickly resolved. In the Daily Fluctuation Scenario (Figure 126b), good agreement was observed at the top surface throughout, with minor differences in internal and bottom temperatures likely due to complexities in solar radiation modeling. Strain results in Figure 126c (Synthetic Scenario) and 126d (Daily Fluctuation Scenario) showed consistent trends, with predicted and experimental strains aligning well after stabilization. However, slight delays in predicted strain response, approximately one hour, were noted, likely due to challenges in modeling the interaction between concrete and reinforcing steel and the structural boundary conditions.

Table 18 .Material properties of the experimental and numerical models.

<i>Parameter</i>	<i>Experimental</i>	<i>Numerical</i>
<i>Bridge Deck Dimensions</i>		
Length (m)	1.60	1.60
Width (m)	1.00	1.00
Height (cm)	20.00	20.00
Depth of circulation pipes (cm)	8.75	8.75
<i>Circulation Fluid (30% Glycol)</i>		
Flow rate (L/m)	5.50	5.50
Dyncamic Viscosity (mPa·s)	4.80	4.80
Thermal conductivity (W/m·k)	0.40	0.40
Specific heat capacity (J/kg·k)	3538.00	3538.00
Density (kg/m ³)	1070.00	1070.00
<i>Concrete</i>		
Thermal conductivity (W/m·k)	1.00	1.00
Specific heat capacity (J/kg·k)	880.00	880.00
Density (Kg/m ³)	2400.00	2400.00
Coefficient of thermal expansion (µε/°C)	10.00	10.00
Surface emissivity	0.85	0.85
Absorptivity coefficient	0.58	0.58
Top surface convective heat transfer coefficient (W/m ² ·K)	12.00	12.00
Bottom surface convective heat transfer coefficient (W/m ² ·K)	5.00	5.00
<i>Concrete/Rebar Zones</i>		
Top height (cm)	-	9.00
Bottom height (cm)	-	6.67
Top thermal conductivity (W/m.k)	-	1.60
Top specific heat capacity (J/kg.k)	-	874.37
Top density (Kg/m ³)	-	2475.71
Bottom thermal conductivity (W/m.k)	-	2.16
Bottom specific heat capacity (J/kg.k)	-	869.24
Bottom density (Kg/m ³)	-	2544.80

Results and Discussions

Following the development and validation of the numerical model using experimental data, the model was used to simulate system performance under varying conditions representative of Montana's climate. Specifically, two inlet fluid temperatures, 10 °C and 50 °C, were selected based on geothermal well data across the state. A weather program was developed to reflect Montana-specific ambient temperatures and solar radiation conditions, allowing the model to evaluate system behavior under realistic and challenging winter scenarios. Each simulation was run under stabilized conditions to examine the effects of different ambient temperatures and solar intensities, with and without the geothermal system in operation. Transition phases between stages were excluded from the analysis to focus on steady-state thermal behavior.

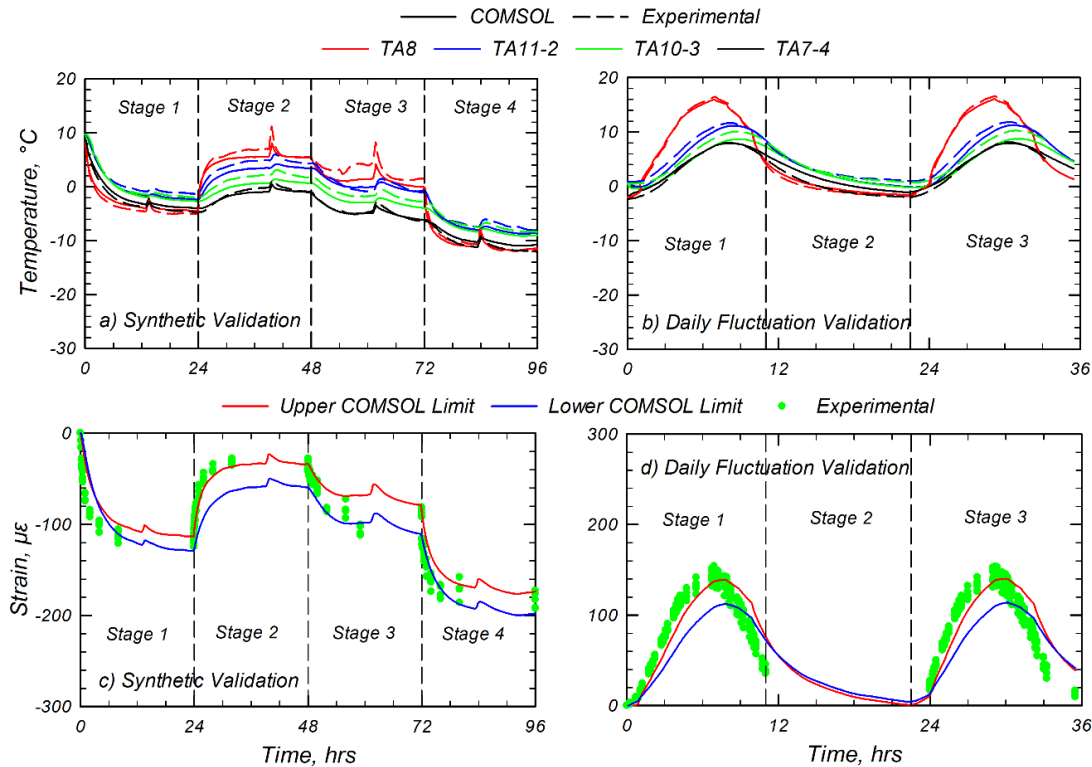


Figure 126. Predicted and experimental temperature results for the (a) Synthetic and (b) Daily Fluctuation Scenarios and strain results for the (c) Synthetic and (d) Daily Fluctuation Scenarios

The top surface temperature of the bridge deck was initially analyzed to assess whether the selected inlet fluid temperatures were sufficient for deicing applications. Once deicing feasibility was confirmed, the model was used to evaluate the system's effectiveness in mitigating frost action by examining whether the minimum concrete temperature remained above 0 °C throughout the various test stages. Maintaining concrete temperatures above freezing, despite subzero ambient conditions, can significantly reduce the number of freeze-thaw cycles experienced by the bridge deck, thereby limiting frost-related damage and deterioration. After analyzing frost mitigation, the study focused on the system's impact on thermal stresses. Thermal stresses in bridge decks arise from thermal movements, temperature gradients, and boundary constraints. Thermal movements, driven by average temperature changes, cause the deck to expand and contract axially. Thermal gradients, on the other hand, are vertical temperature differentials across the depth of the deck, which induce bending due to differential expansion. In unrestrained systems, these temperature-induced strains do not translate into stress; however, in restrained conditions, such as in real bridge decks, supports resist the deformation, generating stress. Additionally, nonlinear temperature gradients can induce self-equilibrating stresses due to strain compatibility through the cross-section.

To quantify these effects, the validated model, based on a mostly unrestrained boundary condition, was used to analyze strains, which can be interpreted as stresses in restrained systems. Axial thermal movements were evaluated using average longitudinal strains, while vertical thermal gradients were analyzed by comparing average temperatures at different depths of the deck. According to AASHTO LRFD Bridge Design Specifications (2021), thermal movement strain can be calculated using the following equation:

$$\varepsilon_T = \alpha(T_{MaxDesign} - T_{MinDesign}) \quad (12)$$

where α is the coefficient of thermal expansion ($\mu\epsilon/^\circ\text{C}$) and $T_{MaxDesign}$ and $T_{MinDesign}$ the design temperature limits from AASHTO (2021). For Montana, the maximum and minimum design temperatures are 41°C and -40°C , respectively. Based on the material properties in Table 17 **Error! Reference source not found.**, the maximum design strain due to thermal movement was calculated to be $810 \mu\epsilon$. The simulations, which ranged from ambient temperatures of 0°C to -20°C , remained well within this design limit.

Design temperature gradients were also evaluated following AASHTO guidelines (2021), as illustrated in Figure 127a. For Montana, positive temperature gradients, when the top surface is warmer, were 8°C and 30°C between the bottom and middle and between the bottom and top, respectively. Negative gradients, when the bottom is warmer, were -2°C and -9°C over the same layers (Figure 127b). Simulated temperature gradients, with and without the geothermal system, were compared to these design values to confirm that they fall within acceptable structural design thresholds. This analysis highlights the potential of geothermal systems not only for deicing but also for reducing thermal stresses and extending the service life of concrete bridge decks.

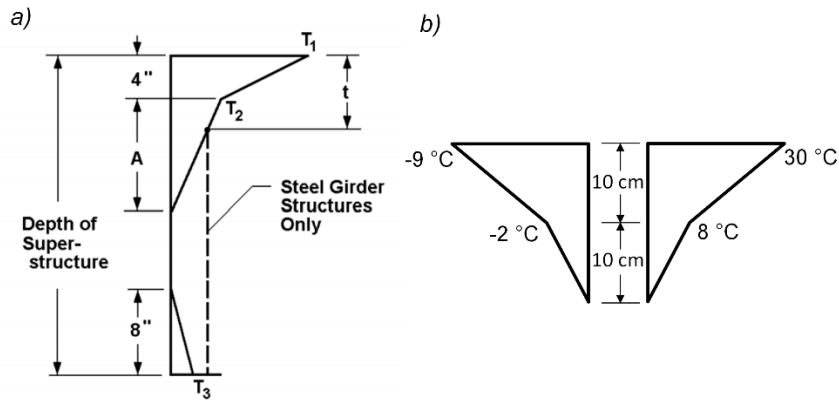


Figure 127. (a) Positive vertical temperature gradient in concrete and steel superstructures (AASHTO 2021) and (b) positive vertical temperature gradient for bridge deck in Montana

Application with 10°C Inlet Fluid Temperature

The effectiveness of the geothermal deicing system in maintaining the average surface temperature of the bridge deck above 0°C was assessed using an inlet fluid temperature of 10°C . Figure 128a presents the average top surface temperatures across different testing stages, both with and without the system activated. Without solar radiation, the system was unable to raise the stabilized surface temperature above freezing. During Stages 1, 4, and 5, the system yielded stabilized surface temperatures of -2°C , -6°C , and -13°C , respectively, consistently higher than the ambient-equilibrated temperatures observed when the system was off. Although the surface remained below freezing, the geothermal system raised the temperature by an average of 5°C compared to the control. When solar radiation was introduced in Stages 2 and 3, surface temperatures exceeded 0°C in both cases. Stage 2 recorded surface temperatures of 10°C with the system on and 9°C without it, while Stage 3 temperatures were 6°C with the system and 4°C without. However, in Stage 6, despite solar input, the surface temperatures dropped below freezing again, registering -1°C with the system and -6°C without it.

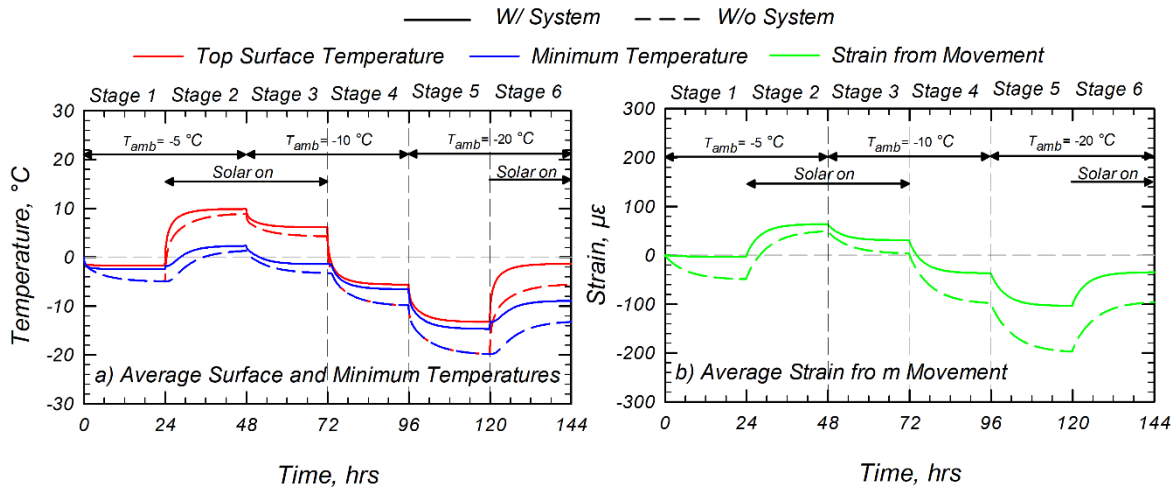


Figure 128. (a) Average surface and minimum temperature and (b) average strain from thermal movement for 10 °C inlet temperature

Figure 128a also illustrates the minimum concrete temperatures throughout the test duration using the 10 °C inlet fluid temperature. Among all stages, only Stage 2, where solar radiation was present, resulted in minimum temperatures above 0 °C, with recorded values of 2 °C and 1 °C for the system-on and system-off cases, respectively. In all other stages, the minimum temperature remained below freezing, regardless of whether the geothermal system was operating. Although the system consistently increased minimum concrete temperatures, it did not reduce the total number of freeze-thaw cycles experienced by the deck. Therefore, to effectively mitigate frost action, the system must prevent the concrete from falling below freezing altogether, a condition not met with an inlet temperature of 10 °C under Montana weather scenarios.

The effect of the system on thermally induced strain due to thermal movements is shown in Figure 128b. In a fully restrained bridge deck, such thermal movements translate directly into internal stresses. The simulations revealed that the system increased the stabilized strain values across all stages, with the largest and smallest differences observed during Stages 5 and 2, at 94 με and 15 με, respectively. Importantly, the overall range of thermal movement strain was reduced by 32%, from 247 με without the system to 167 με with it. This is well below the AASHTO (2021) maximum allowable design strain of 810 με for Montana (Equation 12). These findings indicate that the system effectively mitigates thermal movement effects. The reduction in strain range implies a corresponding reduction in stress for a fully restrained deck. Additionally, the increased strain levels observed with the system reflect a reduction in deck contraction, which is beneficial, as contraction tends to produce tensile stresses, more detrimental to concrete than compressive stresses associated with expansion.

Figure 129 presents the stabilized vertical temperature gradients across all testing stages with the 10 °C inlet fluid temperature. In the absence of solar radiation and system operation, no gradients were observed, as the deck equilibrated to ambient conditions. However, when the geothermal system was active, the top surface was consistently cooler than the bottom surface due to a higher convective heat transfer coefficient at the top boundary (as specified in Table 17). The greatest temperature gradient under these conditions was -1 °C, observed during Stage 5. These gradients were non-linear, which can introduce self-equilibrating stresses within the deck.

When solar radiation was included, temperature gradients were evident both with and without system operation. The maximum difference in gradient magnitude between the two cases was only 1 °C, and most gradients remained linear with minor deviations. All observed gradients remained well below the design temperature gradients specified by AASHTO for Montana (Figure 127b). Thus, while the system did not significantly reduce temperature gradients, it also did not introduce any thermally induced stresses that would exceed allowable design thresholds. The induced gradients, although slightly larger with system operation, remained within safe and acceptable limits.

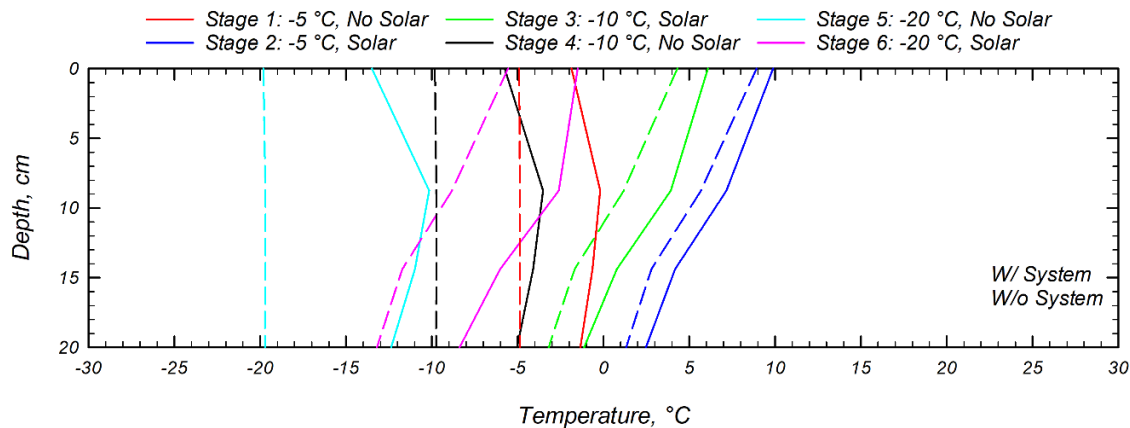


Figure 129. Temperature profile through the bridge deck for 10 °C inlet temperature

Application with 50 °C Inlet Fluid Temperature

Figure 130a illustrates the average top surface temperatures observed across all test stages for an inlet fluid temperature of 50 °C, comparing conditions with and without the geothermal system activated. The system successfully raised the surface temperature above 0 °C in five out of six stages. The only exception was Stage 5, which combined a low ambient temperature of -20 °C with no solar radiation, conditions representative of rare, extreme Montana winters. In this case, while the surface temperature did not reach 0 °C, it still stabilized at -4 °C with the system operating, which was 16 °C warmer than without the system. In Stages 1 and 4, the geothermal system increased surface temperatures to 7 °C and 3 °C, respectively, while temperatures without the system were 12 °C and 13 °C lower. During stages with solar input (Stages 2, 3, and 6), the system maintained an average surface temperature 11 °C higher than the control case. These results indicate that a 50 °C inlet temperature is generally effective for surface deicing under typical Montana winter conditions.

Figure 130b shows the corresponding minimum concrete temperatures. Similar to the surface temperature results, the geothermal system kept the minimum temperature above 0 °C in all but Stage 5. Without the system, minimum temperatures in Stage 5 dropped to -20 °C, while the system raised them to -8 °C. For the non-solar stages (Stages 1 and 4), the system performed well, raising the minimum concrete temperature to 4 °C and approximately 0 °C, respectively, representing increases of 9 °C and 10 °C over the non-heated cases. In solar-assisted stages, minimum temperatures exceeded 0 °C in all cases when the system was running. Notably, only Stage 2 achieved this threshold without system assistance. On average, the geothermal system raised the minimum temperature by 11 °C across the full set of simulations. These findings demonstrate that the system significantly mitigates the potential for frost action by minimizing freeze-thaw cycles.

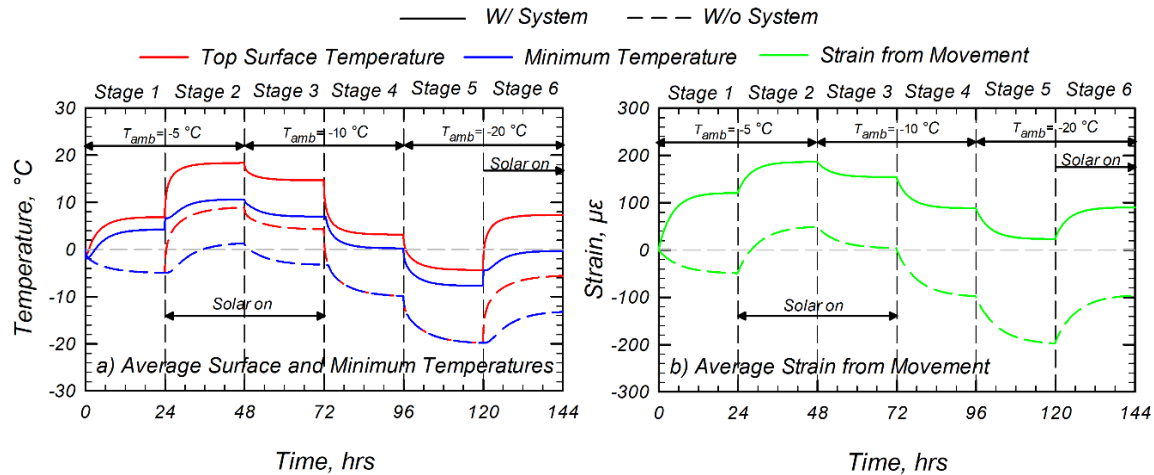


Figure 130. (a) Average surface and minimum temperature and (b) average strain from thermal movement for 50 °C inlet temperature

The system's impact on thermal movements is illustrated in Figure 130b, which compares average strain with and without the geothermal system. Across all stages, stabilized strains were higher with the system in operation, indicating reduced contraction. The strain difference ranged from 137 $\mu\epsilon$ in Stage 2 to a maximum of 221 $\mu\epsilon$ in Stage 5. Additionally, the overall strain range decreased from 247 $\mu\epsilon$ without the system to 163 $\mu\epsilon$ with the system, a 40% reduction. These values remain well below the maximum design strain of 810 $\mu\epsilon$ specified by AASHTO. A similar strain reduction trend was observed in simulations using a 10 °C inlet temperature, but the 50 °C condition yielded larger strains and smaller contraction, confirming superior performance in reducing thermal movements.

Figure 131 displays the stabilized vertical temperature gradients for each test stage with an inlet temperature of 50 °C. In stages without solar radiation, no noticeable gradients were observed without the system. When the geothermal system was active, the bottom surface became up to 3 °C warmer during Stage 5. For stages with solar radiation, the temperature difference between the top and bottom surfaces did not exceed 2 °C when comparing system-on and system-off conditions. Regardless of solar input, the higher inlet temperature created nonlinear temperature gradients across the deck depth. This nonlinearity led to exceedance of AASHTO's design temperature gradient limits in isolated cases. Specifically, during Stage 5, a negative gradient of -8 °C was observed between the top and middle surfaces, surpassing the AASHTO design limit of -7 °C (Figure 127). Similarly, in Stage 6, the positive gradient between the bottom and middle surfaces reached 9 °C, slightly exceeding the 8 °C design threshold. While these gradients exceeded the allowable limits, the margin was only 1 °C and occurred only under extreme ambient conditions of -20 °C. In all other scenarios, the gradients remained within AASHTO-specified limits (Figure 127). Although these exceedances highlight a potential design concern, they were limited to rare weather events and do not significantly undermine the overall effectiveness of the system.

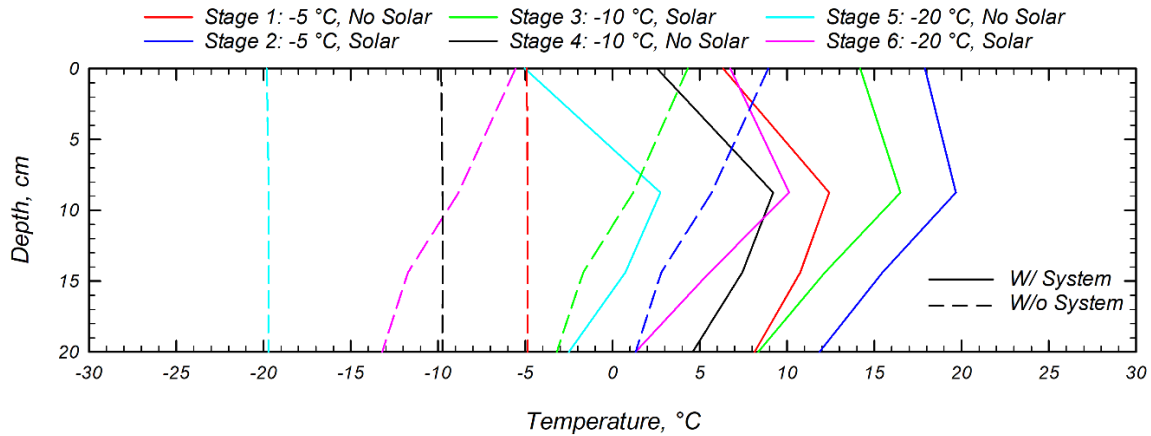


Figure 131. Temperature profile through the bridge deck for 50 °C inlet temperature

Sensitivity Analysis

To evaluate the relative impact of different system parameters on the geothermal bridge deck deicing system, tornado diagrams were developed for scenarios both with and without solar radiation. These diagrams illustrate how various parameters influence the system's ability to deice surfaces and mitigate frost action, thermal movements, and vertical thermal gradients. The baseline configuration consisted of an inlet fluid temperature of 10 °C, a tube spacing of 20 cm, and an ambient temperature of -10 °C. The choice of a 10 °C inlet was based on its much higher likelihood in Montana compared to 50 °C, according to well temperature data. A higher inlet temperature scenario (50 °C) may be relevant near geothermal hotspots, but assessing that scenario would require a separate sensitivity analysis. A temperature range from 4 °C to 16 °C was also considered, representing the 95% confidence interval from Montana geothermal well distributions. The baseline tube spacing of 20 cm was selected based on prior studies (Ghasemi-Fare et al. 2015; Bowers 2016), with additional tests at 10 cm and 30 cm to capture feasible variations. Ambient temperatures of -5 °C, -10 °C, and -20 °C were drawn from historical Montana weather records and previously tested simulations, with -10 °C serving as the baseline to illustrate effects of both increasing and decreasing temperature conditions.

As shown in Figure 132a, ambient temperature had the most significant impact on top surface temperatures in simulations without solar radiation. For the baseline scenario at -10 °C, the surface stabilized at -5.6 °C. When ambient temperature dropped to -20 °C, the surface temperature fell sharply to -13.2 °C, while increasing it to -5 °C raised the surface temperature to -1.7 °C, resulting in a total range of 11.5 °C. By contrast, inlet temperature adjustments only affected the surface by 2.6 °C, ranging from -6.9 °C to -4.3 °C. Changes in tube spacing had an even smaller influence, producing temperatures between -6.3 °C and -3.8 °C, a 2.5 °C range. When solar radiation was included (Figure 132b), ambient temperature continued to dominate, with surface temperatures ranging from -1.3 °C to 9.9 °C, an 11.2 °C shift. Inlet temperature effects remained consistent at 2.6 °C (4.9 °C to 7.5 °C), while the impact of tube spacing was further diminished to just a 1.1 °C change (5.8 °C to 6.9 °C).

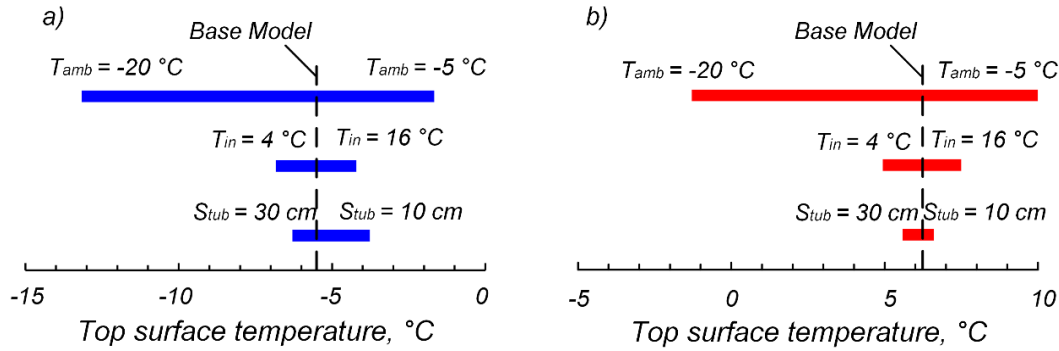


Figure 132. Effect of various parameters on top surface temperature (a) without and (b) with solar radiation

Similar trends were observed for the minimum internal concrete temperatures, as shown in Figure 133. Without solar radiation, the baseline model yielded a minimum temperature of -6.5 °C. Ambient temperature once again had the strongest effect, with variations producing a range from -14.7 °C to -2.9 °C, a 12.2 °C difference. Inlet temperature and tube spacing changes each caused a smaller but equal 2.0 °C shift: inlet temperature varied results from -7.6 °C to -5.5 °C, and tube spacing ranged from -7.8 °C to -5.8 °C. Under solar radiation, the minimum temperature in the baseline scenario increased to -1.4 °C. Ambient temperature still drove the largest change (11.3 °C), shifting results from -8.9 °C to 2.4 °C. Inlet fluid adjustments had a 2.6 °C effect, while tube spacing effects dropped to just 1.0 °C (ranging from -2.0 °C to -1.0 °C).

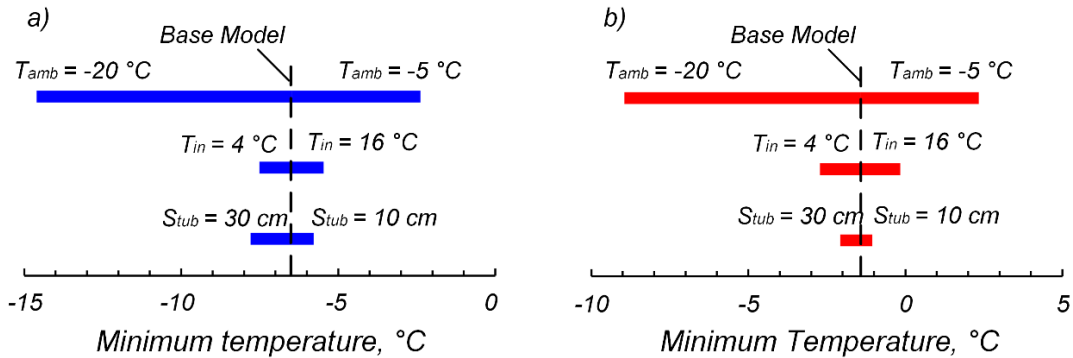


Figure 133. Effect of various parameters on the minimum concrete temperature (a) without and (b) with solar radiation

When evaluating strain due to thermal movement (Figure 134a), the influence of ambient temperature persisted but with relatively smaller margins compared to temperature values. Without solar radiation, the baseline strain was -36.5 $\mu\epsilon$. Ambient temperature shifts produced strains between -103.4 $\mu\epsilon$ and -2.9 $\mu\epsilon$, a 100.4 $\mu\epsilon$ range. Inlet fluid temperature adjustments resulted in a 37.5 $\mu\epsilon$ change (from -55.5 $\mu\epsilon$ to -17.9 $\mu\epsilon$), while tube spacing produced a nearly identical effect of 35.8 $\mu\epsilon$ (from -47.5 $\mu\epsilon$ to -11.7 $\mu\epsilon$). With solar radiation (Figure 134b), the baseline strain increased to 31.0 $\mu\epsilon$. Ambient temperature still caused the largest variation (from -34.9 $\mu\epsilon$ to 63.9 $\mu\epsilon$, a 98.8 $\mu\epsilon$ range), while inlet temperature and tube spacing produced changes of 37.3 $\mu\epsilon$ and 15.9 $\mu\epsilon$, respectively.

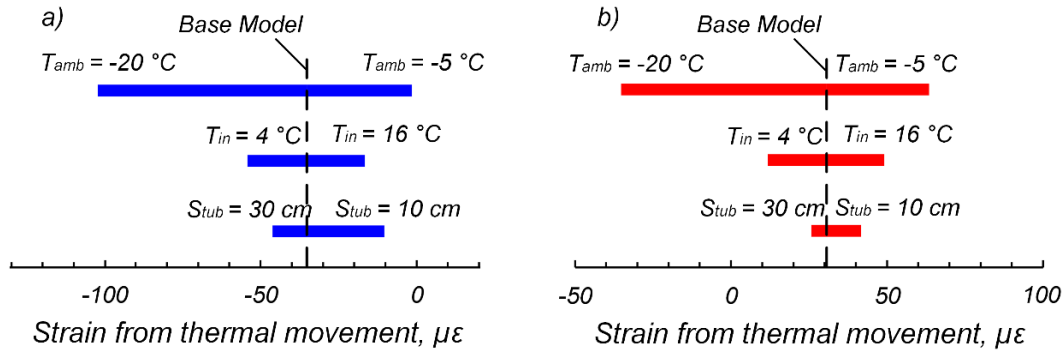


Figure 134. Effect of various parameters on strain due to thermal movement (a) without and (b) with solar radiation

Analysis of vertical thermal gradients between the top and bottom of the concrete deck revealed distinct trends (Figure 135a). Without solar radiation, the baseline model produced a gradient of 0.6°C . While ambient temperature remained the most influential factor, its impact was modest, altering gradients from 0.4°C to 0.9°C , a 0.5°C shift. Inlet temperature and tube spacing each produced similar effects, ranging from 0.4°C to 0.7°C . When solar radiation was introduced (Figure 135b), the baseline gradient rose significantly to 7.3°C . Yet even under these conditions, the impact of individual parameters was minimal: ambient temperature produced only a 0.4°C change, inlet fluid temperature 0.3°C , and tube spacing just 0.1°C . Overall, the vertical temperature gradients remained largely consistent across the scenarios, indicating that this performance metric is relatively insensitive to changes in the studied parameters.

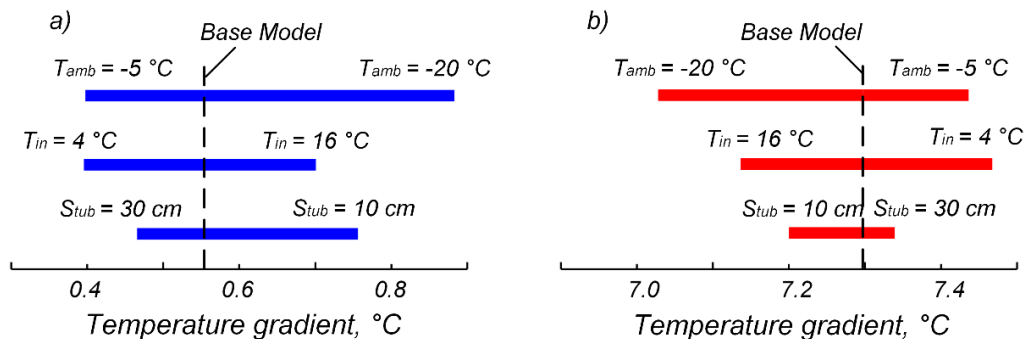


Figure 135. Effect of various parameters on the temperature gradient between the top and bottom surfaces (a) without and (b) with solar radiation

CHAPTER 7: MACHINE LEARNING BASED FEASIBILITY ANALYSIS OF GEOTHERMAL BRIDGE DECK DEICING SYSTEMS IN MONTANA

Bridge decks in cold regions like Montana are prone to rapid snow accumulation, freeze–thaw cycling, and premature deterioration due to their full exposure to ambient conditions. Traditional deicing methods, primarily involving salts and plowing, pose environmental risks, degrade infrastructure, and require frequent reapplication during storms. As a sustainable alternative, geothermal bridge deck deicing systems, particularly those based on ground-source heat pumps (GSHPs), offer a promising low-energy solution for maintaining safe winter travel conditions. However, their feasibility is highly site-specific, dependent on local climate, soil thermal properties, and bridge geometry, which complicates broad implementation. To address this challenge, this chapter presents a two-pronged feasibility analysis framework comprising:

1. A deterministic simulation-based approach using geospatial datasets, and
2. A machine learning (ML)-based predictive modeling framework trained on over 2,000 high-fidelity numerical simulations.

The chapter begins by detailing the data collection and preprocessing strategy, which integrates diverse environmental and infrastructure datasets across Montana. These include ambient and surface temperature profiles, wind speed, solar radiation, soil thermal properties, and geothermal gradients, obtained from RWIS stations, borehole records, and GIS sources. The data are statistically processed, interpolated, and mapped to inform boundary conditions for numerical simulations and machine learning models.

Next, the chapter presents a deterministic feasibility analysis based on a GIS-integrated energy modeling framework. The methodology involves computing the shallow geothermal potential across Montana using the G.POT method, which incorporates ground thermal conductivity, undisturbed ground temperature, borehole design parameters, and heating season duration. In parallel, the net thermal energy demand for bridge deck deicing and cooling is estimated using an energy balance approach that accounts for shortwave solar radiation, convective and sensible heat exchange, and latent heat effects. These energy supply and demand maps are used to evaluate the thermal compatibility of geothermal systems across the state. The analysis categorizes Montana into heating-dominant, cooling-dominant, and mixed zones, enabling spatial prioritization for system deployment based on thermal feasibility.

Finally, the chapter introduces a machine learning-based feasibility framework built upon a validated 3D COMSOL Multiphysics model, which simulates heat transfer in geothermal bridge deck systems under varying environmental and design conditions. Parametric studies were used to identify key input features, including ambient temperature, wind speed, solar radiation, inlet fluid temperature, flow rate, tube spacing, and bridge length, which were used to generate a structured dataset of over 2,000 simulations. Two supervised learning models were developed: Model 1 predicts system-level performance indicators (e.g., stabilized surface temperature, time to $>0^{\circ}\text{C}$, and time to stabilize), while Model 2 reconstructs full surface temperature profiles at 0.1-hour resolution. A variety of ML algorithms (e.g., linear regression, XGBoost, fully connected neural networks) were trained and evaluated using standard metrics (MAE, RMSE, R^2). The final models

enable rapid, scalable predictions that emulate the thermal response of complex simulations, supporting efficient design and assessment of geothermal deicing systems across diverse site conditions.

Data Collection/Simulation and Preprocessing

This section outlines the data collection, simulation setup, and preprocessing steps used to support both the GIS-based deterministic energy analysis and the machine learning (ML)-based predictive modeling framework. For the deterministic analysis, statewide datasets, including ground thermal conductivity, undisturbed ground temperature, and borehole parameters, were compiled to estimate geothermal energy availability using the G.POT method. Meteorological datasets, such as ambient temperature, solar radiation, and wind speed, were similarly processed to quantify the thermal demand for bridge deck deicing and cooling. For the ML-based approach, a high-fidelity 3D numerical model was developed in COMSOL Multiphysics and validated using experimental data from Turner et al. (2024). Once validated, this model was used to generate simulation outputs under a wide range of conditions. The input ranges for these simulations were derived from statistical analysis of localized environmental data (e.g., RWIS-based ambient temperature, wind speed, and solar radiation) and geothermal ground temperature distributions (e.g., borehole and well data across Montana). Bridge-specific design variables, such as inlet temperature, fluid flow rate, tube spacing, and bridge length, were also included. This process resulted in a large, structured dataset used to train and validate ML models. Across both workflows, data preprocessing ensured spatial consistency, physical relevance, and statistical robustness to support accurate, scalable evaluation of geothermal bridge deck systems.

Bridge Locations and Highways

Bridge location data was collected from MDT (MDT, 2022). Figure 136(a) shows the geospatial distribution of bridge structures overlaid with major state and federal highways. Data for the electric transmission line locations was obtained from Homeland Infrastructure Foundation-Level Data (HIFLD, 2022). Figure 136(b) shows the locations of electric transmission lines in Montana. Although geothermal deicing systems primarily rely on subsurface heat, they may require electrical components for pumping, control systems, or hybrid integration with solar or grid power. Therefore, the availability and proximity of electrical infrastructure can influence installation feasibility. Proximity to these lines can significantly reduce the cost and complexity of integrating monitoring sensors, programmable thermostats, and auxiliary heating components in a geothermal deicing system.

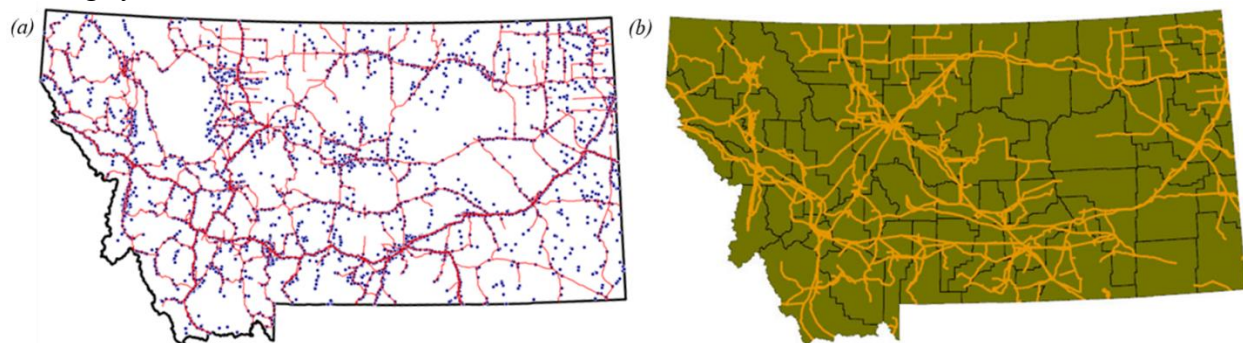


Figure 136. (a) Map of bridges and major roads, and (b) electric transmission lines locations in Montana

Meteorological Data

The datasets used in this study were sourced from the Montana Department of Transportation's Road Weather Information System (RWIS), which provides continuous, high-resolution environmental monitoring across the state. RWIS includes 73 stations strategically located across Montana's varied landscapes, including mountainous areas, valleys, and plains, ensuring comprehensive spatial coverage (Al-Kaisy & Ewan, 2017). Each station records a range of meteorological variables critical to winter road maintenance, including ambient temperature, wind speed and direction, pavement temperature, humidity, solar radiation, and precipitation. For this study, data from 24 RWIS stations with complete records were selected (Figure 137). A four-year dataset (2016–2019) was used to develop climate time series, monthly averages, and cumulative distributions, capturing both seasonal variability and extreme weather conditions relevant to geothermal system performance.

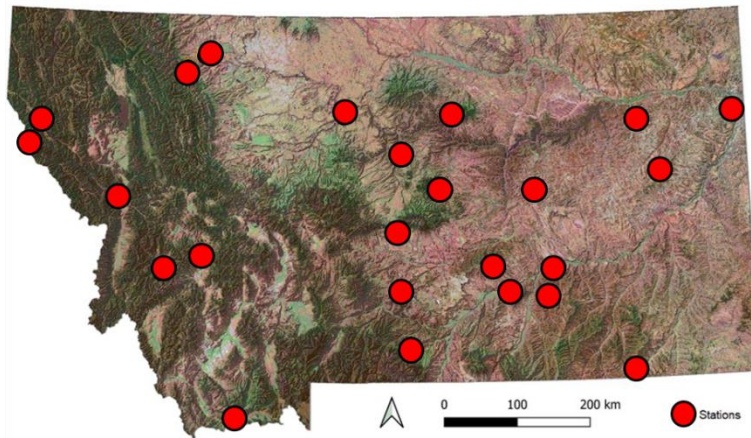


Figure 137. Locations of MDT RWIS stations across Montana

Ambient Temperature: Figure 138(a) shows the locations of the 73 RWIS stations in Montana. Figure 138(b) shows the distribution histogram of average ambient temperature for Montana. Temperature data were recorded at 10-minute intervals from 2016 to 2019 at 24 locations across the state. For each 12-hour period, the average temperature was calculated as the mean of all 10-minute readings, while the maximum and minimum represent the highest and lowest values within that same interval. These 12-hour average, maximum, and minimum temperatures were used for analysis. Figure 138(c) presents the time series of ambient temperatures for site ID 150000, located west of Montana, including the average, maximum, and minimum temperature values. The plot shows the maximum, average and minimum ambient temperature values for 2016-2019. The data show that a bridge deck deicing system should be designed for the months of November through March because they have the lowest average temperatures, as low as -10°C .

Figure 139 illustrates the spatial distribution of monthly average ambient temperatures across Montana. The coldest conditions occur from November through February, with average temperatures dropping below -10°C in northern and high-elevation regions, and minimum values reaching -19.2°C in January. In contrast, the warmest months, June through August, exhibit widespread average temperatures above 20°C , peaking at 33.0°C in July. This seasonal variability is critical for identifying operational windows for geothermal system activation and informs the

selection of representative temperature inputs for both deterministic energy calculations and numerical simulation scenarios.

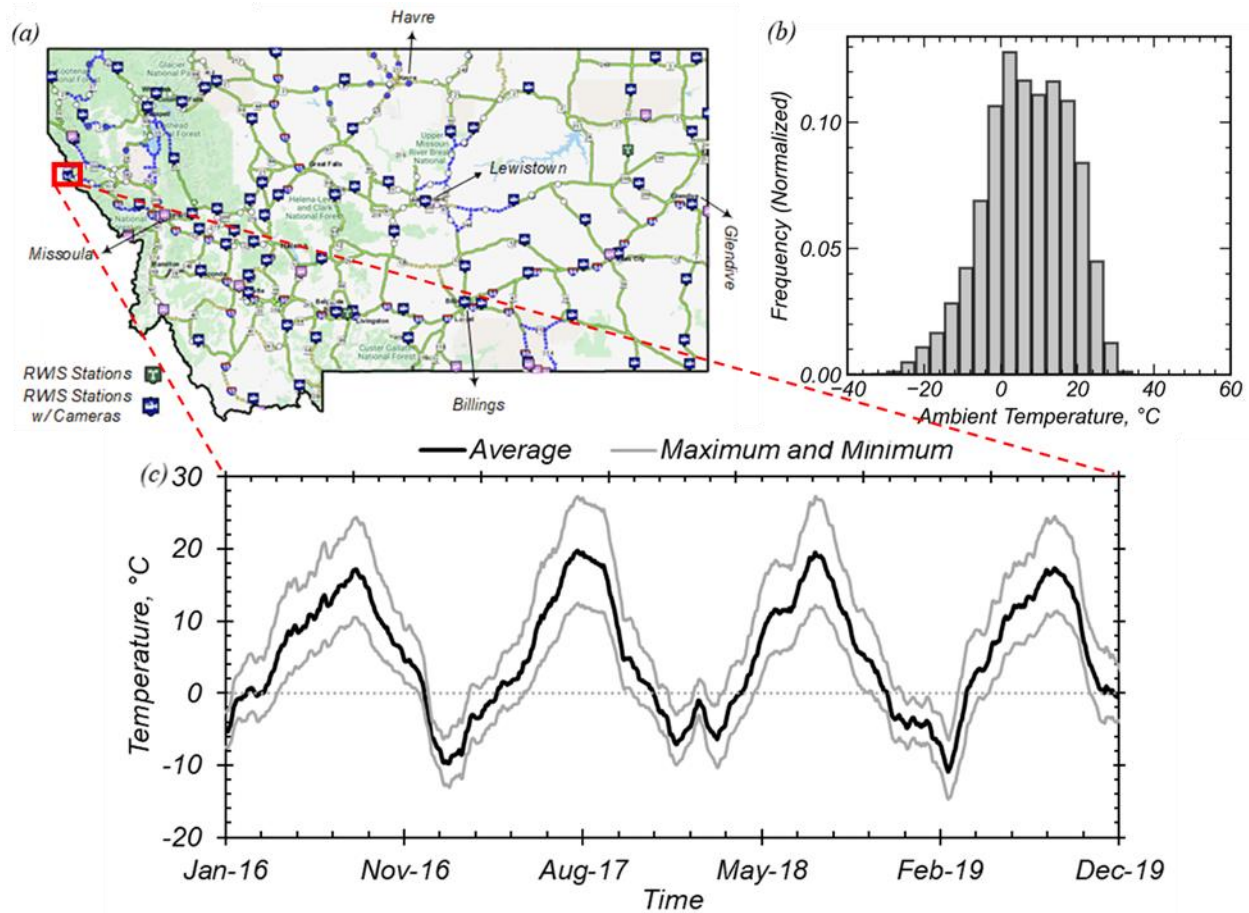


Figure 138. (a) Locations of MDT RWIS sites (map source: <https://roadreport.mdt.gov/>), (b) average ambient temperature distribution histogram for Montana, and (c) time series of ambient temperatures for 2016–2019 (site ID 150000)

Wind Speed: Figure 140 presents the statistical distribution and spatial variability of wind speed across Montana, based on measurements from 26 monitoring stations. Figure 140(a) displays the normalized frequency histogram of recorded wind speeds. The distribution exhibits a pronounced positive skew, with the majority of wind speeds concentrated between approximately 5 km/h and 20 km/h, and a peak frequency occurring near 10 km/h. The tail of the distribution extends toward higher wind speeds, with occasional events reaching up to 50–60 km/h, although these occurrences are relatively rare. This distribution shows that moderate wind conditions are common across the state, with extreme wind events being infrequent. Figure 140(b) shows the spatial distribution of the coefficient of variation (COV) of wind speed across the 26 station locations. The coefficient of variation, defined as:

$$\text{COV} = \sigma / \mu \quad (1)$$

where σ is the standard deviation and μ is the mean wind speed. This provides a normalized measure of variability relative to the mean value.

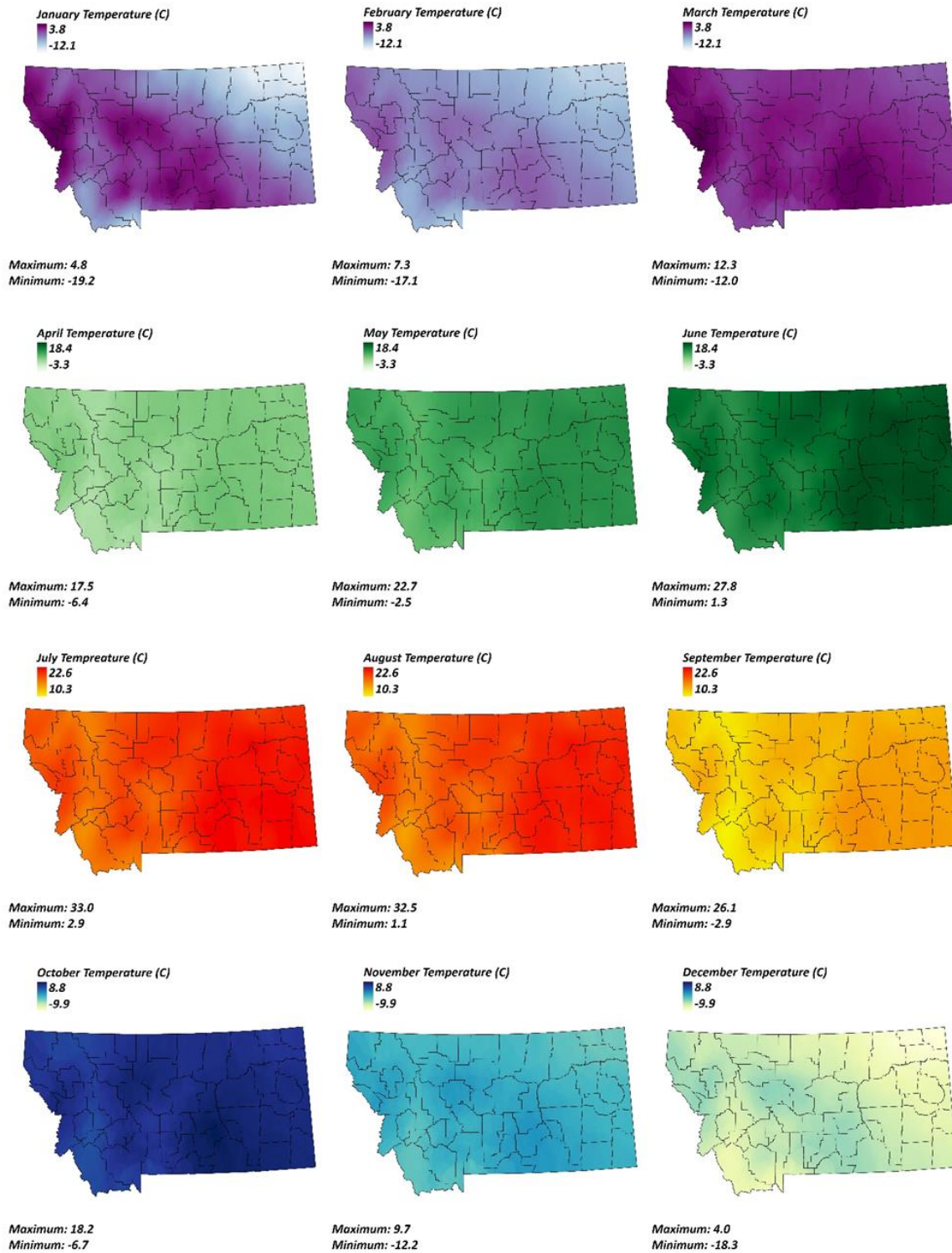


Figure 139. Monthly average ambient temperature across Montana

Spatially, the COV values vary from approximately 0.45 to 0.82 across the state. Higher COV values, indicated by yellow and green markers, suggest regions where wind speed is highly variable relative to the mean, whereas lower COV values (purple hues) represent areas with more consistent wind conditions. Notably, some western and southern parts of Montana show more variability in wind speeds. Higher and more variable wind speeds can significantly increase convective heat loss from the bridge surface during winter conditions, leading to lower surface temperatures. As a result, geothermal systems would require additional energy input to maintain the bridge deck above freezing. Both the average wind speeds and their variability are therefore important for predicting operational efficiency of geothermal deicing systems across Montana.

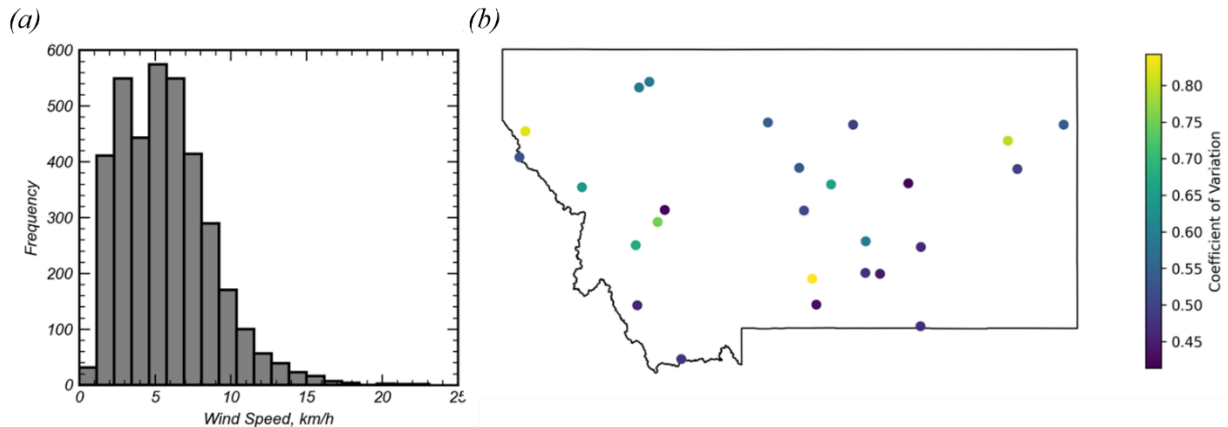


Figure 140. a) Histogram of wind speed distribution, and b) Coefficient of variation for wind speed in Montana

Figure 141 presents monthly average precipitation across Montana, including both total depth and partitioning between rainfall and snowfall. Snow accumulation plays a dual role in geothermal bridge deck performance: it modifies thermal boundary conditions by acting as an insulating layer, reducing convective and radiative heat losses, while simultaneously increasing the system's thermal load due to the energy required for snow melting and phase change. The figure reveals that peak snowfall occurs from November through March, with over 80% of precipitation falling as snow during these months. In contrast, precipitation during June through September is dominated by rainfall, with nearly 100% of precipitation falling as rain in July and August. Spatially, western and mountainous regions receive significantly higher precipitation volumes year-round, while eastern plains experience lower but more uniform distributions. These temporal and spatial patterns have important implications for geothermal system design. Regions with high winter snowfall not only face more frequent icing events but also require greater energy capacity for snow removal, making accurate precipitation modeling essential for system sizing, activation scheduling, and energy demand forecasting.

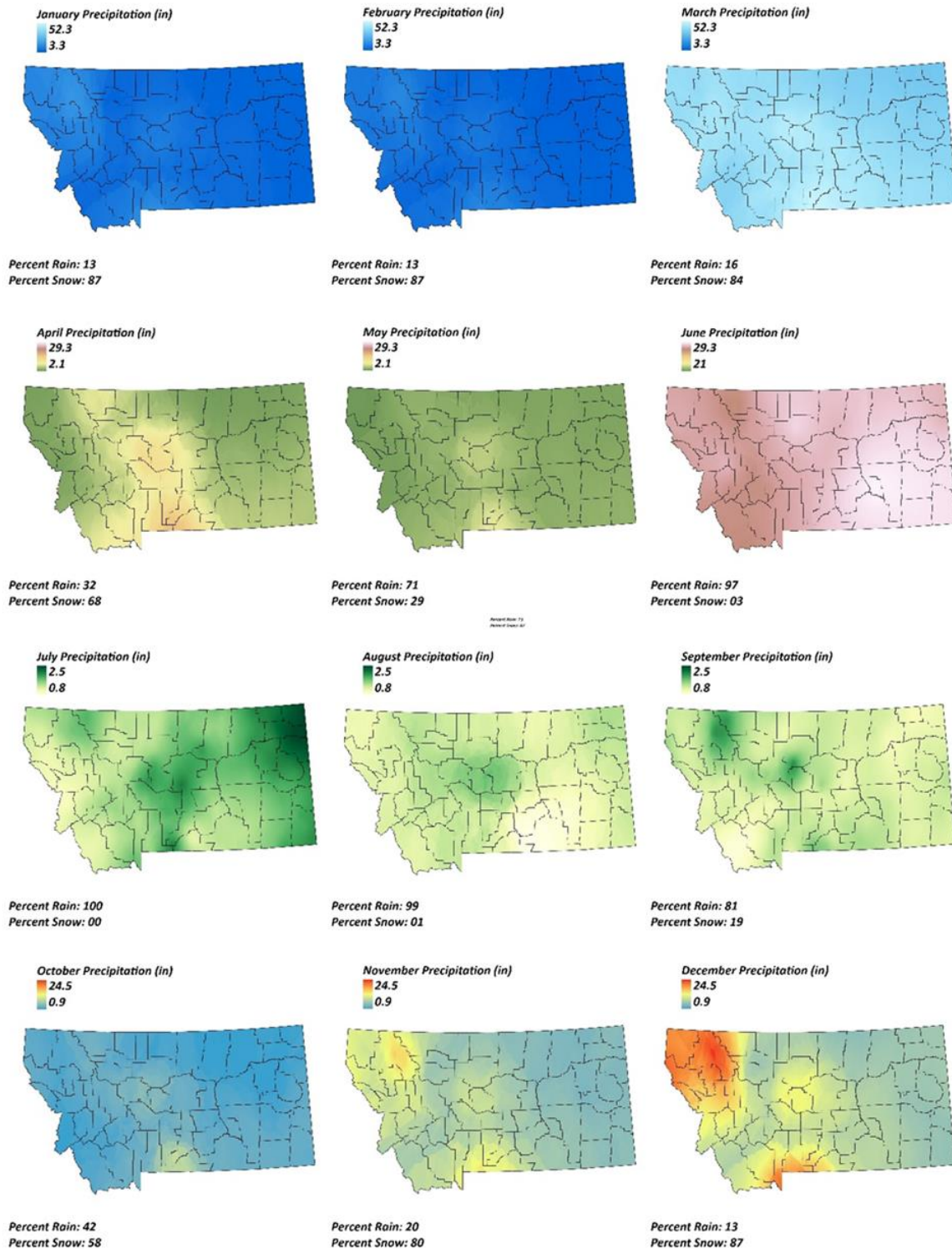


Figure 141. Monthly average precipitation across Montana

Solar Radiation: Figure 142 shows the normalized frequency distribution of shortwave surface downward solar radiation under all-sky conditions, representing the solar energy incident on bridge deck surfaces. The distribution is positively skewed, with a pronounced peak occurring between

approximately 75 and 125 W/m². This indicates that relatively low to moderate solar radiation levels are most common across the study area. Beyond the peak, the frequency gradually decreases as solar radiation increases, with substantial occurrences observed up to approximately 300 W/m². All-sky solar radiation was plotted, as it accounts for the combined effects of clear, partly cloudy, and overcast conditions, thus providing a realistic representation of the actual solar energy reaching the bridge surface. The observed trend suggests that, for most of the time, bridge decks are subjected to solar radiations ranging from 75 to 300 W/m².

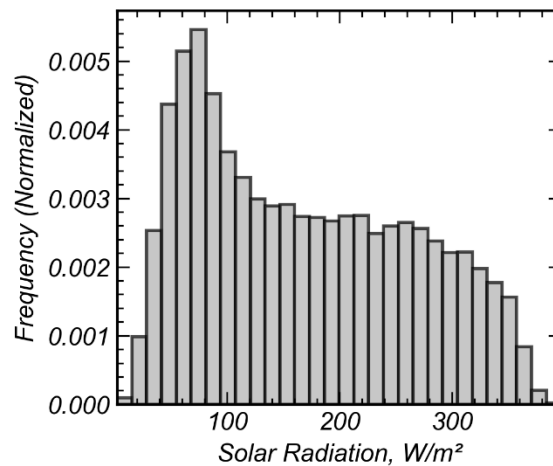


Figure 142. Frequency distribution of shortwave solar radiation in Montana

Lithological Variability: Lithology determines the mineral composition, porosity, and water content of subsurface formations, all of which affect heat transfer. For example, siltstone and shale exhibit lower thermal conductivities, while igneous and metamorphic rocks tend to transfer heat more efficiently. Figure 143 presents a statewide lithological map of Montana. The state's complex geological history has resulted in a diverse subsurface, ranging from sedimentary basins in the east to igneous intrusions and metamorphic formations in the west. This spatial variability must be accounted for when predicting system performance at different bridge locations, especially when borehole depth and soil-structure interaction play a role in heat delivery.

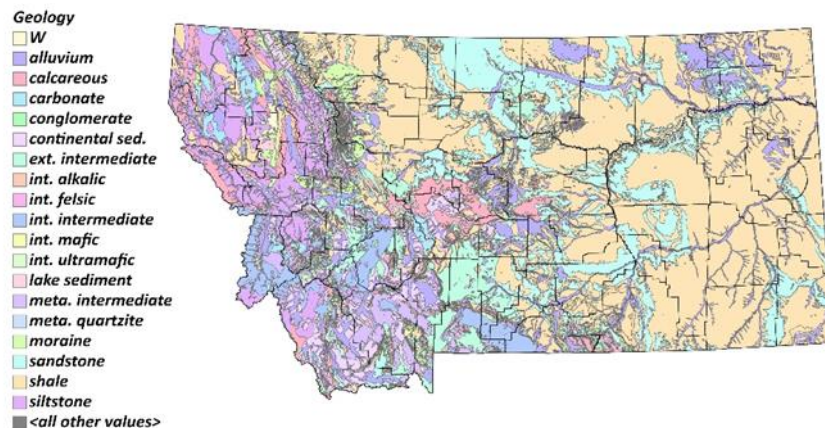


Figure 143. Lithologies in Montana

Ground Properties: Figure 144 shows the spatial distribution of soil thermal properties across Montana, derived from the United States Geological Survey (USGS) soil classification system (Robertson, 1988). The values of thermal conductivity and thermal capacity were interpolated over the state. Figure 144(a) presents the variation in thermal conductivity (W/mK), a measure of the soil's ability to conduct heat. Thermal conductivity values across the state range from approximately 1.0 W/mK to 3.5 W/mK . Higher thermal conductivities are observed in the mountainous and rocky regions of north-western Montana, and most parts of central Montana, indicated by darker brown hues, whereas lower thermal conductivity values are more concentrated in the western part of the state. This spatial variability is significant for evaluating the heat transfer efficiency from geothermal systems embedded within different soil types. Figure 144(b) displays the spatial variation of thermal capacity ($\text{MJ/m}^3\text{K}$), which represents the amount of heat required to change the temperature of a unit volume of soil by one degree Kelvin. Thermal capacity values range from approximately 2.0 to $2.9 \text{ MJ/m}^3\text{K}$. Generally, higher thermal capacities are associated with regions containing higher moisture content or denser soils, as indicated in the plot along the mountainous belts. And lower thermal capacities are observed in the drier and less dense soils across the eastern plains.

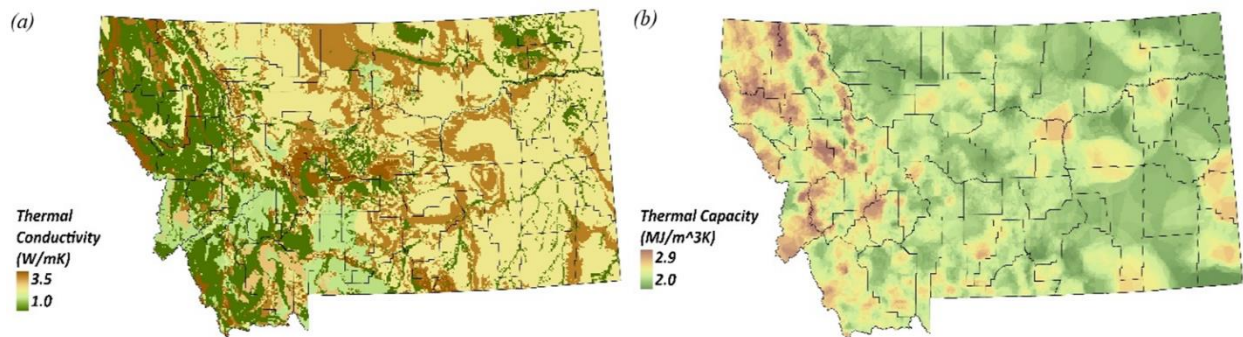


Figure 144. Soil thermal properties across Montana: (a) spatial distribution of thermal conductivity based on USGS soil classification, and (b) spatial distribution of thermal capacity based on USGS soil classification

Ground Temperature: Figure 145 provides an overview of the ground temperature characteristics across Montana, based on data collected from over 1,000 wells statewide. Figure 145(a) presents the normalized frequency distribution of ground temperatures. The majority of ground temperatures cluster between approximately 3.6°C and 20°C , consistent with the expectation that shallow ground temperatures broadly reflect the average annual ambient temperature. However, a distinct secondary peak is observed near 50°C , which can be attributed to the presence of geothermal anomalies, specifically hot springs, that are distributed across various regions in Montana. This bimodal distribution highlights the unique geothermal character of the state. Figure 145(b) illustrates the relationship between ground temperature and depth. The scatter plot reveals that ground temperature appears largely independent of depth within the observed range, with similar temperatures recorded from shallow to deeper wells (up to 150 meters). This finding suggests that localized geothermal conditions, rather than thermal gradients with depth, primarily control ground temperature variations in Montana. Figure 145(c) maps the spatial distribution of ground temperatures, with red dots representing well locations. The kriging interpolation reveals that most of the state exhibits ground temperatures ranging from 3.6°C to about 20°C , while

concentrated hotspots with elevated temperatures up to 49.5°C are evident, particularly in southwestern and south-central Montana. These localized zones correspond to areas of geothermal activity, reinforcing the influence of natural hot springs on regional ground temperature variability. The wide spatial coverage and variability in ground temperatures captured here are important to define the capacity for geothermal resource assessments across Montana.

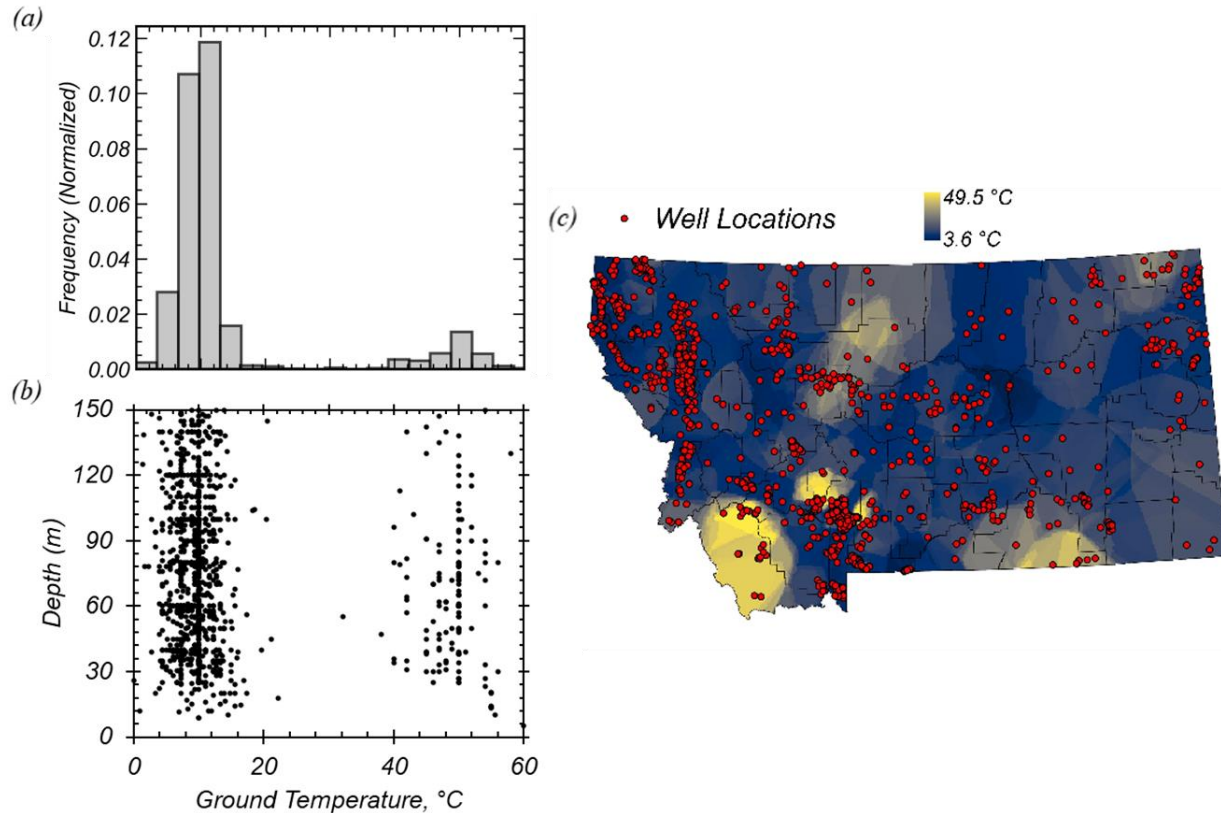


Figure 145. Ground temperature characteristics across Montana: (a) normalized frequency distribution of ground temperatures, (b) ground temperature versus depth, and (c) spatial distribution of ground temperatures and well locations

Data Generation Using COMSOL for ML based feasibility Analysis

The first step in developing a predictive ML model is identifying the most relevant input features. These features should represent the physical variables that influence surface temperature response and deicing performance. Based on the parametric studies, presented in previous chapters, feature sensitivity, and engineering domain knowledge, ambient temperature (°C), wind speed (km/h), solar radiation (W/m²), inlet fluid temperature (°C), flow rate (L/min), tube spacing (cm), and bridge deck length (m), were selected as input features for the machine learning models.

The second step involved generating a comprehensive dataset through numerical simulation. The validated COMSOL model was used in conjunction with LiveLink for MATLAB to automate simulations across a wide range of input combinations. To capture realistic boundary conditions, environmental data were obtained from MDT's RWIS stations and analyzed statistically. Figure 146 presents histograms of key variables, ambient temperature, wind speed, solar radiation, and inlet fluid temperature, used to inform simulation inputs. For each variable, appropriate probability

distributions were fitted, and the 1st, 5th, 95th, and 99th percentiles were extracted from both empirical and fitted distributions to define representative input ranges (see Table 19).

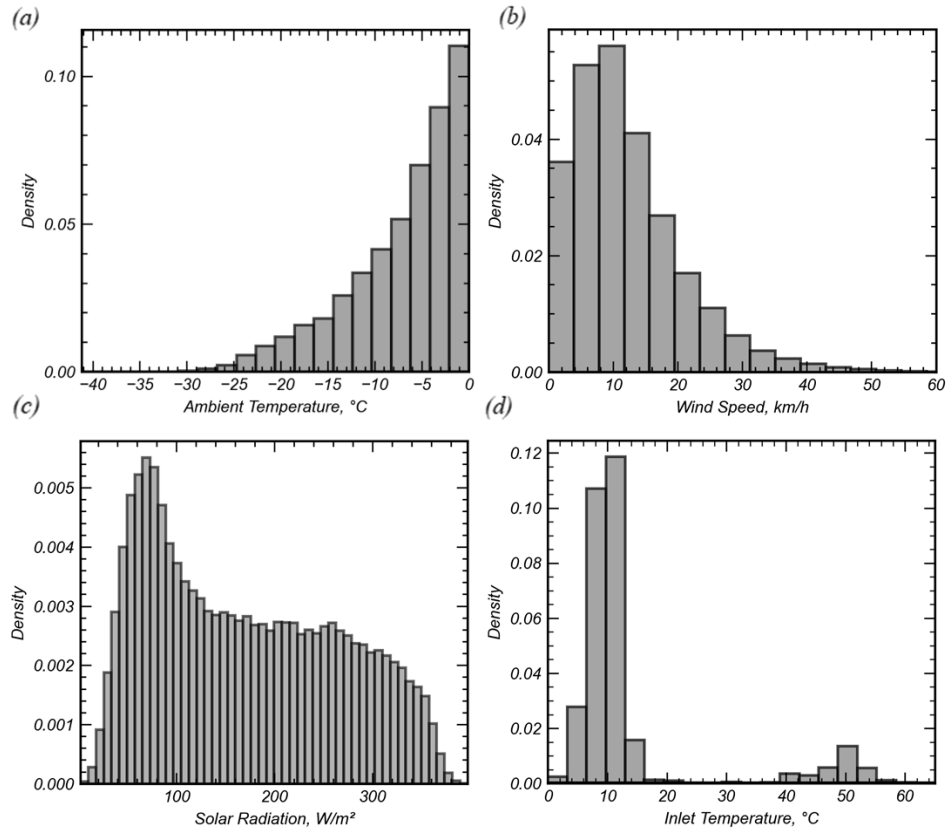


Figure 146. Distribution histograms of important features, a) Ambient temperature, b) Wind speed, c) Solar radiation, and d) Inlet temperature

Table 19. Different levels of percentiles for empirical values and fitted distributions for ambient temperature, wind speed, and solar radiation

Parameter	Value			
<i>Empirical Values</i>	1 st Percentile	5 th Percentile	95 th Percentile	99 th Percentile
Ambient Temperature, °C	-24.31	-19.48	-0.44	-0.08
Wind Speed, km/h	0.36	1.56	28.86	40.91
Solar Radiation, W/m ²	25.84	42.09	335.03	361.28
<i>Fitted Distribution</i>				
Ambient Temperature, °C	-32.43	-21.10	-0.36	-0.07
Wind Speed, km/h	0.45	1.57	28.97	37.85
Solar Radiation, W/m ²	25.58	42.28	359.12	461.46

Ambient temperatures during winter months range from $-35\text{ }^{\circ}\text{C}$ to $0\text{ }^{\circ}\text{C}$, with a strong skew toward higher values. Approximately 95% of observed values fall above $-25\text{ }^{\circ}\text{C}$, and 50% exceed $-10\text{ }^{\circ}\text{C}$. Wind speeds are mostly below 20 km/h, with over 90% of observations under this threshold, indicating moderate convective heat loss is typical. Solar radiation varies widely between 0 and 350 W/m², with a mode near 60 W/m², reflecting frequent overcast conditions during winter.

Inlet fluid temperatures show a clear bimodal distribution, reflecting geothermal heterogeneity across the state. One peak centers near 10 °C, consistent with shallow ground heat, while a second peak around 50 °C represents geothermal hot spring sources. Each mode was fit using separate normal distributions, and the corresponding mean and standard deviation values are listed in Table 20.

Table 20. Mean and standard deviation of fitted distributions for inlet temperature

<i>Parameter</i>	<i>Value</i>	
<i>Inlet Temperature</i>	1 st Distribution	2 nd Distribution
Means of Fitted Distributions, °C	9.26	48.57
Standard Deviations of Fitted Distributions, °C	2.61	5.11

For design-related variables such as bridge deck length, tube spacing, and fluid flow rate, the parameter bounds were selected based on the results of the parametric sensitivity analyses presented in previous chapters. These ranges were chosen to capture realistic design scenarios while ensuring sufficient resolution across the design space. The finalized ranges were used to construct a comprehensive input matrix for numerical simulations. In total, 555 simulations were performed for the without tubing configuration, varying key environmental parameters including ambient temperature (0 to −20 °C), wind speed (0–40 km/h), solar radiation (0–490 W/m²), and initial surface temperature (±10 to 20 °C relative to ambient), as summarized in Table 21.

Table 21. Parameter ranges, combinations and total number of models for generating the dataset without tubing from the numerical model

<i>Parameter</i>	<i>Value</i>	
	Range	Values
Ambient Temperature, °C	0 to -20	0, -5, -10, -15, -20
Initial Temperature, °C	-10 to +20 of Ambient Temperature	-10, -5, 0, 5, 10, 20 of Ambient Temperature
Wind Speed, km/h	0 to 40	0, 5, 10, 20, 30, 40
Solar Radiation, W/m ²	0 to 490	0, 160, 260, 360, 490
Bridge Length, m	1.6 to 4.8	1.6, 3.2, 4.8
Total Number of Models	555	

For the with tubing configuration, 1,836 simulations were conducted, incorporating additional system parameters such as inlet fluid temperature (8–50 °C), flow rate (5–25 L/min), and tube spacing (20–30 cm), while keeping consistent ranges for environmental inputs. Table 22 details the full parameter set and discretized input values used in the simulations. These simulations form a rich dataset for evaluating system performance under diverse operating conditions, enabling robust evaluation of de-icing effectiveness and informing the development of predictive models and design optimization strategies.

Deterministic Analysis

The deterministic analysis conducted in the GIS workspace provides a spatially resolved framework for evaluating the feasibility of geothermal bridge deck heating systems across Montana. This analysis consists of three key stages: (1) estimating shallow geothermal energy potential using the G.POT method based on subsurface temperature and conductivity data (Casasso et al., 2016); (2) calculating specific heat extraction rates that reflect local geologic and design

constraints; and (3) assessing energy demand by integrating meteorological inputs such as ambient temperature, wind speed, and solar radiation to estimate thermal loads for deicing and cooling (Canada by Liu et al., 2018 and Ritter, 2012). By comparing available geothermal supply with localized thermal demand, this framework enables regional screening, supports preliminary design, and identifies areas where supplemental systems may be required.

Table 22. Parameter ranges, combinations and total number of models for generating the dataset with tubing from the numerical model

Parameter	Value	
	Range	Values
Ambient Temperature, °C	0 to -20	0, -5, -10, -15, -20
Initial Temperature, °C	-10 to +20 of Ambient Temperature	-10, -5, 0, 5, 10, 20 of Ambient Temperature
Wind Speed, km/h	0 to 40	0, 5, 10, 20, 30, 40
Solar Radiation, W/m ²	0 to 490	0, 160, 260, 360, 490
Inlet Temperature, °C	8 to 50	8, 10, 50
Fluid Flowrate, L/min	5 to 25	5, 10, 25
Tube Spacing, cm	20 to 30	20, 30
Bridge Length, m	1.6 to 4.8	1.6, 3.2, 4.8
Total Number of Models	1836	

G.POT Method

The G.POT method is used to compute the shallow potential geothermal energy and specific heat extraction rate in large spatial areas. This method can be used for both heating and cooling modes, but analysis must be completed separately. The shallow potential geothermal energy can be calculated through equation 13. This equation depends on properties of the borehole, the thermal properties of the ground, undisturbed ground temperature, the length of cooling or heating season, and the simulated design life of the system.

$$Q_{BHE} = \frac{\alpha(T_0 - T_{lim}) * \lambda * L * t'_c}{-0.619t'_c * \log(u'_s) + (0.532t'_c - 0.962) * \log(u'_c) - 0.455t'_c - 1.619 + 4\pi\lambda * R_b} \quad (13)$$

In equation (1), $\alpha=8$ if the shallow potential geothermal energy is in W or, $\alpha=0.0701$ if it is in MWh/y. The available potential geothermal energy is a function of the maximum thermal alteration fluid which is the difference between the undisturbed ground temperature (T_0) and the maximum or minimum temperature of the carrier fluid (T_{lim}) in the system expressed in degrees Celsius. The thermal conductivity of the ground is symbolized as λ and is expressed in W/mK, L is the length of the borehole in meters, and R_b is the thermal resistance of the borehole in mK/W. t'_c , u'_s , and u'_c are non-dimensional variables depending on the simulation time and length of the heating or cooling season; $t'_c = t_c/t_y$ where t_c is the length of the heating or cooling season in days and t_y is the length of the year, $u'_s = \frac{r_b^2}{4 * \alpha' * t_s}$ and $u'_c = \frac{r_b^2}{4 * \alpha' * t_c}$ where t_s is the simulation time, α' is the thermal capacity of the ground, and r_b is the radius of the borehole. The non-spatial varying values used for equation (13) in Montana are shown in Table 23. The specific heat extraction rate can be calculated from equation (13) by using a 1-meter borehole depth and 1-hour simulation time.

Table 23. QBHE Variables

$T_{lim\ Cooling}$	-2	°C
$T_{lim\ Heating}$	20	°C
L	100	M
R_b	6.74e-2	mK/W
$t_C\ Cooling$	153	d
$t_C\ Heating$	212	d
t_y	1	y
t_s	50	y
r_b	0.075	m

Energy Balance

The required energy for deicing bridge decks and cooling bridge surfaces can be calculated by determining the energy balance at bridge decks based on the unit area. The energy balance at the bridge decks can be calculated using equation (14).

$$q_n = q_s + q_m + q_{conv} + q_{solar} \quad (14)$$

Where q_n is the net heat flux in W/m, q_{solar} is the solar radiation, q_m is the latent heat of fusion or vaporization depending on the heating or cooling season, q_{conv} is the convective heat flux at the surface of the bridge, and q_s is the sensible heat flux. The solar radiation is the short-wave radiation was calculated using a pre-existing area solar radiation tool in ArcGIS pro.

For the heating season, the sensible heat flux is the energy required to raise the temperature of snow to its melting point and to increase the subsequent water to a liquid film temperature for easier removal. In the cooling season, the sensible heat flux is used to change the precipitation on the bridge deck to the desired temperature for evaporation. Equation (15) shows the calculations for the heating season and equation (16) shows the calculations for the cooling season.

$$q_{s\ Heating} = \rho_w * s(t) * (c_p^i(T_m - T_a) + c_p^w(T_f - T_m)) \quad (15)$$

$$q_{s\ Cooling} = \rho_v * r(t) * (c_p^w(T_e - T_a)) \quad (16)$$

Where ρ_w and ρ_v are the water density and water vapor density respectively in kg/m³. The parameters $s(t)$ is the snowfall rate in m/s, and $r(t)$ is the rain fall rate in m/s. T_m is the melting point of snow set to 0°C, T_a is the ambient air temperature in °C, T_e is the evaporation temperature set to 32 °C, and T_f is the liquid film temperature set at 0.56 °C. The specific heat of water is represented as c_p^w and is set to 4200 J/kg×K and the specific heat of ice is symbolized as c_p^i and is set to 2100 J/kg×K.

The latent heat flux is used to determine the energy absorbed by either snow or water during phase change. Equation (16) shows the calculation made during the heating season and equation (17) shows the calculations done during the cooling season.

$$q_{m\ Heating} = \rho_w * s(t) * h_{if} \quad (17)$$

$$q_{m\ Cooling} = \rho_v * r(t) * h_{iv} \quad (18)$$

Where h_{if} is the heat of fusion, set to $3.3e5$ J/kg and h_{iv} is the heat of vaporization set to $2.26e5$ J/kg.

The convective heat flux is based on the time required for the deck slab to change temperature. In this energy balance, we are looking at the surface convective heat flux which is the energy transferred from the surface of the bridge deck to the atmosphere. This calculation can be made using equation (19).

$$q_{conv} = h_{conv} * (T_a - T_s) \quad (19)$$

Where T_s is the surface temperature ($^{\circ}\text{C}$) and h_{conv} is the convective heat flux transfer coefficient determined by equation (20).

$$h_{conv} = 2 * \frac{k_a}{L} \begin{cases} \frac{0.3387 * P_r^{\frac{2}{3}} * R_{eL}^{\frac{1}{2}}}{\left(1 + \left(\frac{0.0468}{P_r}\right)^{\frac{2}{3}}\right)^{\frac{1}{4}}} \text{ if } R_{eL} \leq 5 * 10^5 \\ P_r^{\frac{1}{3}} * \left(0.037 R_{eL}^{\frac{4}{5}} - 871\right) \text{ if } R_{eL} > 5 * 10^5 \end{cases} \quad (20)$$

Where k_a is the thermal conductivity of air set as 0.02 w/mK, L is the characteristic length of the bridge slab in the direction of wind in meters, P_r is the Prandtl number for air set as 0.7 , and R_{eL} is Reynolds number based on the characteristic length calculated by equation (21).

$$R_{eL} = \frac{V * L}{v_{air}} \quad (21)$$

Where V is the wind speed in m/s and v_{air} is the kinematic viscosity of air set to $1.1e-5$ m²/s.

Energy Results

To determine the shallow potential geothermal and energy demand, Montana was separated into three categories, heating predominant mode, cooling predominant mode, and mixed mode (Figure 147). The modes were determined using the energy demand, the modes were determined based on the total energy demand in the heating and cooling seasons. Heating mode occurs where over 60% of the total energy demand comes from the heating period, cooling mode occurs where over 60% of the total energy demand comes from the cooling period, and mixed mode occurs where 40-60% of the energy comes from both energy periods.

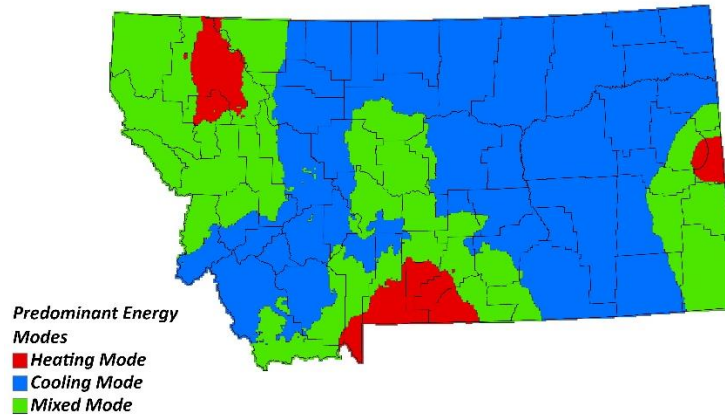


Figure 147. Montana split into three energy modes based on the total energy demand over the year

The potential geothermal energy and specific heat extraction rate determined from the method outlined in Casasso et al. (2016) (Figure 148). The available energy across the state ranges between 0 and 60 MWh/y, with lower ranges occurring mostly in the eastern plains. Based on the results of the energy analysis, the systems are most feasible in areas of higher geothermal activity such as southwest Montana as the available energy is directly related to the ground temperature. The sHE shows the watts of energy that can be extracted per meter in the borehole. This ranges between less than 30 to 130 w/m. Comparing this to the shallow potential geothermal energy. At least some energy can be extracted into the ground pump systems in all parts of the states.

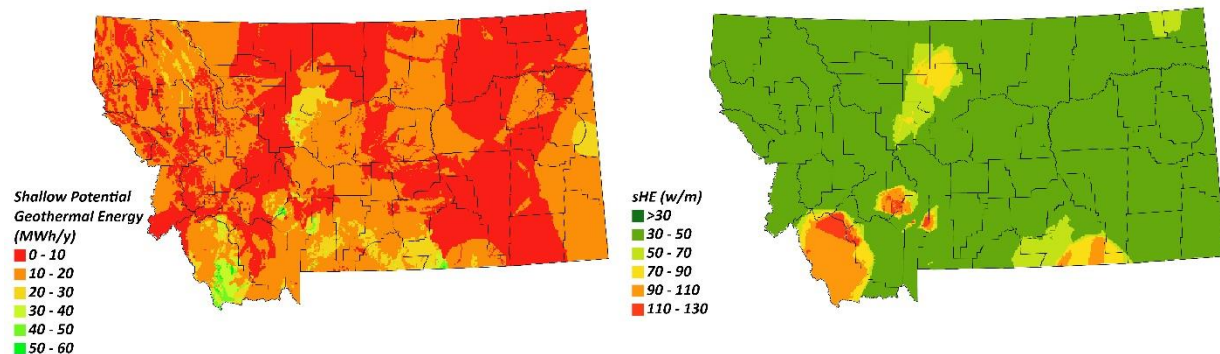


Figure 148. Available Energy Analysis Results

The required energy for bridge deck melting and cooling and the subsequent power demand across the state is shown in (Figure 149). The energy demand ranges from 600 w/m^2 to 1200 w/m^2 . The power demand was determined by multiplying this value by the average bridge deck area in m^2 . Comparing the maps showing the energy demand and available energy, generally larger demand areas occur where there is more available. From comparing the different aspects of the energy analysis, the GSHP's will be feasible across most of the state.

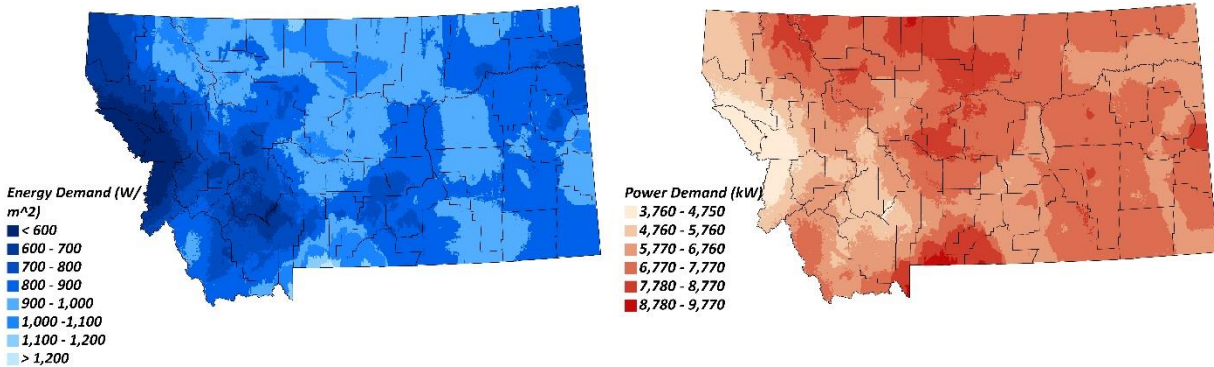
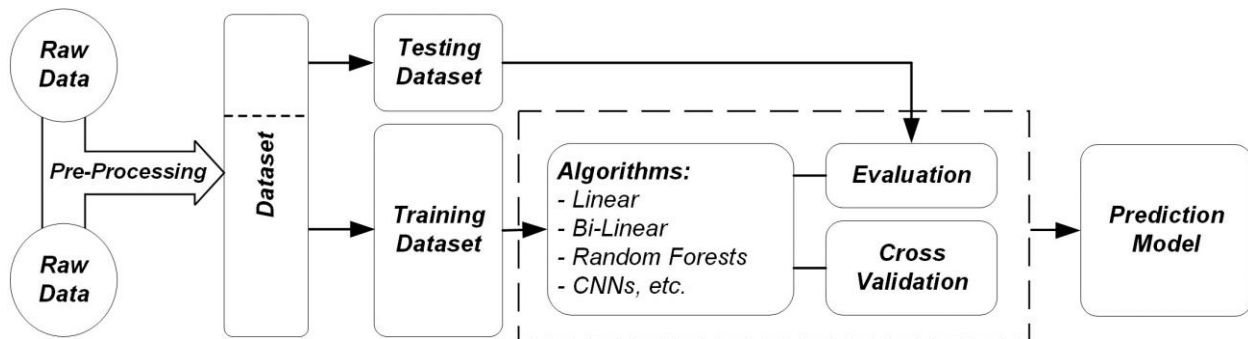


Figure 149. Energy Demand Analysis Results

Machine-Learning Based Feasibility Analysis

Error! Reference source not found. summarizes the machine learning model development process for training and evaluating the prediction models. For this study, the machine learning development was carried out in six steps.



The first step, feature selection, involved identifying the most physically relevant and influential parameters affecting bridge deck surface temperature. This was accomplished through detailed parametric studies conducted using the validated numerical model (Chapter 2). Each parameter was systematically varied, and its impact on the thermal response was evaluated. Based on these analyses, a final set of seven features was selected: ambient temperature, wind speed, solar radiation, inlet fluid temperature, flow rate, tube spacing, and bridge length. These features were chosen to ensure that both environmental variability and design-dependent behaviors were captured in the training dataset. The second step involved generating a comprehensive dataset using COMSOL-based simulations automated through MATLAB LiveLink. More than 2,000 simulations were performed across a structured design space that encompassed combinations of the selected features. The simulations captured surface temperature responses under both "with tubing" and "without tubing" conditions. This dataset formed the foundation for training machine learning models capable of replicating the thermal behavior of geothermal bridge deck systems. In the third step, data splitting and experimental design were applied. The dataset was divided using an 80/20 train-test split, and five-fold cross-validation was implemented to reduce overfitting and ensure robustness. The fourth step focused on model selection and training. Two predictive models were developed: Model 1, designed to estimate system performance metrics such as stabilized surface temperature, time to reach above 0°C, and time to stabilization; and Model 2, which provided continuous surface temperature predictions at every 0.1-hour interval. Both models used

the same input features but differed in output structure. A wide range of supervised learning algorithms were employed for both models, including linear regression, polynomial regression, decision trees, random forests, XGBoost, and fully connected neural networks (FCNN). Each algorithm was trained on the simulation-derived dataset, and model selection was subsequently performed based on lowest cross validation error. In the fifth step, model evaluation was performed using three standard metrics: mean absolute error (MAE), root mean squared error (RMSE), and coefficient of determination (R^2). These metrics allowed for quantitative comparison across different algorithms and configurations. The final step involved sensitivity analysis to further understand model interpretability. A permutation-based approach was used, where each input feature was shuffled independently while observing the resulting increase in prediction error. This analysis revealed that inlet temperature, ambient temperature, wind speed, and solar radiation were the most influential predictors. The findings were consistent with the results from parametric studies.

Data Splitting and Experimental Design

The generated dataset was divided into a training set (80%) and a testing set (20%) to ensure unbiased model evaluation. To improve generalizability and prevent overfitting, a 5-fold cross-validation scheme was implemented, where the training data were further divided into five subsets. Each model was trained on four folds and validated on the fifth, rotating through all folds. This approach ensured robust estimation of performance metrics across unseen data.

Model Selection and Training

Two types of machine learning models were developed to meet different prediction objectives. The selected input features and target variables are shown in Table 24.

Table 24. Machine learning models used with the features and target variables for Model 1 and Model 2

<i>Features</i>	<i>Targets</i>	
	Model 1	Model 2
Ambient Temperature, °C	- Stabilized Temperature	- Average Surface Temperature (every 0.1 hours interval)
Initial Temperature, °C		
Wind Speed, km/h	- Time to Reach Above 0°C	
Solar Radiation, W/m ²		
Inlet Temperature, °C	- Time to Reach Stabilized Temperature	
Fluid Flowrate, L/min		
Tube Spacing, cm		
Bridge Length, m		

Figure 150 presents a schematic definition of three key system performance indicators used in Model 1: stabilized surface temperature (T_f), time to reach stabilized temperature (t_s), and time to reach above 0 °C (t_o). T_f is defined as the surface temperature at the point where its rate of change remains below 0.5% over three consecutive hours, indicating thermal equilibrium, while t_s is the duration required for the system to reach this steady-state condition. t_o quantifies how quickly the surface reaches the threshold required for ice melting.

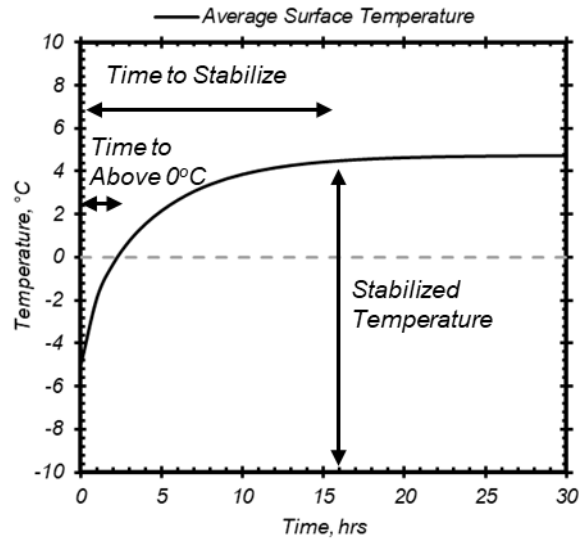


Figure 150. Schematic for stabilized temperature, time to reach stabilized temperature, and time to reach above 0°C

Model 2 was constructed to provide granular predictions of surface temperature at every 0.1-hour interval throughout the simulation period. This model used the same input features but replaced high-level targets with full temperature time series as the prediction output (Figure 151). Model 2 enables dynamic thermal profile monitoring and is particularly useful for forecasting thermal behavior under changing conditions.

Model 1 Output	
- Stabilized Temperature	= 4.5°C
- Time to Reach Stabilized Temperature	= 16.8 hrs
- Time to Reach Above 0°C	= 4.6 hrs

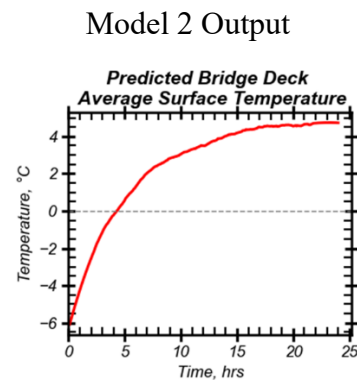


Figure 151. Outputs from Model 1 and Model 2

A key innovation in Model 2 was its adaptive time-stepping mechanism. When environmental or operational conditions changed, the model treated the last predicted surface temperature as the new initial condition and reset the simulation clock to zero. This allowed the model to capture the rapid response typically observed after condition changes, before the system reaches thermal equilibrium.

Model Evaluation

The predictive performance of both Model 1 and Model 2 was evaluated using the following metrics:

Mean Absolute Error (MAE): is a widely used regression metric that quantifies the average magnitude of prediction errors, regardless of direction. It is defined as:

$$\text{MAE} = \frac{1}{n} \sum |y_i - \hat{y}_i| \quad (6)$$

where, y_i is the actual (true) value, \hat{y}_i represents the predicted value from the machine learning model, and n is the total number of data points. MAE measures the mean absolute difference between predicted and actual values, offering an intuitive indication of model accuracy. Because it treats all errors equally, without squaring them, MAE is less sensitive to outliers compared to metrics like RMSE. This property makes it particularly suitable for evaluating models where consistent predictive performance is desired across a broad range of scenarios.

Root Mean Squared Error (RMSE): is a standard metric used to evaluate the predictive accuracy of regression models by measuring the square root of the average squared differences between predicted and actual values. It is defined as:

$$\text{RMSE} = \sqrt{\frac{1}{n} \sum (y_i - \hat{y}_i)^2} \quad (7)$$

where, y_i is the actual (true) value, \hat{y}_i represents the predicted value from the machine learning model, and n is the total number of data points. Unlike MAE, RMSE penalizes larger errors more heavily due to the squaring operation, making it particularly sensitive to outliers and useful for identifying models that fail under extreme conditions. Additionally, RMSE is differentiable, which makes it well-suited as a loss function during model training. Since its units match those of the target variable, RMSE provides an interpretable measure of model performance in real-world physical systems.

Coefficient of Determination (R^2): measures the proportion of variance in the observed data that is captured by the model's predictions. It is defined as

$$R^2 = 1 - \frac{\sum (y_i - \hat{y}_i)^2}{\sum (y_i - \bar{y})^2} \quad (8)$$

where, y_i is the actual (true) value, \hat{y}_i represents the predicted value from the machine learning model, and \bar{y} is the mean of the actual values. R^2 ranges from 0 to 1, with higher values indicating better model performance. An R^2 value near 1 implies that the model accounts for most of the variability in the target data, while a value near 0 suggests poor predictive alignment. As a relative metric, R^2 is particularly useful for comparing the explanatory power of different models or configurations under the same dataset.

Performance Results

Model 1-Without Tubing:

Figure 152 and Table 25 summarize the performance of various machine learning models, Linear Regression (LR), Polynomial Regression (PR), Decision Tree (DT), Random Forest (RF), XGBoost (XGB), and Fully Connected Neural Network (FCNN), in predicting three key performance indicators: stabilized surface temperature, time to reach above 0 °C, and time to reach thermal stabilization. The metrics reported include MAE, RMSE, and R^2 .

In terms of MAE, XGBoost model demonstrates low average prediction errors across all three targets. For stabilized temperature, XGBoost reports the lowest MAE at 0.54, followed closely by FCNN at 0.56. For time to $>0^{\circ}\text{C}$, where XGBoost again has the lowest MAE of 0.24, while decision tree yields a slightly higher value of 0.35. For time to stabilize, both XGBoost and decision tree record an MAE of 1.13 indicating their relative reliability in minimizing average prediction error.

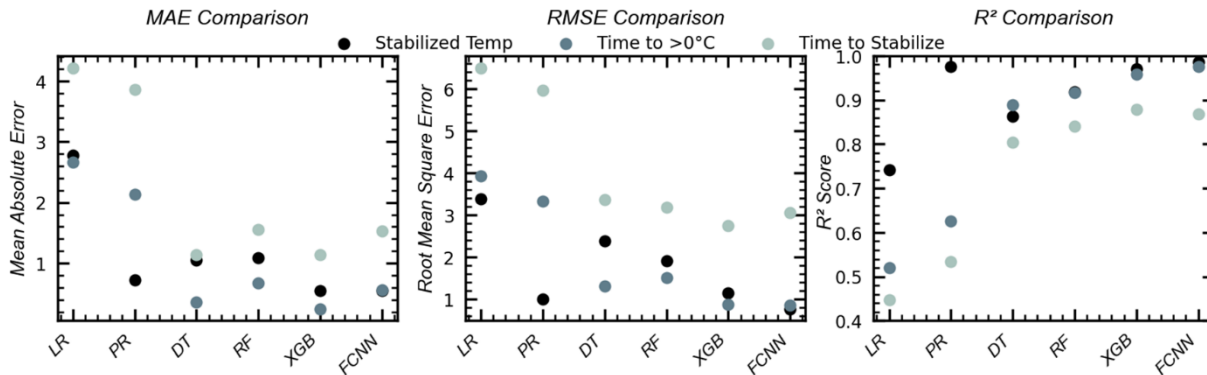


Figure 152. MAE, RMSE, and R2 score comparison for Model 1 without tubing for Stabilized temperature, time to reach stabilized temperature, and time to reach above 0°C

With regard to RMSE, which emphasizes larger deviations and provides a more sensitive measure of prediction robustness, FCNN achieves the lowest RMSE for stabilized temperature at 0.78, suggesting stable and accurate prediction with minimal large errors. Meanwhile, XGBoost produces the lowest RMSE for time to $>0^{\circ}\text{C}$ and time to stabilize, at 0.86 and 2.74 respectively. These results imply that XGBoost may offer more consistent performance when predicting temperature transitions over time, particularly in contexts where larger errors are more consequential.

Looking at the coefficient of determination (R^2), FCNN achieves the highest values for stabilized temperature with an R^2 of 98.59%. While XGBoost has the highest values for two other target variables. It attains R^2 of 95.85% for time to $>0^{\circ}\text{C}$, and an R^2 of 87.91% for time to stabilize indicating strong explanatory power and an ability to capture most of the variance in the data. Overall, both models, FCNN and XGBoost exhibit strong predictive capabilities, with FCNN performing well on steady-state temperature predictions, while XGBoost shows strength in capturing temporal stabilization trends.

Model 1-With Tubing:

Figure 153 and Table 26 present the comparative performance of machine learning models for predicting stabilized surface temperature, time to reach above 0°C , and time to reach stabilization, under configurations where tubing is included in the system. The metrics reported include MAE, RMSE, and R^2 .

In terms of MAE, XGBoost demonstrates the lowest average errors across multiple targets. It records an MAE of 0.22 for stabilized temperature and 0.73 for time to $>0^{\circ}\text{C}$, indicating minimal average deviation from actual values in both early and steady-state phases. For time to stabilize,

random forest achieves the lowest MAE of 1.14, closely followed by XGBoost at 1.17, suggesting that both models provide comparable accuracy in predicting the longer stabilization period.

Table 25. MAE, RMSE, and R2 score values for Model 1 without tubing for Stabilized temperature, time to reach stabilized temperature, and time to reach above 0oC

Parameter	Value		
Mean Absolute Error	Stabilized Temp.	Time to > 0°C	Time to Stabilize
Linear Regression	2.77	2.66	4.21
Polynomial Regression	0.72	2.13	3.85
Decision Tree	1.05	0.35	1.13
Random Forest	1.09	0.67	1.55
XGBoost	0.54	0.24	1.13
Fully Connected Neural Network	0.56	0.60	1.70
Root Mean Squared Error			
Linear Regression	3.38	3.92	6.49
Polynomial Regression	0.99	3.33	5.95
Decision Tree	2.38	1.30	3.35
Random Forest	1.91	1.50	3.17
XGBoost	1.14	0.86	2.74
Fully Connected Neural Network	0.78	1.10	3.30
R ² Score (%)			
Linear Regression	74.25	51.98	44.66
Polynomial Regression	97.63	62.62	53.38
Decision Tree	86.34	88.96	80.43
Random Forest	91.76	91.64	84.10
XGBoost	96.97	95.85	87.91
Fully Connected Neural Network	98.59	95.60	83.54

For RMSE, XGBoost yields the lowest values for all three target variables. It reports an RMSE of 0.46 for stabilized temperature, 1.75 for time to >0°C, and 2.39 for time to stabilize. These lower RMSE values indicate that XGBoost predictions are not only accurate on average but also less affected by large individual errors, making the model more robust in scenarios where minimizing significant deviations is critical.

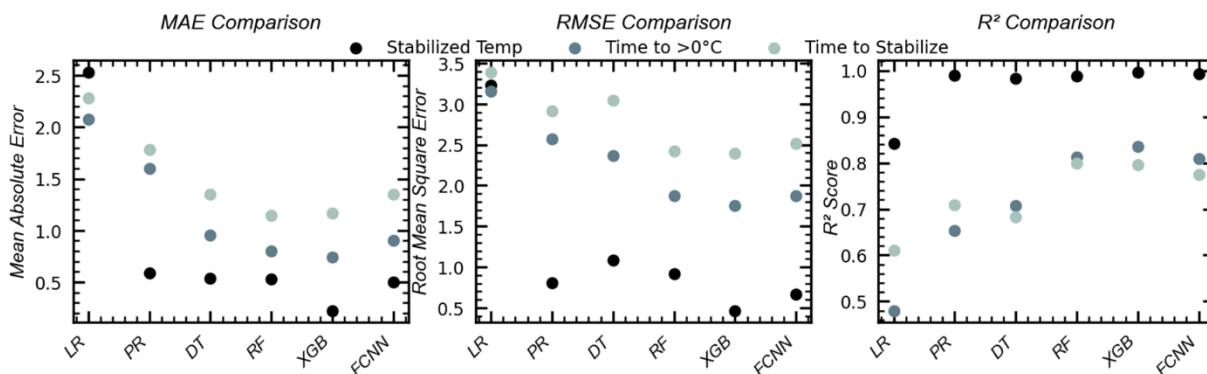


Figure 153. MAE, RMSE, and R2 score comparison for Model 1 with tubing for Stabilized temperature, time to reach stabilized temperature, and time to reach above 0oC

With respect to the coefficient of determination (R^2), XGBoost achieves the highest value for time to $>0^\circ\text{C}$ at 83.52%, suggesting it captures a substantial portion of the variance in this early-phase response. For time to stabilize, random forest shows the highest R^2 at 79.84%, though XGBoost follows closely at 79.61%, indicating similar explanatory power. For stabilized temperature, XGBoost attains an R^2 of 99.66%, reflecting its effectiveness in modeling the final steady-state condition of the system.

Due to the relatively simple nature of the target variables in Model 1, particularly the stabilized surface temperature, which is a single-value summary of the full thermal response, most machine learning models were able to achieve higher R^2 scores when predicting this metric.

Table 26. MAE, RMSE, and R^2 score values for Model 1 with tubing for Stabilized temperature, time to reach stabilized temperature, and time to reach above 0°C

<i>Parameter</i>	<i>Value</i>		
<i>Mean Absolute Error</i>	Stabilized Temp.	Time to $> 0^\circ\text{C}$	Time to Stabilize
Linear Regression	2.53	2.07	2.28
Polynomial Regression	0.58	1.59	1.78
Decision Tree	0.53	0.95	1.35
Random Forest	0.52	0.80	1.14
XGBoost	0.22	0.73	1.17
Fully Connected Neural Network	0.44	0.91	1.30
<i>Root Mean Squared Error</i>			
Linear Regression	3.22	3.15	3.39
Polynomial Regression	0.80	2.56	2.91
Decision Tree	1.08	2.36	3.04
Random Forest	0.91	1.87	2.41
XGBoost	0.46	1.75	2.39
Fully Connected Neural Network	0.59	1.89	2.41
<i>R^2 Score (%)</i>			
Linear Regression	84.19	48.00	61.08
Polynomial Regression	99.02	65.28	70.92
Decision Tree	98.21	70.71	68.33
Random Forest	98.71	81.31	79.84
XGBoost	99.66	83.52	79.61
Fully Connected Neural Network	99.45	79.66	78.53

Model 2-Without Tubing:

Figure 154 and Table 27 present a performance comparison of various machine learning models for Model 2 output without tubing, evaluated using MAE, RMSE, and R^2 .

In terms of MAE, the fully connected neural network (FCNN) reports the lowest value at 0.29, followed by XGBoost at 0.37. These low MAE values indicate that both models consistently produce predictions with small average deviations from the actual values. Other models, including polynomial regression (0.89), decision tree (0.51), and random forest (0.61), also perform reasonably well, while linear regression shows a substantially higher MAE of 2.93, indicating the non-linearity relationships that were not captured by the linear model.

RMSE values further highlight the performance differences across models, especially with respect to the penalization of larger errors. The FCNN achieves the lowest RMSE at 0.41, suggesting strong robustness against extreme deviations. XGBoost follows with an RMSE of 0.90, also reflecting consistent performance. Polynomial regression and random forest share an RMSE of 1.22, while decision tree and linear regression show higher values at 1.50 and 3.93, respectively.

Regarding the coefficient of determination (R^2), FCNN attains the highest value at 99.79%, indicating that it explains nearly all of the variance in the observed data. XGBoost also achieves a high R^2 score of 99.17%, showing its strong predictive capability. Polynomial regression (98.69%), random forest (98.46%), and decision tree (97.56%) all demonstrate good explanatory power, while linear regression lags behind with an R^2 of 86.31%. These results show that both FCNN and XGBoost offer accurate and consistent predictions, making them more suitable for modeling system behavior in the absence of tubing.

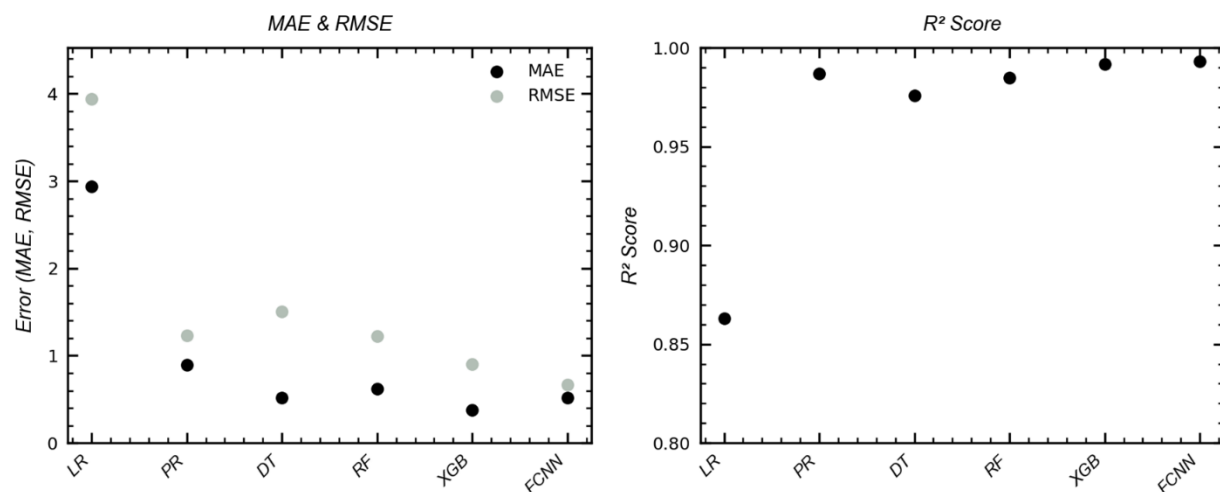


Figure 154. MAE, RMSE, and R2 score comparison for Model 2 output without tubing

Table 27. MAE, RMSE, and R2 score values for Model 2 output without tubing

Parameter	Value		
	MAE	RMSE	R ² Score (%)
Linear Regression	2.93	3.93	86.31
Polynomial Regression	0.89	1.22	98.69
Decision Tree	0.51	1.50	97.56
Random Forest	0.61	1.22	98.46
XGBoost	0.37	0.90	99.17
Fully Connected Neural Network	0.29	0.41	99.79

In the case of Model 2 without tubing, the surface temperature profiles were comparatively simpler to predict due to the reduced number of influencing parameters and the absence of active heating effects. As a result, the temperature trends exhibited smoother and more predictable behavior over time. This simplicity allowed most machine learning models to perform well, achieving relatively high predictive accuracy even with less complexity.

Model 2-With Tubing:

Figure 155 and Table 28 present the model performance comparison for Model 2 output with tubing, evaluated using MAE, RMSE, and R^2 score.

In terms of MAE, the fully connected neural network (FCNN) demonstrates the lowest error at 0.64, indicating minimal average deviation between predicted and actual values. XGBoost follows closely with an MAE of 0.68, also reflecting high predictive accuracy. Random forest (0.91), polynomial regression (1.06), and decision tree (1.09) show moderate average errors, while linear regression reports the highest MAE of 3.23, suggesting weaker performance in modeling the system with tubing.

RMSE values further differentiate the models based on their sensitivity to larger errors. FCNN records the lowest RMSE at 2.26, suggesting strong robustness and reduced influence from outliers or large deviations. XGBoost again performs well with an RMSE of 2.57, followed by polynomial regression at 2.74. In contrast, random forest (3.28), decision tree (4.45), and linear regression (4.77) show higher RMSE values, indicating more pronounced larger prediction errors.

For the coefficient of determination (R^2), FCNN achieves the highest score at 95.79%, reflecting its strong ability to explain the variance in the data. XGBoost also shows a high R^2 value of 94.29%, while polynomial regression (93.52%) and random forest (90.83%) perform slightly lower. Decision tree and linear regression record R^2 scores of 83.05% and 84.11%, respectively. These results indicate that both FCNN and XGBoost offer consistent and accurate predictions for system behavior with tubing, supported by high variance explanation and low error metrics.

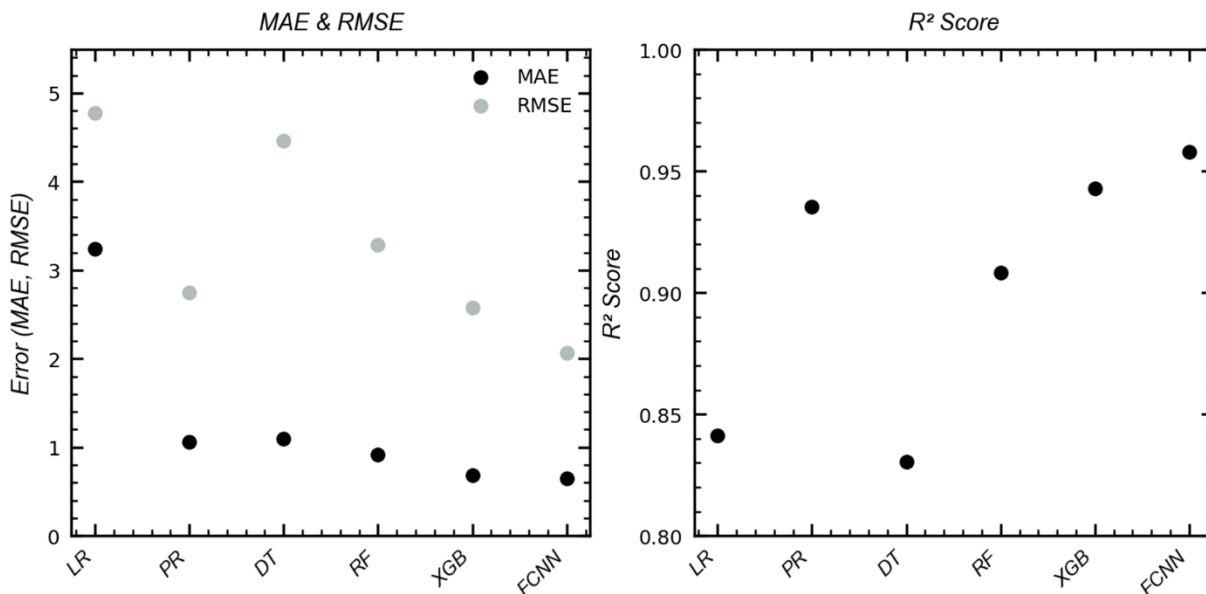


Figure 155. MAE, RMSE, and R^2 score comparison for Model 2 output with tubing

Given its detailed and dynamic predictions, Model 2 using the FCNN architecture was selected as the preferred model for subsequent analysis and application.

Table 28. MAE, RMSE, and R2 score values for Model 2 output with tubing

Parameter	Value		
	MAE	RMSE	R ² Score (%)
Linear Regression	3.23	4.77	84.11
Polynomial Regression	1.06	2.74	93.52
Decision Tree	1.09	4.45	83.05
Random Forest	0.91	3.28	90.83
XGBoost	0.68	2.57	94.29
Fully Connected Neural Network	0.64	2.26	95.79

Feature Importance Analysis

To evaluate the relative importance of each input feature on the model's predictive performance, permutation feature importance was applied to the fully connected neural network (FCNN). In this method, the trained FCNN model was kept fixed, and the input validation dataset was systematically perturbed. For each feature, its values were randomly shuffled across all samples, effectively disrupting the original relationship between that feature and the target variable, while leaving all other features unchanged. The perturbed input dataset was then fed through the FCNN to generate new predictions. The mean absolute error (MAE) was computed for each perturbed case and compared to the baseline MAE obtained using the unaltered dataset. The increase in MAE after permuting a given feature quantifies the loss of predictive accuracy caused by breaking the feature-target relationship, and thus serves as a direct measure of that feature's importance. Features causing greater degradation in model performance were considered more influential. Finally, the importance scores were normalized to enable comparison across features and visualized using a radar plot.

The results, shown in Figure 156, highlight that Inlet Temperature, Ambient Temperature, Wind Speed, and Solar Radiation are the most critical features affecting surface temperature predictions. Initial Temperature showed moderate importance, while Bridge Length, Tube Spacing, and Flowrate had the least influence on model predictions. This aligns with prior sensitivity findings and underscores the physical relevance of the selected inputs.

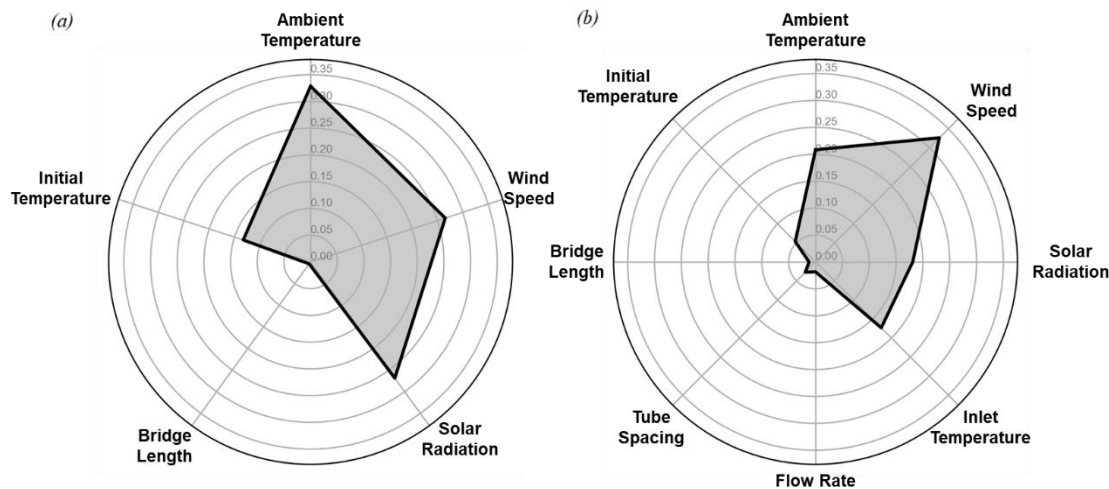


Figure 156. Permutation-based feature importance for FCNN model predictions visualized as radar plot: a) without tubing, and b) with tubing

Temperature Prediction Interactive Tool

To support practical deployment and real-time decision-making, an interactive tool was developed that integrates a trained fully connected neural network (FCNN) with a web-based interface. The tool features an embedded interactive map of Montana that displays the geographic locations of all bridge decks analyzed in this study. When a user selects a specific bridge location on the map, the tool retrieves and displays the live ambient temperature ($^{\circ}\text{C}$), wind speed (km/h), and solar radiation (W/m^2) for that site, using real-time weather data sources. Figure 157 shows the interactive map interface with bridge locations across Montana.

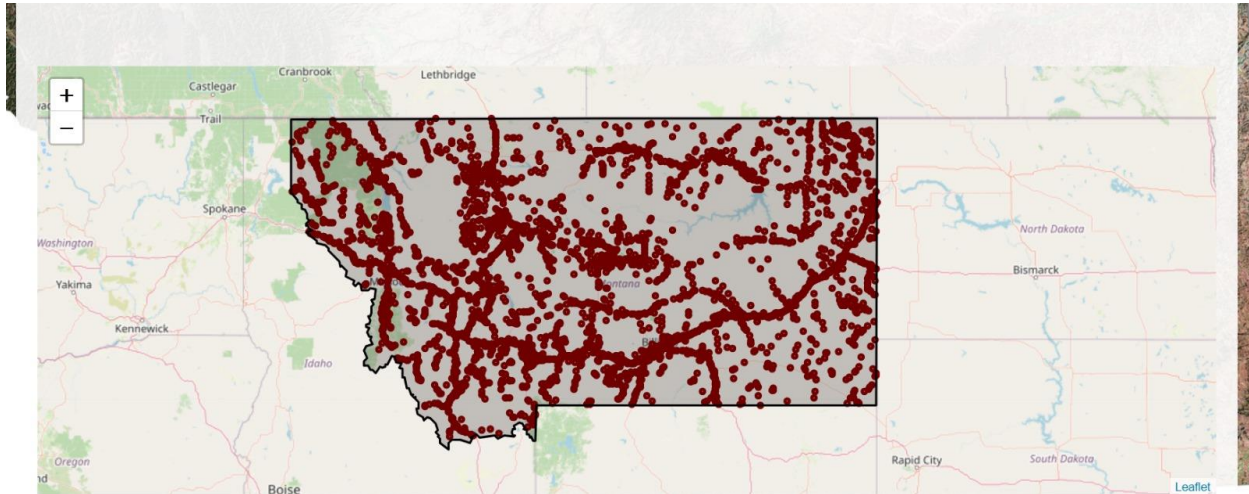


Figure 157. Interactive map of Montana showing bridge deck locations

The core of the tool is the embedded FCNN model, which predicts bridge deck surface temperature under various design and environmental conditions. Users are prompted to specify two types of input parameters: (1) fixed values that remain constant throughout the simulation and (2) time-varying values that may change during the prediction window. The fixed parameters include bridge length (m), initial surface temperature ($^{\circ}\text{C}$), inlet fluid temperature ($^{\circ}\text{C}$), flow rate (L/min), and tube spacing (cm). The tool also allows users to choose between the “with tubing” or “without tubing” configurations to reflect different design scenarios. Figure 159(a) and Figure 159(b) display the fixed and variable input sections of the tool interface, respectively.

For the time-varying parameters, the user provides a sequence of ambient temperature ($^{\circ}\text{C}$), wind speed (km/h), and solar radiation (W/m^2) values, along with the duration (hours) for which each set of conditions remains constant. The tool supports the addition of an unlimited number of segments, allowing users to simulate realistic environmental transitions over time. For each segment, the model uses the ending surface temperature of the previous segment as the initial condition for the next. This sequential logic ensures that transient effects and thermal lag are appropriately captured. Once the input is defined, the tool predicts and plots the surface temperature versus time, enabling dynamic evaluation of system behavior.

Figure 159 presents the prediction output for a two-segment scenario under the “with tubing” condition, with a bridge length of 1.5 m, initial surface temperature of -10°C , inlet temperature of 10°C , flow rate of 25 L/min, and tube spacing of 20 cm. The first segment simulates 12 hours of conditions with ambient temperature of -10°C , wind speed of 10 km/h, and solar radiation of 0

W/m². The second segment maintains the same ambient temperature and wind speed but increases the solar radiation to 490 W/m², sustained for an additional 12 hours. The output plot visualizes how the surface temperature evolves in response to these environmental changes.

(a)

Bridge Deck Surface Temperature Predictor

Select System Type:

Bridge Length (m):

Initial Surface Temp (°C):

Inlet Temperature (°C):

Flow Rate (L/min):

Tube Spacing (cm):

(b)

Environmental Segments

<input type="text" value="Ambient Temp"/>	<input type="text" value="Wind Speed"/>	<input type="text" value="Solar Radiation"/>	<input type="text" value="Duration (hrs)"/>
<input type="text" value="Ambient Temp"/>	<input type="text" value="Wind Speed"/>	<input type="text" value="Solar Radiation"/>	<input type="text" value="Duration (hrs)"/>
<input type="text" value="Ambient Temp"/>	<input type="text" value="Wind Speed"/>	<input type="text" value="Solar Radiation"/>	<input type="text" value="Duration (hrs)"/>

+ Add Segment

Predict Temperature

Figure 158. Input parameters interface for: (a) fixed parameters, and (b) variable parameters

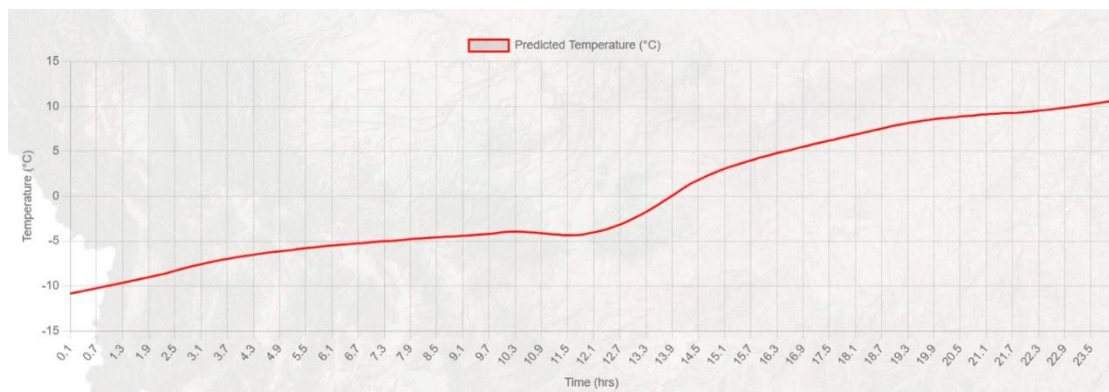


Figure 159. Predicted surface temperature over time for a two-segment “with tubing” scenario

CHAPTER 8: NUMERICAL MODELING – CULVERT

Seasonal and extreme cold weather conditions pose persistent challenges to maintaining the functionality and safety of roadway infrastructure in northern regions. Ice formation within and around culverts can obstruct water flow, cause localized flooding, and hinder aquatic organism passage, resulting in both ecological disruption and economic losses. Repeated freeze–thaw cycles in the soil surrounding the culvert degrade the mechanical properties of the backfill material, weakening the support zone and accelerating erosion or slope instability. Maintaining the temperature of the surrounding soil above 0 °C can help mitigate these effects, ensuring long-term geotechnical stability and reducing the risk of structural failure or maintenance-intensive erosion repairs. This chapter presents data collected and analyzed from numerical simulations to evaluate the effectiveness of a geothermal culvert deicing system in mitigating ice buildup and thermal degradation of frost-susceptible soils. The research summarized here will be submitted for publication in a peer-reviewed journal.

Model Development and Validation

To assess the feasibility and effectiveness of a geothermal culvert deicing system under Montana's cold climate conditions, a three-dimensional numerical model was developed using COMSOL Multiphysics. This model simulated the thermal behavior of a concrete culvert embedded in frost-susceptible soil, incorporating embedded geothermal heat exchanger tubing through which a glycol-water mixture circulated. The model focused on capturing transient heat transfer processes within the culvert structure and surrounding soil, using thermal physics interfaces available in COMSOL Multiphysics. Thermal conduction was considered the primary mechanism through the concrete and soil, while convection was modeled both internally within the tubing (between the fluid and the pipe walls) and externally at culvert faces exposed to ambient air. Radiative heat loss was also included at these exposed boundaries to simulate energy exchange with the environment. Solar input and snow accumulation were intentionally excluded to focus the study on thermal performance during wintertime freezing conditions.

The model geometry included a 2 m × 2 m × 2 m soil domain with a centrally placed concrete culvert with an internal radius of 30.5 cm and wall thickness of 7.5 cm. Heat exchanger tubing was embedded in a spiral configuration along the culvert wall. Fluid flow from inlet to outlet was defined along this tubing network, with flow properties derived from laboratory standards. The soil and culvert domains were discretized using a structured mesh, enabling high-resolution tracking of temperature gradients around the heat source.

To ensure that the model provided realistic and reliable outputs, the numerical model was validated using already previously published studies. Following the validation, model was used to simulate realistic operating scenarios for geothermal culvert heating in Montana. Ground and ambient temperature inputs were derived from site-specific datasets, and simulations were run for a range of inlet fluid temperatures, boundary conditions, and operational configurations. These scenarios laid the foundation for the parametric and sensitivity analyses presented later in the study, with the validated model serving as a reliable tool for evaluating system performance under diverse environmental conditions.

Results and Discussion

This section summarizes the thermal performance of a geothermal culvert deicing system based on three dimensional numerical simulations. The primary aim was to assess the system's ability to raise culvert and soil temperatures under winter conditions, using inlet fluid temperatures of 10°C and 50°C, representing low and high geothermal potential in Montana. Simulations incorporated validated material properties and realistic thermal boundary conditions. In addition, sensitivity analyses were conducted to evaluate the influence of parameters such as ambient temperature, inlet temperature, fluid flowrate, soil conductivity, tube spacing, and operating duration.

Two heat exchanger tubing configurations, spiral and longitudinal, were tested to identify which produced more uniform heating. Both configurations had approximately equal tubing length and contact area. Results after 50 hours showed that while soil temperatures were comparable, the spiral configuration resulted in more consistent temperatures within the culvert, minimizing cold spots. The longitudinal layout created concentrated heating along tube paths. Based on this outcome, the spiral configuration was selected for subsequent simulations.

A baseline model was developed with -8°C ambient temperature, 20 cm tube spacing, 20 L/min flowrate, and $2.0\text{ W/m}\cdot\text{K}$ soil conductivity, conditions representative of Montana's winter climate and typical backfill properties. Quantitative results illustrate that with a 10°C inlet, culvert surface temperatures rose to $\sim 3^{\circ}\text{C}$, while 50°C inlet led to more than 25°C at the culvert surface and sustained above-freezing soil temperatures in the surrounding domain. All heated simulations showed a thermal peak along the culvert wall where the tubing was embedded.

The simulations demonstrated that geothermal heating can effectively elevate culvert and subgrade temperatures under cold conditions. Performance was strongly influenced by inlet fluid temperature, 50°C inlet provided broader heat distribution than 10°C . The tubing layout also played a significant role, with spiral configurations offering better thermal uniformity than longitudinal arrangements. These results serve as a basis for future optimization and practical deployment of geothermal deicing systems in cold climates.

Parametric Studies

To assess how various environmental and design factors influence the thermal behavior of the geothermal culvert deicing system, a set of controlled parametric simulations was performed. Each scenario was derived from the baseline model by varying a single parameter while holding all others constant, allowing for a clear evaluation of its individual influence. The temperature distribution for each case was extracted along the same vertical plane, which was 0.5 m from the front culvert surface, to ensure consistent interpretation across scenarios. Parameters examined included ambient temperature, heating duration, tube spacing, fluid flowrate, and soil thermal properties.

Figure 160 presents the system's response to varying ambient temperatures, ranging from 0°C to -20°C , for both low (10°C) and high (50°C) inlet fluid temperatures. At 10°C inlet temperature, the culvert surface could be warmed above freezing for ambient temperatures down to approximately -16°C , demonstrating its potential for mitigating surface icing under moderately severe winter conditions. However, thermal gains in the surrounding soil were more limited; at a radial distance equal to the culvert's radius (0.33 m), soil temperatures exceeded 0°C only when

the ambient temperature was -4°C or higher. When the inlet fluid temperature was raised to 50°C , the system exhibited substantially improved thermal coverage. Culvert surface temperatures rose to over 30°C at 0°C ambient air, and remained near 23°C even under -20°C conditions. Moreover, at a radial distance of 0.33 m , soil temperatures stayed above freezing across the entire ambient temperature range tested. At twice that distance (0.66 m), corresponding to the culvert diameter, the soil remained thawed for ambient conditions as cold as -8°C . These results underscore the capability of high-temperature geothermal inputs to deliver reliable structural and subsurface deicing, even in extreme cold climates.

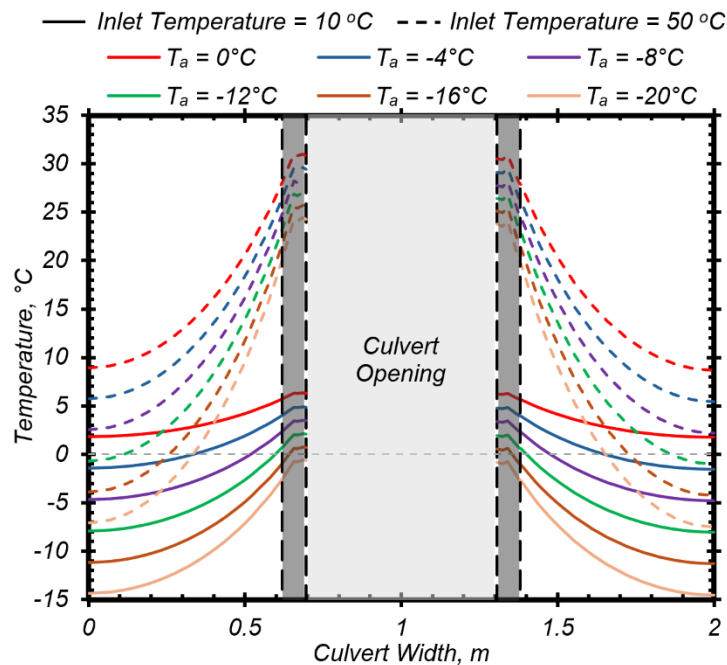


Figure 160. Effect of different ambient temperatures along the studied cut line

Figure 161 illustrates how operational duration influences the thermal behavior of the geothermal culvert deicing system. This evaluation is intended to inform how long the system must be operated to achieve effective deicing in both the culvert structure and surrounding soil during winter weather. Figure 161a displays the temperature profiles along the predefined cut line (0.5 m from the front culvert face) after varying operational periods, ranging from 5 to 45 hours. Figure 161b and 162c provide temperature contour plots for the 5 -hour and 45 -hour cases, respectively. The findings highlight the time-dependent progression of heat diffusion from the tubing through the concrete and into the soil. For a 10°C inlet fluid temperature, the culvert wall temperature rises to a range of approximately -2°C to 0°C after 5 hours. However, this initial warming remains largely confined to the concrete, with little measurable impact on the soil beyond roughly 0.33 meters, the culvert's radius. By 15 hours, the culvert temperature surpasses the freezing point, suggesting that extended operation is needed to sustain deicing. At 50°C inlet temperature, thermal effects develop much faster, after 5 hours, the culvert temperature exceeds 15°C . Still, the warming remains near the tubing in the early phase. By 15 hours, however, temperatures at 0.33 meters into the soil rise above 0°C , indicating faster heat transfer with higher inlet temperatures. After 45 hours, the thermal influence extends to roughly 0.66 meters from the culvert, equal to its diameter, raising temperatures above freezing even in more distant frost-prone soils. This progression is clearly

depicted in the contour plots, which show expanding heat fronts over time, radiating outward from the culvert wall.

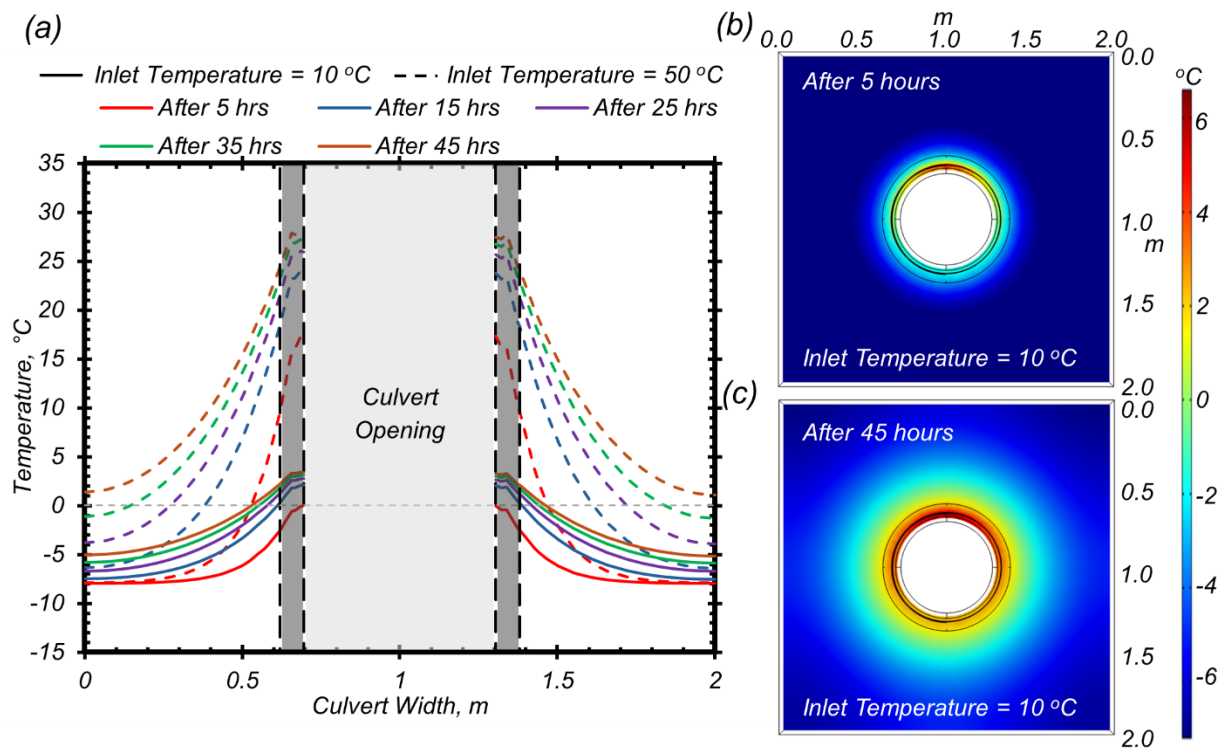


Figure 161. (a) Effect of different operational times on temperature along the studied cut line, (b) temperature contours after 5 hours, and (c) temperature contours after 45 hours

Figure 162 shows how varying the spacing between heat exchanger tubes influences the temperature distribution within the culvert and adjacent soil after 50 hours of system operation. For each tube spacing configuration, the temperature profile was extracted along a cut line positioned midway between adjacent tubing loops to capture the area most distant from the heating source. This method ensured a consistent and conservative evaluation of system performance, focusing on regions most susceptible to insufficient heating. Tube spacing refers to the center-to-center distance between successive spirals. Results indicated that smaller spacing led to more consistent and elevated temperatures throughout the culvert cross-section. As shown in Figure 162a, with a 10 °C inlet temperature, the system maintained culvert wall temperatures above freezing for 20 cm, 25 cm, and 30 cm spacings. However, in the 35 cm case, temperatures remained marginally below 0 °C, although the rising trend suggested that longer operation might achieve deicing. These results also revealed that increasing spacing reduces temperature uniformity, creating cooler zones between heat paths, a critical consideration under harsher weather or shorter heating durations. When the inlet fluid temperature was raised to 50 °C, the system successfully elevated culvert and soil temperatures above freezing for all tested spacings (20–40 cm) at a distance of 0.33 m from the culvert. However, only the 20 cm, 25 cm, and 30 cm cases achieved above-freezing conditions at 0.66 m from the culvert wall. These findings highlight that although higher fluid temperatures can improve performance at wider spacings, closer tube placement is still crucial for achieving widespread and reliable heating in frost-prone areas.

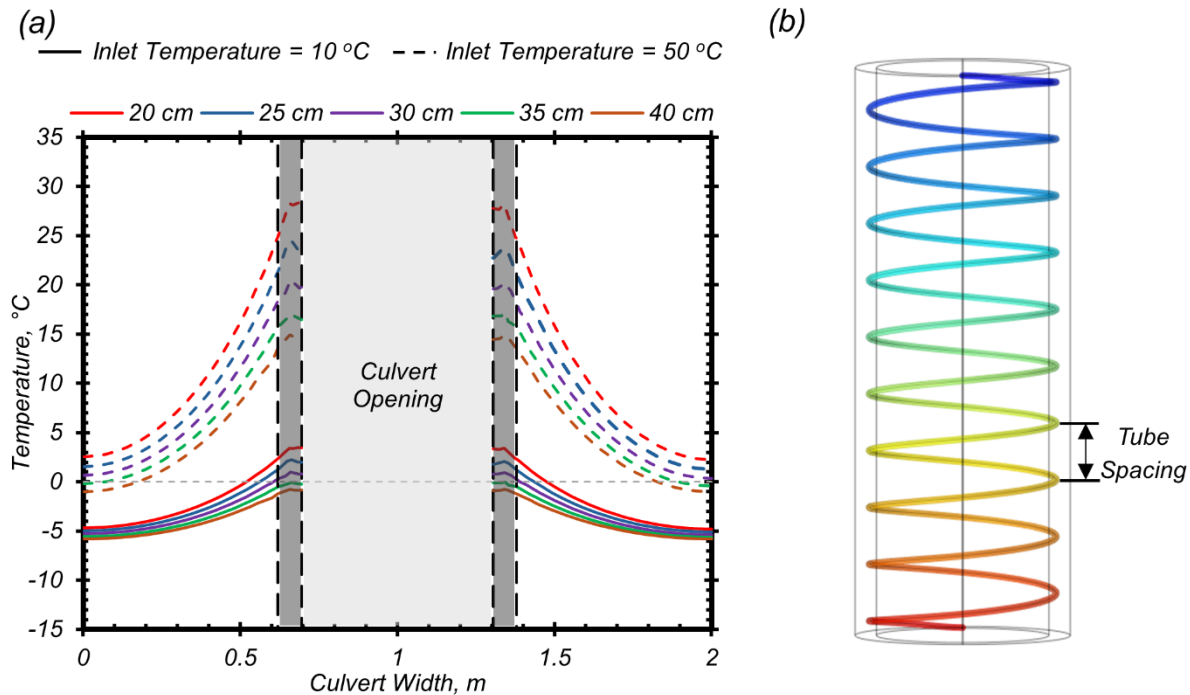


Figure 162. (a) Effect of different tube spacings on temperature along the studied cut line, and (b) plan view of culvert showing tube spacing

Figure 163 illustrates the influence of varying fluid flowrates, 10, 15, 20, and 25 L/min, on the thermal performance of the geothermal culvert deicing system. These relatively high flowrates were chosen to ensure minimal temperature drop along the tubing length, allowing the fluid to maintain near-inlet temperatures and deliver heat uniformly throughout the culvert. As a result, only small differences in temperature were observed across the tested flowrates. With a 10°C inlet temperature, the culvert surface consistently reached above freezing, demonstrating sufficient heating for deicing across the full range of flowrates. Slight increases in temperature at higher flowrates were attributed to improved convective transfer at the pipe-wall interface, although overall performance remained similar. Under the 50°C inlet condition, the system maintained soil temperatures above 0°C even at 0.66 m from the culvert, regardless of flowrate, demonstrating better deicing capability. These findings suggest that once flowrate is adequate to minimize heat loss along the tubing, further increases yield diminishing returns in thermal performance. However, significantly lower flowrates, such as 1–2 L/min, would likely result in more pronounced thermal losses along the tubing and diminished heating at the downstream end, especially under extreme cold conditions.

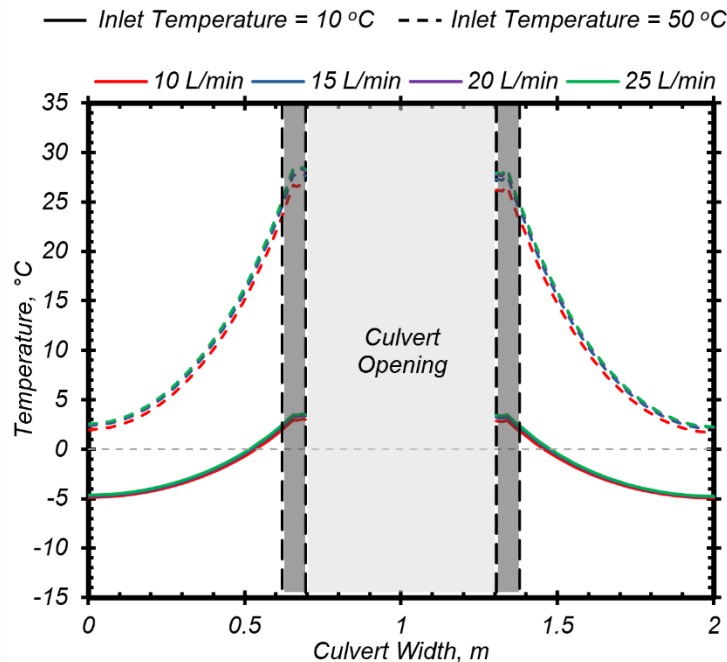


Figure 163. Effect of different fluid flow rates on temperature along the studied cut line

Figure 164 shows how soil thermal conductivity affects the performance of the geothermal culvert deicing system. Simulations were conducted using soil conductivities of 1.5, 2.0, and 2.5 W/m·K to reflect typical variations in compaction and moisture content encountered in field conditions. While culvert temperatures remained consistent across all cases, differences in heat propagation became evident in the surrounding soil. Lower conductivity soils (1.5 W/m·K) showed more localized heating, with elevated temperatures concentrated near the culvert and limited reach into the surrounding backfill. In contrast, higher conductivity soils (2.5 W/m·K) enabled greater heat diffusion but resulted in slightly lower temperatures near the culvert due to more distributed energy flow. This trade-off reflects the fixed thermal input in each case: in low-conductivity soils, heat remains localized, while in high-conductivity soils, it spreads more widely. For the 10°C inlet case, the culvert consistently reached above 0°C regardless of soil type. At 50°C, both culvert and soil temperatures exceeded freezing even at a distance of one culvert diameter (0.66 m). However, beyond this range, deicing performance diminished in low-conductivity soils. These findings highlight the importance of considering soil thermal properties during system design, as they directly influence the spatial extent and uniformity of heating in frost-susceptible zones.

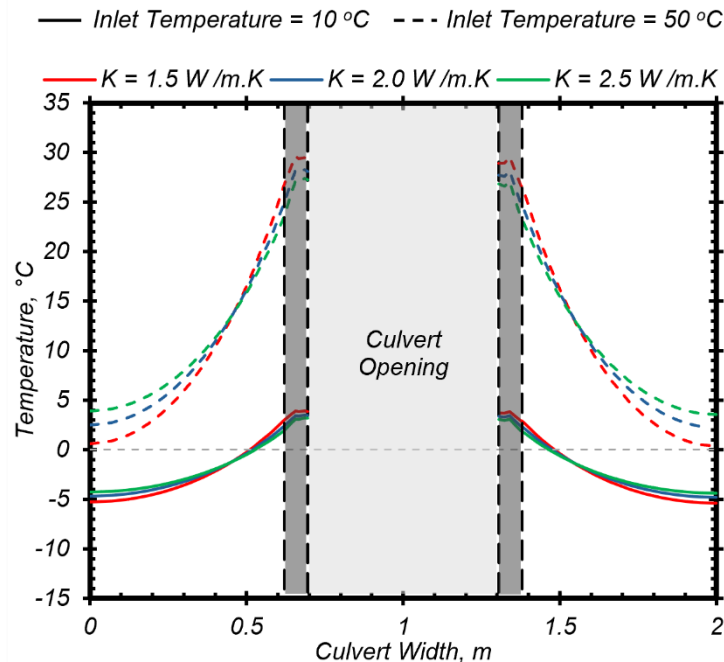


Figure 164. Effect of thermal conductivity of soil on temperature along the studied cut line

Effect of Boundary Conditions

To evaluate how internal culvert conditions affect thermal performance, simulations were carried out under two boundary scenarios: one with the culvert interior filled with ice, and another with stagnant water. These scenarios reflect common winter and transitional seasonal conditions, where culverts may either freeze completely or retain trapped water. The aim was to assess how the internal phase, solid or liquid, modulates heat transfer within the culvert and its surroundings, and whether it hinders or enhances deicing efficiency. Simulations were conducted for both 10°C and 50°C inlet fluid temperatures across multiple ambient conditions.

Figure 165 illustrates the thermal behavior of the system when the culvert is initially filled with ice. To realistically capture this condition, the model incorporated phase change to simulate the melting process. The ice was assumed to begin at ambient temperature, consistent with prolonged cold exposure. Figure 165a presents temperature profiles along the defined cut line after 50 hours for ambient temperatures of 0°C, -4°C, and -8°C, while Figure 165b and 165c display temperature contours for the -8°C case at 5 and 50 hours, respectively. Results indicate that the presence of ice increases the system's thermal load due to the latent heat required for melting. Despite this, the surrounding concrete and soil temperatures closely mirror those from previous scenarios without internal ice, suggesting limited impact on external heat transfer. The results suggested that after 50 hours, ice near the culvert wall has melted, but central ice remains below zero.

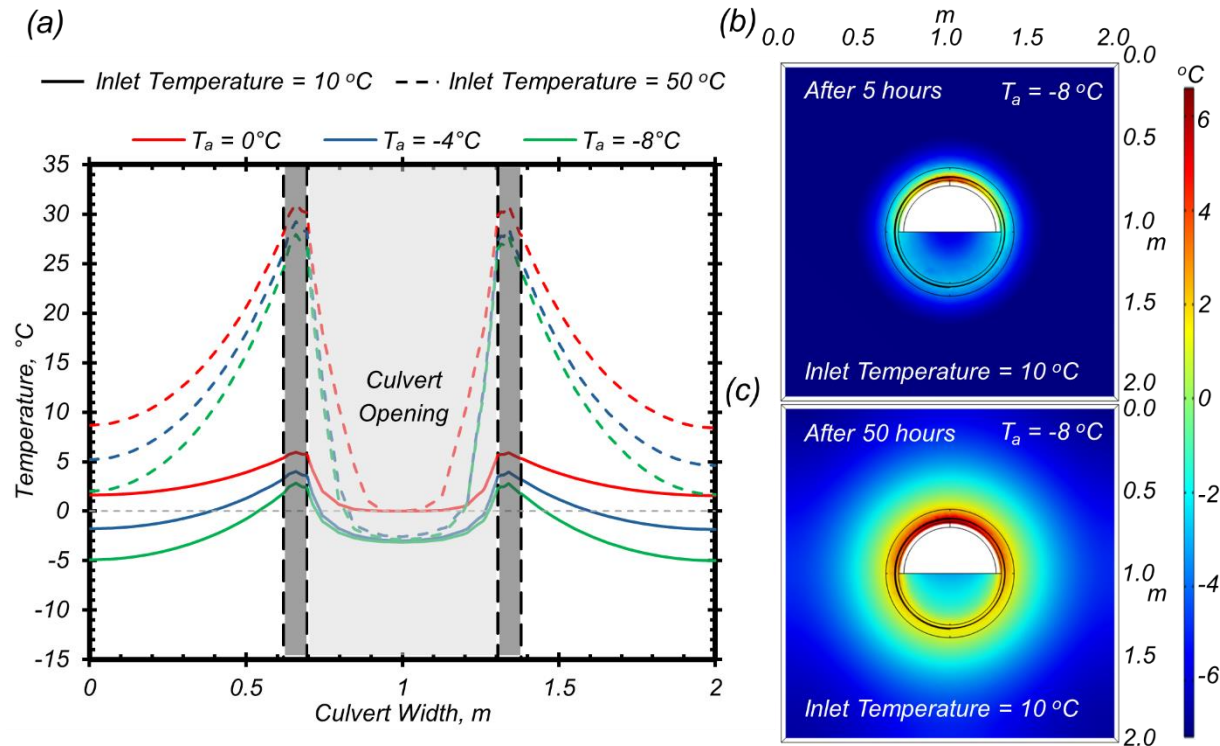


Figure 165. (a) Effect of ambient temperature with ice inside culvert along the studied cut line, (b) temperature contours after 5 hours, and (c) temperature contours after 50 hours

Figure 166 shows the system's thermal performance when the culvert is filled with stagnant water, assumed to remain at a constant initial temperature of 4°C . This setup represents a conservative case, as stagnant water, lacking convective mixing, is more prone to freezing than flowing water. Figure 166a shows temperature profiles along the designated cut line after 50 hours of operation for ambient temperatures of 0°C , -4°C , and -8°C , while Figure 166b and 15c present contour plots at 5 and 50 hours for the -8°C condition. The presence of water inside the culvert had minimal influence on the surrounding thermal field. Temperature distributions within the concrete and adjacent soil closely aligned with results from earlier simulations, including those with ice-filled culverts. Notably, the internal water temperature remained above freezing throughout the simulation period for both 10°C and 50°C inlet conditions. These results indicate that the geothermal system effectively prevents freezing within the culvert, even under extended exposure to subfreezing ambient temperatures, thereby reducing the likelihood of internal ice formation in stagnant water scenarios.

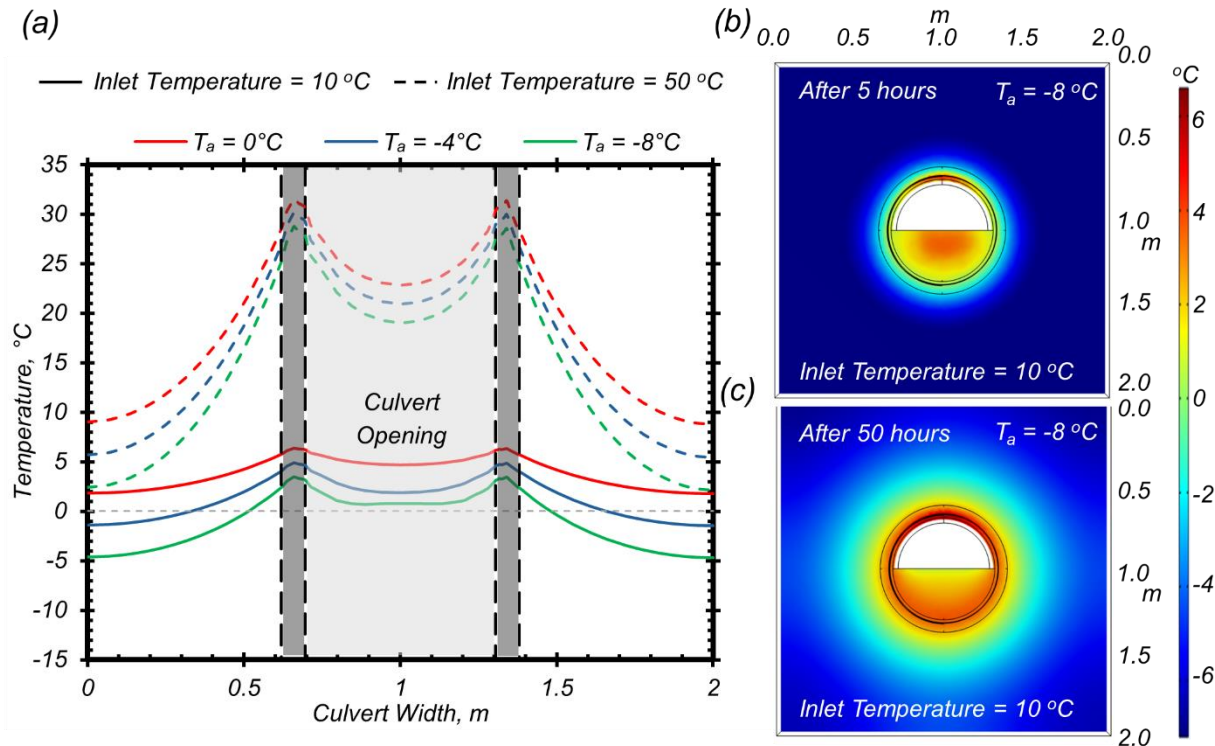


Figure 166. (a) Effect of ambient temperature with water inside culvert along the studied cut line, (b) temperature contours after 5 hours, and (c) temperature contours after 50 hours

Sensitivity Analysis

A sensitivity analysis was performed to identify which parameters most significantly influence the thermal effectiveness of a geothermal culvert deicing system. The analysis focused on soil temperatures at two representative distances from the culvert: one corresponding to the culvert's radius (0.33 m) and the other to its diameter (0.66 m). These distances were selected to evaluate how well the system performs both near the culvert wall and farther into the surrounding soil. The baseline model used for comparison incorporated moderate winter conditions, with an ambient air temperature of -8°C , a 20°C inlet fluid temperature, a 30-hour operational duration, a spiral tubing arrangement with 20 cm spacing, soil thermal conductivity of $2.0 \text{ W/m}\cdot\text{K}$, and a fluid flowrate of 20 L/min. This setup represented average values within the parameter ranges examined, providing a balanced basis for assessing the influence of both increases and decreases in each parameter.

At the location near the culvert wall, the soil temperature under baseline conditions was approximately -2.0°C . Among the parameters evaluated, ambient air temperature had the most significant impact. Lowering the ambient temperature to -20°C caused the soil temperature to drop by over 9°C , while raising it to 0°C increased the soil temperature by more than 6°C , indicating a total variation of around 15°C . Inlet fluid temperature was the second most influential factor, with changes from 10°C to 50°C leading to an approximate 8°C difference in soil temperature. Operational time also played a major role, extending the heating duration from 5 to 50 hours produced a temperature difference of nearly 8°C . Parameters such as tube spacing, soil thermal conductivity, and flowrate demonstrated a lesser but still noticeable influence. Changes to these

inputs affected the temperature to a smaller degree compared to ambient conditions, inlet temperature, and operational time, particularly within the immediate vicinity of the culvert.

At the farther distance corresponding to the culvert diameter, the trends remained consistent, though the magnitude of temperature differences varied. Ambient temperature continued to dominate, with a total impact of nearly 18°C across the tested range. Inlet temperature produced a smaller change in soil temperature, approximately 6°C, compared to its influence closer to the culvert. Similarly, the impact of operational time was reduced, yielding around a 5°C difference between the shortest and longest durations tested. The remaining parameters exhibited even less pronounced effects at this greater distance, indicating their limited influence on soil temperatures beyond the near-field zone.

In summary, ambient air temperature, inlet fluid temperature, and operational duration are the most critical factors influencing the thermal reach and intensity of the deicing system. These parameters should be given priority during system design and planning to maximize performance. Although parameters like tube spacing, soil thermal conductivity, and fluid flow rate also contribute, their effects are more modest, particularly in areas farther from the culvert wall.

CHAPTER 9: SUMMARY AND CONCLUSION

Summary

This report presents a comprehensive study of shallow geothermal bridge deck deicing systems, tailored for cold climates such as those in Montana. The research integrates field surveys, literature review, experimental testing, numerical modeling, and machine learning to evaluate the feasibility and performance of these systems under representative winter conditions. The primary objective was to understand the potential of geothermal systems to prevent snow accumulation, mitigate ice formation, and reduce concrete deterioration due to thermal gradients and freeze–thaw cycling.

The study begins with a statewide survey of current winter maintenance practices by the Montana Department of Transportation (MDT). Findings highlighted current reliance on traditional deicing methods such as salt and sand application, which incur significant environmental and operational costs.

A detailed literature review followed, covering shallow geothermal energy fundamentals, system components (primary and secondary units), and construction methods. Global case studies from China, Japan, Switzerland, and the U.S. were reviewed, along with laboratory and numerical investigations on tube spacing, fluid temperature, and soil properties. These references provided a contextual basis for Montana’s climate and infrastructure needs.

To experimentally evaluate geothermal system performance, two model-scale bridge decks were constructed and tested in Montana State University’s Subzero Research Laboratory. One model focused on snow melting and frost mitigation; the second addressed early-age cracking in cold-cured concrete. Representative Montana weather conditions were simulated using data from RWIS stations. Strain gauges and thermocouples were installed at different depths in the bridge deck. The experiments demonstrated the system’s ability to elevate deck surface temperatures and reduce thermal gradients under moderate winter scenarios. In the early-age curing tests, the geothermal system moderated peak curing temperatures, mitigating thermal shrinkage risk.

To simulate a wider range of conditions, a three-dimensional finite element model was developed in COMSOL Multiphysics. This model was calibrated using experimental data and used to simulate scenarios with 10°C and 50°C inlet fluid temperatures. The 10°C condition represents typical shallow geothermal potential in Montana, while 50°C reflects higher geothermal zones such as those near hot springs. The numerical simulations evaluated heat transfer in the concrete deck and surrounding soil and assessed operational effectiveness under various ambient conditions, inlet temperatures, flowrates, tubing layouts, and durations.

Additionally, snow melting performance was evaluated in a controlled lab environment using staged snow application and solar radiation simulation. Tests with and without geothermal heating showed that passive solar gain alone was inadequate to melt snow due to its insulating nature. However, the active geothermal system consistently raised deck surface temperatures to above freezing, initiating melt under both light and moderate snow loads.

To enhance decision-making capability, a machine learning (ML) framework was developed using results from over 2,000 COMSOL simulations. Two ML models were created: one to predict stabilized outcomes like deicing time and final surface temperature, and another for continuous surface temperature prediction at 0.1-hour intervals. ML algorithms including XGBoost and

FCNN were trained on environmental and design variables. Feature importance analysis aligned with earlier simulation results, highlighting ambient temperature, inlet temperature, and solar radiation as dominant factors.

In addition to bridge deck systems, the study also evaluated the feasibility of using geothermal heating for deicing concrete culverts and protecting surrounding frost-susceptible soils. A separate three-dimensional COMSOL Multiphysics model was developed to simulate heat transfer within a culvert structure embedded in compacted sandy soil. The model was validated using experimental and field data from prior geothermal studies. Simulations with 10°C and 50°C inlet fluid temperatures were conducted under representative Montana winter conditions, including scenarios with water- and ice-filled culverts. The results demonstrated that the geothermal system could raise culvert and adjacent soil temperatures above freezing, mitigating risks of ice blockage, frost heave, and freeze–thaw degradation. Parametric and sensitivity analyses showed that ambient temperature, inlet fluid temperature, and operational duration were the most influential variables affecting system performance. These findings highlight the broader applicability of geothermal systems beyond bridge decks and support their integration into winter infrastructure maintenance strategies.

Conclusion

Bridge deck deicing system

This study concludes that shallow geothermal systems are a promising solution for winter bridge deck deicing and the mitigation of concrete deterioration in cold climates like Montana. Through integrated laboratory testing, numerical modeling, and predictive analytics, the research demonstrates the system’s ability to raise deck temperatures, reduce thermal strain, and mitigate risks associated with snow, ice, and freeze–thaw cycles.

Two physical bridge deck models were tested in MSU’s Subzero Research Laboratory. The first model, targeting snow and ice removal and frost action mitigation, was tested under controlled Montana weather conditions. With an inlet fluid temperature of approximately 8°C, the system successfully raised bridge deck surface temperatures above 0°C under mild conditions. The system also reduced thermal strains, average strains dropped by 40%, and peak strains by 18%, compared to the case without heating. While the system did not fully eliminate frost action or thermal gradients, it notably improved the internal thermal profile. The second model, designed for early-age concrete behavior, showed that the geothermal system helped reduce the difference between peak curing and stabilized temperatures, suggesting improved control over thermal shrinkage during early-age curing.

The validated COMSOL model simulated the system under Montana-specific boundary conditions. For an inlet fluid temperature of 10°C, the system effectively raised deck surface temperatures above freezing and reduced strain under moderate winter conditions. The 50°C fluid condition demonstrated better performance, achieving soil and concrete temperatures above freezing even during extreme cold scenarios and providing meaningful reductions in frost penetration.

In laboratory snow-melting tests, the geothermal system proved more effective than passive solar radiation alone. Snow applied at deck temperature showed minimal melting under solar input,

highlighting the insulating effects of snow. Activation of the geothermal system elevated deck surface temperatures to 0°C, initiating melting under both light and moderate snow conditions. This finding shows the importance of proactive geothermal systems during overcast or heavy snowfall events.

The machine learning models provided accurate and efficient predictions of deck surface temperatures under a wide range of environmental and operational inputs. XGBoost performed better for stabilized outcome predictions, while the FCNN model performed better in continuous temperature time-series forecasting. Feature importance analysis showed ambient temperature had the greatest effect on system performance, followed by inlet fluid temperature and solar radiation. Flowrate and tube spacing had secondary influence, suggesting that geothermal system design should prioritize responsiveness to external weather conditions.

Ambient temperature consistently emerged as the most influential parameter across experimental, numerical, and machine learning results. In sensitivity analyses, reducing ambient temperature from 0°C to -20°C lowered surface temperature by over 15°C, demonstrating its dominant role in thermal performance. While other parameters such as inlet temperature and operational duration showed notable impacts, their effects were comparatively smaller.

Finally, geospatial analysis showed that geothermal viability in Montana varies significantly by location. Subsurface temperature data from over 1,000 wells ranged from 3.6°C to 49.5°C, with higher values representing hot spring locations. Coupled with weather data from RWIS stations, these findings support targeted deployment of geothermal systems in high-priority areas where thermal demand and geothermal potential align.

In conclusion, this study establishes a validated, data-driven framework for geothermal bridge deck deicing in Montana. The results indicate that shallow geothermal systems offer substantial potential for reducing infrastructure deterioration, improving winter maintenance effectiveness, and enhancing public safety. Future work should focus on conducting long-term field trials, assessing economic feasibility, and developing integrated smart operational controls to support widespread implementation.

Culvert deicing system

The numerical modeling results for culvert showed that a 10°C inlet fluid temperature could elevate culvert surface temperatures to approximately 3°C and maintain near-surface soil temperatures above freezing under moderate winter conditions. With a 50°C inlet fluid temperature, the system demonstrated significantly improved performance, raising culvert wall temperatures to over 25°C and maintaining soil temperatures above 0°C at distances up to 0.66 m from the culvert surface, even at ambient temperatures as low as -20°C. Spiral tubing layouts produced more uniform heat distribution than longitudinal configurations. Simulations with internal ice or water showed that the culvert fill material had minimal influence on external soil temperature distribution, although ice required extended heating due to latent heat effects. Sensitivity analysis showed ambient temperature as the most influential parameter, followed by inlet temperature and operational time. These results highlight the potential of geothermal systems for culvert deicing and subgrade protection, especially when high inlet temperatures and extended operational periods are feasible.

REFERENCES

- Abbasy, F. (2009). Thermal conductivity of mine backfill [*Doctoral dissertation, Concordia University*].
- Adam, D., & Markiewicz, R. (2009). Energy from earth-coupled structures, foundations, tunnels and sewers. *Géotechnique*, 59(3), 229-236.
- Agent, K. R., & Deen, R. C. (1976). Highway accidents at bridges. *Journal of the Transportation Research Board, Transportation Research Record* (601).
- Akrouch, G. A., Sánchez, M., & Briaud, J.-L. (2014). Thermo-mechanical behavior of energy piles in high plasticity clays. *Acta Geotechnica*, 9(3), 399-412.
- Al-Kaisy, A., & Ewan, L. (2017). Prioritization scheme for proposed road weather information system sites: Montana case study. *Frontiers in built environment*, 3, 45.
- Allan, M., & Philippacopoulos, A. (1999). Ground water protection issues with geothermal heat pumps. (No. BNL-66666; EF4001). *Brookhaven National Lab.*, Upton, NY (US).
- Alrtimi, A., Rouainia, M., & Haigh, S. (2016). Thermal conductivity of a sandy soil. *Applied Thermal Engineering*, 106, 551-560.
- Alungbe, G., Tia, M., & Bloomquist D. (1992). Effects of aggregate, water/cement ratio, and curing on the coefficient of linear thermal expansion of concrete. *Transportation Research Record* 1335 (pp. 44-51).
- American Association of State Highway and Transportation Officials (AASHTO) (2021). AASHTO LRFD Bridge Design Specifications, Customary U.S. Units. *American Association of State Highway and Transportation Officials* (AASHTO), S.I.
- American Society of Heating Refrigerating and Air-Conditioning Engineers (ASHRAE) (1999). ASHRAE Handbook - Fundamentals (SI Edition), *American Society of Heating, Refrigerating and Air-Conditioning Engineers, Inc.*
- American Society of Heating Refrigerating and Air-Conditioning Engineers (ASHRAE) (2013). ASHRAE Handbook - Fundamentals (SI Edition), *American Society of Heating, Refrigerating and Air-Conditioning Engineers, Inc.*
- ASHRAE, B. A. I., & Design, E. (2011). ASHRAE Handbook-HVAC Applications (SI). *American Society of Heating, Refrigerating and Air-Conditioning Engineers, Inc., Atlanta, USA*.
- ASTM Standard C42, (2020). Standard Test Method for Obtaining and Testing Drilled Cores and Sawed Beams of Concrete. *ASTM International*, West Conshohocken, PA, 2020, DOI: 10.1520/C0042-20, www.astm.org.
- Atalay, F. (2019). Engineered transition zone systems for enhanced heat transfer in thermo-active foundations [*Doctoral dissertation, Georgia Institute of Technology*].
- ATSDR, A. (1997). Agency for toxic substances and disease registry. *Case Studies in environmental medicine*. <http://www.atsdr.cdc.gov/HEC/CSEM/csem.html>.
- Babaei, K., & Fouladgar, A. (1997). Solutions to concrete bridge deck cracking. *Concrete International*, 19(7), 34-37.
- Baboian, R. (1992). Synergistic effects of acid deposition and road salts on corrosion. In *Corrosion forms and control for infrastructure* (pp. 17-29). ASTM International.

- Bach, B., Werling, J., Ommen, T., Münster, M., Morales, J. M., & Elmegaard, B. (2016). Integration of large-scale heat pumps in the district heating systems of Greater Copenhagen. *Energy*, 107, 321-334.
- Bakker, M., Zondag, H., Elswijk, M., Strootman, K., & Jong, M. (2005). Performance and costs of a roof-sized PV/thermal array combined with a ground coupled heat pump. *Solar energy*, 78(2), 331-339.
- Balbay, A., & Esen, M. (2010). Experimental investigation of using ground source heat pump system for snow melting on pavements and bridge decks. *Scientific Research and Essays*, 5(24), 3955-3966.
- Barnes, K. (2017). Design memo - minimum bridge deck thickness. *Montana Department of Transportation*.
- Balbay, A., & Esen, M. (2013). Temperature distributions in pavement and bridge slabs heated by using vertical ground-source heat pump systems. *Acta Scientiarum. Technology*, 35(4), 677-685.
- Beck, M., Bayer, P., de Paly, M., Hecht-Méndez, J., & Zell, A. (2013). Geometric arrangement and operation mode adjustment in low-enthalpy geothermal borehole fields for heating. *Energy*, 49, 434-443.
- Bejan, A. (2013). Convection heat transfer. *John wiley & sons*.
- Beran, D., & Wilfong, T. (1998). US wind profilers: a review. *Office of the Federal Coordinator for Meteorological Services and Supporting Research (OFCM) Rep*.
- Bergman, T. L., Incropera, F. P., DeWitt, D. P., & Lavine, A. S. (2011). Fundamentals of heat and mass transfer. *John Wiley & Sons*.
- Bernier, M., & Shirazi, A. S. (2007). Solar heat injection into boreholes: a preliminary analysis, *Canadian Solar Buildings Conference, Calgary*, June 10-13, 2007. paper T1-1-1.
- Bloomquist, R. G. (2000). Geothermal heat pumps five plus decades of experience in the United States. *Proceedings World Geothermal Congress 2000*.
- Bowers, J., G Allen, & Olgun, C. G. (2014). Ground-source bridge deck deicing systems using energy foundations. *Geo-Congress 2014: Geo-characterization and Modeling for Sustainability*.
- Bowers Jr, G. A. (2016). Ground-source bridge deck deicing and integrated shallow geothermal energy harvesting systems [Doctoral dissertation, Virginia Tech].
- Bowers Jr, G. A., & Olgun, C. G. (2020). Optimization of Energy Pile Grids during Unbalanced Heating and Cooling Operations. *Geo-Congress 2020: Geo-Systems, Sustainability, Geoenvironmental Engineering, and Unsaturated Soil Mechanics, Geoenvironmental Engineering, and Unsaturated Soil Mechanics* (pp. 70-79). Reston, VA: American Society of Civil Engineers.
- Boyd, T. L. (2003). New snow melt projects in Klamath Falls, OR. *Geo-Heat Center Quarterly Bulletin*, 24(3), 12-15.
- Bozis, D., Papakostas, K., & Kyriakis, N. (2011). On the evaluation of design parameters effects on the heat transfer efficiency of energy piles. *Energy and buildings*, 43(4), 1020-1029.
- Brandl, H. (2006). Energy foundations and other thermo-active ground structures. *Géotechnique*, 56(2), 81-122.
- Carey, K. L. (1984). Solving problems of ice-blocked drainage. US Army Corps of Engineers, *Cold Regions Research & Engineering Laboratory*, (No. 84).
- Chapman, W.P. (1952). Design of snow melting system. *Heating and Ventilating*, (49) 4: 95-102.

- Chen, X., Kong, G., Liu, H., Yang, T., & Zhu, X. (2020). Experimental on thermal performance of bridge deck with hydronic heating system. *Cold regions science and technology*, 178, 103130.
- Chou, C.-W., Seagren, E. A., Aydilek, A. H., & Lai, M. (2011). Biocalcification of sand through ureolysis. *Journal of Geotechnical and Geoenvironmental Engineering*, 137(12), 1179-1189.
- Chowdhury, M. (2019). Analytical and numerical modeling of externally heated geothermal bridge deck [Doctoral dissertation, University of Texa].
- COMSOL. (2017). "COMSOL Multiphysics™ Version 5.3: Pipe Flow Module User's Guide." COMSOL Inc., Burlington, MA.
- COMSOL. (2018a). "COMSOL Multiphysics™ Version 5.4: Heat Transfer Module User's Guide." COMSOL Inc., Burlington, MA.
- COMSOL. (2018b). "COMSOL Multiphysics™ Version 5.4: Structural Mechanics Module User's Guide." COMSOL Inc., Burlington, MA.
- Cuthbert, M. O., McMillan, L. A., Handley-Sidhu, S., Riley, M. S., Tobler, D. J., & Phoenix, V. R. (2013). A field and modeling study of fractured rock permeability reduction using microbially induced calcite precipitation. *Environmental science & technology*, 47(23), 13637-13643.
- Dawoud, B., Amer, E. H., & Gross, D. M. (2007). Experimental investigation of an adsorptive thermal energy storage. *International Journal of Energy Research*, 31(2), 135-147.
- De Moel, M., Bach, P. M., Bouazza, A., Singh, R. M., & Sun, J. O. (2010). Technological advances and applications of geothermal energy pile foundations and their feasibility in Australia. *Renewable and Sustainable Energy Reviews*, 14(9), 2683-2696.
- de Paly, M., Hecht-Méndez, J., Beck, M., Blum, P., Zell, A., & Bayer, P. (2012). Optimization of energy extraction for closed shallow geothermal systems using linear programming. *Geothermics*, 43, 57-65.
- DeJong, J. T., Fritzges, M. B., & Nüsslein, K. (2006). Microbially induced cementation to control sand response to undrained shear. *Journal of Geotechnical and Geoenvironmental Engineering*, 132(11), 1381-1392.
- DeJong, J. T., Mortensen, B. M., Martinez, B. C., & Nelson, D. C. (2010). Bio-mediated soil improvement. *Ecological Engineering*, 36(2), 197-210.
- Deng, Y., Phares, B., & Harrington, D. (2016). Causes of early cracking in concrete bridge decks. *The Long-Term Plan for Concrete Pavement Research and Technology (CP Road Map)*.
- Duffie, J. A., Beckman, W. A., & Blair, N. (2020). Solar engineering of thermal processes, photovoltaics and wind. *John Wiley & Sons*.
- Ebigbo, A., Phillips, A., Gerlach, R., Helmig, R., Cunningham, A. B., Class, H., & Spangler, L. H. (2012). Darcy-scale modeling of microbially induced carbonate mineral precipitation in sand columns. *Water Resources Research*, 48(7).
- Eugster, W. J. (2007). Road and bridge heating using geothermal energy. overview and examples. *Proceedings European geothermal congress*, (Vol. 2007).
- Faizal, M., Bouazza, A., McCartney, J. S., & Haberfield, C. (2019). Effects of cyclic temperature variations on thermal response of an energy pile under a residential building. *Journal of Geotechnical and Geoenvironmental Engineering*, 145(10), 04019066.
- Faizal, M., Bouazza, A., & Singh, R. M. (2016). Heat transfer enhancement of geothermal energy piles. *Renewable and Sustainable Energy Reviews*, 57, 16-33.

- Farouki, O. T. (1981). The thermal properties of soils in cold regions. *Cold regions science and technology*, 5(1), 67-75.
- Feng, J., & Yin, G. (2019). Thermal Analyses and Responses of Bridge Deck Hydronic Snow Melting System. *Advances in Civil Engineering*, 2019.
- Feng, K., & Montoya, B. (2015). Drained shear strength of MICP sand at varying cementation levels. In *IFCEE 2015* (pp. 2242-2251).
- FHWA. (2013). Highway statistics 2013. (FHWA, *Office of Highway Policy Information, Highway Statistics Series, Table DL-22-Highway Statistics* 2013). <http://www.fhwa.dot.gov/policyinformation/statistics/2013/dl22.cfm>
- Fischel, M. (2001). Evaluation of selected deicers based on a review of the literature. *CDOT-DTD-R-2001-15*, 160. (Colorado Department of Transportation).
- Fliegel, J., Flyer, J., Katz, M., Le, A., Ngo, T., Roberts, K., Santoro, A., Sun, C., & Weyforth, T. (2010). Design and evaluation of a retrofittable electric snow melting system for pavements [Doctoral dissertation, University of Maryland].
- Frederickson, W., Grothaus, J., & Schaefer, K. (2005). Minnesota Snow and Ice Control Field Handbook.
- Gao, J., Zhang, X., Liu, J., Li, K. S., & Yang, J. (2008). Thermal performance and ground temperature of vertical pile-foundation heat exchangers: A case study. *Applied Thermal Engineering*, 28(17-18), 2295-2304.
- Ghasemi-Fare, O., & Basu, P. (2016). Predictive assessment of heat exchange performance of geothermal piles. *Renewable Energy*, 86, 1178-1196.
- Ghasemi-Fare, O., Bowers, G. A., Kramer, C. A., Ozudogru, T. Y., Basu, P., Olgun, C. G., Bulbul, T., & Sutman, M. (2015). *A feasibility study of bridge deck deicing using geothermal energy*.
- Goodwin, L. C., & Pisano, P. (2003). Best practices for road weather management. *Road Weather, FHWA-OP-03-081*, 131.
- Granata, R., & Hartt, W. H. (2009). Integrity of infrastructure materials and structures. *U.S.D.o.T. FHWA, ed., FHWA, U.S. Department of Transportation, United States*, 90p.
- Habibzadeh-Bigdarvish, O., Yu, X., Lei, G., Li, T., & Puppala, A. J. (2019). Life-Cycle cost-benefit analysis of Bridge deck de-icing using geothermal heat pump system: A case study of North Texas. *Sustainable cities and society*, 47, 101492.
- Hamada, Y., Saitoh, H., Nakamura, M., Kubota, H., & Ochifuji, K. (2007). Field performance of an energy pile system for space heating. *Energy and buildings*, 39(5), 517-524.
- Han, C., & Yu, X. B. (2017). Feasibility of geothermal heat exchanger pile-based bridge deck snow melting system: A simulation based analysis. *Renewable Energy*, 101, 214-224.
- Heinonen, E., Tapscott, R., Wilden, M., & Bell, A. (1996). Assessment of Anti-Freeze Solutions for Ground Source Heat Pumps. *New Mexico Engineering Research Institute NMERI 96/15/32580*, 156 p.
- Hiller, C. (2000). Grouting for Vertical Geothermal Heat Pump Systems: Engineering Design and Field Procedures Manual. *International Ground Source Heat Pump Association*.
- Ho, I.-H., & Dickson, M. (2017). Numerical modeling of heat production using geothermal energy for a snow-melting system. *Geomechanics for Energy and the Environment*, 10, 42-51.
- Ho, I.-H., Li, S., & Abudureyimu, S. (2019). Alternative hydronic pavement heating system using deep direct use of geothermal hot water. *Cold regions science and technology*, 160, 194-208.

- Hommel, J., Lauchnor, E., Phillips, A., Gerlach, R., Cunningham, A. B., Helmig, R., Ebigo, A., & Class, H. (2015). A revised model for microbially induced calcite precipitation: Improvements and new insights based on recent experiments. *Water Resources Research*, 51(5), 3695-3715.
- Howell, J. R., Mengüç, M. P., Daun, K., & Siegel, R. (2020). Thermal radiation heat transfer. *CRC press*.
- Incropera, F. P., DeWitt, D. P., Bergman, T. L., & Lavine, A. S. (2006). Transient conduction. *Fundamentals of heat and mass transfer*, 3, 243-245.
- Ismail, A. F., Hassan, A. R., & Cheer, N. B. (2002). Effect of shear rate on the performance of nanofiltration membrane for water desalination. *Songklanakarin J. Sci. Technol*, 24, 879-889.
- Jackson, F. (1944). Concretes containing air-entraining agents. *ACI Journal Proceedings*, 40. <https://doi.org/10.14359/8671>.
- Johnson, J. (2005). Concrete bridge deck behavior under thermal loads [*Masters Thesis, Montana State*].
- Johnston, I., Narsilio, G., & Colls, S. (2011). Emerging geothermal energy technologies. *KSCE Journal of Civil Engineering*, 15(4), 643-653.
- Kelting, D. L., & Laxon, C. L. (2010). Review of effects and costs of road de-icing with recommendations for winter road management in the Adirondack Park. *Adirondack Watershed Institute*.
- Kim, K. H., Jeon, S. E., Kim, J. K., & Yang, S. (2003). An experimental study on thermal conductivity of concrete. *Cement and concrete research*, 33(3), 363-371.
- Kim, T., Olek, J., & Jeong, H. (2015). Alkali-silica reaction: kinetics of chemistry of pore solution and calcium hydroxide content in cementitious system. *Cement and Concrete Research*, 71, 36-45.
- Koch, G. H., Brongers, M. P., Thompson, N. G., Virmani, Y. P., & Payer, J. H. (2002). Corrosion cost and preventive strategies in the United States. *FHWA, U.S. Department of Transportation, United States*, 790p.
- Kong, G., Wu, D., Liu, H., Laloui, L., Cheng, X., & Zhu, X. (2019). Performance of a geothermal energy deicing system for bridge deck using a pile heat exchanger. *International Journal of Energy Research*, 43(1), 596-603.
- Kuishan, L., Xu, Z., Jun, G., & Jun, L. (2007). Research of Heat transfer performance of Pile-foundation groundcoupled heat pump and soil temperature rise. Hangzhou: *the 2007 academic conference of the Chinese association of refrigeration-innovation and development*, 54-59.
- Kusuda, T., & Achenbach, P. R. (1965). Earth temperature and thermal diffusivity at selected stations in the United States, *National Bureau of Standards Gaithersburg MD (No. NBS-8972)*.
- Lee, C., & Lam, H. (2013). A simplified model of energy pile for ground-source heat pump systems. *Energy*, 55, 838-845.
- Lee, C., Lee, K., Choi, H., & Choi, H.-P. (2010). Characteristics of thermally-enhanced bentonite grouts for geothermal heat exchanger in South Korea. *Science in China Series E: Technological Sciences*, 53(1), 123-128.
- Leenders, F., Schaap, A., van der Ree, B., & Van der Helden, W. v. (2000). Technology review on PV/Thermal concepts. edited by H. Scheer et al. James and James, *Proceedings of the 16th European Photovoltaic solar energy conference. Glasgow*.
- Levinson, R. & H. Akbari, (2001). Effects of composition and exposure on the solar reflectance of Portland cement concrete, LBNL-48334, *Heat Island Group, Environmental Energy Technologies Division, Lawrence Berkeley National Laboratory, University of California, Berkeley, CA*.

- Likos, W. J. (2015). Pore-scale model for thermal conductivity of unsaturated sand. *Geotechnical and Geological Engineering*, 33(2), 179-192.
- Lin, H., Suleiman, M. T., Brown, D. G., & Kavazanjian Jr, E. (2016). Mechanical behavior of sands treated by microbially induced carbonate precipitation. *Journal of Geotechnical and Geoenvironmental Engineering*, 142(2), 04015066.
- Liu, H., Maghoul, P., & Holländer, H. M. (2019). Sensitivity analysis and optimum design of a hydronic snow melting system during snowfall. *Physics and Chemistry of the Earth, Parts A/B/C*, 113, 31-42.
- Liu, X. (2005). Development and experimental validation of simulation of hydronic snow melting systems for bridges [Doctoral dissertation, Oklahoma State University].
- Liu, X., Rees, S. J., & Spitler, J. D. (2007). Modeling snow melting on heated pavement surfaces. Part I: Model development. *Applied Thermal Engineering*, 27(5-6), 1115-1124.
- Loveridge, F. (2012). The thermal performance of foundation piles used as heat exchangers in ground energy systems [Doctoral dissertation, University of Southampton].
- Loveridge, F., McCartney, J. S., Narsilio, G. A., & Sanchez, M. (2020). Energy geostructures: a review of analysis approaches, in situ testing and model scale experiments. *Geomechanics for Energy and the Environment*, 22, 100173.
- Lund, J., & Boyd, T. (2016). Direct utilization of geothermal energy 2015 Worldwide review. *Geothermics*, 60, pp. 66-93.
- Lund, J. W., & Toth, A. N. (2020). Direct Utilization of geothermal energy 2020 Worldwide review. *Geothermics*, 101915.
- Martin, M., & P. Berdahl, (1984). Characteristics of infrared sky radiation in the United States. *Solar Energy*, 33(3/4): 321-336.
- Martinez, A., Huang, L., & Gomez, M. (2019). Thermal conductivity of MICP-treated sands at varying degrees of saturation. *Géotechnique Letters*, 9(1), 15-21.
- McCartney, J. S., Sánchez, M., & Tomac, I. (2016). Energy geotechnics: Advances in subsurface energy recovery, storage, exchange, and waste management. *Computers and Geotechnics*, 75, 244-256.
- Mehta, K. P., & Monteiro, P. J. (2014). Concrete: Microstructure, Properties, and Materials (4th Edition ed.). New York: McGraw-Hill.
- Midttomme, K., & Roaldset, E. (1998). The effect of grain size on thermal conductivity of quartz sands and silts. *Petroleum Geoscience*, 4(2), 165-172.
- Mimouni, T. (2014). Thermomechanical characterization of energy geostructures with emphasis on energy piles [Doctoral dissertation, EPFL].
- Minsk, L. D. (1999). Heated Bridge Technology-Report on ISTE A Sec. 6005 Program.
- Mitchell, A. C., Phillips, A., Schultz, L., Parks, S., Spangler, L., Cunningham, A. B., & Gerlach, R. (2013). Microbial CaCO₃ mineral formation and stability in an experimentally simulated high pressure saline aquifer with supercritical CO₂. *International Journal of Greenhouse Gas Control*, 15, 86-96.
- Mohammadzadeh, A., Jazi, F., Ghasemi-Fare, O., & Sun, Z. (2023). Analyzing the feasibility of using shallow geothermal energy to prohibit pavement thermal cracking: field testing. Geo-Congress 2023: Soil Improvement, Geoenvironmental, and Sustainability. <https://doi.org/10.1061/9780784484661.063>.

- Montana Department of Transportation (2002). Montana structures manual – Part II. Retrieved from <https://www.mdt.mt.gov/publications/manuals.aspx>.
- Montoya, B., & DeJong, J. (2015). Stress-strain behavior of sands cemented by microbially induced calcite precipitation. *Journal of Geotechnical and Geoenvironmental Engineering*, 141(6), 04015019.
- Nagai, N., Miyamoto, S., Tsuda, T., & Yamahata, S. (2009). Experimental demonstrations and optimal design conditions of snow-melting system using geothermal and solar energy. *Heat Transfer Summer Conference*, 43581, 767-771.
- Nagy, B., & Szagri, D. (2018). Thermophysical behaviour of reinforced concretes. In *Proc., 6th Int. Conf. Contemporary Achievements in Civil Engineer* (pp. 243-253).
- Ozudogru, T. Y., Ghasemi-Fare, O., Olgun, C. G., & Basu, P. (2015). Numerical modeling of vertical geothermal heat exchangers using finite difference and finite element techniques. *Geotechnical and Geological Engineering*, 33(2), 291-306.
- Pahud, D. (2013). A case study: the Dock Midfield of zurich Airport. *Energy Geostructures: Innovation in Underground Engineering*, 281-296.
- Park, H., Lee, S.-R., Yoon, S., & Choi, J.-C. (2013). Evaluation of thermal response and performance of PHC energy pile: Field experiments and numerical simulation. *Applied Energy*, 103, 12-24.
- Park, H., Lee, S.-R., Yoon, S., Shin, H., & Lee, D.-S. (2012). Case study of heat transfer behavior of helical ground heat exchanger. *Energy and buildings*, 53, 137-144.
- Phillips, A. J. (2013). Biofilm-induced calcium carbonate precipitation: Application in the subsurface [Doctoral dissertation, Montana State University-Bozeman, College of Engineering].
- Phillips, A. J., Cunningham, A. B., Gerlach, R., Hiebert, R., Hwang, C., Lomans, B. P., Westrich, J., Mantilla, C., Kirksey, J., & Esposito, R. (2016). Fracture sealing with microbially-induced calcium carbonate precipitation: A field study. *Environmental science & technology*, 50(7), 4111-4117.
- Phillips, A. J., Gerlach, R., Lauchnor, E., Mitchell, A. C., Cunningham, A. B., & Spangler, L. (2013). Engineered applications of ureolytic biomineralization: a review. *Biofouling*, 29(6), 715-733.
- Pourakbar, M., Plymesser, K., Khosravi M., Gunyol, P., Phillips, A., SEN, T., & Perkins, S. (2021). Task Report No 2: A feasibility of road culvert/bridge deck deicing using geothermal energy. Available online (https://www.mdt.mt.gov/other/webdata/external/research/docs/research_proj/DEICING-GEOTHERMAL/Task-2-Report.pdf).
- Preene, M., & Powrie, W. (2009). Ground energy systems: from analysis to geotechnical design. *Géotechnique*, 59(3), 261-271.
- Radolli, M. & Green, R. (1975). Thermal stresses in concrete bridge superstructures under summer conditions. *54th Annual Meeting of the Transportation Research Board*, 23-36.
- Rafferty, K. D. (2009). Commercial open loop heat pump systems. *Ashrae Journal*, 51(3), 52-59.
- Ramsey, J.W, H.D. Chiang, & R.J. Goldstein. (1982). A Study of the Incoming Longwave Atmospheric Radiation from a Clear Sky. *Journal of Applied meteorology*, 21: 566- 578.
- Rawlings, R., & Sykulski, J. (1999). Ground source heat pumps: a technology review. *Building Services Engineering Research and Technology*, 20(3), 119-129.
- Reynolds, J. & Emanuel, J. (1974). Thermal stresses and movements in bridges. *Journal of the Structural Division*, 100(1), 63–78. <https://doi.org/10.1061/jsdeag.0003705>.

- Roeder, C., & Moorthy, S. (1991). Thermal movements in bridges. *Transportation Research Record 1290*, 135-143.
- Rojas, E., Barr, P., & Halling, M. (2014). Bridge response due to temperature variations (Report No. CAIT-UTC-034). Center for Advanced Infrastructure and Transportation, Utah State University.
- Sani, A. K., Singh, R. M., Amis, T., & Cavarretta, I. (2019). A review on the performance of geothermal energy pile foundation, its design process and applications. *Renewable and Sustainable Energy Reviews*, 106, 54-78.
- Sanner, B., & Knoblich, K. (1991). Advances in drilling and installation for vertical ground heat exchangers. *Proc. Workshop Ground Source Heat Pumps, Montreal, IEA Heat Pump Center*, Report HPC-WR-8.
- Sarbu, I., & Sebarchievici, C. (2014). General review of ground-source heat pump systems for heating and cooling of buildings. *Energy and buildings*, 70, 441-454.
- Shahed, A. M., & Harrison, S. J. (2009). Preliminary review of geothermal solar assisted heat pumps. *Proc. 4th Canadian Solar Buildings Conference*, 104p.
- Shi, X., Du, S., & Fay, L. (2018). Environmental Risks of Snow and Ice Control Materials. *Sustainable Winter Road Operations*, 180-210.
- Sinyak, Y. (1994). Global climate and energy systems. *Science of the total environment*, 143(1), 31-51.
- Tagliabue, L. C., Maistrello, M., & Del Pero, C. (2012). Solar heating and air-conditioning by GSHP coupled to PV system for a cost effective high energy performance building. *Energy Procedia*, 30, 683-692.
- Thompson III, W. H. (2013). Numerical analysis of thermal behavior and fluid flow in geothermal energy piles [Doctoral dissertation, Virginia Tech].
- Trillat-Berdal, V., Souyri, B., & Fraisse, G. (2006). Experimental study of a ground-coupled heat pump combined with thermal solar collectors. *Energy and buildings*, 38(12), 1477-1484.
- Tunstall, L. E., Ley, M. T., & Scherer, G. W. (2021). Air entraining admixtures: Mechanisms, evaluations, and interactions. *Cement and Concrete Research*, 150. <https://doi.org/10.1016/j.cemconres.2021.106557>.
- Turner, E., Plymesser, K., Khosravi, M., Matteson, K., & McNamara, G. (2023). Numerical simulation of a geothermal bridge deck deicing system for use in Montana. Geo-Congress 2023: Soil Improvement, Geoenvironmental, and Sustainability. <https://doi.org/10.1061/9780784484661.062>.
- Turner, E., Khosravi, M., Matteson, K., Plymesser, K., McKittrick, L. Toomani, P. (2024a). Feasibility of a Ground-Source Bridge Deck Deicing System to Mitigate Concrete Deterioration from Temperature Fluctuation. Geo-Congress 2024: : Geotechnical Site and Soil Characterization. <https://doi.org/10.1061/9780784485330.070>.
- Turner, E., Khosravi, M., Matteson, K., Plymesser, K., Toomani, P., McKittrick, L. (2024b). Application of Geothermal Bridge Deck Deicing Systems to Mitigate Concrete Deterioration from Temperature Fluctuation: Model Scale Experiments. (Accepted by ASCE Journal Bridge Engineering).
- van Paassen, L. A., Ghose, R., van der Linden, T. J., van der Star, W. R., & van Loosdrecht, M. C. (2010). Quantifying biomediated ground improvement by ureolysis: large-scale biogROUT experiment. *Journal of Geotechnical and Geoenvironmental Engineering*, 136(12), 1721-1728.
- Venuleo, S., Laloui, L., Terzis, D., Hueckel, T., & Hassan, M. (2016). Microbially induced calcite precipitation effect on soil thermal conductivity. *Géotechnique Letters*, 6(1), 39-44.

- Virmani, Y., Clear, K., Pasko Jr, T., Jones, W., & Jones, D. (1983). Time-to-corrosion of reinforcing steel in concrete slabs. Volume 5: Calcium nitrite admixture or epoxy-coated reinforcing bars as corrosion protection systems. *STIN*, 84, 32578.
- Virmani, Y. P., Jones, W. R., & Jones, D. H. (1984). pH at Corrosion Sites. *Public Roads*, 48(3), 96-102.
- Wan, B., Foley, C., & Komp, J. (2010). Concrete cracking in new bridge decks and overlays (Report No. WHRP 10-05). Department of Civil & Environmental Engineering, Marquette University, Milwaukee, WI.
- Wang, Z., Zhang, N., Lin, F., Ding, J., & Yang, H. (2019). Thermal conductivity of dry sands treated with microbial-induced calcium carbonate precipitation. *Advances in Materials Science and Engineering*, 2019.
- Wardeh, G., Mohamed, M. A. S., & Ghorbel, E. (2011). Analysis of concrete internal deterioration due to frost action. *Journal of Building Physics*, 35(1), 54–82, <https://doi.org/10.1177/1744259110370854>.
- Whiffin, V. S., Van Paassen, L. A., & Harkes, M. P. (2007). Microbial carbonate precipitation as a soil improvement technique. *Geomicrobiology Journal*, 24(5), 417-423.
- White, D., Sritharan, S., Suleiman, M. T., & Chetlur, S. (2005). Identification of the best practices for design, construction, and repair of bridge approaches. *Final Report, Iowa DOT TR-481*, CTRE Report 02-118.
- Williams, G.P. (1973). Heat Requirements of Snow Melting Systems in Canada. Proc., *National Conference on Snow and Ice Control*. Roads and Transportation Association of Canada, Ottawa, April 1973, P. 179-197.
- Wood, C. J., Liu, H., & Riffat, S. B. (2012). Comparative performance of ‘U-tube’ and ‘coaxial’ loop designs for use with a ground source heat pump. *Applied Thermal Engineering*, 37, 190-195.
- Yoshitake, I., Yasumura, N., Syobuzako, M., & Scanlon, A. (2011). Pipe heating system with underground water tank for snow thawing and ice prevention on roads and bridge decks. *Journal of Cold Regions Engineering*, 25(2), 71-86.
- You, S., Cheng, X., Guo, H., & Yao, Z. (2016). Experimental study on structural response of CFG energy piles. *Applied Thermal Engineering*, 96, 640-651.
- Yu, X., Hurley, M. T., Li, T., Lei, G., Pedarla, A., & Puppala, A. J. (2020). Experimental feasibility study of a new attached hydronic loop design for geothermal heating of bridge decks. *Applied Thermal Engineering*, 164, 114507.
- Yu, X., Puppala, A. J., & Zhang, N. (2017). Use of geothermal energy for deicing approach pavement slabs and bridge decks, phase 1. *Texas. Dept. of Transportation. Research and Technology Implementation Office*, No. FHWA/TX-18/0-6872-1.
- Yunovich, M., Thompson, N., & Virmani, Y. P. (2003). Life cycle cost analysis for reinforced concrete bridge decks. *CORROSION 2003, San Diego, California*, 03309.
- Zarella, A., De Carli, M., & Galgaro, A. (2013). Thermal performance of two types of energy foundation pile: helical pipe and triple U-tube. *Applied Thermal Engineering*, 61(2), 301-310.

APPENDIX A: SURVEY OF ROAD MAINTENANCE ACTIVITIES WITHIN MONTANA STATE

The purpose of this study is to investigate the feasibility of the use of a ground-coupled system that utilizes heat energy harvested from the ground as an alternative for deicing/anti-icing bridges and culverts. This study is being conducted through Montana State University. This questionnaire asks about the typical road/bridge maintenance activities in Montana. Your response will be anonymous, and your participation is entirely voluntary. If there are items you do not feel comfortable answering, please skip them. Thank you for cooperation.

- 1- Based on the pavement condition (e.g. low, medium, and high), what are the fundamental strategies of MDT for road maintenance operation in winter?

<i>Strategies and Tactics</i>	<i>Pavement Condition** Within-winter weather event</i>			<i>Pavement Condition** After/end-of-winter weather event</i>		
	<i>Low¹</i>	<i>Medium²</i>	<i>High³</i>	<i>Low¹</i>	<i>Medium²</i>	<i>High³</i>
Anti-icing/Pre-wetting						
Deicing						
Mechanical removal alone						
Mechanical removal and abrasive*						
Mechanical removal and anti-icing						
Mechanical removal and deicing						
Combination of tactics (Please describe them here)						

* Abrasive materials are listed in item 9

** Pavement Condition Categories

<i>Pavement Condition</i>	<i>Pavement Snow and Ice Conditions</i>
¹ Low	Conditions 5 and 6
² Medium	Conditions 3 and 4
³ High	Conditions 1 and 2

Condition 1: Dry/wet pavement conditions.

Condition 2: Snow accumulation occurs occasionally. There are patches of ice or packed snow.

Condition 3: Snow accumulation occurs regularly. Loose snow or slush ranging up to 5 cm (2 inches) are accumulated on the pavement surface.

Condition 4: Snow accumulation occurs regularly. Ice or packed snow with only bare wheel tracks.

Condition 5: Pavement surface is covered with ice and compacted snow.

Condition 6: Pavement surface is covered with significant amounts of snow. Unpassable.

- 2- What chemicals are being used by MDT for deicing/anti-icing bridge decks? In what form?

<i>Chemical</i>	<i>Solid</i>	<i>Temperature Range</i>	<i>Liquid</i>	<i>Temperature Range</i>
Sodium chloride (NaCl)				
Calcium chloride (CaCl ₂)				
Magnesium Chloride (MgCl ₂)				
Calcium Magnesium Acetate (CMA)				
Potassium Acetate (KAc)				
Blended Products				
Other (Please describe them here)				

3- Please provide an estimate of the average annual cost of each product used (per gallon or per ton).

4- Does MDT use any of the following bridge deck deicing/anti-icing technologies?

<i>Bridge deck deicing/anti-icing technology</i>	<i>Yes</i>	<i>No</i>
Pre-wetting of solid chemical- in the stockpile		
Pre-wetting of solid chemical- in the spreader		
Pre-wetting of solid chemical- at the point of discharge		
Liquid application directly on the pavement		
Other (Please list them here)		

5- Please provide an estimate of the average annual cost of each technology used.

6- Please provide an estimate of the average annual maintenance and repair cost due to corrosion.

7- How important are the following aspects associated with using chemicals?

	<i>Very Important</i>	<i>Somewhat Important</i>	<i>Not Important</i>
Cost of material			
Environmental impacts			
Increased corrosion			
Pavement deterioration			
Improved Safety			
Public feedback			

Other (Please list them here)

8- What factors aid in the decision about which chemicals are used?

Cost	
Ease of apply	
Effectiveness	
Availability	
Reduced environmental impacts	
Decreased Corrosion	
Public feedback	

Other (Please list them here)

9- What abrasives materials are being used by MDT?

Crushed Stone	
Sand	
Metallurgical Slag	
Bottom Ash	
Natural River Sand	
Others (Please list them here)	

10- Does MDT have an abrasive clean-up plan in place?

11- How important is entry of abrasives into waterways as a negative aspect of using abrasive?

12- Does MDT have access to the following weather information systems to aid in winter road maintenance activities? At what level?

RWIS ¹	
Weather Channel (Cable)	
NWS ² /NOAA ³	
DTN ⁴	
Other special weather information service (Please list them here)	

¹ RWIS: Road Weather Information System

² NWS: National Weather System

³ NOAA: National Oceanic and Atmospheric Administration

⁴ DTN: Data Transmission Network

APPENDIX B: SURVEY OF CULVERT MAINTENANCE ACTIVITIES WITHIN MONTANA STATE

The purpose of this study is to investigate the feasibility of the use of a ground-coupled system that utilizes heat energy harvested from the ground as an alternative for deicing/anti-icing bridges and culverts. This study is being conducted through Montana State University. This questionnaire asks about the typical road culvert maintenance activities in Montana. Your response will be anonymous, and your participation is entirely voluntary. If there are items you do not feel comfortable answering, please skip them. Thank you for cooperation.

1- What are the fundamental strategies of MDT for culvert maintenance operations in winter?

<i>Strategies and Tactics</i>	<i>Within-winter weather event</i>		<i>After-winter weather event</i>	
	<i>Before Ice Jam</i>	<i>After Ice Jam</i>	<i>Before Ice Jam</i>	<i>After Ice Jam</i>
Anti-icing				
Deicing				
Mechanical removal alone				
Mechanical removal and anti-icing				
Mechanical and removal deicing				
Using electric heat cables				
Combination of tactics (Please describe them here)				

2- Please provide an estimate of the average annual cost of each technology used.

3- Does MDT use any of the following chemicals for anti-icing/deicing of road culverts? In what form?

<i>Chemical</i>	<i>Solid</i>	<i>Temperature Range</i>	<i>Liquid</i>	<i>Temperature Range</i>
Sodium chloride (NaCl)				
Calcium chloride (CaCl ₂)				
Magnesium Chloride (MgCl ₂)				
Calcium Magnesium Acetate (CMA)				
Potassium Acetate (KAc)				
Blended Products				
Other (Please describe them here)				

4- Please provide an estimate of the average annual cost of each product used (per gallon or per ton).

5- How important are the following aspects associated with using chemicals?

	<i>Very Important</i>	<i>Somewhat Important</i>	<i>Not Important</i>
Cost of material			
Environmental impacts			
Increased corrosion			
Pavement deterioration			
Improved Safety			
Public feedback			
Other (Please list them here)			

6- What factors aid in the decision about which chemicals are used?

Cost	
Ease of apply	
Effectiveness	
Availability	
Reduced environmental impacts	
Decreased Corrosion	
Public feedback	
Other (Please list them here)	

7- What factors are considered in the maintenance of culverts?

Water PH	
Abrasion and erosion	
Freeze-thaw	
Inlet fluid temperature	
Crown corrosion due to seepage of ground water that contains road salts	
Other (Please describe them here)	

8- Please provide an estimate of the average annual maintenance and repair cost due to corrosion.

APPENDIX C: REQUIRED INFORMATION

The purpose of this study is to investigate the feasibility of the use of a ground-coupled system that utilizes heat energy harvested from the ground as an alternative for deicing/anti-icing bridges and culverts. This study is being conducted through Montana State University. This questionnaire asks about: 1) the most common type of bridges and culverts in the state of Montana, 2) the availability of time histories of the weather information for 73 stations of Road Weather Information System, RWIS, and 3) Montana statewide car crashes with snow or ice as a contributing factor. Your response will be anonymous, and your participation is entirely voluntary. If there are items you do not feel comfortable answering, please skip them. Thank you for cooperation.

- 1- Typical **bridge culvert** dimensions (Critical culvert size) in sites where icing and maintenance are known to be a problem.

- Bridge Culverts: Structures exceeding 6.1 meters measured along centerline of roadway

<i>Geometry</i>	<i>Steel Culvert</i>		<i>Concrete Culvert</i>
	<i>With Concrete Base</i>	<i>Without Concrete Base</i>	
Cover height			
Cross-dimensional Shape			
Thickness of culvert			
Length of Culvert			
Width of Culvert			
Culvert coating			

- 2- Typical **road culvert** dimensions (Critical culvert size) in sites where icing and maintenance are known to be a problem.

<i>Geometry</i>	<i>Steel Culvert</i>		<i>Concrete Culvert</i>
	<i>With Concrete Base</i>	<i>Without Concrete Base</i>	
Cover height			
Cross-dimensional Shape			
Thickness of culvert			
Length of Culvert			
Width of Culvert			
Culvert coating			

- 3- Typical dimensions of cast-in-place concrete type of bridges in Montana.

<i>Geometry</i>	
Length of span	Varies widely. Most are between 50 and 300 ft.
Width of span	Varies. Most are between 28 and 40 ft.
Deck Thickness	Most common are between 6.5 and 8 inches.
Reinforcement cover	Varies between 0.5 and 2.5 inches

4- Representative mix design for cast-in-place concrete which is approved over the past few years.

Type of Aggregate	
Type of Cement	
Cement-aggregate- water ratio	
Type of additives	
Type of reinforcement	Mostly uncoated rebar < 1980's, mostly epoxy-coated rebar in decks since.
Type of wearing surface	Mostly bare concrete, some PMS overlay or thin epoxy, etc.
Type of protection	

5- Time histories of the following weather information from 73 stations of RWIS?

Weather Information	Duration		
	5 Year	10 Year	30 Year
Average snowfall accumulation			
Average temperature			
Wind Speed			
Pavement surface temperature			
Pavement Temperature (2 to 10 cm below the pavement surface)			

6- How many of Montana statewide car crashes had snow or ice as a contributing factor between 2010-2020??

Year	Ice		Slush		Snow	
	Road	Bridge	Road	Bridge	Road	Bridge
2010						
2011						
2012						
2013						
2014						
2015						
2016						
2017						
2018						
2019						
2020						